UNIVERSITY OF SOUTHAMPTON

Faculty of Engineering and Physical Sciences
Institute of Sound and Vibration Research

Modelling the Effect of Implants and Intracochlear Excitation on Cochlear Mechanics

DOI: 10.5258/SOTON/T0034

Volume 1 of 1

by

David H. Slater

BSc(Eng), MSc(Eng), C Eng, MIET

ORCiD: 0000-0003-3906-993X

A thesis for the degree of
Doctor of Philosophy

June 2022

University of Southampton

Abstract

Faculty of Engineering and Physical Sciences
Institute of Sound and Vibration Research

Doctor of Philosophy

Modelling the Effect of Implants and Intracochlear Excitation on Cochlear Mechanics

by David H. Slater

To help with the design of remedies for the preservation of acoustic hearing for cochlear implant patients, a two chamber finite element model has been developed. The model has been used to quantify the hearing loss that would result from the mechanical stiffening of the round window that is expected to occur as a result of inserting an implant into the scala tympani. Each element or collection of elements of the model can contain an additional compliance to replace that lost from the round window. Each element can also contain an excitation source to emulate an intracochlear actuator for use as part of an electro-acoustic stimulation system. The results of the new model compare closely with those of two established models: one single chamber and one two chamber model, and it enables simulation of the effects of inserting an implant on the mechanics of the cochlea. It has been shown that an achievable bubble could compensate for virtually all of the hearing loss caused by the stiffening of the round window by implantation. It has also been shown that if an actuator could be manufactured that would fit in an implant, it would restore acoustic hearing for frequencies between 100 Hz and 1 kHz. Various actuator technologies have been explored to assess their fundamental capability to meet the required acoustic output when scaled down to an acceptable size to fit in an implant.

Contents

List of Figures

List of Tables

Declaration of Authorship

I declare that this thesis and the work presented in it is my own and has been generated by me as the result of my own original research.

I confirm that:

1. This work was done wholly or mainly while in candidature for a research degree at this University;
2. Where any part of this thesis has previously been submitted for a degree or any other qualification at this University or any other institution, this has been clearly stated;
3. Where I have consulted the published work of others, this is always clearly attributed;
4. Where I have quoted from the work of others, the source is always given. With the exception of such quotations, this thesis is entirely my own work;
5. I have acknowledged all main sources of help;
6. Where the thesis is based on work done by myself jointly with others, I have made clear exactly what was done by others and what I have contributed myself;
7. None of this work has been published before submission

Signed:..... Date:.....

Acknowledgements

Thanks to Professors Steve Elliott and Carl Verschuur, my supervisors, without whose help, advice, guidance and support I would not have been able to complete this project.

To Barbara, my wife.

Definitions and Abbreviations

Symbol	Description
AT	Ampère Turns, a unit of magnetomotive force
NICE	National Institute for Health and Care Excellence
ISVR	Institute of Sound and Vibration Research
BM	Basilar Membrane
B	BM Width
c_0	Velocity of sound
C	Ratio of bubble or actuator width to BM width
CA	Cochlear Aqueduct
CF	Characteristic frequency - sometimes called best frequency
Δ	Length along the cochlea (in the x direction) of an element of the model
f	frequency
L	Uncoiled Cochlea Length
ρ	Density
μ	Dynamic Viscosity
Pr	Prandtl number
FN	No of frequencies used in calculations and plots
XN	No of elements along the cochlea
A_{ST}	Stapes Area
A_{RW}	Round Window Area
A_{CH}	Average Chamber Area
SPL	Sound pressure Level
HL	Hearing Level: SPL in excess of the normal hearing threshold
ECHL	Ear canal pressure rel to Normal Hearing Threshold
c_0	Velocity of sound in cochlear fluids
f	frequency
ϕ	phase
$i = \sqrt{-1}$	
k	wave number
K	Stiffness
M	Mass or inertance
ME	Middle ear
mmf	magneto-motive force

OoC	Organ of Corti
R	Damping Resistance
RW	Round Window
ρ	Density
sf	RW stiffening factor
SNR	Signal to Noise Ratio
ST	Scala Tympani - the lower chamber of the cochlear
SV	Scala Vestibuli (The upper chamber is the SV and the scala media.)
T	Tesla - SI unit of magnetic flux density
TM	Tectorial Membrane
VA	Vestibular Aqueduct
W	Width of the upper and lower chambers of the cochlea, assumed the same for each chamber and constant along the cochlea.
a	BM elasticity exponent
A	BM elasticity co-efficient
p	pressure
p_{U}	Upper chamber pressure
p_{L}	Lower chamber pressure
t	time
v	linear or mechanical velocity
v_{EB}	BM Excitation linear velocity from 1st element
Y_{FC}	Fluid coupling admittance
z_{B}	Basilar Membrane Linear Impedance
Z_{M}	Reverse Middle Ear Volume Impedance
Z_{R}	Round Window Volume Impedance
Z_{b}	Bubble Volume Impedance
ω	angular frequency
NB	Except where otherwise stated, the SI system of units is used for all values used in this thesis.

Chapter 1

Introduction and Contributions

1.1 Project Background

This project aims to contribute to improving the experience of patients with cochlear implants by addressing the mechanics of the loss of acoustic hearing that can follow cochlear implantation, and by modelling proposed potential remedies for both post-implantation hearing loss and previous hearing impairment.

A cochlear implant is now an established remedy that is approved by health regulators in most countries, including NICE in the UK, for patients with profound or severe hearing loss. The system normally consists of two parts: one is an external device; the other is implanted under the scalp and in the inner ear. The external part is similar to a conventional hearing aid that sits behind the ear, and contains the power source in the form of a replaceable battery. It is wired to an assembly of a coil of wire and a magnet that engages with an encapsulated coil of wire that is implanted under the scalp near the ear. When coupled together magnetically, the two coils send power and signals along a small implanted cable to a long thin silicone rubber device, which has 20 or so platinum electrodes spaced along its length. This electrode array is inserted into the lower chamber of the cochlea through or near the round window. The external device contains a microphone that picks up sound waves and passes them through an amplifier to a signal processor, which translates them into signals that are passed through the external and implanted coils to the electrode array. The platinum electrodes inject short pulses of tiny voltages and currents into the cochlear fluid in the lower chamber, and these trigger excitations of the auditory nerve, similar to those triggered by vibration of the cochlear partition in a normal ear. The internal part of a cochlear implant is shown in Figure 2.6, and Figure 2.1 is a diagram of the ear.

1.2 Project Purpose

The purpose of the project is to extend established elemental mathematical descriptions of cochlear mechanics, such as Elliott and Ni (2018), to model the possible adverse effects of cochlear implants on residual hearing, as reported by Verschuur et al. (2016) for example, and to provide a model that will evaluate feasible remedies.

The cochlea contains two chambers, separated by a flexible partition. Movement of the stapes causes a sound wave to pass along the upper chamber, through the partition and into the lower chamber. The passage of sound through the partition causes it to vibrate, and movement of the partition gives rise to the sensation of hearing. Most established models simplify the structure of the cochlea by considering it as a single chamber, in which the acoustic pressure is equal to the difference between the pressures in the upper and lower chambers, which are the mirror image of the other. The movement of the flexible partition between the two chambers is dependent on the pressure difference, and so this simplification is valid, for a normal cochlea with two very similar chambers. However, when a cochlear implant is introduced through the round window to the lower chamber, it changes the acoustic properties of the round window. This reduces the round window's ability to act as a pressure release for low frequency sound waves, and so the amplitude of the wave generated by stapes excitation is diminished. Similarly, any remedy within the implant will occupy only the lower chamber, and so it will no longer be valid to consider the two chambers to be similar. It is therefore necessary to enhance conventional modelling methodology to consider the two chambers independently. Other assumptions that have been made to simplify existing models are reviewed and revised appropriately, according to their validity when an implant is introduced.

The bulk of a cochlear implant is silicone rubber, which has a similar density to the liquids that fill the chambers. The speed of sound in these liquids is also similar to that in silicone rubber, and so the occupation of space by the implant within the lower chamber is not considered to have any significant effect on wave propagation.

Hearing loss occurring after implantation can result from a variety of causes, as described in Chapter 2. The principal effect considered in this thesis (of implantation on low frequency hearing loss) is the stiffening of the round window. Other potential causes of hearing loss resulting from implantation are not considered here, for example, see Causon et al. (2013).

1.3 Overall Approach and Thesis Structure

1.3.1 Approach and Method

The approach taken has been that of deriving the model from well-established first principles, including the laws of conservation of mass and momentum. This is done as an assurance that the model can be enhanced to cover different circumstances, without need to produce a new basic derivation to suit the circumstances of each enhancement. Where it is necessary to make assumptions or approximations that are dependent on the purpose of the model, they are noted and associated with the circumstances concerned; an example of this is the assumption that the action of the basilar membrane is linear, which is valid only at high amplitudes for people with normal hearing, when the cochlear amplifier is not operating. Patients fitted with cochlear implants, however, generally have at least severe if not profound hearing loss and so the non-linearity due to the cochlear amplifier is absent, and the cochlear behaves linearly over the whole dynamic range. At each stage of extending the model, the aim has been to revise only those parts of the formulation that are dependent on the assumption(s) that it is necessary to change.

Using this approach, a single chamber MatLab model was built from first principles independently, and its results compared with the results of previous models. The model was then enhanced to accommodate two different chambers, bounded at the basal end with windows of different impedances. The formulation of this model was verified and validated as follows:

- The model was loaded with data for two identical chambers and windows, and the results were compared with those of established single chamber models.
- Comparisons with established lumped component models have been used to verify the model.
- It was also loaded with the input data used in an early two-chamber model (Peterson and Bogert, 1950), and the results compared.
- The model was verified by comparing its results with those of two distributed models and two lumped component models.

The verification and validation of the model are described in Chapter 4.

As well as the model being used to replicate the acoustic effects of implantation caused by stiffening of the round window, it has also been used to simulate remedies for the resultant hearing loss. The model's results are compared with measured results of acoustical hearing loss that followed implantation. The results of using the model are shown in Chapter 5.

1.3.2 Thesis Structure

Existing models and related research are reviewed in Chapter 2 to assess their applicability to the project purpose and the extent to which they are validated by measurement.

The new model and its derivation are described in Chapter 3, and the model's results are compared with available measured data in Chapter 5. Details of its verification and validation are given in Chapter 4.

Results are given in Chapter 5 of using the model to predict the effect of stiffening the round window.

The inclusion of a bubble within the implant is considered as a potential remedy in Chapter 6.

The alternative remedy of incorporating an intracochlea actuator within the implant is considered in Chapter 7.

Various actuator technologies for intracochlear excitation are explored in Chapter 8 and their feasibility is assessed.

The methodology and the results are discussed and summarized in Chapter 9.

1.4 Contributions

The work reported here extends the widely used single-chamber model of fluid coupling in the cochlea, so that the effect of elements in two dissimilar chambers can be modelled. The resultant computer model is used to simulate the effects on residual acoustic hearing of both implants and proposed modifications to cochlear implants to remedy adverse effects of implantation. In particular the novel contributions of the thesis are:

- A new two-chamber model that has been derived from first principles that takes into account middle ear, round window and aqueduct impedances, together with cochlear fluid compressibility.
- Some minor improvements have been made to methods of calculation of the properties of cochlear components. These are detailed in Appendix A.
- The model has been used to explore the effect on post implantation residual acoustic hearing of introducing a compliant element within the cochlear implant.
- The model has been used to simulate the effects of acoustic excitation sources at various positions within the implant. The characteristics have then been derived

of an intracochlear acoustic actuator for the direct stimulation of residual acoustic hearing in cochlear implant patients, in particular the required volume velocity.

- Various technologies have been reviewed for the implementation of such an intracochlear acoustic actuator, and it is shown that at least one appears feasible if sufficient miniaturization is possible.
- A method has been developed to relate ear canal acoustic pressure in a deaf ear to that in a normal ear, so that the same hearing sensation occurs in each case.

1.5 Publications

- A presentation was given at an internal conference of the Signal Processing and Control Group of ISVR in June 2018.
- A poster was presented at the British Cochlear Implant Group AGM and Annual Conference in April 2019.
- A poster was presented at the Basic Acoustic Science Annual Conference in July 2019.
- A poster was presented at the virtual Annual Conference of the British Society of Audiologists in October 2020.
- An abstract for a paper was submitted to be presented at the 2020 Mechanics of Hearing conference, and it has been accepted. Unfortunately, the conference has been postponed, because of the COVID 19 pandemic, and so the paper has yet to be presented or published. The conference has been rescheduled for July 2022, and the paper has been accepted for oral presentation.

Chapter 2

Historical Review of Cochlear Modelling and Cochlear Implants

This literature review is divided into four sections: literature on the cochlea, literature on related measurements, literature on cochlear implants and literature on models of cochlear mechanics.

2.1 The Cochlea

This section sets down information from the literature that has been used to understand the operation of the cochlea, to determine the mechanical properties of its physiological components and to show how the values of these properties have been validated by measurement.

2.1.1 Biology and Physiology

The cochlea is part of the inner ear, and its main function is to convert into nerve impulses the acoustic waves generated in its liquid filled chambers by the movement of the ossicles of the middle ear.

Figures 2.1 and 2.2 show the shapes and relative locations of the components of the ear: the first figure is an overall diagram of the ear, from the inner end of the ear canal to the cochlea; the second shows a cross-section of a single turn of the cochlea, showing the fluid chambers and the Basilar Membrane. Although the cochlea has three fluid chambers, since Reisner's membrane divides the upper chamber; this is thought to be sufficiently flexible not to play an important rôle in the acoustics of the upper chamber. Endolymph and perilymph are the chemically different aqueous liquids on either side of Reisner's membrane that have similar acoustic properties, and

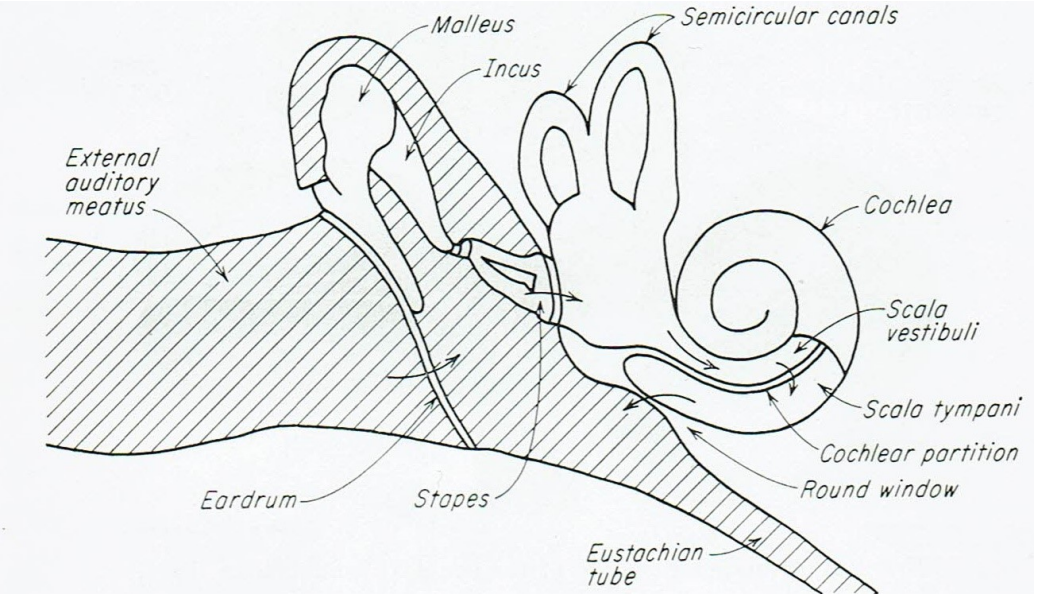

FIGURE 2.1: Diagram of the Ear, after Helmholz (1863). Republished with permission of McGraw Hill LLC, from Experiments in Hearing, Békésy and Wever,1960; permission conveyed through Copyright Clearance Center,Inc.

so effectively there are two fluid chambers, one either side of the basilar membrane. The organ of Corti sits on top of the BM, and together they form the cochlear partition. The organ of Corti contains both inner hair cells, which convert motion into signals in sensory nerves and outer hair cells, which drive the cochlear partition mechanically in response to impulses from efferent nerves. The result is an increase in the motion of the basilar membrane for quiet sounds, and so the effect is referred to as the cochlear amplifier. Because this thesis focuses on the very limited residual acoustic hearing in patients fitted with cochlear implants, it will assume that the cochlear amplifier is not significant and the organ of Corti just acts as a passive sensory system via the inner hair cells. When the cochlear amplifier is not active, the cochlea and its models are said to be passive, and this thesis describes a passive cochlear model and how it can be used to emulate a cochlea with little residual acoustic hearing.

The cochlea is a coiled structure, similar to that of a snail's shell, but the coiling is not thought to play an important part in its mechanics. Luo et al. (2011) and Pietsch et al. (2017) both conclude that the coiled form of the mammalian cochlea evolved to save space within the skull, and that it conferred no direct advantage to hearing.

Citing Ross (1906), van de Water (2012) states that Aristotle postulated the theory that the inner ear was filled with purified air. Aristotle's theory was probably the first recorded mention of the existence and function of the cochlea. The next significant theory was that of Helmholtz [Helmholtz and Helmholtz (1877) and Helmholtz (1885)] in which they postulated that the basilar membrane gave a maximum response to a continuous tone at a point where it was resonant at the frequency of excitation. This was followed by the standing wave theory of Ewald (1899). These two theories prevailed until Zwislocki published his travelling wave theory [Zwislocki-Mościcki

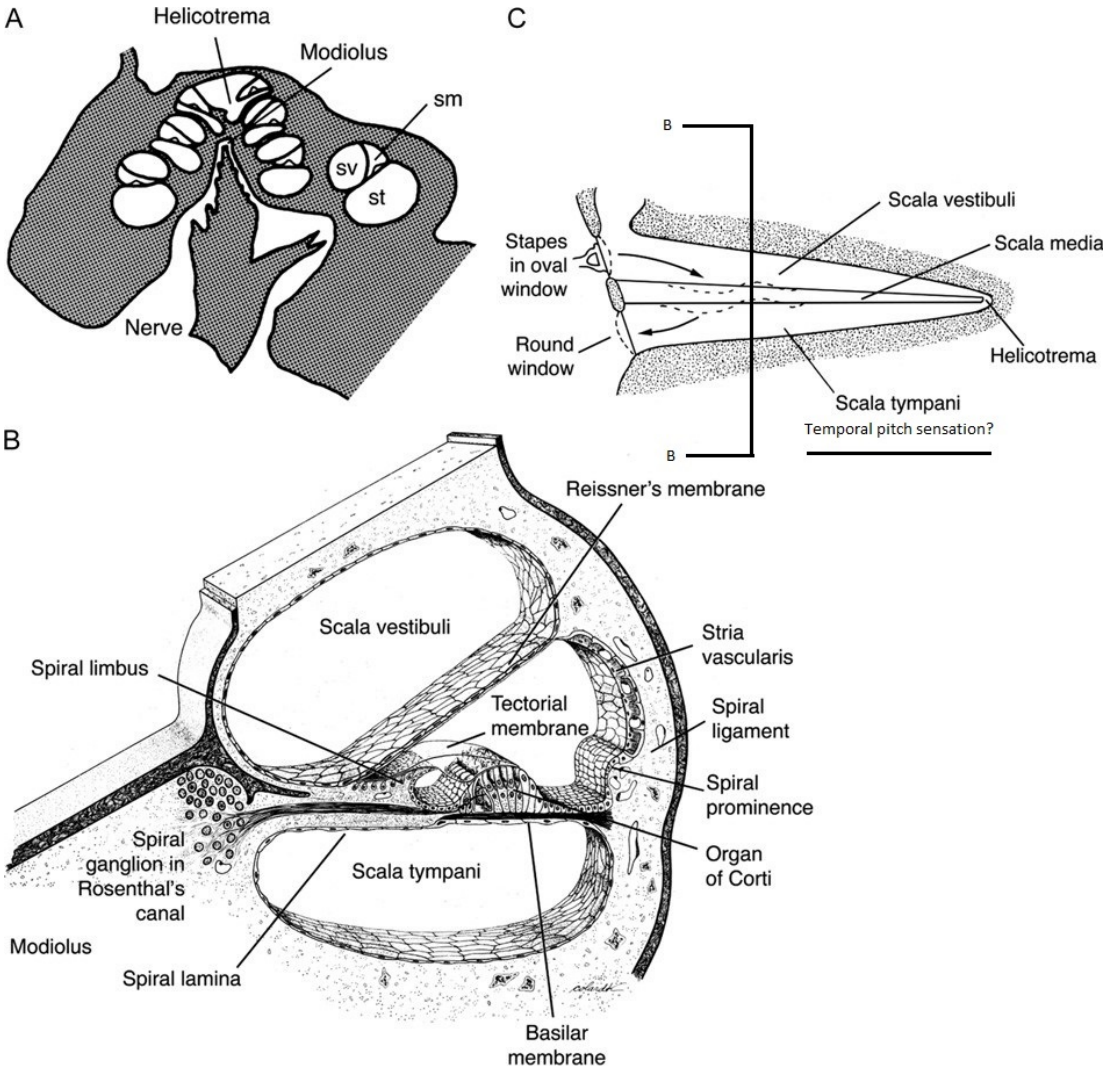

FIGURE 2.2: Diagrams of the Cochlea : (A) In a transverse section of the whole cochlea, the cochlear duct is cut across several times as it coils round and round. Abbreviations: sv, scala vestibuli; sm, scala media; st, scala tympani. (B) The three scalae and associated structures are shown in a magnified view of a cross section of the cochlear duct. Reproduced from Fawcett (1986), Fig. 35.11. (C) The path of vibrations in the cochlea is shown in a schematic diagram in which the cochlear duct is depicted as unrolled. Republished with permission of Brill, from Pickles (2012); permission conveyed through Copyright Clearance Center, Inc.

(1948) and Zwislocki (1950)]. This postulated that the excitation of the cochlea by the stapes caused a travelling wave to pass along the upper chamber[1] and the flexible basilar membrane, so that its amplitude increased to just before the resonant point, by which time most of its energy had passed through the BM and into the lower chamber[2]. Beyond that point, the wave became evanescent and diminished rapidly. According to Békésy (1928 and 1929) this theory was originally proposed by Kuile (1900), but there was at that time neither opportunity to validate it against

[1]The upper chamber consists of two acoustically similar spaces: the scala vestibuli, which is filled with perilymph and the scala media which is filled with endolymph. These are separated by Reisner's membrane, and together, they are referred to as the upper chamber. The scala timpani is referred to as the lower chamber.

measurements, nor to develop it into a mathematical model. This theory was validated for higher frequencies by the Békésy and Wever (1960) series of experiments, reported in English in 1960, from which he concluded that the explanation of cochlear action was that the excitation of the cochlea by the stapes caused a travelling wave, and which Zwislocki expressed in mathematical formulae in 1948. This explanation has remained as the basis of our understanding of the action of the cochlea, with some reservation concerning behaviour near the apex at low frequencies. (The travelling wave theory is similar to, but significantly different from the standing wave theory previously postulated by Ewald (1899), in which a wave is generated from the base to the apex, with a peak amplitude at a place that is dependent on the frequency; the 1899 explanation did not provide as good a match to the performance of the ear that was measured later.)

Von Békésy's 1960 text includes a another, simpler explanation, which he calls the telephone theory, which assumes that the BM vibrates as a rigid beam with suspension whose compliance, and hence amplitude of vibration, increases from base to apex. Clearly, this theory provides no explanation of discrimination of frequencies, which would need to be provided by other mechanisms. It remains possible that this is a valid cochlear mechanism for determining the pitch of low frequency tones, in which excitations of nerve cells that are triggered once or more per cycle of the wave are counted in the brain as pulses to compute frequency. Wever (1949) published a book entitled Theory of Hearing, that put forward his alternative explanation, called the (neural) volley or volley-resonance theory. As well as supporting the resonance theory of Helmholtz, this went some of the way to explaining the discrepancy between the measured range of elasticity of the cochlea partition and that required by Zwislocki's travelling wave theory to explain the range of discernible frequencies. Effectively, this suggested that a "place" (travelling wave, standing wave or resonance) mechanism applied to higher frequencies, while a "telephone" mechanism applied to lower frequencies. Békésy and Wever (1960) measured the stiffness of the basilar membrane directly, by two methods: one using hydrostatic pressure in the upper chamber, with the helicotrema blocked (1948 in English); the other using a hair to provide local pressure (1947). The hair-pressure method is useful for showing local variation of elasticity, but the absolute value is too dependent on the shape of the tip of the hair. Von Békésy (1960) notes that the stiffness of the BM varies about one hundred fold from base to apex, and a minor extrapolation of his graph of his measurements shows a ratio of 171. Clearly, this is insufficient to explain a 1000 ratio of the highest and lowest discernible frequencies, when the frequency ratio is proportional to the square root of the stiffness ratio. Steele and Zais (1983) have studied the stiffness of the BM in more detail, taking into account variations of its thickness, width and reinforcement; however, their model does not explain fully the range of frequencies that humans can hear and distinguish. This issue is still under investigation, but it is beyond the scope of this thesis.

Von Békésy's experiments have remained one of the principal sources of measurements of the action of the passive human cochlea.

Having established the broad functional behaviour of the cochlea, it has been necessary to determine the values of the parameters of the model used here. These include the dimensions, mass, damping and stiffness of the basilar membrane, together with the reverse impedance of the middle ear and that of the round window.

Elliott and Ni (2018) summarize the dimensions of the human cochlea; the data provided are the results of measurements made by others on specimens or models. Unless stated otherwise, these values for the human cochlea have been used in the model described here, and are shown in Table 2.1.

Variable	Symbol	Value
Length	L	35 mm
BM width at the base	B_{B}	0.2 mm
BM width at the apex	B_{A}	0.50 mm
Average BM width	B	0.32 mm
Natural frequency at the base	f_{B}	20 kHz
BM Q factor	Q	2.5
Cochlear fluid density	ρ	1000 kg m^{-3}
BM mass per area 1D fluid coupling	m_0	0.28 kg m^{-2}
Average scala area	A_0	0.84 mm^2

TABLE 2.1: Assumed parameters of the elemental passive model for the human cochlea, after Elliott and Ni (2018).

Puria (2003) has measured the reverse impedance of the human middle ear as a function of frequency, and he has derived the parameters of a mass-spring-damper model. His paper shows good correlation between his model and his measured results, as further discussed by Xue et al. (2020). The results of Puria's model have been used for the middle ear in the new model described in this thesis. Nakajima et al. (2009) have similarly measured and modelled the impedance of the round window that is presented to waves in the cochlear fluid, as a function of frequency. They have developed and compared with their measured results a modified spring mass damper model, using six mass damper pairs in a Foster network. In this thesis, it was found more effective to model the round window by making its damping resistance proportional to the square root of frequency and its mass inversely proportional to the square root of frequency, as described in Appendix A.

2.2 Modelling the Action and Physiology of the Basilar Membrane

In 1961, Greenwood proposed an alternative to the exponential taper of BM elasticity from the apex of the cochlea to the base. He validated his equation by comparison

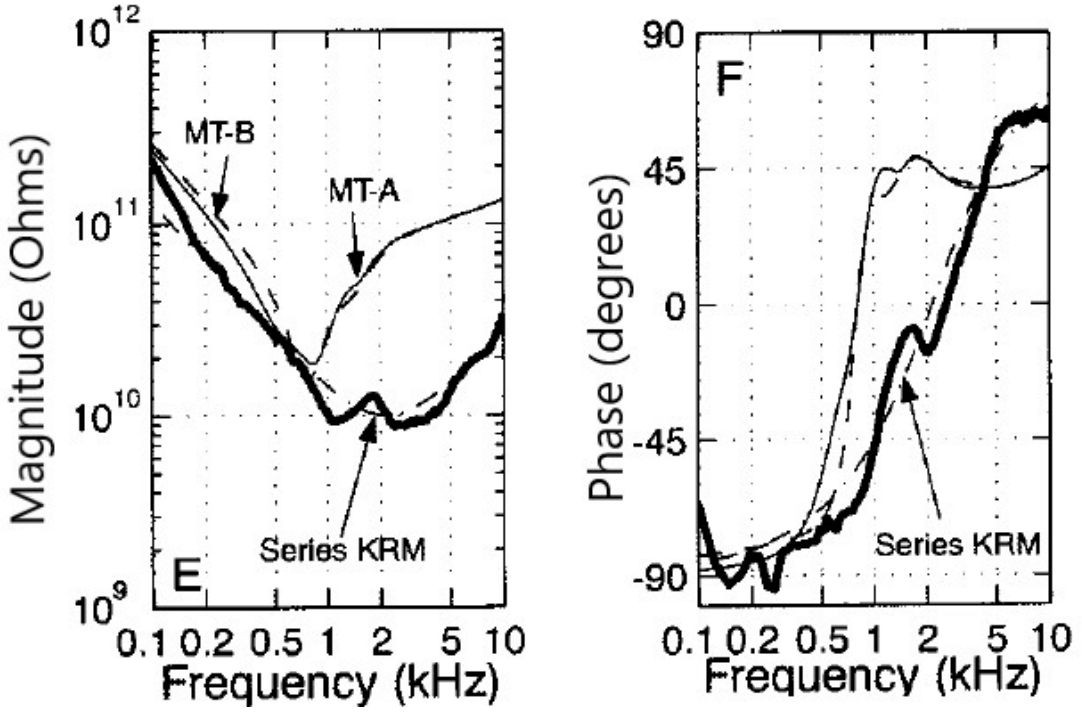

FIGURE 2.3: Reverse Middle Ear Impedance, reprinted with permission from Puria (2003), (Fig. 4), copyright 2003, Acoustic Society of America, showing magnitude and phase for his series Stiffness, Resistance, Mass (KRM) best fit model (_ . _) to his mean measured values. (Also shown are the impedances of the dummy loads used to simulate the ear canal (MTA) and the cochlea (MTB)).

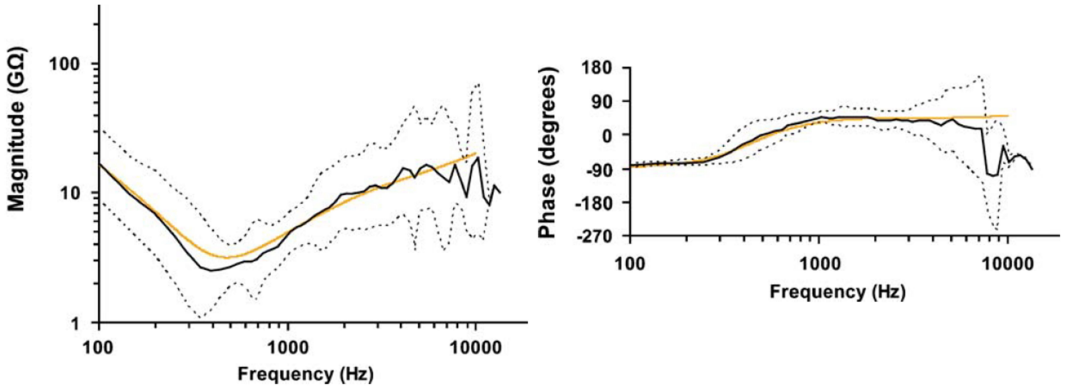

FIGURE 2.4: Round window impedance, ZRW=PST/UStap is plotted with a black line for the mean and dotted lines for the standard deviation. Below 300 Hz, ZRW behaves as a compliance. Above 300 Hz, ZRW becomes dominated by inertia and resistance. This behavior is consistent with distributed loss and inertia, wherein impedance increases as approximately the square root of frequency much as in a system with "skin effect." Behavior of a lumped parameter model for this system is plotted with gold-colored lines. Reprinted by permission from Springer Nature, JARO - Journal of the Association for Research in Otolaryngology, from Differential intracochlear sound pressure measurements in normal human temporal bones,Nakajima et al., © 2009

with his own and the published measurements of others. The current model uses Greenwood's (1961 and 1990) equation to model the variation of best frequency and hence basilar membrane stiffness along the passive cochlea. This gives much better

correlation with von Békésy's measurements, as well as those of Shower and Biddulph (1931) than a pure exponential taper. In 1990, Greenwood published a further paper on the same subject, in which he made comparisons with more recent measurements by others, including some on in vivo non-human mammals. A further 30 years on, there has been no widespread dispute or proposed revision of his equation, although some authors have used the simple exponential taper, presumably for simplicity. Figure 2.5, below, compares Greenwood's equation and its implementation in the present model with both (Békésy, 1949)'s measurements and those of Stevens et al., showing that Greenwood's equation gives a predicted result between the two sets of measurements. Greenwood's equation takes the form:

$$f = A(10^{b(L-x)/L} - k), \text{ or} \tag{2.1}$$

$$f = A(e^{2.303b(L-x)/L} - k), \tag{2.2}$$

where: the constants A=165.4, b=60, and k=0.88, or (2.3)

$$f = A(e^{a(L-x)} - k), \tag{2.4}$$

where: the constant a=138 and (L-x) is expressed in mm. (2.5)

to give maximum and minimum frequencies of 20 kHz and 20 Hz.

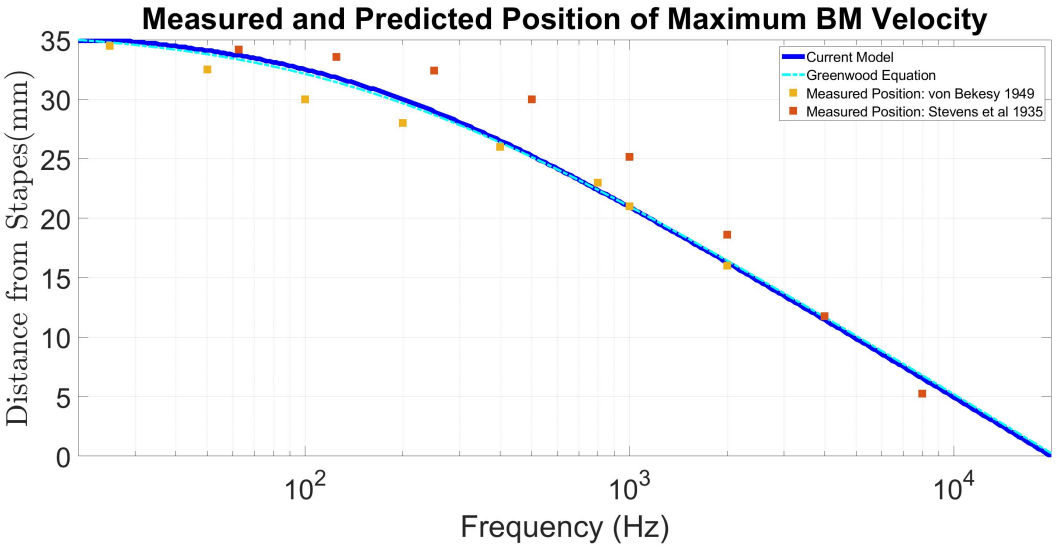

FIGURE 2.5: Greenwood (1990) equation and measurements of Békésy (1949) and of Stevens et al. (1935), together with the results of the current model for the position of maximum response along the cochlea at different excitation frequencies.

2.3 Measurements of Vibration Pattern and Best Place in the Human Cochlea

This section considers the sources of measurements, made by others, that validate Greenwood's equation and the values of the physiological components of the cochlea that it uses. There are a number of established alternatives to the Greenwood's equation, such as a simple exponential taper, and so an appraisal of its validation as a suitable choice for the present model is considered to be worthwhile. As shown in Figure 2.5, Greenwood's equation and hence the present model's implementation of it produces a graph that lies between the direct measurements reported in Békésy (1947) and those reported in Stevens et al. (1935). Neither method of measurement is ideal: the former is prone to influence by the drilling of the cochlear wall, and the latter is prone to influence by temporal coding.

There are three basic techniques that have been used to measure the relationship between frequency and the position of maximum vibration of the cochlea:

- Direct optical microscopic observation of vibrations
- Tonotopic measurement followed by summation of the frequency difference limen (the minimum discernible frequency change) as a function of frequency
- Determination of the relationship between the greatest audible frequency and the position of transition from healthy to dead or missing inner hair-cells

These three methods are discussed in the following subsections.

2.3.1 Measurements of Vibrations

Békésy (1947) made measurements of the location of maximum vibration on both a human preparation and non-biological models, one single chamber and the other two-chamber. Measurements on his non-biological models show reasonable agreement with his measurements on a human cochlea. The greatest frequency at which he could make measurements was 2 kHz; Kringlebotn et al. (1978) reported compatible measurements made by Skarstein over the range 2 - 6 kHz.

He also measured the relationship between the maximum velocity of the BM and the velocity of the stapes. These measurements continue to be useful for validation of the new model described here.

The challenge in making measurements is in doing so without disturbing significantly the action of the cochlea that is being measured. Békésy (1949) claimed to have achieved this by opening the cochlea under water, and eliminating any air bubbles.

Rhode and Cooper (1996) used glass slides to seal the openings that they made, and Dong and Cooper (2006) showed that this was effective until the seal became disrupted after several minutes, which was sufficient time for the measurements to be completed.

There have been many more recent papers reporting basilar membrane action, measured using laser doppler methods, for example. Ren and Nuttall (2001) have published the results of measurements of BM velocity at one position, across a wide range of frequencies for the Gerbil. Olson (2001) has published similar data for intracochlear pressure. These two sets of measurements have been used to validate sophisticated models developed by Yoon et al. (2007) of active and passive cochleas. Rhode and Cooper (1996) have published the results of measured vibrations of the BM using laser methods at discrete locations along the apical turns of chinchillas and guinea-pigs, for click, rather than tone, stimulation of the stapes. There has also recently been considerable work on measuring the motion of the intact organ of Corti using optical coherence tomography, as published, for example, by Cooper et al. (2018) and Ren et al. (2016).

2.3.2 Tonotopic Measurements in Live Humans

Shower and Biddulph (1931) measured the minimum change in frequency detectable, or frequency difference limen, by the ears of five men aged between 20 and 30 years. Stevens et al. (1935) integrated these measured limens to obtain the relationship between frequency and location along the cochlear, assuming that each limen represented a fixed distance from the apex of the cochlea[2]. The graph in Stevens et al. (1935) was used in Békésy (1949) to validate his direct measurements of BM vibration. Direct measurement of BM vibration is very challenging: currently available methods involve mechanical disturbance of the cochlea by drilling holes in the temporal bone, and it is not performed on live humans. The mechanical disturbance can be minimized by sealing the holes with glass plates or by keeping the cochlear submerged in water, but the effectiveness of these techniques is limited. Furthermore, the characteristics of the cochlea change rapidly on death, particularly regarding the cochlear amplifier. New X-ray tomographic imaging techniques are being developed that can be used on living humans, but their resolution is closer to that required to ascertain the position of an implant than to that required to measure BM vibrations. Measurements of the frequency limen can be used to determine the location of

[2] Wright et al. (1987) have used electron microscopy on several ex vivo human subjects, with "normal hearing". The results were gathered from three sources, between them using two slightly different definitions of "normal hearing". (The audiograms were measured before death, whereas the electron microscopy was performed after death.) Their results show that the distribution of inner hair-cells is not quite uniform along the cochlea: the density is reduced near the base. The degree of reduction is dependent on both the age-group and proximity to the base. It is assumed that the reduction of density near the base in older subjects is due to age-related hearing loss, because the degree of reduction increases with age. In foetal subjects and those up to ten years old, there is an approximately linear reduction in density of 25% along the cochlea. This reduction also applies to the 11 - 49 age-group.

maximum BM vibration in living humans, but this technique has potential confounding factors involving neural phase-locking and variations of hair-cell density with both location within the cochlea and with the age of the patient. Although the measurements of frequency limen are now very old, they have continued to be cited comparatively recently, for example in Dooling and Hulse (2014), and they can be used to validate direct measurements and modelled relationships between frequency and BM location, such as Greenwood's equation.

2.3.3 Determination of the relationship between the greatest audible frequency and the position of transition from healthy to dead or missing inner hair-cells

Stevens et al. (1935) damaged the organ of Corti in 20 guinea pigs at some point along its length, and that point correlated with a subsequent change in the audiogram. [3] Although the work done by Wright et al. (1987) on human subjects was more recent, Wright et al. made no comparison between the variation of hair-cell density and the audiogram (which was not published) for each patient. Figure 139 in Stevens and Davis (1938) graphs together the measurements of Shower and Biddulph (1931) and those of Stevens et al. (1935), showing good correlation between the two sets of measurements.

2.4 Electric Excitation of the Cochlea

There are many causes of severe and profound deafness; commonly, such deafness results from death of outer hair cells. When the cochlea does not satisfactorily convert sound into impulses in the auditory nerve, it is now possible to send electrical impulses to the auditory nerve through the cochlear fluid, without using hair-cells or any of the other mechanical components of the cochlea. This technique is known as electric stimulation, and it requires a cochlear implant. An implant provides satisfactory recognition of the verbal content of speech, but it has limitations with speech components at frequencies below about 500 Hz. In many cases, hearing loss is much less at lower frequencies where certain important non-verbal information in speech and music are more readily resolved by natural hearing than by a cochlear implant. Low frequency deafness can often be managed by deploying a conventional hearing aid that sends amplified sound into the ear-canal by air conduction. The technique of combining a cochlear implant with a conventional hearing aid is known as electric acoustic stimulation or EAS.

[3] The procedure for each animal was to record the thresholds for 26 tones between 60 and 12,000 Hz, next to damage the cochlea locally by drilling through the bony wall, and then to repeat the determination of thresholds.

2.4.1 The History of Cochlear Implant Development

According to Mudry and Mills (2013), the first successful cochlear implant was invented by Dr William House in 1969. There had been earlier inventions, but these all stimulated the auditory nerve by direct metallic connection, rather than through the cochlear fluid. According to his obituary in the New York Times, implants of the type invented by House were approved by the Federal Drug Administration in the USA in 1984. An image of a modern Cochlear Implant is shown in figure 2.6, showing both the implanted components, including the electrode array and the internal coupling device that provides a magnetic fixing for the external device and the external part that sits behind the ear. The external part comprises a device containing a microphone, a battery, and the signal processing circuitry, which is wired to the external coupling device that carries power and signals to the implanted part.

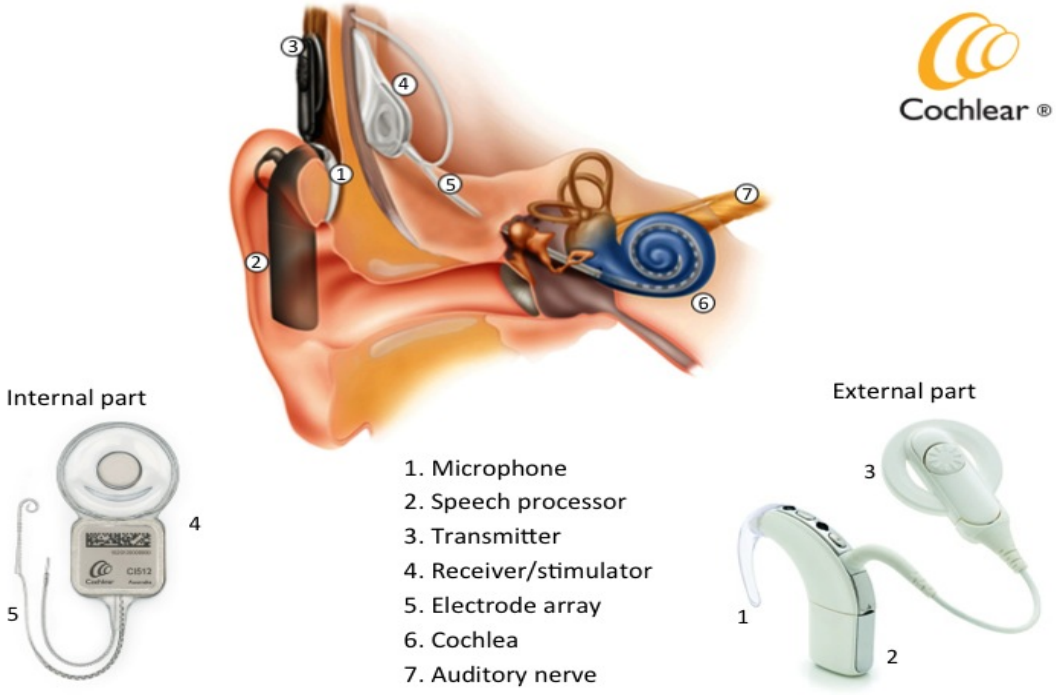

FIGURE 2.6: Example of a cochlear implant manufactured by Cochlear, url: https://lmhofmeyr.co.za/wp-content/uploads/2015/08/Cochlear-implant-website.jpg. (permission to reproduce requested via Cochlear web-site (https://www.cochlear.com/uk/en/connect/contact-us) on 23/10/21 and 22/5/22, as well as from lmhofmeyr@surgeon.co.za, but no response received from any.

Svirsky (2017) records, "only bilaterally, profoundly deaf individuals, with unaided hearing thresholds higher than 90 dB, were considered candidates." Such patients had little residual hearing to lose, but subsequently, hearing thresholds have been progressively relaxed for implant candidates. As a result, those with poor, but useful, acoustic hearing have received implants, and it has been established recently that implantation often impairs acoustic hearing, typically by 20 dB, as measured by

Verschuur et al. (2016). This impairs the ability to recognize speech and the enjoyment of some music.

2.4.2 The Electrode Array and Its Implantation

Details of the surgery involved in implanting an electrode array are beyond the scope of this thesis, but the following outline of the process may be helpful to understanding the implications for the patient's residual acoustic hearing. The array is implanted by drilling a hole from the middle ear in either the centre of the round window, which is about 2 mm in diameter, or through the cochlear wall nearby. The array is 0.5 - 1 mm in diameter, and, when in place, it needs to be a good fit in the drilled hole. If the hole is too small, the array or the round window may be damaged during the insertion, or it may not be fully inserted; if it is too big there could be long term leakage of cochlear fluid, if the array is not adequately sealed into the hole, and it could migrate out of the cochlea. The array is composed mainly of silicone rubber, it is 15 - 32 mm long, and it is often tapered, to facilitate insertion. There are 12 - 24 platinum alloy electrodes spaced along the length that is inserted within the cochlea, and each is individually wired through the silicone rubber to the receiver / stimulator that is just beneath the scalp. Some electrodes cover the entire circumference of the array, others cover only half of the circumference, and some arrays have pairs of electrically connected electrodes at each location. The length of each electrode is typically about a quarter of the spacing between electrodes. Some arrays have one electrode that is designed to be outside the cochlea that is used as a reference electrode to return the current injected into those inside the cochlea. Because the cochlea has a curved shape, many electrode arrays rely on the sides of the lower chamber to guide the array around the spiral curve. The chamber is bounded by delicate tissue, which can be damaged by this process. Some arrays are held curved by a metallic stylet that is withdrawn part way through the insertion process; this is designed to avoid tissue damage, but rarely it can result in the array entering the upper chamber; such arrays are normally relatively short and designed to enter only the first turn of the cochlea. The drilling of the round window or the bone can result in fragments of tissue, bone or drill entering the lower chamber, where they can cause foreign body response and growth of fibrotic tissue, see Foggia et al. (2019). The drilling and insertion processes will inevitably cause some trauma, which will initially cause some stiffening of the round window. The round window acts as a pressure release, allowing the stapes to push and pull fluid in and out of the cochlea and hence moving the basilar membrane. Inserting an array through the round window will stiffen it and hence reduce the movement of cochlear fluid and the basilar membrane. Despite these challenges, the vast majority of implantations are beneficial to the patient; however, it is common for implant patients to experience some residual acoustic hearing loss, see Causon et al. (2013), Causon et al. (2015) and Verschuur et al. (2016). When successfully implanted, the electrode array lies in the lower chamber, occupying between one third and two thirds of the

35 mm length of the cochlea from the round window. Its position in the transverse cross-section of the chamber is difficult to predict, and it is likely to vary from one patient to another and along the length of the array in each patient. Acoustically, the position of the array within the chamber will make little difference, because both the speed of sound in the silicone rubber and its density are very similar to those of the cochlear fluid. However, the precise position of the array will have an impact on delivery of the electrical signal to the auditory neurons (spiral ganglion cells) because physical proximity will be important in determining the required current output, current path and spread. The potential benefits of avoiding tissue damage by using shorter arrays are discussed in the following Section. Minimizing the impact of short arrays on electric stimulation is made possible by using electro-acoustic stimulation.

2.5 Combined Electric and Acoustic Stimulation (EAS)

Many cochlear implant candidates have useful acoustic hearing at frequencies below those at which electric stimulation is effective (typically 500 Hz). This hearing is valuable for listening to music, for speech recognition, for hearing traffic noise and for detecting non-verbal clues in speech. The more this acoustic hearing can be enhanced by amplification to improve hearing, the more useful it becomes for speech recognition, as shown in figures 7 and 8 in Imsiecke et al. (2020). For this reason, the benefits have been investigated of combining electric stimulation from a cochlear implant with amplified acoustic excitation via a conventional hearing aid. A further advantage of EAS is that it can allow implantation of a shorter electrode array, which reduces the risk of tissue damage during insertion.

Gstoettner et al. (2008) concludes that outcomes reveal that all subjects performed significantly better with EAS than they did with a hearing aid only; and thus the benefits of EAS and receiving a CI seem to outweigh the risk of losing hearing as a result of the surgery or due to some other cause at a later time. Imsiecke et al. (2020) confirms that, "Speech reception in the enrolled subjects had a negative mean SRT for all tested fitting strategies in the EAS listening mode with background stationary noise, meaning the speech was softer than the noise for the 50% correctly repeated words estimate of most subjects. The performance was significantly better than the performance with electric listening mode and also better in comparison than the acoustic listening mode across fitting strategies. The analysis of the relation between residual hearing, as expressed by low frequency PTA, and SRT confirmed the advantageous effect of ipsilateral residual hearing on speech reception performance reported by several previous studies (Turner et al. 2004; Gantz et al. 2005; Kiefer et al. 2005; Gstoettner et al. 2008). The data show a steep increase in SRT with low-frequency hearing which reaches a plateau with expanded residual hearing comparable to the results reported by Büchner et al. (2009) and Zhang et al. (2010b). In the ICRA listening mode, however, an increase in residual hearing continuously

improves the SRT, indicating the additional benefit of residual hearing in the medium frequency range for fluctuating noise."

Imsiecke et al. (2020) have shown that speech can be recognized when the signal to noise ratio is significantly lower (more onerous) in individually fitted patients with ipsilateral electro-acoustic stimulation than those with electric stimulation only, for both stationary and fluctuating noise. This means that patients with an implant and a conventional hearing aid in the same ear can recognize speech in noisy backgrounds more effectively than those that rely entirely on either source of stimulation alone. [4] The authors conclude (presumably from the graphs in their Figure 8) that for stationary noise, "The data show a sharp increase in SRT with low-frequency hearing which reaches a plateau with expanded residual hearing ..." It is noted that there are no data points plotted on either the EAS in stationary noise or the ICRA EAS fluctuating noise graph for PTAs greater than about 100 dB. Imsiecke et al. (2020) does not state the hearing aid gain used, but it is common practice to use a gain equal to half the hearing loss (see, for example, Kiefer et al. (2005)), so that the combined effects of recruitment, cochlear amplification and hearing aid amplification approximately compensate for the hearing loss. The maximum gain available from a hearing aid used for EAS is about 48 dB (see, for example, Medel's brochure as viewed on 15/06/22: `https://s3.medel.com/pdf/24666CE_r3_1-synchronyEasFS-WEB.pdf`), which suggests that hearing loss greater than about 100 dB cannot be compensated by existing EAS techniques. This is stated on page 970 of Gstoettner et al. (2008) as,"Three subjects (16.6%) had some hearing preservation, but not enough for acoustic amplification, as determined by the provided gain for the hearing aid." From this it can be concluded that greater amplification would extend the benefits of EAS to patients with greater hearing loss than those who can benefit from existing techniques. It is also possible that greater amplification, combined with more advanced compression to avoid discomfort from louder sounds, would have the effect of improving SRT performance by effectively reducing the PTA. This is in line with the personal experience of the author, who has an approximate 50 dB hearing loss (left ear PTA all frequencies), and who finds subjectively that speech recognition improves when hearing aid gain is increased up to the point where feedback and distortion counteract the benefit.

Imsiecke et al. (2020) have also shown that speech recognition thresholds correlate well with pure tone average hearing level values for low frequencies; the slope is 0.04 dB SNR / dB PTA HL for stationary noise and 0.12 dB SNR / dB PTA HL for fluctuating noise [5]. (In this context, PTA is the average of Hearing Level above normal threshold, measured at 125, 250 and 500 Hz. SRT is speech recognition threshold, measured in this context as the signal to noise ratio (SNR) that resulted in 50% correct

[4] Imsiecke et al.'s measurements are explained in their text relating to their figure 7, which appears to be shown above the caption for their figure 8.

[5] Imsiecke et al.'s conclusions are explained in their text relating to their figure 8, which appears to be shown above the caption for their figure 7.

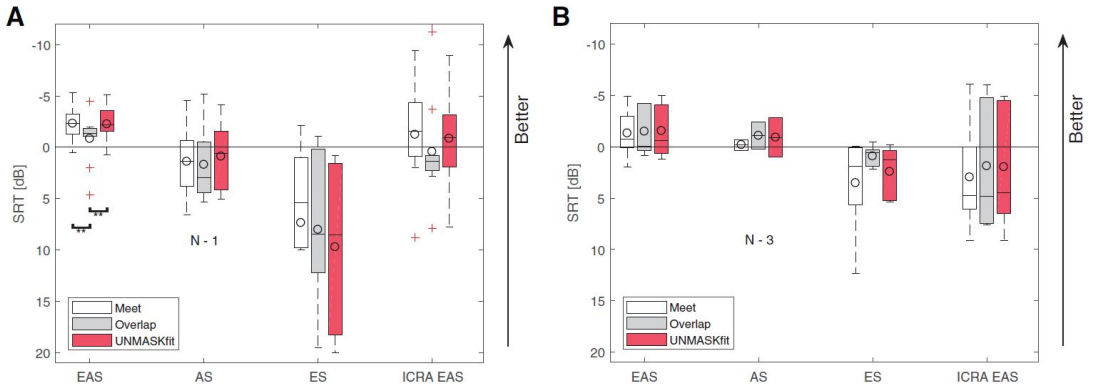

FIGURE 2.7: Figure 7 from Imsiecke et al. (2020) (shown above their caption for their figure 8): Speech reception thresholds for 15 subjects, tested at least 10 months after implantation for conditions EAS, ES, AS, and temporally modulated noise with EAS (ICRA EAS) for grouped subjects with different fitting strategies meet (white), overlap (gray), and UNMASKfit (red). Subjects are grouped according to their fitting, that is, individualized (left) or mean UNMASKfit map (right). Box plots show the group statistics and the circles denote mean values. The text inset N x for acoustic listening mode indicates the number of subjects that could not be tested. AS indicates acoustic only; EAS, electric-acoustic stimulation; ES, electric only stimulation; ICRA EAS, ICRA-5 fluctuating noise with male speaker temporal modulations; UNMASKfit, masking adjusted fitting. This figure is copied from an Open Access article published by Wolters Kluwer Health, Inc., which may be used and reproduced without special permission., see https://www.ncbi.nlm.nih.gov/pmc/about/copyright/

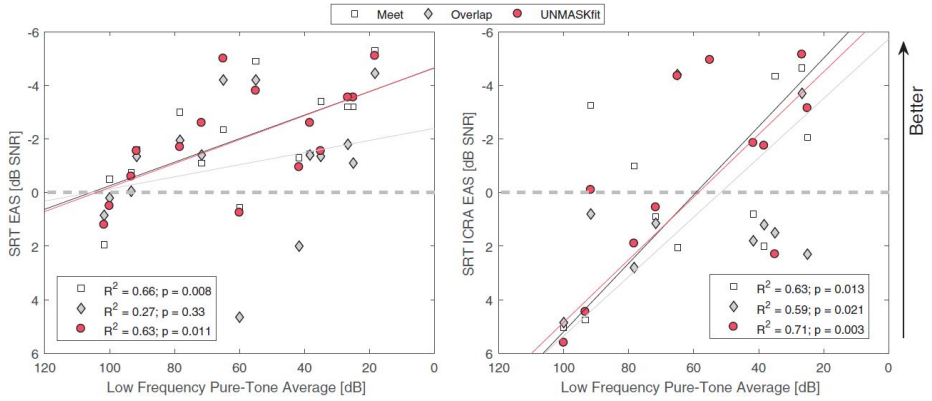

FIGURE 2.8: Figure 8 from Imsiecke et al. (2020) (shown above their caption for their figure 7): Speech Recognition Threshold (SRT) for different fitting strategies: meet, overlap, and UNMASKfit fitting, for the EAS (electric-acoustic stimulation) listening mode in stationary noise (left) and the ICRA (International Collegium of Rehabilitative Audiology) fluctuating noise (right) as a function of the low frequency pure-tone average (125–500 Hz). This figure is copied from an Open Access article published by Wolters Kluwer Health, Inc., which may be used and reproduced without special permission., see https://www.ncbi.nlm.nih.gov/pmc/about/copyright/

recognition of words.) This implies that further improvement in speech recognition could be achieved by greater amplification; this may be due solely to the raising of quieter sounds to a hearing level above the threshold, or due to a combination of this and other causes. Imsiecke et al. conclude that the relation between residual hearing, as expressed by low frequency PTA, and SRT confirmed the advantageous effect of

ipsilateral residual hearing on speech reception performance reported by several previous studies. The maximum amplification that can be achieved with a conventional hearing aid is limited by considerations of acoustic feedback that can be caused by the proximity of the microphone and the actuator. With an intracochlear actuator, as described in Chapter 7, the separation of the microphone and the actuator is much greater, and so greater amplification can be achieved without the risk of feedback.

The reason for deploying contralateral EAS is, presumably, that the deafer ear is normally selected for implantation, and the less deaf ear is a better candidate for air conduction acoustic stimulation, because of the limited amplification achievable with a conventional hearing aid, and the loss of acoustic hearing that often occurs with implantation. Roland Jr et al. (2018) have measured mean pure tone averages for 32 EAS subjects (23 contralateral and 9 ipsilateral), as show in Figure 2.9.

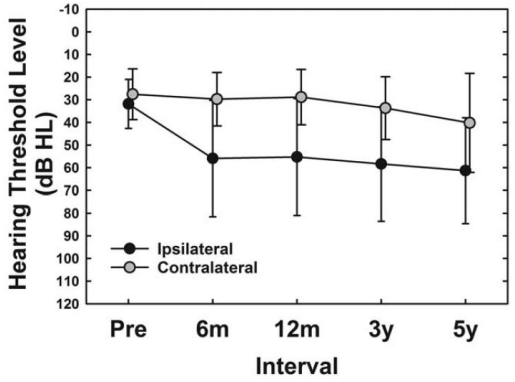

FIGURE 2.9: Fig. 3. from Roland Jr et al. (2018): mean ipsilateral and contralateral three-frequency low-frequency pure-tone average (125, 250, and 500 Hz) over time (N532). Error bars ±1 standard deviation of the mean. Data points dithered for clarification. Reproduced with permission of the publisher. © 2018 The American Laryngological, Rhinological and Otological Society, Inc.

2.6 The Effect of Cochlear Implants on Residual Hearing

2.6.1 Measuring the Impact of Cochlear Implants on Residual Hearing

Implantation has the potential to cause hearing loss by many means, including:

- Reduction of acoustic velocity in the cochlear fluids, caused by stiffening of the round window, obstruction of the scala tympani and callous formation around the implant: Elliott et al. (2016) and Kopelovich et al. (2015)
- Damage caused by inflammation due to the implantation, by infection introduced with the implant, by antibiotics used to prevent infection, or not

prevented by immuno-suppressants used to avoid rejection of the implant: Causon et al. (2013)

- Damage to spiral ganglion neurons caused by excessive electrical stimulation: Kopelovich et al. (2015)
- Mechanical damage to the organ of Corti or the basilar membrane: Dhanasingh and Jolly (2017)

Only the first of these is within the scope of this project. Unfortunately, audiometry provides little evidence to indicate the cause of hearing loss in each case. Some distinction between sudden and gradually operating causes may be made by measuring hearing loss at intervals after implantation, as demonstrated by Quesnel et al. (2016). Some information on causation of hearing loss can be obtained from a time series of audiograms, because some causes are immediate and constant or decrease with time, whilst others increase with time. It is also highly unlikely that an electrode array could cause tissue damage more apically than the location of its distal end, and hence below a certain frequency, but this is useful only when the lengths and insertion depths of the implants are reported.

Kopelovich et al. (2015) provide an overview of the impact of implantation on cochlear action, suggesting acoustic stimulation to augment residual acoustic hearing as a remedy to restore lost hearing. The paper states, "Immediate minor increase in acoustic hearing thresholds after hearing preservation cochlear implantation averaged 12.2 dB and is likely related to insertional trauma or change in fluid dynamics related to placement of the implant in the scala tympani." The conclusion in that paper suggests that hearing loss after implantation is also caused by nerve damage, caused, in turn, by excessive electrical stimulation. A possible further cause mentioned is the growth of callous tissue around the implant, impeding the flow of electric current from the device to the nerve.

Causon et al. (2013 and 2015) provide more detailed overviews of adverse cochlear implant events, although they do not consider round window stiffening specifically.

After implantation through the round window, its impedance will be different once it has healed round the implant; Elliott et al. (2016) have calculated that the stiffness is likely to increase by a factor of about 100 from the pre-implantation value modelled by Nakajima, as a result of inserting a 1 mm diameter implant through a 2 mm diameter round window. For testing the new model, the post-implantation stiffness of the round window has been taken as 170 times that calculated by the author's modified Nakajima model, and as detailed in the Appendix on page 139. This value gave a good match of hearing loss predicted by the present model to acoustic hearing loss published by both Verschuur et al. (2016), measured 3 - 6 months after implantation, and Causon et al. (2015), measured 4 weeks after implantation. The earliest measurements after implantation are used to minimize the effects of time dependent

causes of hearing loss, such as callous growth. (The hearing loss data were kindly provided digitally by Carl Verschuur in private emails sent on 28/5/2019 and 7/6/2019.)

2.6.2 Modelling the Physical Impact of Cochlear Implants

The paper by Elliott et al. (2016) has provided a useful contribution of the effect of an implanted electrode array on the acoustic impedance of the round window. Their method used an equivalent acoustic circuit of lumped components located at the base to predict hearing loss, as shown in Figure 2.10. Equivalent electrical circuits have also been used for lumped component models by, for example, Marquardt and Hensel (2013) and Xue et al. (2020); they are useful for computing the combined effect of components that affect the boundary conditions of the cochlea. As a way of reducing the effect of a stiffened round window, Elliott et al. (2016) proposed implanting a bubble at the base, and they used the equivalent circuit to predict its effect on basilar membrane velocity, and hence acoustic hearing. Since the equivalent circuit can only model the bubble at the base, the bubble was assumed to be in the same position as the round window. In order to investigate the effect on acoustic hearing of positioning the bubble at other locations in the cochlea, a distributed model of cochlear mechanics is needed that accounts for location of components, as described below.

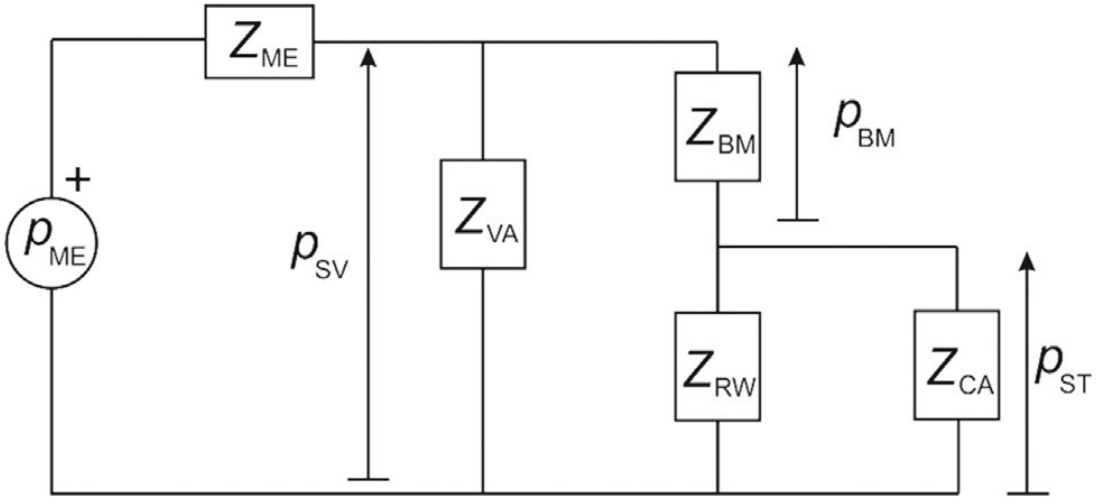

FIGURE 2.10: The impedance model used to study the effect of round window stiffness, included in Z_{RW}, on the pressure across the basilar membrane, p_{BM}, which is the difference between the pressure in the scala vestibuli, p_{SV} and that in the scala tympani p_{ST}, where p_{ME} and Z_{ME} are the Thevenin equivalent source and impedance of the middle ear, Z_{BM} is the impedance across the basilar membrane and Z_{VA} and Z_{CA} are the impedances of the vestibular and cochlear aqueducts. Reproduced licensed by the Creative Commons CC-BY license, which permits unrestricted reproduction, from Elliott et al. (2016). It is stated in the paper that Z_{ME} is the impedance looking out of the cochlea into the middle ear. Elliott et al. used Z_{ME} or M_3 from Puria (2003), who based his modelled value on measurements that were made with an ear canal stimulated by a sound source incorporated into an inserted foam plug.

2.7 Previous Cochlear Models

Distributed Cochlear models can be classified into types as follows:

1. One or two chambers
2. Macro- or micro- mechanical
3. Zero or non-zero longitudinal coupling
4. One, two or three dimensions
5. Viscid or inviscid fluids
6. Active or passive
7. Linear or non-linear
8. Single- or multi-mode

Traditionally, most cochlear models have been simplified by assuming that the mechanical characteristics of the upper and lower chambers are equal, so that the excitation gives rise to symmetrical acoustic waves either side of the basilar membrane. This allows a simplified, single chamber model, with an acoustic pressure equal to the difference between the pressures in the two chambers. The cochlear partition reacts to that pressure difference. At the basal end of the cochlea, the upper chamber is bounded by the oval window, formed from the footplate of the stapes, which is constrained by the reverse impedance of the middle ear, and the lower chamber is bounded by the round window, which acts conventionally as a pressure release. At low frequencies, the impedance of the normal round window is an order of magnitude **less** than that of the middle ear, when viewed from the cochlear. If the round window is stiffened due to implantation by two orders of magnitude, its low frequency impedance becomes an order of magnitude **greater** than that of the middle ear. When considering the acoustic effects of introducing an implant through the round window, these differences are significant, and it is necessary to use a two-chamber model.

Although the cochlea has two acoustically distinct chambers, many finite element models have been simplified to model the acoustics of just one chamber by considering the two chambers of the real cochlea to be similar in every respect. This enables the cochlear model to consider a single sound wave in a single chamber exerting a pressure on the basilar membrane equal to the difference of the pressures in the upper and lower chambers of the real cochlea. The physical representation of this type of model is shown in Allen (1977) as figure 3, which shows just one chamber. The same mathematical approach is used by Neely and Kim (1986) and Elliott and Ni

(2018), for examples. These three models and those like them can be described as symmetric or single chamber models.

Hubbard and Mountain (1996) confirm on their page 80 that to understand the operation of a normal cochlea, a single-chamber model is satisfactory, if one wishes to compute only the BM velocity. This explains why few, if any, two-chamber models have been developed in the last 60+ years. When the two chambers and their boundaries are markedly different, as is the case with an implant, the model needs to consider the two chambers independently, so that the fluid coupling in each chamber is independent of that in the other, and hence, determined solely by the pressure distribution in its own fluid, and not necessarily equal to that of the other chamber.

Whilst each of the symmetric, single chamber models have greatly enhanced the understanding of cochlea mechanics, their assumption of symmetry prevents their use for modelling the effects of stiffening the round window, introducing compressible elements or introducing an actuator into the lower chamber, which are the purpose of this research. As a result, a model has been developed that has two independently configurable chambers, coupled by the basilar membrane. In the present model, the BM reacts to the pressure difference across it, but that difference is not assumed to be twice the pressure in the upper chamber.

Viergever and Kalker (1975) confirm that at low frequencies (30 Hz), the viscous boundary layer thickness in the cochlear fluid is less than one tenth of the scala diameter; at higher frequencies (10 kHz), this diminishes to about one percent of the scala diameter. It is therefore considered that treating the cochlear fluid as inviscid will not introduce any error to the model that is significant for the intended purposes of this research.

For the purpose of this project, it has not been considered necessary to study non-linear or active models, because cochlear implants are provided to those that have very little or no acoustical hearing, as a result of impaired (or absent) cochlear response to pressure waves in the cochlear fluid. In such circumstances, there will be very little amplifying action due to the outer hair cells, and so the nonlinearaties associated with the outer hair-cells are absent and the cochlea will behave almost linearly. Longitudinal coupling along the BM and TM have been shown to be important in active models of the cochlea, but to play a much smaller rôle when the cochlea is passive (Meaud and Grosh (2010). It is thus considered sufficient to use a simple, one-dimensional, single mode, linear model, with no longitudinal mechanical coupling along the basilar membrane.

The model does include provision to model compressibility in the fluid, although this makes little or no difference below about 7 kHz, as confirmed by Geisler and Hubbard (1972).

2.7.1 Two Chamber Models

Hubbard and Mountain (1996) review and interpret the models that constitute the current state of the art at that time. They refer to only two two-chamber models: Peterson and Bogert (1950) and Hubbard and Geisler (1972)). [6] The former is a manually-calculated numerical model, and the latter depended on analogue computing, using a digital computer to set the potentiometers on an analogue computer. A third model is described by (Bogert, 1951); in this, the cochlea is modelled by a large number of discrete electronic components. A paper by Viergever and Kalker (1974) discusses the adequacy of the Peterson and Bogert (1950) one-dimensional model, by comparison with a simplified three-dimensional model. Hubbard and Geisler (1972)) simplify Peterson and Bogert's model by assuming uniform, and similar, cross-sections for the two chambers. Viergever and Kalker (1974) conclude that the Peterson and Bogert model gives good correspondence with their own simplified three dimensional single chamber model for mid and low frequencies away from the location of maximum vibration of the cochlear partition, but not for high frequencies at any position. They show that their simplifications are independent of cochlear geometry. For low and mid frequencies, there is therefore good existing evidence for the validation of the Peterson and Bogert (1950) model, which has been compared with results measured and reported by Békésy (1949 and 1960), provided that appropriate physiological data are used. The paper by Peterson and Bogert has the potential to be useful in providing a comparison with the results of the two-chamber model reported here, when the same physiological data is used. However, the conclusion of Viergever and Kalker (1974) suggests caution in making comparisons at high frequencies.

2.8 Summary

Most recent cochlear models have been either of the lumped component type, or they are distributed single-chamber models. Many, if not all of these publications refer, directly or indirectly, to earlier work, for example, by de Boer (1980, 1984 and 1991), Neely and Kim (1986), Nobili et al. (1998), Steele and Taber (1979a and 1979b), and Zweig et al. (1976). With some significant necessary modifications, the paper by Elliott and Ni (2018) has been used as the basis of the methodology used in developing the model described here. It has also been used to verify the new two-chamber model by making it equivalent to the single chamber model and comparing results.

[6] NB This is not the same paper as Geisler and Hubbard (1972), despite the same two authors publishing it in the same year.

Chapter 3

The Two Chamber Finite Element Model

3.1 Introduction

The established single chamber model has been reformulated on a two chamber basis, in order to investigate the effects of a cochlear implant, a compliant element or an actuator in only one chamber. The equations used by Elliott and Ni (2018) have been re-formulated, removing the assumptions that reduce the two chamber model to one having only a single chamber, and also by adding new terms to distinguish between the two chambers, to allow for compressibility of the fluid and to model compressible elements, which also may contain excitation sources. The excitation sources within the organ of Corti have been retained to facilitate potential future use for modelling an active cochlea, but for the purposes of this project they have all been set to zero.

The cochlea is assumed to consist of two straightened chambers of constant rectangular cross section, separated by the basilar membrane, as shown in figure 3.1, below.

As with most previous models, an elemental approach has been adopted, dividing the length of the cochlea into a large number of small elements. The physical basis of each element within the model is shown in the cross-sectional diagram of an element in figure 3.2, below. Each chamber is now assumed to contain compressible elements that react to the pressure in their own chamber, and that are independent of those in the other chamber, with dynamics modelled by a spring-mass-damper system. The corresponding elements of the two chambers are separated by an incompressible element representing the organ of Corti, with similarly modelled spring-mass-damper dynamics, which moves in response to the difference between the pressures in the two chambers. The normal source of excitation is the stapes / oval window, but sources of excitation are now also modelled within the organ of Corti and within each

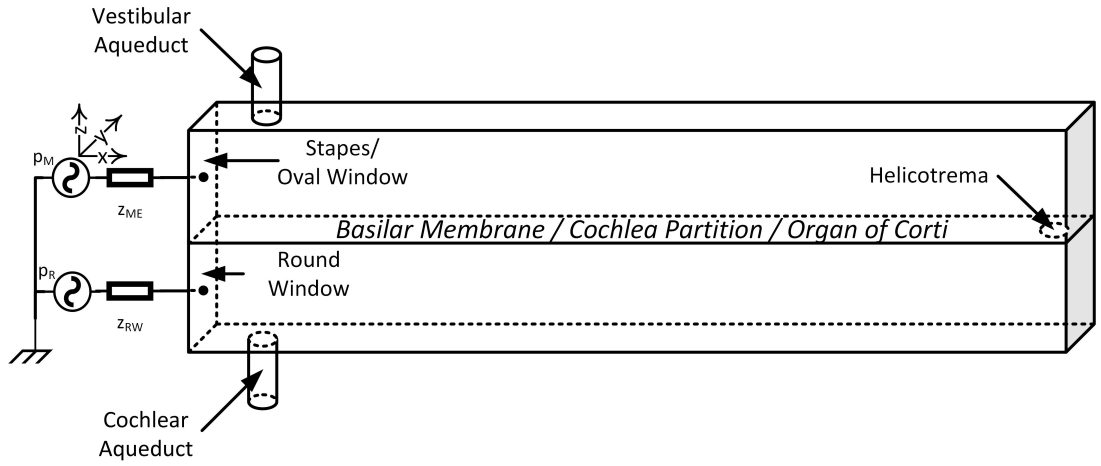

FIGURE 3.1: Model Diagram for Two Independent Chambers - Perspective View.

compressible element. Excitation within the cochlear partition facilitates comparison with single chamber models, and excitation within each compressible element facilitates modelling possible excitation within implants. The width of the basilar membrane is assumed to be constant, and it is given the value B, whereas the width of the compressible elements is given the value C. For simplicity, B and C are considered to be equal in the remainder of this thesis.

A further challenge is to consider the placing of the compressible element in the cross section of the lower chamber, because it is almost impossible to control in practice. Clearly, if the diaphragm of the compressible element is in contact with another structure, its coupling to the cochlear fluid will be adversely affected. As with histological damage, this risk has to be accepted. There are imaging techniques that may enable surgeons to see the position of the implant while it is being inserted; these may be helpful in avoiding this problem.

It is not possible to use the present one-dimensional model to predict the performance of the compressible element as a function of its position within an elemental volume. It is assumed that its position within the cross section of the chamber will make only a small difference to its performance as a pressure release mechanism or an excitation source. Because the real cochlea is three dimensional, a correction factor for the chamber height is included, based on the diaphragm width and velocity profile, as described in subsection 3.2.2. To model precisely the effects of different lateral and radial bubble positions would require a three dimensional model, which is beyond the scope of this thesis. Such an enhancement of the model to enable it to predict the effects of changing the position of a bubble, and actuator or the aqueducts within the elemental volume is included in the list of further work in Chapter 9.

To facilitate modelling of different impedances for the middle ear and the round window for the discrete formulation, the stapes driving element is considered to be a separate Norton velocity source, shunted by a mass-spring-damper impedance within

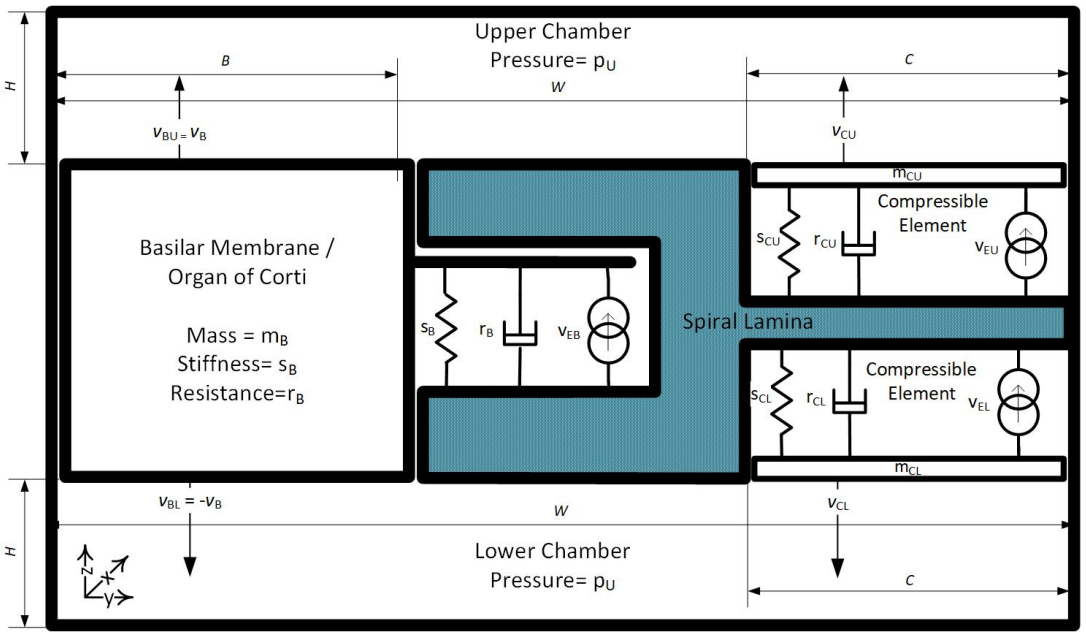

FIGURE 3.2: Cross-section Diagram of Two Independent Chambers of the Cochlea

the first element of the upper chamber, rather than the first element of the basilar membrane, as in the Elliott and Ni single chamber model. The first element of the lower chamber contains a similar velocity source (normally set to zero velocity), shunted by a mass-spring-damper impedance to simulate the dynamics of the round window and a possible excitation source, such as a middle-ear implant attached to a cochlear implant. The second compressible elements in the upper and lower chambers are used to simulate the vestibular and cochlear aqueducts, respectively, whose effect becomes more important when the round window is assumed to be stiffened. A distributed bubble in an implant can be simulated by a succession of compressible elements in the remainder of the cochlea, to make up the length of the bubble.

The model can consider the cochlear fluid to be compressible and hence capable of transmitting normal sound waves, but for simplicity, that feature has not been enabled for producing the graphs in this thesis. The compressibility of the fluid is determined by the speed of sound, c0, and the fluid can be easily modelled as incompressible by setting c0 to 'inf' in the input variables of the Matlab script.

The differential vector equations that describe such a coupled system are outlined in Section 3.2, and the finite difference approximations for these are in Section 3.3, leading to a matrix equation that can be solved to give the coupled response.

3.2 Physical Relationships[1]

At this stage, it is assumed that the wave propagation along the cochlea is governed by one dimensional fluid coupling. That is to say that:

- Other than at the stapes or the round window, the net fluid flow into the chamber is that due to the organ of Corti / basilar membrane and the corresponding compressible element, and so the effects of any flow in the lateral, y direction can be modelled completely by defining an effective chamber height (measured in the z direction). By doing so, all acoustic velocities in the y direction can be considered to be zero.
- The acoustic velocity normal to the BM, in the z direction, reduces linearly to zero from the organ of Corti to the chamber wall.
- There is no longitudinal mechanical coupling in the BM, ie it is locally reacting.
- The effects of viscosity in the fluids occupying the main chambers are considered negligible. Although the present model could be modified to calculate the effect of viscosity on the axial fluid velocity in the two chambers of the cochlea, this has not been included, because the boundary layer thickness is about one twentieth of a chamber diameter or less in the frequency range of interest (100 Hz to 1 kHz), and so the effect on impedance to axial flow will be small; the impedance to axial flow itself has only a small influence on the results of the model. The effects of viscosity in the two chambers will therefore have a negligible effect on the mechanics of the cochlea in the frequency range of interest. However, viscosity has a more significant effect on the impedance of the aqueducts, and this is included in the present model, as explained in Appendix A.

The laws of conservation of mass and momentum apply.

3.2.1 Conservation of Mass

For mass to be conserved, the rate of change of density must be equal and opposite to the rate of change of volume. The linearized equations of mass conservation for a three dimensional acoustic wave in a continuous, homogenous region can be

[1] In this section: scalar quantities (single numbers) are shown in lower case *italics*, spatial vector quantities (those that have both magnitude and direction) are shown in lower case ***bold italics***.

expressed as (Kinsler et al. (2000), equation 5.3.4):

$$\rho_0 \frac{\partial s}{\partial t} + \nabla.(\rho_0 \mathbf{u}) = 0, \text{ where} \tag{3.1}$$

$$s = \frac{\rho_{\text{total}} - \rho_0}{\rho_0} \tag{3.2}$$

ρ_0 = the density at ambient pressure, p_0.

$\mathbf{u}$ = the linear fluid velocity,

with 3 orthogonal components: u_x, u_y, u_z,

$$\nabla.\mathbf{u} = \frac{du_x}{dx} + \frac{du_y}{dy} + \frac{du_z}{dz}$$

$$\frac{\partial \rho}{\partial t} + \rho_0 \nabla.\mathbf{u} = 0, \text{ where} \tag{3.3}$$

ρ = the acoustic density,

$$\frac{\partial \rho}{\partial t} = \frac{\partial \rho}{\partial p}\frac{\partial p}{\partial t} \tag{3.4}$$

When $p = p_0$ and $\rho = \rho_0,\ p = c_0^2 \rho,$ (3.5)

where c_0 = the velocity of sound, and p = the acoustic pressure.

$$\rho = \frac{p}{c_0^2} \tag{3.6}$$

$$\frac{\partial \rho}{\partial p} = \frac{1}{c_0^2} \tag{3.7}$$

When $p = \hat{p}e^{i\omega t}$, $\frac{\partial p}{\partial t} = i\omega p$ (3.8)

Fluid compressibility, $\frac{\partial \rho}{\partial t} = \frac{i\omega p}{c_0^2}$, and so : (3.9)

$$\rho_0 \nabla \cdot \mathbf{u} + \frac{i\omega}{c_0^2} p = 0, \text{ for all } x, z, t \text{ and for both chambers.} \tag{3.10}$$

This is the general acoustic wave equation that applies to all waves that comply with the conditions specified in the first paragraph of this section. Equation (3.10) will be combined with the equation for conservation of momentum.

3.2.2 Conservation of Momentum

The linearized equation of momentum conservation for an inviscid but compressible fluid with no mean (time averaged) flow is given by equation 5.4.10 in Kinsler et al. (2000) as:

$$\rho_0 \frac{d\mathbf{u}}{dt} = -\nabla p, \text{ for all } x, z, t \text{ and for both chambers.} \tag{3.11}$$

Since it is assumed that $\mathbf{u} = \hat{\mathbf{u}}e^{i\omega t}$,

$$\frac{d\mathbf{u}}{dt} = i\omega \mathbf{u} \tag{3.12}$$

$$\mathbf{u} = -\frac{\nabla p}{i\omega \rho_0} \tag{3.13}$$

Equation (3.13) can now be substituted into equation (3.10) to relate the linear velocity of the basilar membrane, $v_B(x)$ to the pressure, $p(x)|_{z=0}$ in each chamber located x m from the stapes, adjacent to the basilar membrane. Before doing so, it is convenient to replace $\nabla \cdot \mathbf{u}$ in equation (3.10) with its orthogonal components, which are a function of only x because $\frac{\partial u_y}{\partial y} = 0$, and it will be shown below that $\frac{\partial u_z}{\partial z}$ is constant with z, proportional to $v_B(x)$:

$$\frac{\partial u_x}{\partial x}(x) + \frac{\partial u_y}{\partial y}(x) + \frac{\partial u_z}{\partial z}(x) + \frac{i\omega}{c_0^2 \rho} p(x)|_{z=0} \quad = \quad 0 \text{ , for all } x, t. \tag{3.14}$$

It is assumed that the wave in the z direction between the BM and the parallel (top and bottom) walls of the cochlea will propagate at approximately the velocity of sound in the cochlear fluid, which is about 1500 m/s. At 20 kHz, the wavelength is 75 mm. The height of each chamber is only a few millimetres, and so the wavelength is much greater than the height. If the wavelength λ of the cochlear wave is large compared with the chamber height, H, then $\frac{\partial u_z}{\partial z}$ is approximately constant with z, so that $|u_z|$ diminishes linearly from the basilar membrane and the compressible element to the opposite wall of the chamber, which are separated by a physical distance of H m. Because the width of the basilar membrane, B and that of the compressible element are less than the full width of the chamber, W, it is necessary to use an effective height, h in place of the actual height, H when calculating $\frac{\partial u_z}{\partial z}$, so that:

$$\frac{\partial u_z}{\partial z} \quad = \quad \frac{v_B}{h} \tag{3.15}$$

The relationship between h and H is given by Elliott et al. (2011):

$$h = \frac{\pi^2 WH}{8B} \tag{3.16}$$

This formula assumes that the BM width is much less than a wavelength and that the BM is hinged to rigid structures at the limits of its width, so that its transverse vibration profile is that of a half sine-wave. It also assumes that there is no longitudinal mechanical coupling within the cochlear partition. These assumptions are appropriate for the purposes of the present model.

To facilitate comparison with models that do not have compressible elements, a single value of h is used here, calculated for the width of the basilar membrane, B, and the velocity of the compressible element is then scaled to become v_{CU} for the compressible element.

$$\frac{\partial u_z}{\partial z} \quad = \quad \frac{v_{CU}}{h} \text{ for compressible element excitation.} \tag{3.17}$$

In the upper chamber, $\frac{\partial u_z}{\partial z}$ is therefore equal to $-\left(v_{CU} + v_B\right)/h$, where v_{CU} is the velocity of the compressible element piston and v_B is the velocity of the basilar membrane. Similarly, in the lower chamber, $\frac{\partial u_z}{\partial z}$ is therefore equal to $-\left(v_{CL} + v_B\right)/h$.

Further simplification is achieved by setting $\frac{\partial u_y}{\partial y}(x) = 0$, in accordance with the assumption that the flow in the lateral, y direction can be ignored. Substituting $-\left(v_{\mathrm{CU}} + v_{\mathrm{B}}\right)/h$ for $\frac{\partial u_z}{\partial z}$ into equation (3.10), it can now be written for the fluid in contact with the basilar membrane in each chamber:

$$\frac{\partial u_x(x)}{\partial x}|_{z=0} - \frac{v_{\mathrm{CU}}(x) + v_{\mathrm{B}}(x)}{h} + \frac{i\omega}{c_0^2\rho} p(x)|_{z=0} = 0, \text{ (upper chamber)} \quad (3.18)$$

$$\frac{\partial u_x(x)}{\partial x}|_{z=0} - \frac{v_{\mathrm{CL}}(x) - v_{\mathrm{B}}(x)}{h} + \frac{i\omega}{c_0^2\rho} p(x)|_{z=0} = 0, \text{ (lower chamber)} \quad (3.19)$$

Similarly, the x-axis component of equation (3.13) can be written:

$$\mathbf{u} = -\frac{\nabla p}{i\omega\rho_0} u_x(x)|_{z=0} \quad (3.20)$$

$$-\frac{\nabla_{\mathbf{x}} p(x)|_{z=0}}{i\omega\rho} = \frac{i}{\omega\rho}\frac{\partial p(x)}{\partial x}|_{z=0} \quad (3.21)$$

Equations (3.18), (3.19) and (3.21) are true for all values of x and t, and equation (3.21) applies to both chambers. For both the upper and lower chambers, $z = 0$ is the height of the layer adjacent to the basilar membrane. In each chamber, the layer of fluid adjacent to the basilar membrane (where $z = 0$) is the focus of these calculations, because it is the pressure in this layer that acts on the impedance of the BM to control its velocity and hence the sensation of acoustic hearing.

By substituting equation (3.21) into equations (3.18) and (3.19), it is will be possible to eliminate all components of the fluid velocity, $\mathbf{u}$ and to express the velocity of the BM, $v_{\mathrm{B}}(x)$ in terms of the pressure in the adjacent fluid, $p(x)|_{z=0}$; this is done after rewriting equations (3.18) and (3.19), in section 3.3, below, to take boundary conditions into account.

3.3 Finite Difference Approximations

To solve the preceding differential equations numerically, the length, L of the cochlea is divided into N equal elements, each of length Δ, as shown in figure 3.3, so that:

$$L = N\Delta \quad (3.22)$$

Assuming that the wavelength of the resulting longitudinal wave, λ, is large compared with the length of an element, Δ, the spatial derivations can be approximated by finite differences. In practice, a rule of thumb is $\Delta < \lambda/6$ is often used. de Boer (1980) provides a formula (his equation 6-ii) for the real part of λ at the point of resonance of the basilar membrane, which is normally considered to be the

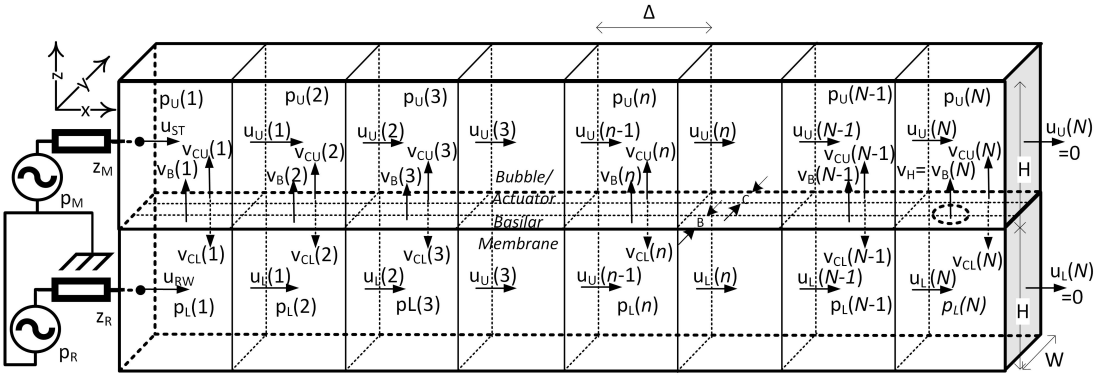

FIGURE 3.3: The Elemental Variables

point of minimum wavelength:

$$\lambda = \pi h \sqrt{\frac{2M_0}{\rho h}} \tag{3.23}$$

Where: M_0 is the superficial mass of the BM, ρ is the fluid density, and h is the chamber height. For an exponential longitudinal elasticity taper in the BM, this value is independent of position of resonance and frequency of resonance. For the physiological values adopted for this thesis, the value of the minimum wavelength calculated using the de Boer formula is 3.2 mm. Using the $\lambda/6$ rule, then Δ should be less than 0.5 mm, and so each chamber of the model should contain more than 70 elemental volumes along its 35 mm length. As a good compromise between execution time and accuracy, the model is normally run with 175 or 350 elements. The present model uses Greenwood's equation, and it also calculates minimum wavelengths over the frequency range of interest varying from 90 mm at the base to 1.7 mm near the apex. λ is calculated from the rate of change of phase with distance along the BM, $\lambda = (\frac{d\Phi}{dx})^{-1}$, where Φ is measured in cycles. This is demonstrated by the spatial domain graphs of frequency response phase (lower left panes) of Figures 5.6 to 5.8, which show the variation of phase with distance along the cochlea for three frequencies covering the range of interest. In each graph, the slope is small and hence λ is large near the base; the slope approaches a maximum, and λ a minimum, at the best place. The same is true for the corresponding graphs in Chapters 6 and 7.

Rather than relating quantities to their longitudinal location by its distance from the stapes, equation (3.21) can now be re-written so that the pressure gradient in the x direction is expressed in terms of the element number, n, and the length of the elements, Δ:

$$\frac{\partial u_x(n)}{\partial x}|_{z=0} = \frac{(u_x(n+1) - u_x(n))|_{z=0}}{\Delta} \tag{3.24}$$

$$u_x(n)|_{z=0} = -\frac{\nabla_{\mathbf{x}} p(n)|_{z=0}}{i\omega\rho} \tag{3.25}$$

$$u_x(n)|_{z=0} = \frac{(p(n) - p(n+1))|_{z=0}}{i\omega\rho\Delta} \tag{3.26}$$

Where $p(n)$is assumed to be at position $x = n\Delta$ and also $z = 0$, ie next to the basilar membrane in element n.

Because equation (3.26) depends on only the properties of the fluid, it applies to both chambers. For the upper chamber, equation (3.18) can be re-written and re-arranged to give $\frac{\partial u_x(n)}{\partial x}|_{z=0}$ in terms of the pressure, $p_U(n)|_{z=0}$ in the element. The expression for $\frac{\partial u_x(n)}{\partial x}|_{z=0}$ in equation (3.24) can then be substituted into the re-arranged equation (3.26), to equate the net flow into the region of an element (LHS of equation 3.27 to the change of volume due to copressibility (RHS). This is done for the fluid layer next to the BM, where $z = 0$. $v_{\mathrm{B}}(n)$ is then computed in terms of the local pressure, $p_{\mathrm{U}}(n)$:

$$\frac{\partial u_x(n)|_{z=0}}{\partial x} - \frac{(v_{\mathrm{CU}}(n) + v_{\mathrm{B}}(n))}{h} = -\frac{i\omega}{c_0^2\rho} p_U(n) \quad (3.27)$$

$$\frac{(u_x(n+1) - u_x(n))|_{z=0}}{\Delta} - \frac{(v_{\mathrm{CU}}(n) + v_{\mathrm{B}}(n))}{h} = -\frac{i\omega}{c_0^2\rho} p_{\mathrm{U}}(n) \quad (3.28)$$

$$\frac{(p_{\mathrm{U}}(n+1) - 2p_{\mathrm{U}}(n) + p_{\mathrm{U}}(n-1))}{i\omega\rho\Delta^2} + \frac{(v_{\mathrm{CU}}(n) + v_{\mathrm{B}}(n))}{h} = \frac{i\omega}{c_0^2\rho} p_{\mathrm{U}}(n) \quad (3.29)$$

$$\frac{h\,(p_{\mathrm{U}}(n+1) - 2p_{\mathrm{U}}(n) + p_{\mathrm{U}}(n-1))}{i\omega\rho\Delta^2} + \frac{(p_{\mathrm{EU}}(n) - p_{\mathrm{U}}(n))}{z_{\mathrm{CU}}(n)} + v_{\mathrm{B}}(n) = \frac{i\omega h}{c_0^2\rho} p_{\mathrm{U}}(n) \quad (3.30)$$

$$\begin{aligned} \text{Where } p_{\mathrm{EU}} &= \text{any excitation pressure within a compressible element} \\ &\quad \text{in the upper chamber (normally zero)} \\ z_{\mathrm{CU}}(n) &= \frac{p_{\mathrm{EU}}(n) - p_{\mathrm{U}}(n)}{v_{\mathrm{CU}}(n)} \end{aligned}$$

This equation can be solved to give an expression for $v_{\mathrm{B}}(n)$.

$$v_{\mathrm{B}}(n) = \frac{i\omega h}{c_0^2\rho} p_{\mathrm{U}}(n) - \frac{p_{\mathrm{EU}}(n) - p_{\mathrm{U}}(n)}{z_{\mathrm{CU}}(n)} - \frac{h\,(p_{\mathrm{U}}(n+1) - 2p_{\mathrm{U}}(n) + p_{\mathrm{U}}(n-1))}{i\omega\rho\Delta^2} \quad (3.31)$$

$$v_{\mathrm{B}}(n) = \frac{i\omega h}{c_0^2\rho} p_{\mathrm{U}}(n) + \frac{p_{\mathrm{U}}(n)}{z_{\mathrm{CU}}(n)} - \frac{p_{\mathrm{EU}}(n)}{z_{\mathrm{CU}}(n)} - \frac{h\,(p_{\mathrm{U}}(n+1) - 2p_{\mathrm{U}}(n) + p_{\mathrm{U}}(n-1))}{i\omega\rho\Delta^2} \quad (3.32)$$

$$v_{\mathrm{B}}(n) = \frac{i\omega h}{c_0^2\rho} p_{\mathrm{U}}(n) + \frac{p_{\mathrm{U}}(n)}{z_{\mathrm{CU}}(n)} - \frac{h\,(p_{\mathrm{U}}(n+1) - 2p_{\mathrm{U}}(n) + p_{\mathrm{U}}(n-1))}{i\omega\rho\Delta^2} - \frac{p_{\mathrm{EU}}(n)}{z_{\mathrm{CU}}(n)} \quad (3.33)$$

For the most basal element (where $n = 1$), the excitation comes from the stapes, as well as the BM or the compressible elements or both, that is $u_x(n-1) = u_{\mathrm{ST}}$.

$$\frac{(u_{\mathrm{ST}} - u_x(1))|_{z=0}}{\Delta} + \frac{(v_{\mathrm{CU}}(1) + v_{\mathrm{B}}(1))}{h} = \frac{i\omega}{c_0^2\rho} p_U(1) \quad (3.34)$$

$$\frac{(p_{\mathrm{U}}(2) - p_{\mathrm{U}}(1))\,|_{z=0}}{i\omega\rho\Delta^2} + \frac{u_{\mathrm{ST}}}{\Delta} + \frac{v_{\mathrm{CU}}(1) + v_{\mathrm{B}}(1)}{h} = \frac{i\omega}{c_0^2\rho} p_U(1) \quad (3.35)$$

$$\frac{h\,(p_{\mathrm{U}}(2) - p_{\mathrm{U}}(1))\,|_{z=0}}{i\omega\rho\Delta^2} + \frac{(p_{\mathrm{M}} - p_{\mathrm{U}}(1))\,|_{z=0}}{z_{\mathrm{M}}} + v_{\mathrm{CU}}(1) + v_{\mathrm{B}}(1) = \frac{i\omega h}{c_0^2\rho} p_U(1) \quad (3.36)$$

Where the reverse middle ear impedance, $z_{\mathrm{M}} = \dfrac{\Delta\,(p_{\mathrm{M}} - p_{\mathrm{U}}(1))}{h u_{\mathrm{ST}}}$

$$\begin{aligned} v_{\mathrm{B}}(1) &= \frac{p_{\mathrm{M}}}{z_{\mathrm{M}}} - \frac{p_{\mathrm{U}}(1)}{z_{\mathrm{M}}} - \frac{h\,(p_{\mathrm{U}}(1) - p_{\mathrm{U}}(2))}{i\omega\rho\Delta^2} - \frac{i\omega h}{c_0^2\rho} p_{\mathrm{U}}(1) + \frac{p_{\mathrm{EU}}(1)}{z_{\mathrm{CU}}(1)} \\ &\quad - \frac{p_{\mathrm{U}}(1)}{z_{\mathrm{CU}}(1)} \end{aligned} \quad (3.37)$$

and for the most apical element:

$$\begin{aligned} v_{\mathrm{B}}(N) &= \frac{p_{\mathrm{M}}}{z_{\mathrm{M}}} - \frac{p_{\mathrm{U}}(N)}{z_{\mathrm{M}}} - \frac{h\,(p_{\mathrm{U}}(N-1) - p_{\mathrm{U}}(N))}{i\omega\rho\Delta^2} - \frac{i\omega h}{c_0^2\rho} p_{\mathrm{U}}(N) + \frac{p_{\mathrm{EU}}(N)}{z_{\mathrm{CU}}(N)} \\ &\quad - \frac{p_{\mathrm{U}}(N)}{z_{\mathrm{CU}}(N)} \end{aligned} \quad (3.38)$$

In section 3.4 below, equations 3.33 and 3.37 to 3.38 are combined into one matrix equation.

Equation (3.33) can be re-written and re-arranged similarly for the lower chamber:

$$v_{\mathrm{B}}(n) = \frac{p_{\mathrm{EL}}(n)}{z_{\mathrm{CL}}(n)} - \frac{p_{\mathrm{L}}(n)}{z_{\mathrm{CL}}(n)} + \frac{h\,(p_{\mathrm{L}}(n+1) - 2p_{\mathrm{L}}(n) + p_{\mathrm{L}}(n-1))}{i\omega\rho\Delta^2} - \frac{i\omega h}{c_0^2\rho} p_{\mathrm{L}}(n) \quad (3.39)$$

Similarly, for the most basal element $(n = 1)$, excitation of the round window is also possible, and so $u_x(n-1) = u_x(0) = u_{\mathrm{RW.}}$

$$v_{\mathrm{B}}(1) = \frac{p_{\mathrm{R}}}{z_{\mathrm{R}}} - \frac{p_{\mathrm{L}}(1)}{z_{\mathrm{R}}} - \frac{h\,(p_{\mathrm{L}}(1) - p_{\mathrm{L}}(2))}{i\omega\rho\Delta^2} - \frac{i\omega h}{c_0^2\rho} p_{\mathrm{L}}(1) + \frac{p_{\mathrm{EL}}(1)}{z_{\mathrm{CL}}(1)} - \frac{p_{\mathrm{L}}(1)}{z_{\mathrm{CL}}(1)} \quad (3.40)$$

and for the most apical element: (3.41)

$$v_{\mathrm{B}}(N) = \frac{p_{\mathrm{R}}}{z_{\mathrm{R}}} - \frac{p_{\mathrm{L}}(N)}{z_{\mathrm{R}}} - \frac{h\,(p_{\mathrm{L}}(N-1) - p_{\mathrm{L}}(N))}{i\omega\rho\Delta^2} - \frac{i\omega h}{c_0^2\rho} p_{\mathrm{L}}(N) + \frac{p_{\mathrm{EL}}(N)}{z_{\mathrm{CL}}(N)} - \frac{p_{\mathrm{L}}(N)}{z_{\mathrm{CL}}(N)} \quad (3.42)$$

In section 3.4 below, equations (3.39) to (3.42) are combined into one matrix equation.

3.4 Matrix Equations[2]

Equations 3.37 for the most basal element and 3.33 for the remainder are then combined to be written as a matrix equation (3.43) for the total linear flow into the region of the upper chamber where $z = 0$. This is then re-written, to give equation (3.44) for $\mathbf{v}_B$, changing $-\frac{h}{i\omega\rho\Delta^2}$ to $+\frac{ih}{\omega\rho\Delta^2}$:

$$\mathbf{0} = \mathbf{v}_B + \mathbf{v}_{CU} + \frac{h\mathbf{u}_{ST}}{\Delta} + \frac{h}{i\omega\rho\Delta^2}\begin{bmatrix} -1 & 1 & 0 & 0 & 0 & 0 \\ 1 & -2 & 1 & 0 & 0 & 0 \\ 0 & 1 & -2 & 1 & 0 & 0 \\ 0 & 0 & \ddots & \ddots & \ddots & 0 \\ 0 & 0 & 0 & 1 & -2 & 1 \\ 0 & 0 & 0 & 0 & 1 & -1 \end{bmatrix}\mathbf{p}_U - \frac{i\omega h}{c_0^2\rho}\mathbf{p}_U \tag{3.43}$$

The terms on the RHS of this equation are: BM velocity, velocity of the compressible element diaphragm, ME velocity, fluid coupling velocity and velocity due to compressibility of the fluid. So that:

$$\begin{aligned}\mathbf{v}_B = {} & \mathbf{Y}_{CU}(\mathbf{p}_U - \mathbf{p}_{EU}) + \mathbf{Y}_M(\mathbf{p}_U - \mathbf{p}_M) \\ & + \frac{ih}{\omega\rho\Delta^2}\begin{bmatrix} -1 & 1 & 0 & 0 & 0 & 0 \\ 1 & -2 & 1 & 0 & 0 & 0 \\ 0 & 1 & -2 & 1 & 0 & 0 \\ 0 & 0 & \ddots & \ddots & \ddots & 0 \\ 0 & 0 & 0 & 1 & -2 & 1 \\ 0 & 0 & 0 & 0 & 1 & -1 \end{bmatrix}\mathbf{p}_U + \frac{i\omega h}{c_0^2\rho}\mathbf{p}_U\end{aligned} \tag{3.44}$$

[2] In this section the following notation is used: two dimensional matrices of are shown in **BOLD UPPER CASE** and vectors (one dimensional matrices) are shown in **bold lower case**.

Where the vectors of velocities and pressures along the upper chamber of the cochlea are defined as:

$$
\begin{aligned}
\mathbf{v}_{\mathrm{B}} &= [v_{\mathrm{B}}(1), v_{\mathrm{B}}(2), \cdots, v_{\mathrm{B}}(N)]^{\mathrm{T}} \\
\mathbf{v}_{\mathrm{CU}} &= [v_{\mathrm{CU}}(1), v_{\mathrm{CU}}(2), \cdots, v_{\mathrm{CU}}(N)]^{\mathrm{T}} \\
\mathbf{u}_{\mathrm{ST}} &= \text{Stapes linear velocity} = [u_{\mathrm{ST}}, 0, \cdots, 0]^{\mathrm{T}} \\
\mathbf{p}_{\mathrm{M}} &= \text{Unloaded stapes / middle ear pressure} = [p_{\mathrm{M}}, 0, \cdots, 0]^{\mathrm{T}} \\
\mathbf{p}_{\mathrm{U}} &= [p_{\mathrm{U}}(1)|_{z=0}, p_{\mathrm{U}}(2)|_{z=0}, \cdots, p_{\mathrm{U}}(N)|_{z=0}]^{\mathrm{T}} \\
\mathbf{p}_{\mathrm{EU}} &= [p_{\mathrm{EU}}(1)|_{z=0}, p_{\mathrm{EU}}(2)|_{z=0}, \cdots, p_{\mathrm{EU}}(N)|_{z=0}]^{\mathrm{T}} \\
\mathbf{Y}_{\mathrm{CU}} &= \begin{bmatrix} 1/z_{\mathrm{CU}}(1) & 0 & 0 & \cdots & 0 \\ 0 & 1/z_{\mathrm{CU}}(2) & 0 & \cdots & 0 \\ 0 & \ddots & \ddots & \ddots & 0 \\ 0 & 0 & 0 & \cdots & 1/z_{\mathrm{CU}}(N) \end{bmatrix} \\
\mathbf{Y}_{\mathrm{M}} &= \frac{h}{\Delta} \times \text{Middle ear linear admittance} = \frac{h}{\Delta} \begin{bmatrix} 1/z_{\mathrm{ME}} & 0 & 0 & 0 \\ 0 & 0 & 0 & 0 \\ \vdots & \vdots & \vdots & \vdots \\ 0 & 0 & 0 & 0 \end{bmatrix} \\
y_{\mathrm{C}} &= \frac{i\omega h}{c_0^2 \rho}
\end{aligned}
$$

Equation (3.44) can be abbreviated by writing the inversion of the fluid coupling impedance matrix as:

$$
\mathbf{Y}_{\mathrm{FC}} = [\mathbf{Z}_{\mathrm{FC}}]^{-1} = \frac{h}{i\omega\rho\Delta^2} \begin{bmatrix} 1 & -1 & 0 & 0 & 0 & 0 \\ -1 & 2 & -1 & 0 & 0 & 0 \\ 0 & -1 & 2 & -1 & 0 & 0 \\ \vdots & \ddots & \ddots & \ddots & \ddots & \vdots \\ 0 & 0 & 0 & -1 & 2 & -1 \\ 0 & 0 & 0 & 0 & -1 & 1 \end{bmatrix} \tag{3.45}
$$

Note the changes of sign in the matrix, so that:

$$
\mathbf{v}_{\mathrm{B}} = \mathbf{Y}_{\mathrm{CU}}(\mathbf{p}_{\mathrm{U}} - \mathbf{p}_{\mathrm{EU}}) + \mathbf{Y}_{\mathrm{M}}(\mathbf{p}_{\mathrm{U}} - \mathbf{p}_{\mathrm{M}}) + \mathbf{Y}_{\mathrm{FC}}\mathbf{p}_{\mathrm{U}} + y_{\mathrm{C}}\mathbf{p}_{\mathrm{U}} \tag{3.46}
$$

Similarly, the matrix equation for the lower chamber is:

$$
\mathbf{v}_{\mathrm{B}} = \mathbf{Y}_{\mathrm{CL}}(\mathbf{p}_{\mathrm{L}} - \mathbf{p}_{\mathrm{EL}}) + \mathbf{Y}_{\mathrm{R}}(\mathbf{p}_{\mathrm{L}} - \mathbf{p}_{\mathrm{M}}) + \mathbf{Y}_{\mathrm{FC}}\mathbf{p}_{\mathrm{L}} + y_{\mathrm{C}}\mathbf{p}_{\mathrm{L}} \tag{3.47}
$$

$$
\begin{aligned}
\text{Where : } \mathbf{p}_{\mathrm{R}} &= \text{Unloaded round window pressure, normally zero} = [p_{\mathrm{R}}, 0, \cdots, 0]^{\mathrm{T}} \\
\mathbf{p}_{\mathrm{EL}} &= [p_{\mathrm{EL}}(1)|_{z=0}, p_{\mathrm{EL}}(2)|_{z=0}, \cdots, p_{\mathrm{L}}(N)|_{z=0}]^{\mathrm{T}} \\
\mathbf{p}_{\mathrm{L}} &= [p_{\mathrm{L}}(1)|_{z=0}, p_{\mathrm{L}}(2)|_{z=0}, \cdots, p_{\mathrm{L}}(N)|_{z=0}]^{\mathrm{T}} \\
\mathbf{y}_{\mathrm{CL}} &= [1/z_{\mathrm{CL}}(1), 1/z_{\mathrm{CL}}(2), \cdots, 1/z_{\mathrm{CL}}(N)]^{\mathrm{T}} \\
\mathbf{y}_{\mathrm{R}} &= \frac{h}{\Delta} \times \text{Round window linear admittance} = \frac{h}{\Delta}\,[1/z_{\mathrm{R}}, 0, \cdots, 0]^{\mathrm{T}}
\end{aligned}
$$

Equations 3.46 and 3.47 can be expressed diagrammatically as shown in figure 3.4, below. (In figures 3.4 to 3.7, elements that have been included for completeness, but not used for this project, are shown in grey.)

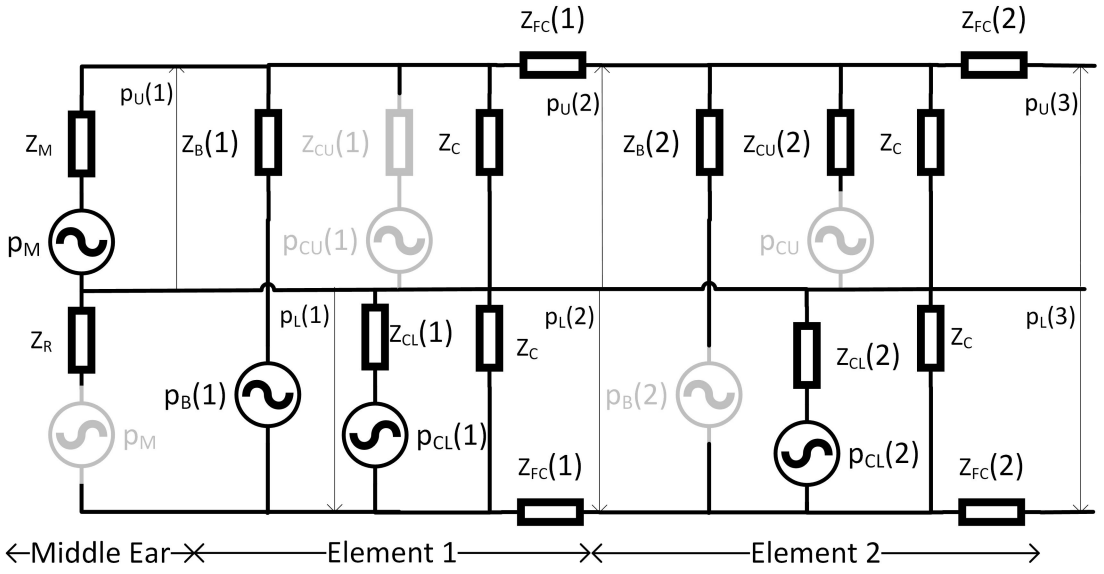

FIGURE 3.4: Circuit Diagram with Pressure Sources of Excitation. (In this diagram and the three following figures, components that are available in the model, but not used, are shown in grey. Unused pressure sources are replaced with short circuits; other unused components are replaced with open circuits.)

The Thevenin pressure sources with their series impedances are then converted to their equivalent Norton velocity sources with their respective admittances in parallel, as shown in figure 3.5, below. $z_{\mathrm{FC}}(n)$ is the fluid coupling impedance between elements n and $n+1$.

As usual, each admittance has the value of the reciprocal of the corresponding impedance in figure 3.4, above, and each velocity source has the value of the corresponding pressure source multiplied by the associated admittance.

Further simplification is achieved by adding velocity sources and admittances that are in parallel, as shown in figure 3.6, below.

Greater clarity can be achieved if the circuit in figure 3.6 is made planar by moving the reference node from the middle to the outside, as in figure 3.7, below.

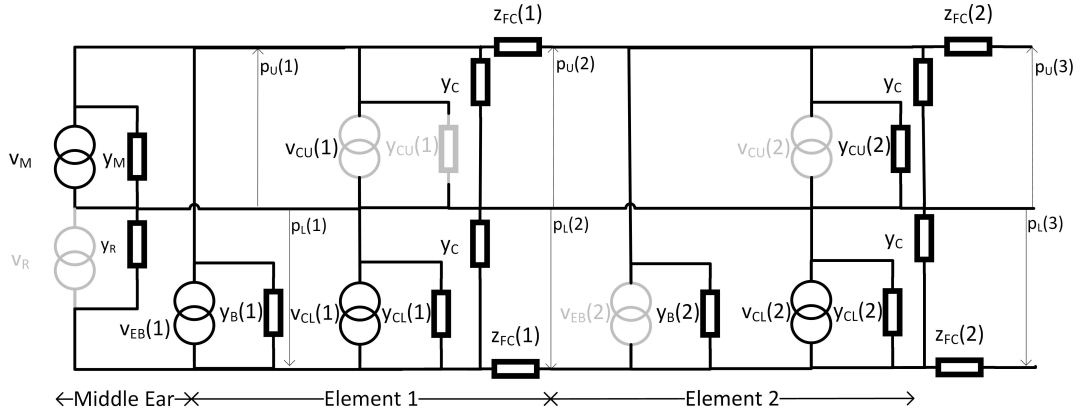

FIGURE 3.5: Circuit Diagram with Velocity Sources. (This is the Norton equivalent of the previous diagram.)

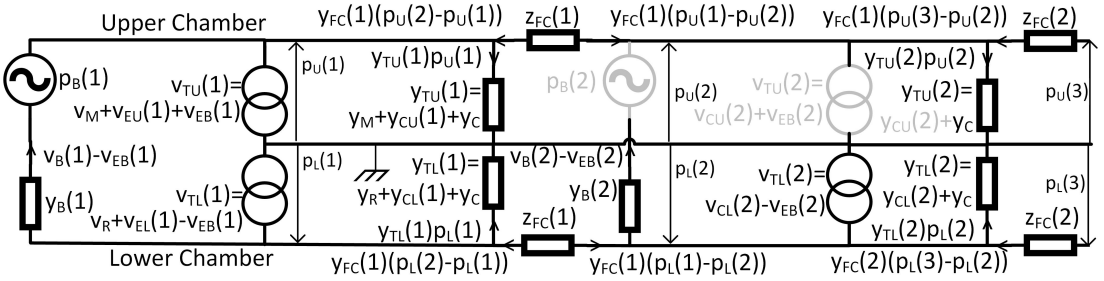

FIGURE 3.6: Circuit Diagram with Parallel Sources and Admittances

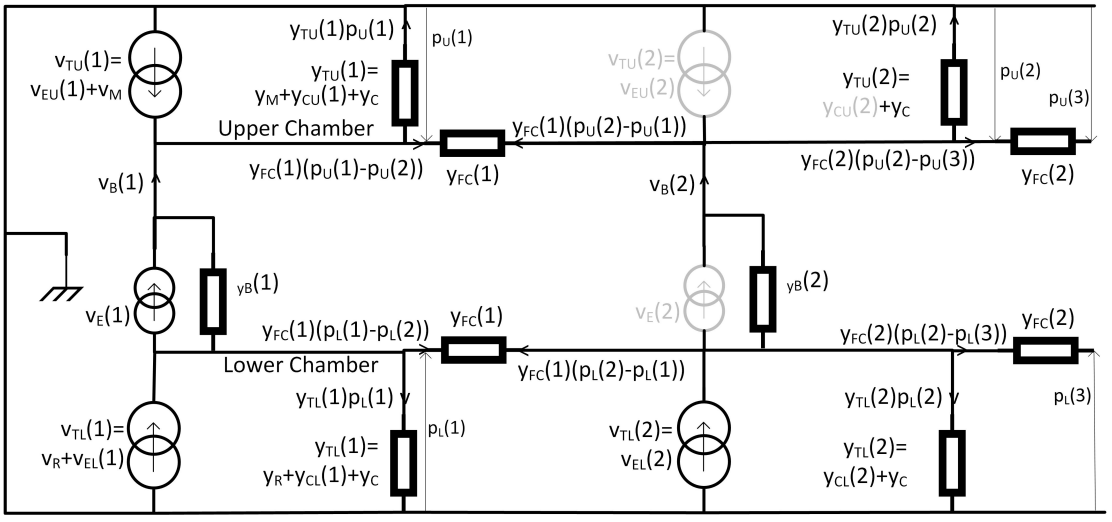

FIGURE 3.7: Planar Circuit Diagram with Parallel Sources and Admittances

Equations (3.46) and (3.47) can be simplified by replacing $[\mathbf{Z}_{\mathrm{FC}}]^{-1}$ with $\mathbf{Y}_{\mathrm{FC}}$ and the component pressure sources and impedances of each element by their corresponding

velocity sources and admittances, and then by their combined values.

$$\begin{aligned}
\mathbf{v}_B &= \mathbf{Y}_{CU}\mathbf{p}_U + \mathbf{Y}_M\mathbf{p}_U + \mathbf{Y}_{FC}\mathbf{p}_U + y_C\mathbf{p}_U - \mathbf{v}_{EU} - \mathbf{v}_M && (3.48)\\
\mathbf{v}_B &= (\mathbf{Y}_{TU} + \mathbf{Y}_{FC})\,\mathbf{p}_U - \mathbf{v}_{TU} && (3.49)\\
\mathbf{v}_B &= -\mathbf{Y}_{CL}\mathbf{p}_L - \mathbf{Y}_R\mathbf{p}_L - \mathbf{Y}_{FC}\mathbf{p}_L - y_C\mathbf{p}_L + \mathbf{v}_{EL} + v_R && (3.50)\\
\mathbf{v}_B &= \mathbf{v}_{TL} - (\mathbf{Y}_{TL} + \mathbf{Y}_{FC})\,\mathbf{p}_L && (3.51)\\
\text{Where } \mathbf{Y}_{TU} &= \mathbf{Y}_{CU} + \mathbf{Y}_M + y_C\\
\mathbf{v}_{TU} &= v_M + \mathbf{v}_{EU}\\
\mathbf{Y}_{TL} &= \mathbf{Y}_{CL} + \mathbf{Y}_R + y_C\\
\mathbf{v}_{TL} &= v_R + \mathbf{v}_{EL}
\end{aligned}$$

Equations (3.49) and (3.51) can now be inverted to give $\mathbf{p}_U$ and $\mathbf{p}_L$ in terms of $\mathbf{v}_B$, and then the difference between the pressure vectors in the upper and lower chambers is computed in equation (3.54), below. This pressure difference, $\mathbf{p}_D$ is also related to $\mathbf{v}_B$ in equation (3.56).

$$\begin{aligned}
\mathbf{p}_U &= [\mathbf{Y}_{TU} + \mathbf{Y}_{FC}]^{-1}\,(\mathbf{v}_{TU} + \mathbf{v}_B) && (3.52)\\
\mathbf{p}_L &= [\mathbf{Y}_{TL} + \mathbf{Y}_{FC}]^{-1}\,(\mathbf{v}_{TL} - \mathbf{v}_B) && (3.53)\\
\mathbf{p}_D = \mathbf{p}_U - \mathbf{p}_L &= [\mathbf{Y}_{TU} + \mathbf{Y}_{FC}]^{-1}\,(\mathbf{v}_{TU} + \mathbf{v}_B) - [\mathbf{Y}_{TL} + \mathbf{Y}_{FC}]^{-1}\,(\mathbf{v}_{TL} - \mathbf{v}_B)\\
\mathbf{p}_D &= \mathbf{Z}_U\mathbf{v}_{TU} - \mathbf{Z}_L\mathbf{v}_{TL} + (\mathbf{Z}_U + \mathbf{Z}_L)\,\mathbf{v}_B && (3.54)\\
\text{Where } \mathbf{Z}_U &= [\mathbf{Y}_{TU} + \mathbf{Y}_{FC}]^{-1} \text{ and } \mathbf{Z}_L = [\mathbf{Y}_{TL} + \mathbf{Y}_{FC}]^{-1}\\
\mathbf{p}_D &= \mathbf{p}_{EB} - \mathbf{Z}_B\mathbf{v}_B && (3.55)\\
\mathbf{Y}_B\mathbf{p}_D &= \mathbf{v}_{EB} - \mathbf{v}_B && (3.56)\\
\text{Where: } \mathbf{Z}_B &= \begin{bmatrix} z_B(1) & 0 & 0 & \cdots & 0\\ 0 & z_B(2) & 0 & \cdots & 0\\ 0 & \ddots & \ddots & \ddots & 0\\ 0 & 0 & 0 & 0 & z_B(N) \end{bmatrix} && (3.57)\\
\text{and } \mathbf{Y}_B &= [\mathbf{Z}_B]^{-1} && (3.58)\\
\mathbf{p}_{EB} - \mathbf{Z}_B\mathbf{v}_B &= \mathbf{Z}_U\mathbf{v}_{TU} - \mathbf{Z}_L\mathbf{v}_{TL} + (\mathbf{Z}_U + \mathbf{Z}_L)\,\mathbf{v}_B && (3.59)\\
\mathbf{v}_{EB} - \mathbf{v}_B &= \mathbf{Y}_B\,(\mathbf{Z}_U\mathbf{v}_{TU} - \mathbf{Z}_L\mathbf{v}_{TL} + (\mathbf{Z}_U + \mathbf{Z}_L)\,\mathbf{v}_B) && (3.60)\\
\mathbf{Z}_B\mathbf{v}_B + (\mathbf{Z}_U + \mathbf{Z}_L)\,\mathbf{v}_B &= \mathbf{Z}_B\mathbf{v}_{EB} - \mathbf{Z}_U\mathbf{v}_{TU} + \mathbf{Z}_L\mathbf{v}_{TL} && (3.61)
\end{aligned}$$

The vector of BM velocity, $\mathbf{v}_B$, can thus be written in terms of the matrices of impedance of the compliant elements in the upper and lower chambers, $\mathbf{Z}_U$, $\mathbf{Z}_L$, and $\mathbf{Y}_B$, the admittance matrix of the BM, together with the vectors of excitation velocities $\mathbf{v}_{EB}$, $\mathbf{v}_{TU}$ and $\mathbf{v}_{TL}$.

$$\begin{aligned}
\mathbf{v}_B &= [\mathbf{Z}_U\mathbf{Y}_B + \mathbf{Z}_L\mathbf{Y}_B + \mathbf{I}]^{-1}\,(\mathbf{v}_{EB} - \mathbf{Z}_U\mathbf{Y}_B\mathbf{v}_{TU} + \mathbf{Z}_L\mathbf{Y}_B\mathbf{v}_{TL}) && (3.62)\\
\mathbf{v}_B &= [\mathbf{Z}_U + \mathbf{Z}_L + \mathbf{Z}_B]^{-1}\,(\mathbf{Z}_B\mathbf{v}_{EB} - \mathbf{Z}_U\mathbf{v}_{TU} + \mathbf{Z}_L\mathbf{v}_{TL}) && (3.63)
\end{aligned}$$

It is this equation that is used in Matlab to compute $\mathbf{v}_B$. It can model compressible fluid and excitation from the stapes, an intracochlear actuator or the round window,

3.5 Stiffening the Round Window

The effect of stiffening the round window by implantation has been simulated by decreasing $\mathbf{y}_R$ and hence increasing $\mathbf{Z}_L$. The associated hearing loss is then calculated. The effect of incorporating a bubble within the implant has also been simulated by increasing $\mathbf{y}_{CL}$, and then calculating the reduction in hearing loss.

In the formulation below, for the passive cochlea, the superficial impedance (pressure per unit linear velocity), $z_B(n)$, of each finite element of the basilar membrane is modelled as a stiffness, s, a resistance, r and a mass, m, per unit area in each case, as shown in the diagram in figure 3.2. Each of these components is expressed as a superficial quantity, that is a value per unit area, relating the pressure to the linear velocity in m/s.

$$z_B(n) = \frac{s(x)}{i\omega} + r(x) + i\omega m(x), \text{ where :} \tag{3.64}$$

$x = n\Delta =$ the distance of element, n from the base.

$m(x) = m_0$, which is assumed constant with x.

$$r(x) = r(1)(e^{-ax} - 0.88e^{aL}), \text{ from Greenwood's Equation (1990)} \tag{3.65}$$

$$s(x) = s(1)(e^{-ax} - 0.88e^{aL})^2, \text{ and} \tag{3.66}$$

$$s(1) = (\omega_{max})^2 m_0, \text{ and} \tag{3.67}$$

$$r(1) = \frac{\sqrt{s(1)m_0}}{Q}, \text{ and so} \tag{3.68}$$

$$\omega_n(x) = \sqrt{\frac{s(x)}{m(x)}} = \text{natural frequency of uncoupled BM at } x. \tag{3.69}$$

Where: $L = N\Delta$ is the length of the cochlea,

ω_{max} = the angular frequency that causes the maximum BM response to be at element 1,

and Q = the Q factor of each finite element, which is assumed independent of x, and

= 2.5

This formulation, or a version based on a simple exponential stiffness taper, is used in many previous models, and the interpretation of $\omega_n(x)$ often implicitly assumes that the maximum BM response occurs where the micromechanical element resonates, so that $\omega_n(x)$ is the "best frequency" for a given place. This is incorrect, because the wave along the cochlea becomes evanescent before the resonant point is reached, and so the maximum response occurs closer to the base than does the resonance. To avoid this

problem, an empirical factor of 1.3 has been used here to implement this model; the value of $\omega_{\max}$ used for calculating $s(1)$ is thus the maximum audible frequency (conventionally 20 kHz) multiplied by 1.3, which causes the maximum BM response to occur at element 1, when the frequency is 20 kHz.
Each finite compressible element is assumed to be governed by a mass, spring, damper system whose impedance and admittance is calculated as:

$$z_C(n) = \frac{s_C(n)}{i\omega} + r_C(n) + i\omega m(n) \tag{3.70}$$

for both upper and lower chambers.

The components of the elements of z_C can be set individually to model the features of the upper and lower chambers, enabling the impedance of a cochlear implant in the lower chamber to be modelled, along with any bubbles within it. The excitation source of the stapes p_M, together with the impedance of the middle ear z_M can be included within the first compressible element of the upper chamber, and the round window impedance, z_R can be modelled by including it within the first element of the lower chamber. Any of the compressible elements of either chamber can be modelled as an excitation pressure source behind a mass-spring-damper series impedance. The second element from the base in each chamber is used to model the respective aqueduct as an impedance, with no spring and no excitation, and so $z_{CU}(2) = z_{VA}$ and $z_{CL}(2) = z_{CA}$. When the round window is stiffened, it has been found necessary to account for the effects of the vestibular and cochlear aqueduct impedances, whose impedances are discussed in Appendix A. All the remaining compressible elements in the upper chamber are normally set to have no excitation source and zero admittance. Those in the lower chamber can be used to simulate bubbles or actuators. The excitation sources in the basilar membrane are also normally set to zero, but they are included to allow future enhancement to model an active cochlea. The round window can also be given an excitation source, to allow for middle ear implant excitation; this is normally set to zero.

The physiological properties of the middle ear / stapes / oval window are taken from Puria (2003). Those of the round window are taken from Nakajima et al (2008). Those of the aqueducts are computed from physical dimension measurements published by Stenfelt (2015). Measured cochlear aqueduct dimensions with ranges have also been published by Anson (1965). In Appendix A, the aqueduct sizes are used to compute the respective aqueduct impedances, Z_{VA} and Z_{CA}, which are then inverted and incorporated into the model as $y_{CU}(2)$ and $y_{CL}(2)$.

The physical properties of a bubble within the implant are computed from first principles, using the published properties of silicone rubber and the best dimensions that can be reasonably considered to be achievable, as described in Chapter 6. Details of the Matlab version used for producing the graphs and calculations have been

obtained by using the Matlab 'ver support' command, and they are as follows: » ver support
MATLAB Version: 9.9.0.1467703 (R2020b)
MATLAB License Number: 648372
Operating System: Microsoft Windows 10 Enterprise Version 10.0 (Build 18363)
Java Version: Java 1.8.0_202-b08 with Oracle Corporation Java HotSpot(TM) 64-Bit Server VM mixed mode.

Chapter 4

Verification and Validation of the Model

Any model that is used for scientific prediction of performance needs to be validated against experimental data. It is generally more expeditious first to verify the code of the model by comparison with the calculated results of existing models that have, themselves, been the subject of peer review and validated by comparison with measurements.

In the context of this thesis, the term verification is used to mean checking that the formulation and coding of the model correctly process the input data and assumptions to calculate the results. Correspondingly, validation means an overall check on whether the model, together with its input data and assumptions, provide an adequate representation of a real cochlea, and that the model is deployed so that its results are fit for purpose.

4.1 Verification

4.1.1 Comparison with a Distributed Single Chamber Model

One way in which the model has been verified is by comparison with the single chamber elemental model developed and published by Elliott and Ni (2018), setting the properties of the two chambers to be identical and as equal as possible to those used in their paper. For example, the shunt admittances of the round window and the stapes have been set to very low values (zero causes ill-conditioned matrices). The compressibility of the cochlear fluid has been set to zero (infinite speed of sound), as have the admittances of the aqueducts (infinite viscosity) and the admittance of the first element of the BM. The excitation source is the first element of the basilar membrane, rather than the stapes. For the comparison, the taper of the basilar

membrane elasticity used in the two chamber model has been set to a simple exponential one, as used in the Elliott and Ni paper, as opposed to the Greenwood equation normally used for the model described in this thesis. A comparison between the position of maximum response along the cochlea against frequency with various measurements and Greenwood's formula has already been made in Section 2.3.3 on page 16. It has not been possible to set the impedance of the first basilar membrane element to zero, as in the Elliott and Ni model, but it has been set to a negligibly low value, which allows an accurate comparison, but avoids division by zero. In their 2018 paper, Elliott and Ni comprehensively compare their model with earlier models, showing consistency and compatibility. Those earlier models have been published and peer reviewed, so that the Elliott and Ni (2018) model, for which the Matlab code is publicly available, is therefore considered to be a suitable model for verification by comparison. The results from the two models are compared in figure 4.1.

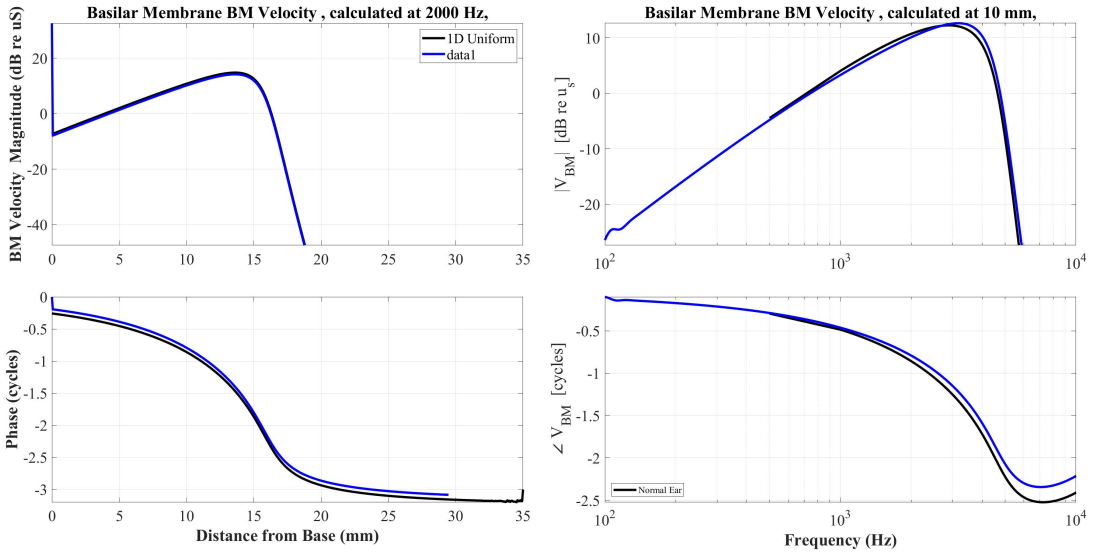

FIGURE 4.1: Comparison with Elliott and Ni (2018) Single-Chamber Model in terms of spatial response at an excitation frequency of 2 kHz (left hand plots) and frequency response at a position 10 mm along the cochlea from the base (right hand plots). Blue line = this model; black line = Elliott and Ni model uniform 1D.

Although the results of using the two models are not precisely the same, the magnitude difference in both the spatial and frequency domains is much less than 1 dB up to the characteristic frequency, and the phase difference is less than 45°. (Three minor differences have been found between the published paper that describes the single chamber model and the Matlab code that implements it. The present model originally used the values and formulae in the paper, rather than the Matlab code. Changing the corresponding values in the present model from those in the paper to those in the code has reduced the minor differences from those found on first comparison. There still remain some very minor differences between the input variables used for each of the compared models, as discussed in Appendix A, which account for the small differences seen in Figure 4.1.

4.1.2 Comparison with a Distributed Two Chamber Model

Peterson and Bogert (1950) describe a two chamber model, but this is some 70 years old. It was solved partly analytically and partly numerically for particular parameters, and so it cannot practicably be run with different input variables to show the effects of including an implant, a bubble or an excitation source within the cochlea. A comparison between the current model and the pressures in the two chambers reported by Peterson and Bogert (1950) without these complications is described in Subsection 4.1.2. Comparisons for models including bubbles and internal excitation have been made with lumped element models that have been published more recently. The results of using these to model the hearing loss with a bubble and an actuator adjacent to the round window are compared with the corresponding results from the present model in Chapters 6 and 7, respectively.

Peterson and Bogert's model 1950 was formulated before suitable digital computers were available, and so the computation was performed manually. Such computations cannot now be repeated at reasonable cost with inputs that simulate an implanted cochlea, nor can they be readily repeated to produce additional output graphs to show, for example, basilar membrane velocity. The graph of pressure at 1000 Hz published as their Fig 14 is shown in Figure 4.2, and that produced by the model described here (using Peterson and Bogert's geometric data) is shown in Figure 4.4. To avoid the singularity that challenged Peterson and Bogert in 1950, damping[1] of the basilar membrane, and the taper of elasticity and damping along the cochlea was set to their simple exponential taper. With these changes, the present model produces results that are very similar to those of Peterson and Bogert. There are small differences of the location and height of the crossing points of amplitudes of the two chamber pressures; these small differences are attributed to the modelling by Peterson and Bogert of the taper of the chambers that is not included in the present model. The uniform cross-section chambers of the present model cause the pressure to diminish more rapidly with distance from the stapes, and so the point of maximum vibration in the present model is closer to the stapes than when the chambers are tapered. The purple line in Figure 4.4 is a graph of the pressure difference between the two chambers, which is very similar to the solid line in Fig 5 in Bogert (1951), reproduced here as Figure 4.3. At the base, the pressure in the SV is determined by the stapes velocity , and that in the ST is zero, due to the total pressure-release at the flexible round window. The pressures in the two chambers are given by the sum of a uniform mean pressure, equal to half that at the base of the SV and plus or minus half the pressure difference. The pressure difference drives the motion of the BM and generates the "slow wave", which causes the BM response to peak at the best place. The mean pressure does not drive the BM motion, since it is the same in both chambers, but it could generate a compressional "fast wave".

[1] The value used was taken from Bogert (1951), which is based on measurements by Békésy (1949).

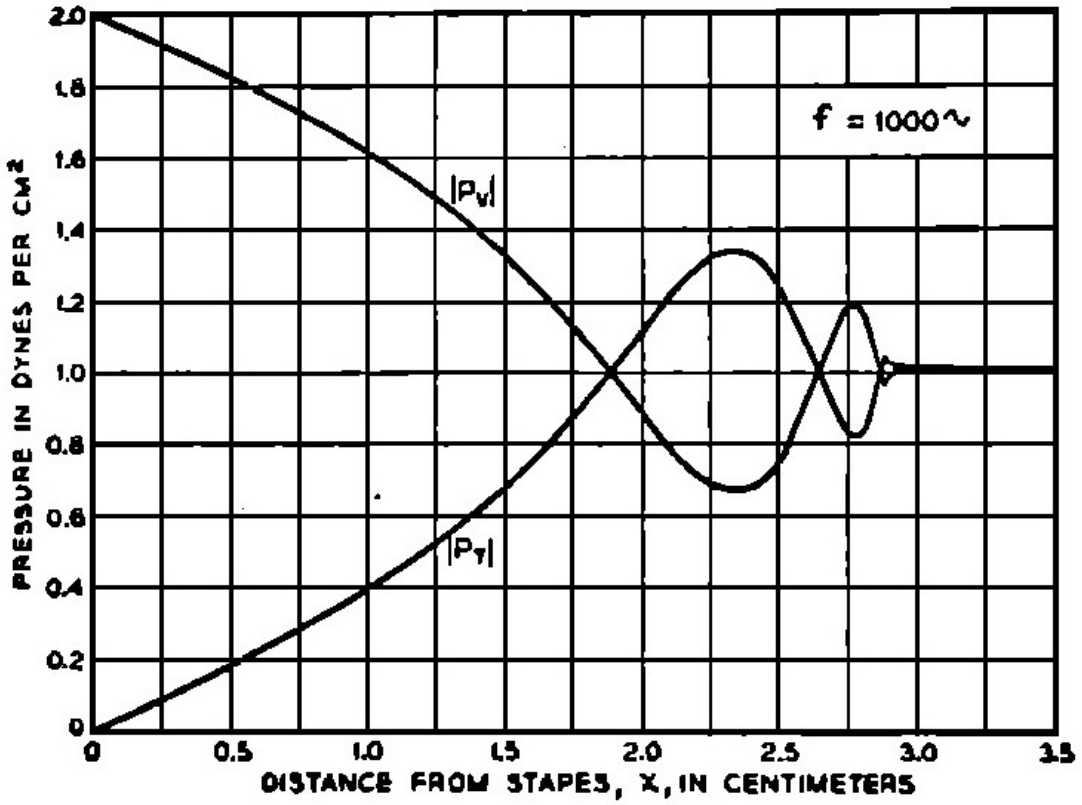

FIGURE 4.2: Pressure magnitude in the scala vestibulae $|P_v|$ and in the scala tympani $|P_t|$ versus distance along the basilar membrane for $f = 1000$Hz. Reprinted with permission from Peterson and Bogert (1950) (Fig 14). Copyright 1950, Acoustic Society of America.

The numerical values, used by Peterson and Bogert and loaded, in SI units, into the present model are:

$$\begin{aligned}
\text{BM stiffness, } s &= 1.72x10^9 * e^{2x} \text{ dyne/cm}^3, \text{ (NB } x \text{ is in cm.)} \\
\text{BM damping resistance, } r &= 6.737 * 10^3 * e^x \text{ g/cm}^2\text{.s}, \\
\text{BM superficial mass, } m &= 0.143 \text{ g/cm}^2, \\
\text{Cochlear fluid density, } \rho_0 &= 1 \text{ g/cm}^3 \\
\text{Chamber height, } H &\approx 0.1 \text{ cm} \\
\text{Frequency range } 10^2 &< \omega < 10^5 \text{ c.p.s.}
\end{aligned}$$

4.1.3 Comparison with Two Chamber Lumped Element Models

There are several published lumped element models; comparison with one such model is made for a normal ear and for an ear with a stiffened RW and an ideal bubble in Chapter 6. In Chapter 7 comparisons are made with two such models for an ear with an intracochlear point actuator adjacent to a stiffened RW.

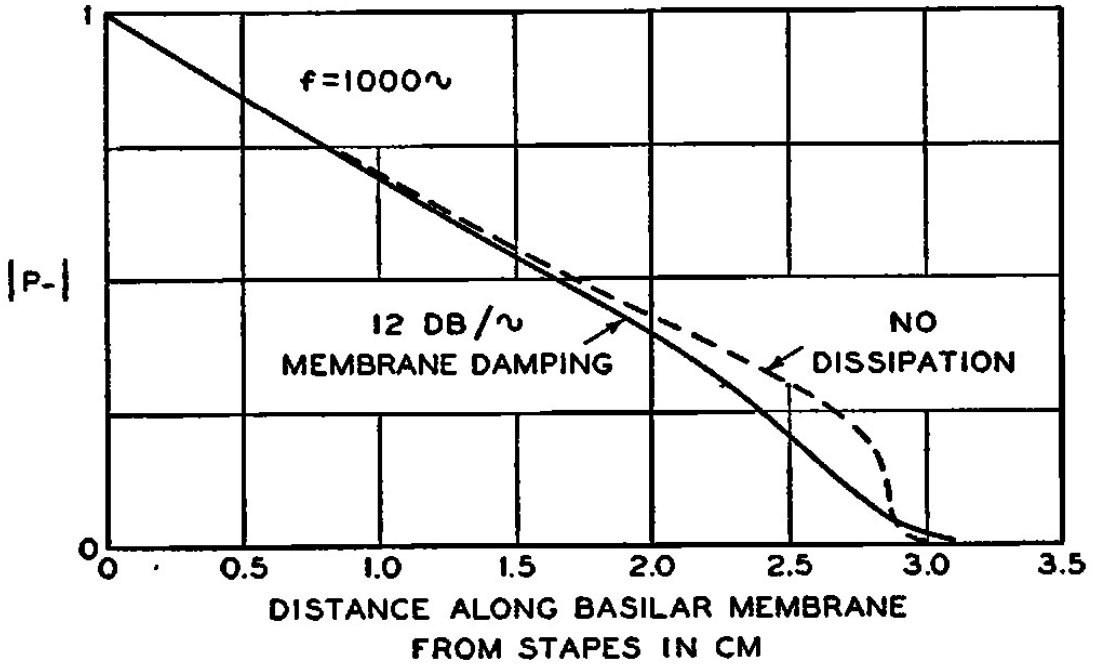

FIGURE 4.3: "Pressure difference $|P-|$ across the cochlear partition as a function of distance for a frequency of 1,000 cps. Solid curve: dissipation corresponding to a decay of the basilar membrane of 12 db per cycle. Dotted curve: no dissipation. (This is the same graph as $|P-|$ in Fig 7 of Peterson and Bogert (1950). Reprinted with permission from Bogert (1951) (Fig 5). Copyright 1951, Acoustic Society of America.

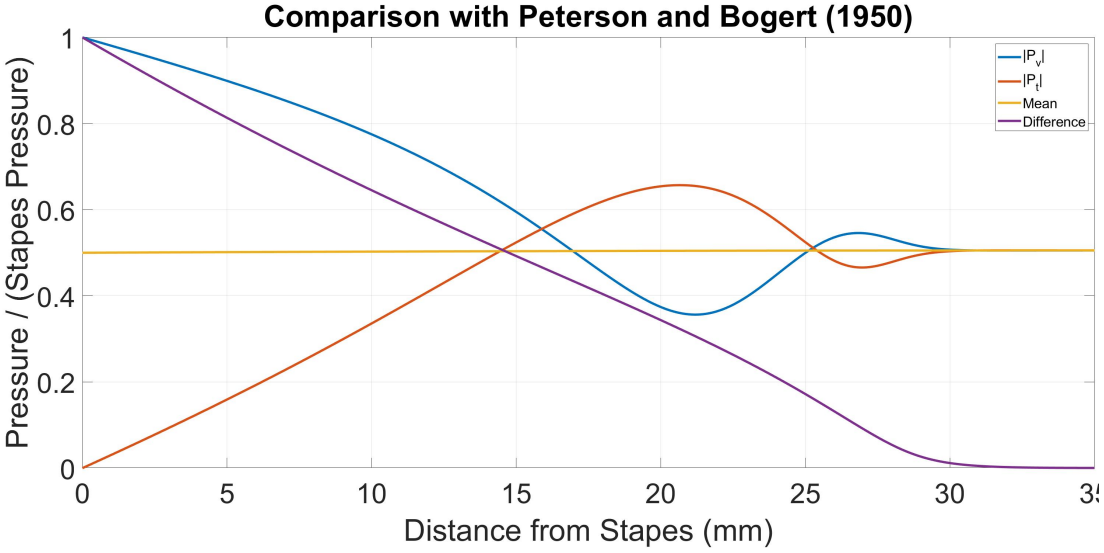

FIGURE 4.4: Pressure magnitude in the scala vestibulae $|P_v|$ and in the scala tympani $|P_t|$ versus distance along the basilar membrane for $f = 1002.4$Hz normalized to the middle ear or stapes pressure P_{ME}. The magnitude of the mean pressure and the pressure difference are also plotted.

4.2 Validation

4.2.1 Validation by Comparing Predicted and Measured Best Places

Some validation is obtained by comparing the model's prediction of the location of best place as a function of frequency with two sets of measured results. Figure 2.5 in Chapter 2 shows the comparison.

4.2.2 Validation by Comparing Predicted and Measured Hearing Loss

Some further validation is obtained by comparing the model's prediction of hearing loss due to RW stiffening as a function of frequency with two sets of measured loss following implantation. Figure 5.10 in Chapter 5 shows the comparison.

Chapter 5

Simulating Middle Ear Excitation in a Two Chamber Model

In this Chapter, the two chamber model is used to calculate the cochlear response to middle ear excitation with both a normally functioning round window and with a round window stiffened due to cochlear implantation. Since the stiffening of the round window affects the cochlear input impedance it is necessary to reproduce the subsequent change in the loading of the middle ear. It is thus not sufficient to assume a constant stapes velocity, as was done in the previous chapter, and a more complete model of excitation from the middle ear is necessary. For completeness, all of the parameters used for the model are listed in Table 5.1.

The values of those parameters are simply examples taken from the literature to illustrate the working of the model. In the main, the values are those used in the papers 2016 and 2018 by Elliott et al. The few exceptions to this generality are explained in the thesis wherever they are relevant. Alternative values can be input by changing the related text file.

Elliott et al. (2016) used finite element analysis to model the stiffening of the round window resulting from insertion through it of the implant. They conclude for low frequencies (c 100 Hz) that insertion of a typical (1 mm diameter) implant would increase the stiffness of a round window by a factor of 40, and that this would be increased to a factor of 170 when account is taken of doubling the thickness of the RW as a result of the surgery. Because a thickening of the RW is likely to result immediately from the trauma of surgery and subsequently from the growth of fibrotic or callous tissue, a stiffening factor of 170 is used in this thesis to illustrate use of the model and to test the feasibility of the proposed remedies for recovering acoustic hearing loss.

TABLE 5.1: Input parameters used by the model.

General			
Symbol	Value	Unit	Description
B	0.00032	m	BM Width
L	0.035	m	Cochlea Length
fmin	20	Hz	Min Frequency
fmax	20000	Hz	Max Frequency
rho	1000	kg/m^3	Density of Cochlear Fluids
mu	7e-4	Pa s	Dynamic Viscosity of Cochlear Fluids
Pr	4.71		Prandtl number of Cochlear Fluids
FN	301		No of Frequencies
XN	350		No of Elements
AST	3.2e-6	m^2	Stapes Area
ARW	3e-6	m^2	Round Window Area
ACH	0.84e-6	m^2	Average Chamber Area
ECHL	115	dB	pEC Relative to Normal Hearing Threshold
c0	1500	m/s	Velocity of Sound in Cochlear Fluids
sf	170		RW Stiffening Factor
a	60	/m	BM Elasticity Exponent
A	0.88		BM Elasticity Co-efficient
vEB1	0	mm/s	BM Excitation Velocity in 1st Element of OoC

Impedances					
Symbol	Unit	Inertance	Resistance	Stiffness	Description
zB	Pa s/m	0.28	1.41e4	7.47e9	BM Impedance
ZM	Pa s/m^3	4.4e5	1.0e10	8.1e13	Rev ME Impedance
ZR	Pa s/m^3	$56e6/\sqrt{\omega}$	$4.4e7*\sqrt{\omega}$	1.0e13	RW Impedance
Zb	Pa s/m^3	1.85e3	9.2e7	1e14	$15 \times 0.32 \times 0.3$ mm. Bubble Impedance

Aqueducts			
Parameter	Radius	length	Units
CA	0.075	10	mm
VAinner	0.15	1.5	mm
VAouter	0.3	8.5	mm

5.1 Basilar Membrane Responses

Clearly, the response of the basilar membrane is very dependent on the magnitude of the excitation. To be able to calculate hearing loss when the characteristics of the cochlea are altered, it is necessary to refer the BM response to an excitation source whose output is unaffected by changes to the downstream cochlea, for example those resulting from stiffening the round window. The excitation source has an impedance, which affects its output, when it is loaded by the impedance presented to it by the cochlea. The load presented to the stapes is the input impedance of the cochlea, which is significantly altered when the round window is stiffened, and so referencing to the stapes vibration is not suitable for the purposes of this work. The excitation mechanism can be modelled as a constant pressure source in series with an impedance

or a constant velocity source, in parallel with an admittance. These are often known as Thevenin and Norton sources respectively. The constant pressure and constant velocity sources do not change their output when their load changes, and so they can be used to normalize the cochlear response to a quantity that is independent of the characteristics of the cochlea itself. Figure 5.1 shows the equivalent circuit diagram of the Norton source, q_M, the reverse middle ear impedance, Z_M or M_3 and the cochlear input impedance, Z_C.

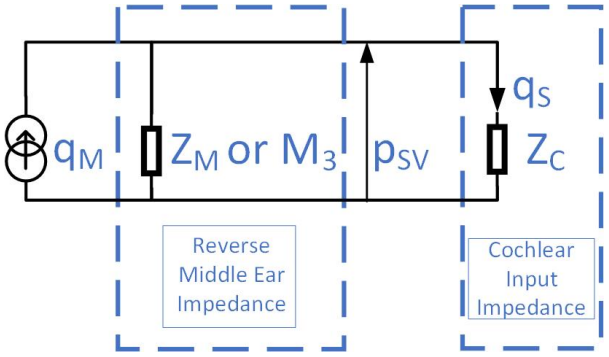

FIGURE 5.1: Diagram, showing a simplified arrangement of the acoustic excitation of the cochlea using a Norton equivalent of the middle ear.

This formulation allows modelling of hearing loss caused by stiffening the RW, and it also allows determination of the cochlear response to the output of an intracochlear actuator, which may have a different impedance from the ear upstream of the stapes, and which may be loaded by a different cochlear impedance from that presented to the stapes. Unfortunately, there is no point within the middle or outer ear that has a measurable pressure or velocity that corresponds to that of an ideal constant source, whose output is unaffected by the downstream load. The pressure presented to the ear canal is a better choice for the reference quantity, as it is not affected significantly by changes in the RW impedance. Ear canal pressure can be measured, and it can be used as the input to a microphone that drives an actuator. In this sub-section, the Norton equivalent source is calculated assuming a given ear canal pressure. This can be achieved by initially considering the case in which the round window is not stiffened, in which case the parameters of the middle ear impedance and the cochlear input impedance are well known. Xue et al. (2020) have modelled the middle ear pressure gain ratio (M_{1X}) of the pressure in the scala vestibuli to the ear canal pressure, the middle ear impedance (M_{3X}) and the cochlear input impedance (Z_{CX}), and their modelled results have been checked against results of measurements of the same quantities made by a number of others. The Norton equivalent middle ear acoustic velocity, q_M can be calculated, as a function of ear canal pressure, p_{EC}, from these three quantities using the circuit diagram in 5.1.

The Norton equivalent velocity is first related to the stapes velocity by considering the pressure p_{SV} in Figure 5.1, where the specific values of M_3 and Z_C from Xue et al. (2020), M_{3X} and Z_{CX}, are now used.

$$p_{SV} = q_M \frac{M_{3X} Z_{CX}}{M_{3X} + Z_{CX}} = q_S Z_{CX}, \text{ thus} \tag{5.1}$$

$$\frac{q_M}{q_S} = \frac{M_{3X} + Z_{CX}}{M_{3X}} \tag{5.2}$$

The stapes volume velocity under these conditions is now related to the ear canal pressure, p_{EC}, using the middle ear pressure gain, M_{1X}, and the cochlear input impedance, M_{3X}.

$$q_S = p_{EC} M_{1X} / Z_{CX}, \text{ thus} \tag{5.3}$$

$$\frac{q_M}{p_{EC}} = \frac{M_{3X} + Z_{CX}}{M_{3X} Z_{CX}} M_{1X} \tag{5.4}$$

It is important to ensure that all of the quantities M_{3X}, Z_{CX} and M_{1X} are taken from the same model, because the loaded stapes velocity will be dependent on both the load Z_{CX} and the upstream impedance feeding it, M_{3X}.

The present model calculates q_M / p_{EC}, as a function of frequency, using the value of M_{3X}, and approximations to Z_{CX} and M_{1X} from the model developed by Xue et al. The resultant value of q_M is then used as an input to the present model. This is valid for all the cases considered in this thesis, because q_M does not vary , when M_3 and Z_C alter, whereas measured values of M_1, and hence the modelled values that match them, are dependent on both the load (Z_C) and the upstream impedance (M_3) feeding it in each case.

For simplicity, rather than re-computing the value of M_{1X} and Z_{CX} produced by the model in Xue et al. (2020), polynomial approximations have been used in the present model, in combination with the value of M_{3X} computed from the inertance, resistance and stiffness values, given by Xue et al. (2020) to compute the Norton equivalent middle ear velocity, q_M. The two chamber model can then use a different value for M_3, because doing so will not cause q_M to change. The value given by Puria (2003) has been chosen, because that paper gives both measured values and mass, spring, damper values that fit the measurements.) Figure 5.2 shows Xue et al.'s modelled values of M_{1X} and the quartic approximation used by the present model. Figure 5.3 shows the magnitude and phase of Z_{ME} or M_3, as a function of frequency, from figure 8(a) of Xue et al. (2020) and the corresponding values used by the present model. The magnitude and phase of Z_{CX} are shown in Figure 5.4, as a function of frequency, which also shows the corresponding polynomial approximations used as inputs to the present model.

Finally, Figure 5.5 shows the middle ear Norton velocity normalized by the ear canal pressure calculated from equation 5.4 using M_{3X} and the approximations to M_{1X} and Z_{CX} defined above.

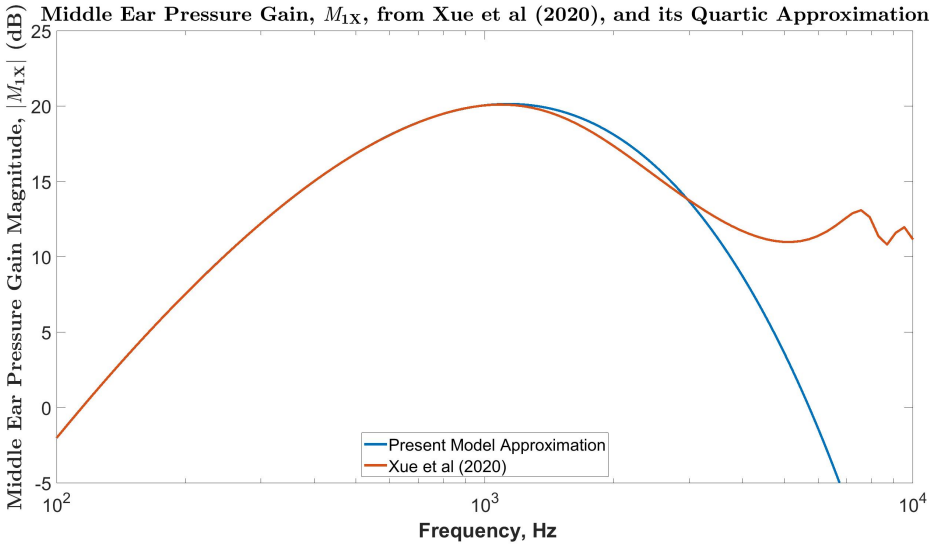

FIGURE 5.2: A comparison of the middle ear pressure gain (M_{1X}) from Figure 7 of Xue et al. (2020) with its fourth order polynomial approximation used by the present model.

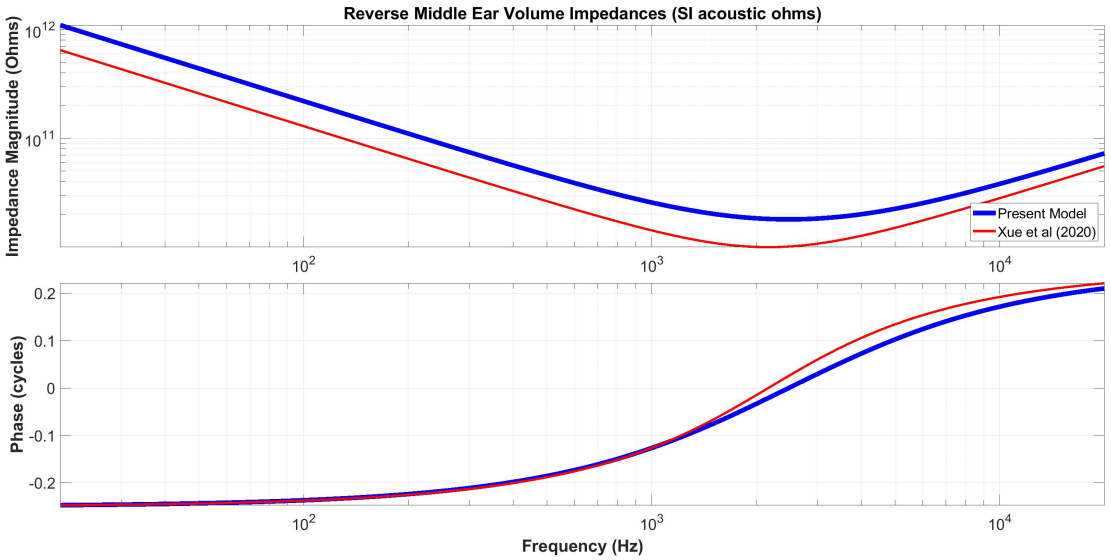

FIGURE 5.3: A comparison of the reverse middle ear impedance (Z_{ME} or M_{3X}) from Figure 8(a) of Xue et al. (2020) with the corresponding impedance used by the present model. (The difference occurs because the present model uses parameters from Puria (2003), and Xue et al. (2020) uses slightly different values. Both papers use simple mass, spring, damper models, and so no approximation is needed.)

The author is very grateful to Professor Houguang Liu, who is the corresponding author for Xue et al. (2020), for sharing the data plotted in that paper, and which are re-plotted here in Figures 5.2 to 5.4 and 7.23.

The model used in these calculations is shown diagrammatically in Figure 5.1.

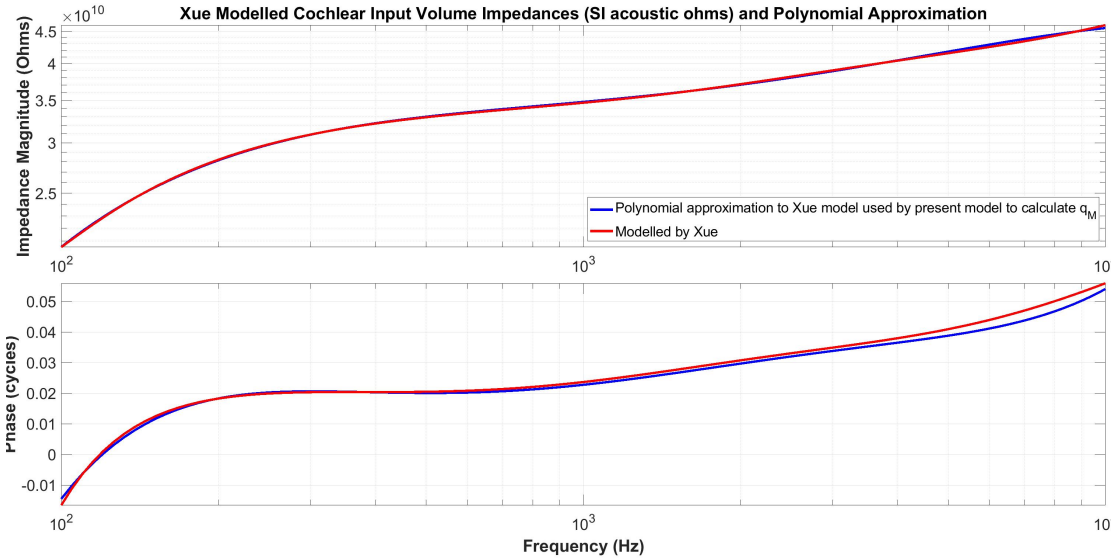

FIGURE 5.4: Cochlear Input Acoustic Impedance modelled by Xue et al. together with its polynomial approximation, used as an input to the present model.

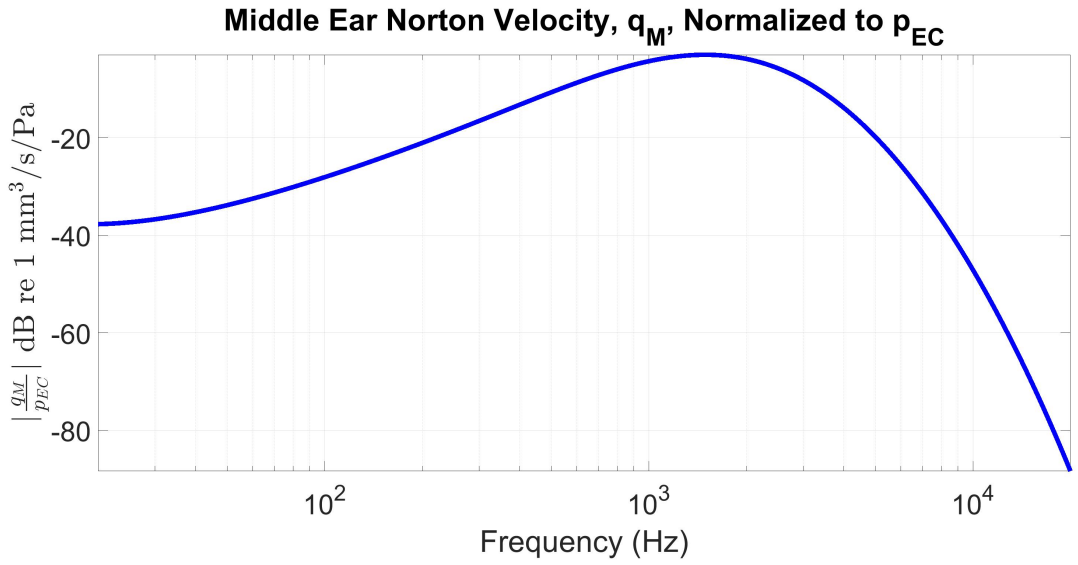

FIGURE 5.5: Normalized Middle Ear Norton Acoustic Velocity for a constant ear canal pressure, calculated using the quartic approximation to M_1, and used as an input to the present model.

5.2 Modelling the BM response to Ear Canal Pressure

The present two-chamber model of the cochlea can be configured to include oval and round windows with different impedances, but its correct use to model the BM response for different cochleae is dependent on deriving a relationship between ear canal pressure,p_{EC} and cochlear excitation that is independent of the cochlear input impedance. This has been achieved, as set down in Section 5.1, and it enables the model to predict the performance of the cochlea when an implant is inserted through the round window, causing it to stiffen and thereby impairing its ability to act as a pressure release. Stiffening of the RW increases the impedance of the RW itself, and it

also changes the input impedance of the whole cochlea, as presented to the excitation source. The functionality of the two-chamber model also enables it to emulate the effects of including a bubble, to act as a substitute pressure release, or an actuator in the implant as an alternative source of acoustic excitation. These opportunities are discussed in Chapters 6 and 7.

The behaviour of the cochlea can be portrayed, as in other published work, using graphs of the amplitude and phase of the basilar membrane (BM) velocity in both the spatial and frequency domains, examples of which are shown in Figures 5.6 to 5.8. Similar graphs can be generated by the model for the pressure difference across the basilar membrane, but they are less informative than the BM velocity graphs, and so they are not shown here.

These graphs are shown for a normal round window stiffness (blue lines), as given in Table 5.1, and for a round window stiffened by the stiffening factor of 170 given in the same table.

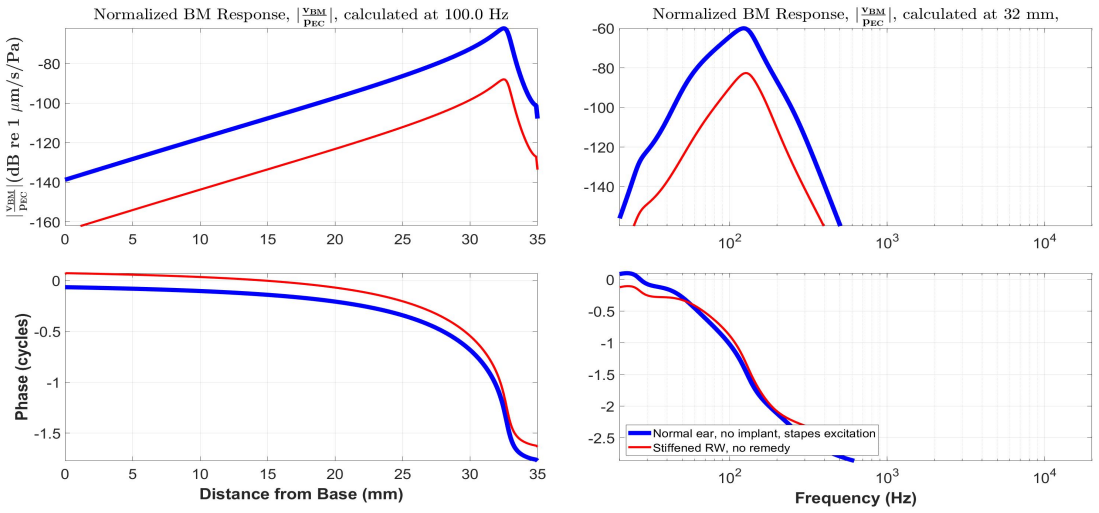

FIGURE 5.6: BM Velocity Response divided by the Ear Canal Pressure in the Spatial Domain at 100 Hz and in the Frequency Domain at 32 mm from the Base, for a Normal and a Stiffened RW.

For these graphs, frequencies of 100, 250 and 1000 Hz, have been chosen to be the lower and upper limits of the frequency range of interest and an arbitrary mid-range frequency. Those frequencies are paired with the corresponding characteristic 'best place' positions of 32, 29 and 21 mm from the base, respectively, as shown in Figure 2.5.

The spatial domain amplitude responses for each of the three chosen frequencies increase uniformly from the base to approaching the characteristic place, followed by a steep fall from the characteristic place to the helicotrema, as shown in the left hand sides of Figures 5.6 to 5.8. Although not shown here, this remains so for frequencies outside the range of interest. This is similar to the predictions of previous models. The gap between the graphs for normal and stiffened round windows varies according to

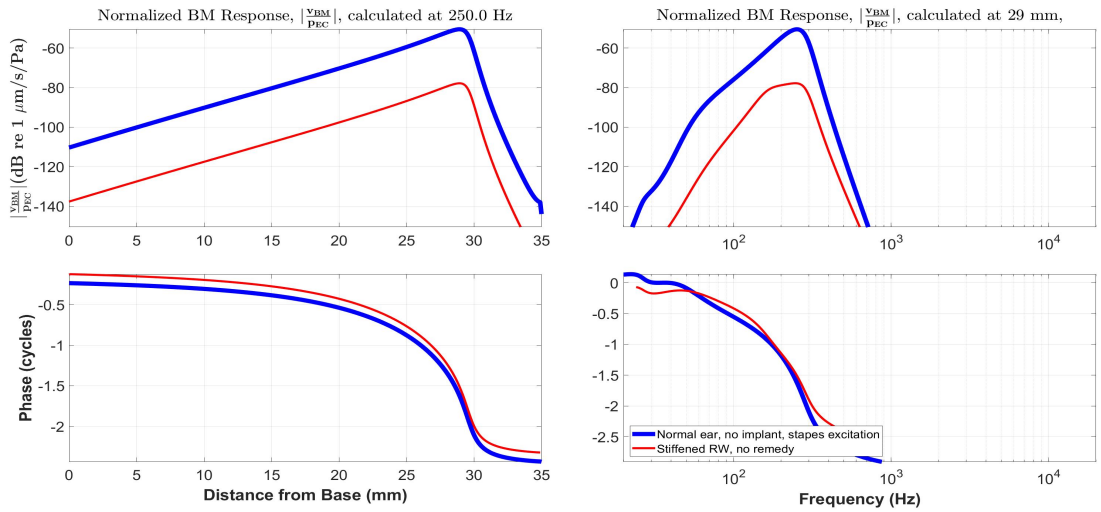

FIGURE 5.7: BM Velocity Response divided by the Ear Canal Pressure in the Spatial Domain at 250 Hz and in the Frequency Domain at 29 mm from the Base, for a Normal and a Stiffened RW.

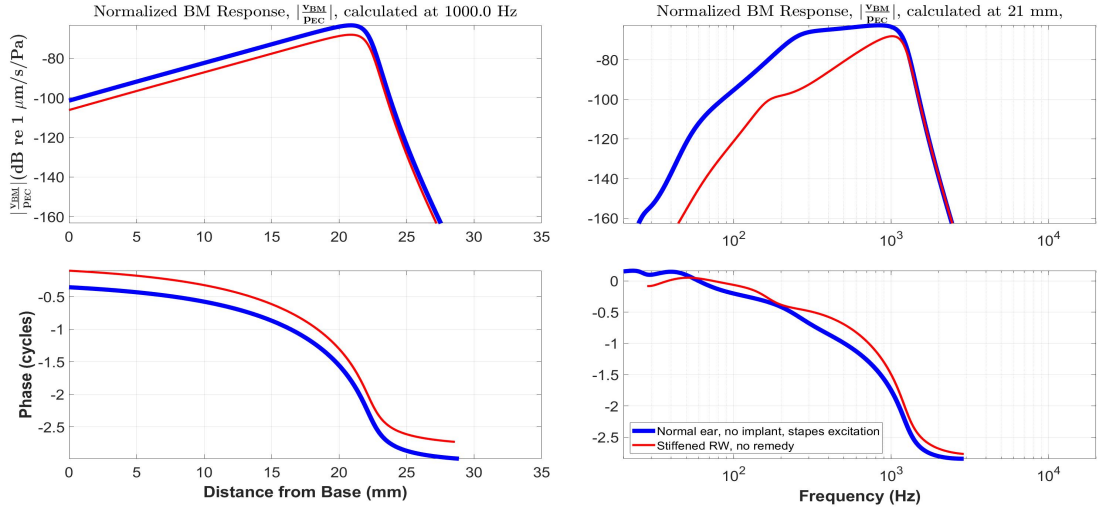

FIGURE 5.8: BM Velocity Response divided by the Ear Canal Pressure in the Spatial Domain at 1 kHz and in the Frequency Domain at 21 mm from the Base, for a Normal and a Stiffened RW.

the effect of the stiffening at the particular frequency, which will be generally greater at lower frequencies than at higher frequencies, wherever the BM response is determined by the stiffness of the round window.

The loss of BM velocity amplitude at 100 Hz due to implantation is calculated to be close to 26 dB, wherever the reduction is measured along the cochlea.

At 250 Hz, the loss is similar and also constant at 27 dB.

At 1 kHz, the reduction is also constant with distance from the stapes, and it is calculated to be about 5 dB.

In the frequency domain, the BM velocity responses to ear-canal pressure at a given place are also shown on the right hand sides of Figures 5.6 to 5.8. The results are now

slightly complicated by the frequency response of the of the Norton equivalent middle ear velocity and by the interaction between the reverse middle ear impedance and the cochlear input impedance, both of which vary with frequency.

At frequencies above the range of interest (100 - 1000 Hz) the loss continues to diminish as the impedance of the unstiffened round window becomes less dependent on its stiffness. At these frequencies, the round window impedance becomes dominated by its resistance and its inertance, which are not significantly affected by implantation.

5.3 The Cochlear Input Impedance of the Two Chamber Model

Figure 5.9 shows the magnitude and phase of the modelled cochlear input impedance calculated using the two chamber model before and after stiffening of the round window. In this graph, the magnitude of the input impedance of a normal ear is modelled as a little under 2×10^{10} Ω at 100 Hz, which aligns reasonably closely with the magnitude measurements of Puria (2003), Nakajima et al. (2009), Marquardt and Hensel (2013) and Frear et al. (2018), and very closely with that of Aibara et al. (2001) and the average of the others. However, the present model predicts the rate of rise with frequency as about 10 dB/decade from 70 Hz up to a few kHz, whereas the lumped element models show slopes starting from higher frequencies between 100 and 1000 Hz and with slopes much less steep. The present model shows the impedance rising to a gentle peak at almost 10 kHz, whereas the magnitudes given by the measurements and the lumped element models, except Marquardt and Hensel's, show a sharper peak at a few kHz, followed by a decline. Also the present model gives a phase angle that is generally greater than that of the measurements and the lumped element models. The reason for these discrepancies is thought to be caused by limitations of the present model, which does not allow for the taper of the fluid chambers, or the damping caused by the viscosity of the cochlear fluids in the chambers. Taper has the effect of reducing the phase angle of the cochlear input impedance, by reducing the inertance where the chamber area is increased near the base. Because the acoustic flow starts at the base in the upper chamber and finishes at the base in the lower chamber, irrespective of where the flow passes through the BM, the reduction in inertance will apply at virtually all frequencies. The absence of taper in the present model means that it will predict a greater inertance than the measured results at virtually all frequencies. This increased inertance will have a greater impact on the cochlear input impedance at high frequencies than at low frequencies, because its contribution to the input impedance is proportional to frequency. Qualitatively, this explains why the increased inertance in the present model only changes the phase angle of the input impedance at low frequencies, and also significantly increases the

magnitude at high frequencies. Because the three dimensional shape of the two chambers is complex, particularly near the base in the upper chamber, a quantitative explanation of these discrepancies is beyond the scope of this thesis. A theoretical analysis of the effects of taper is provided by Shera and Zweig (1991), and this is summarised in a readily understood graphical presentation to the Workshop on the Mathematics of Hearing at the Fields Institute by Shera (2017). It is noted, however, that these publications assume an exponential taper of BM stiffness and damping, whereas the present model uses Greenwood's (1961 and 1990) equation. The predicted increase in the cochlear input impedance after stiffening of the round window appears reasonable. Marquardt and Hensel (2013), for example, model the cochlea input impedance as the series combination of an almost entirely real impedance across the BM and the round window stiffness. To compare the effect of stiffening the round window on the results of another model, it can be seen from figure 5B in that paper that increasing Z_{RW} by two orders of magnitude for frequencies up to about 400 Hz and by an amount diminishing to zero up to a few kHz would increase Z_C by about half an order of magnitude, as predicted by the present model.

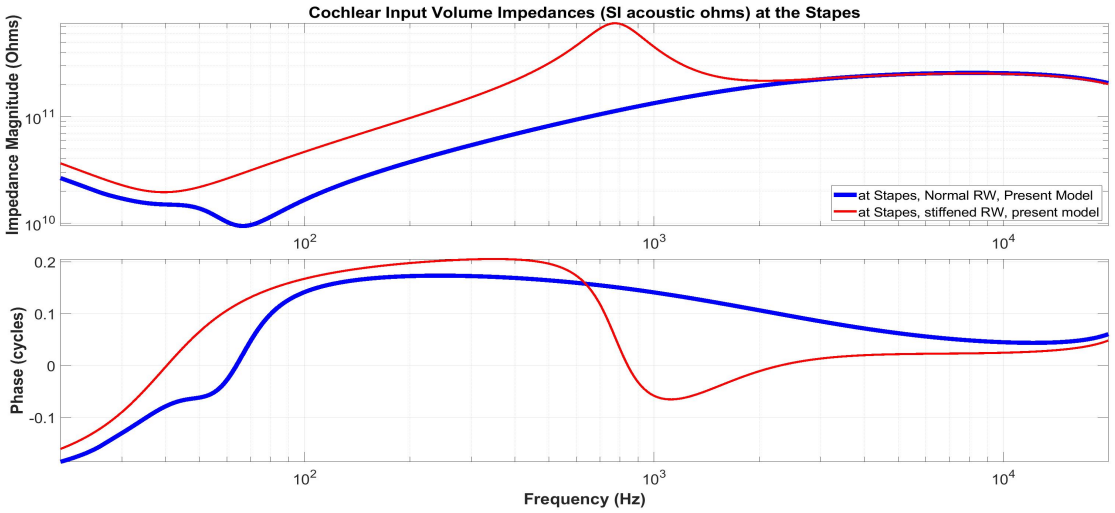

FIGURE 5.9: Modelled Cochlear Input Impedance, with and without an Implant.

5.4 Hearing Loss

The most important use of the model as far as the present work is concerned is the prediction of hearing loss as a function of frequency. This is calculated as the difference between the BM mechanical velocity at the best place with a normal and a stiffened RW.

Figure 5.10 shows the calculated difference between the peak responses predicted by the model at different frequencies before and after stiffening of the round window as a function of excitation frequency. Also shown are the means and standard deviations of two sets of measured values, from Causon et al. (2015) and Verschuur et al. (2016).

Within the frequency range of interest (100 – 1000 Hz), the hearing loss graph has a minimum at 159 Hz, where there is a resonance between the middle ear and the vestibular aqueduct when the round window is stiffened and the lower chamber has a high impedance, giving rise to a peak in the BM velocity. A normal RW has a much lower impedance in parallel with the vestibular aqueduct, and so there is no resonance and no peak. Because there is a response peak with a stiffened RW, but no peak with a normal RW, the hearing loss is a minimum at this frequency. At 263 Hz, the cochlear aqueduct resonates with the parallel stiffened RW to give a high impedance and a low BM response. With a normal RW the resonant frequency is 20 Hz, and there are no peaks or troughs in the BM response. Because stiffening the RW causes a trough in the BM response that does not occur with a normal RW, the hearing loss peaks at about 263 Hz.

Although outside the frequency range of interest, there is a resonance between the normal RW and the vestibular aqueduct at 53 Hz. This causes a peak in the hearing loss at that frequency. There is also a minor loss peak at about 28 Hz, which is caused by a resonance between the helicotrema and the other components of the wave impedance, as modelled and reported by Marquardt and Hensel (2013).

5.4.1 Comparison with Hearing Loss Measurements

As well as showing the loss in residual acoustic hearing predicted by the two chamber model, Figure 5.10 also shows the measured hearing loss after implantation by both Verschuur et al. (2016), and Causon et al. (2015). The ± 1 standard deviation value is shown for these measurements, as well as the mean. It should be explained that there are many potential causes of residual hearing loss after implantation, such as tissue damage, trauma and fibrotic growth, as described by Causon et al. (2015). The difference between the modelled and the measured values of loss at each frequency, however, is less than half the standard deviation of the measurements, and the rms difference over the frequency range of interest (100 - 1000 Hz) is 6.7 dB. In Figure 5.10, the measured hearing loss at each frequency has been calculated by the authors of these papers as the difference between the pre- and post-implantation hearing thresholds, averaged over the 90 or so patients reported in each study. The graph compares these measured results with the prediction of the new model, expressed as a reduction in the maximum BM velocity.

Comparison of the measured and predicted hearing loss should be treated with caution, because there are many potential causes of hearing loss, and the present model predicts only the part of the loss that is caused by stiffening of the round window. The measured hearing loss changes with time after implantation as well as with frequency. Scar tissue from the trauma of insertion can cause additional stiffening, but that additional stiffening diminishes over a period of a few months. Foreign body response and fibrosis growth can also cause hearing loss by effectively

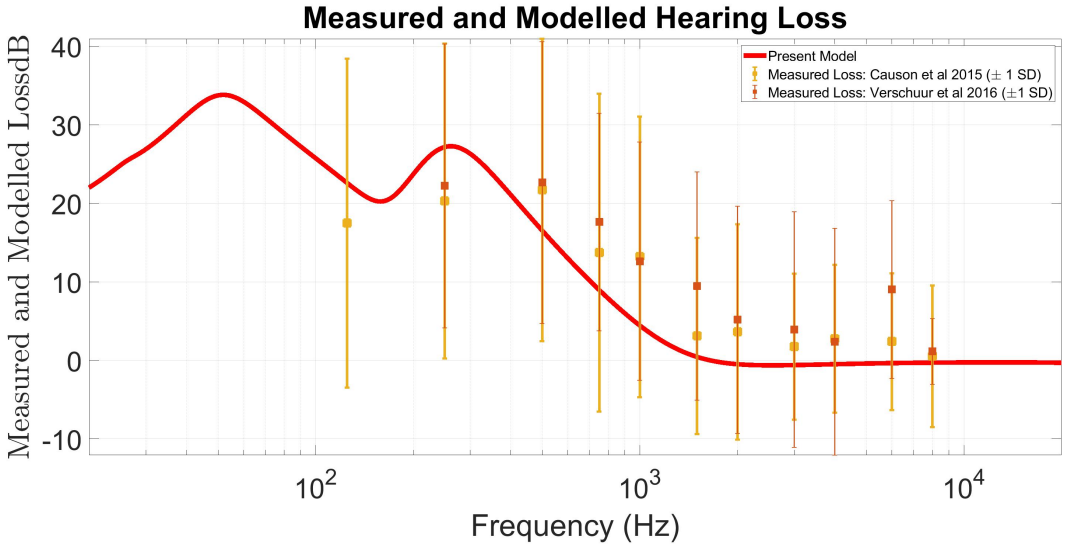

FIGURE 5.10: A comparison of measured and modelled post implantation hearing loss, calculated as the difference in basilar membrane velocities before and after implantation. For Verschuur data, n=93 (250-1000 Hz); for Causon data, n=91 for (125-1000 Hz), showing the mean measured losses as squares and the ± SD variance as vertical lines.

stiffening the round window, but this can take months to accumulate according to, for example, Foggia et al. (2019), who has published a review of 90 papers on the subject; the data collated by Causon and used for this comparison were measured within two months of implantation; Verschuur's measurements were made within 6 months of implantation. By choosing the measured data for comparison in this way, some of the hearing loss caused by implantation trauma and fibrotic growth can be eliminated. Most implants occupy only the most basal 24 mm or so of the length of the lower chamber; at 24 mm the characteristic place has a characteristic frequency of about 700 Hz. It is not possible for an implant to cause tissue damage in the most apical 12 mm of the cochlea, because it does not reach that far, and so it is unlikely that such damage would cause hearing loss at frequencies below 700 Hz. By taking the mean of 100 or so measurements in each study, the impact of rare occurrences is greatly diminished. It thus appears reasonable to assume that at least some of the average measured hearing loss can be predicted using a model of the cochlear mechanics, incorporating a stiffened round window.

5.5 Bubble and Actuator Inclusion

The model can also be used to predict the effects of incorporating a small bubble or an electro-acoustic actuator at different points along the cochlea. Either of these concepts could be developed to restore low frequency acoustic hearing, and they are discussed in the following three chapters. The input parameters of the model can be varied to model bubbles and actuators of different sizes and at different positions.

The model could also be used to predict the performance of middle ear implants that deliver excitation through the round window, although this is not explored further in this thesis.

Chapter 6

Integration of a Bubble in the Cochlear Implant

In this Chapter the effects of including a compliant element in the lower chamber are simulated. This compliant element may either be concentrated at a single element of the model or distributed along the cochlea, and it may be integrated as a gas-filled bubble incorporated within a cochlear implant. The aim is to re-introduce sufficient compliance to overcome the detrimental effects of the stiffening of the round window that can occur after implantation, as discussed in Chapter 5.

When the compliant element is modelled as an ideal bubble concentrated into a single element of the model, it is modelled with a compliance exactly equal to the compliance lost from the lower chamber by the assumed stiffening of the round window. For ideal point bubbles their mechanical impedance is calculated using the equation:

$$z_{\mathrm{b}} = \frac{-i\, K_{\mathrm{RW}}\, sf}{\omega B \Delta (sf - 1)} \tag{6.1}$$

When the volume of a point bubble is specified, the mechanical impedance is calculated using the equation:

$$z_{\mathrm{b}} = \frac{-i\, \rho c_0^2}{\omega B \Delta V_{\mathrm{b}}} \tag{6.2}$$

Where ρ and c_0 are the density of and velocity of sound in the gas in the bubble, which is assumed to be air at 37 °C and at atmospheric pressure.

For an achievable bubble, the impedance of the gas in the bubble is first calculated using equation 6.2, and then the impedance of the diaphragm is added, as shown in Appendix D.

In this Chapter, the same physiological input data have been used for the two-chamber finite element model as were given in Table 5.1 of the previous Chapter. This model has been used to compute the normalised BM velocity and pressure

TABLE 6.1: Input variables used by Elliott et al. (2016).

Input parameters			
	SI units	Elliott et al.	Elliott et al. Symbol
Cochlear inertance	kg.m-4	7.00E+07	LFL
Wave resistance	kg.s-1.m-4	2.00E+10	RWA
RW inertance	kg.m-4	1.00E+06	LRW
RW stiffness	kg.s-2.m-4	1.00E+13	$1/C_0$
RW resistance	kg.s-1.m-4	2.50E+09	RRW
VA inertance	kg.m-4	5.10E+07	LVA
VA resistance	kg.s-1.m-4	1.10E+10	RVA
CA inertance	kg.m-4	5.60E+08	LCA
CA resistance	kg.s-1.m-4	3.50E+11	RCA
ME stiffness	kg.s-2.m-4	8.33E+13	1/CME
ME resistance	kg.s-1.m-4	1.00E+10	RME
ME inertance	kg.m-4	4.40E+05	LME
Source		Elliott et al. (2016) table 1	

difference at the base of the cochlea, with a normal RW and a stiffened RW with and without an adjacent single bubble, whose size is chosen to restore the compliance of the normal RW. The normalised BM velocity and pressure difference have also been calculated as described in Chapter 5 and shown in Figure 6.1 with the bubble impedance added, using the parameters listed in Table 6.1 as used in Elliott et al. (2016). Figure 6.2 shows the normalised pressure differences and figure 6.3 the normalised BM velocities in all of these cases.

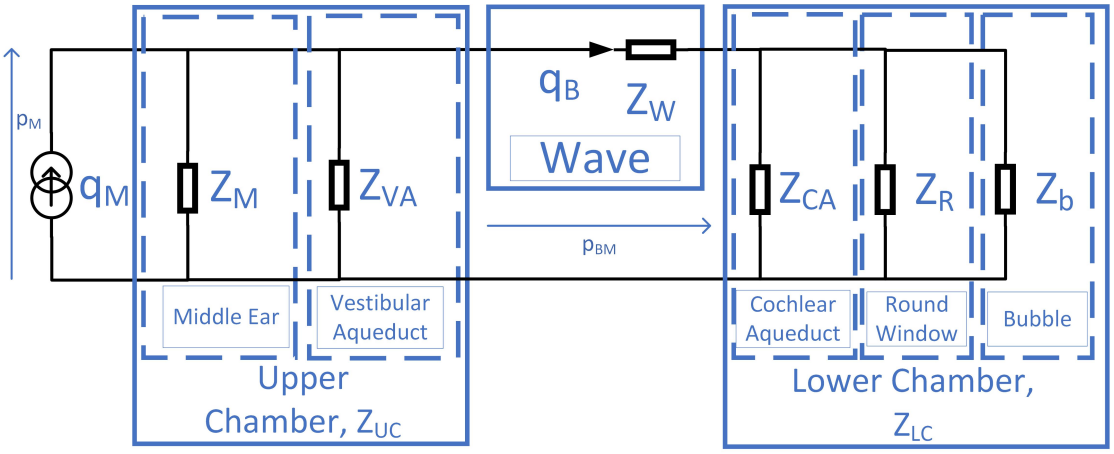

FIGURE 6.1: Cochlear Structures Diagram, showing a simplified arrangement of the acoustic structures of the cochlea and a bubble at the RW. Z_W is the sum of the fluid impedance in the upper chamber, the impedance of the BM and the fluid impedance in the lower chamber.

Below the 400 Hz resonant frequency of the normal round window, the two chamber model produces a broadly similar result to the model by Elliott et al (2016) model. Above that frequency, the two chamber model imitates the shape of the lumped element model, but they diverge by more than 15 dB, as frequency is increased. This

difference is caused by the computation by the two chamber model of a significantly different value for the wave impedance. Elliott et al. (2016) have modelled their Z_{BM} as a constant resistance in parallel with an inertance; the two chamber model allows for variable BM resistance, but it does not model taper of the dimensions of the cochlear chambers or the Basilar membrane. In a finite element (distributed) model, most of the acoustic velocity flows through the BM between the stapes and the place of maximum velocity, which is slightly nearer the stapes than the point of resonance. The bulk of the volume velocity will therefore pass through the BM where its impedance will be dominated by its resistance and/or its stiffness. This effect is exaggerated by the lack of taper of the chambers in the two chamber model, which also leads to the difference between the modelled and measured cochlea input impedance graphed and explained in Chapter 5.

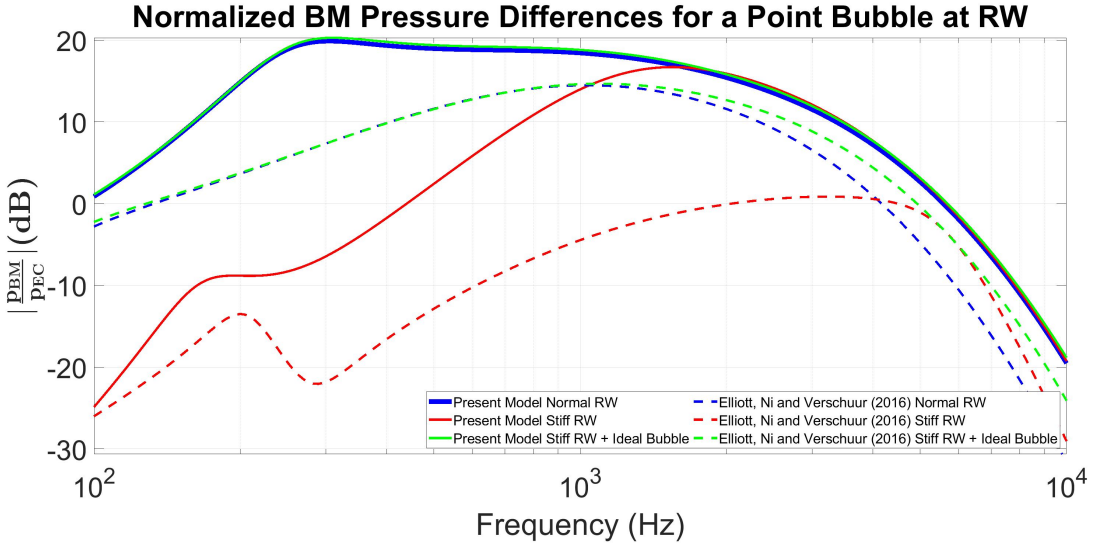

FIGURE 6.2: Normalized BM Pressure Difference Response with RW Stiffening Factor of 170, computed for a normal ear (blue), a stiffened RW (red) and a stiffened RW with an adjacent ideal single element bubble (green), using both the two chamber model (solid Lines) and that of Elliott et al. (2016) (dashed lines). The compliance of the ideal bubble is chosen to reverse the effect of stiffening the RW.

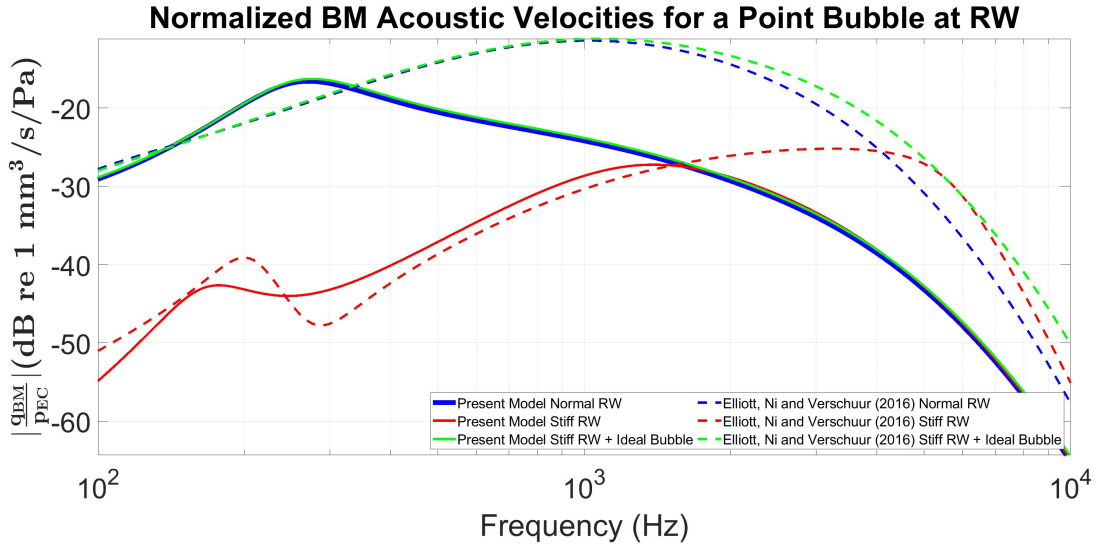

FIGURE 6.3: Normalized BM Volume velocity Response with RW Stiffening Factor of 170, computed for a normal ear (blue), a stiffened RW (red) and a stiffened RW with an adjacent ideal single element bubble (green), using both the two chamber model (solid Lines) and that of Elliott et al. (2016) (dashed lines). The compliance of the ideal bubble is chosen to reverse the effect of stiffening the RW.

6.1 Changing the Bubble Position

In this section the two chamber finite element model has been used to compute the normalised pressure difference and BM velocity distributions under the following conditions:

Case	Name
1	Normal ear, no implant
2	Stiffened RW
3	Stiffened RW, with bubble 0 mm from RW
4	Stiffened RW, with bubble at 10 mm from RW
5	Stiffened RW, with bubble at 20 mm from RW
6	Stiffened RW, with bubble 1 to 16 mm from RW

The two chamber model has been used to show the effects of changing the location of a point bubble and of using a bubble of finite length.

6.1.1 Pressure and Velocity Normalized Responses from the Stapes to the BM

Figures 6.4 to 6.9, below, show graphs of the amplitude and phase of basilar membrane velocity in both the spatial and frequency domains, as in other published work for four different bubble configurations (theoretical point bubbles at 0, 10,

20 mm and an achievable long bubble, extending from 1 to 16 mm from the round window). The theoretical point bubbles are set to occupy only a single element, and the compliance of each is set to match the compliance lost by stiffening the round window; this is done for simplicity and to allow comparison with lumped element models, but it is recognized that a sufficiently compliant point bubble cannot be achieved in practice. The 15 mm long bubble can be achieved in practice, and it compensates reasonably, but not completely, for the hearing loss over the frequency range of interest (100 to 1000 Hz). Below 100 Hz the achievable bubble does not compensate well for the stiffening of the RW, because it has insufficient compliance to compensate for the predicted loss of compliance due to implantation.

Each of Figures 6.4 to 6.9 provides a snap-shot at a particular selected pair of a frequency and a position; three frequencies have been chosen, 100, 250 and 1000 Hz approximately; each is paired with the position of the corresponding characteristic place (32, 29 and 21 mm from the base, respectively). [1] For Figures 6.4 to 6.9, as well as Figures 6.13 to 6.14, the pressure across the BM and its velocity have been normalized to the ear canal pressure.

The loss of amplitude due to implantation at 100 Hz is a little over 20 dB, and all of this can be recovered fairly precisely by including a theoretical point bubble adjacent to the round window. When the bubble is at a distance from the RW, the inertance of the fluid in the path from the excitation source (stapes) to the pressure release (bubble) is shortened, decreasing the inertance in the moving fluid and thereby shifting the frequency response graphs to slightly higher frequencies (to the right) in the frequency domain. Within the frequency range of interest, the maximum frequency shift occurs at 1 kHz when the bubble is located at 21 mm; the length of moving fluid then halves, the inertance approximately also halves, and the frequency shifts by a factor of no more than 1.4. Near to the best frequency, the shift is reduced, because the inertance of the BM and other structures are a significant fraction of the total inertance. Reducing the fluid inertance and shifting the frequency also changes the damping in the lower chamber and the interaction of the various stiffnesses and inertances of the cochlear structures. An exact explanation of the frequency responses resulting from different bubble positions is complex, particularly at frequencies greater than the range of interest.

However, deducing the hearing loss from the frequency response graphs is somewhat simpler. At any frequency, the hearing loss is the difference between the BM velocities of a normal ear and with a stiffened RW and a bubble. For each bubble position there is a small frequency shift, and the hearing loss will be that shift multiplied by the

[1] The frequencies are not exact, because only a finite number of frequencies are modelled, and so the nearest frequency may not be exactly equal to the nominal value. Similarly, only a finite number of positions are modelled, but careful choice of the number will allow the actual to exactly match the nominal. Setting the positions and frequencies modelled is easily changed by entering the numbers in a text file. In each case, the implant is considered to have increased the stiffness of the round window by a factor of 170.

difference in slopes of the two BM responses.

$$HL(\text{dB}) = \left(\frac{dHL}{df}\text{normal} - \frac{dHL}{df}\text{stiffened + bubble}\right) \times \Delta f \qquad (6.3)$$

Where $HL(\text{dB})$ is the hearing loss measured in dB, and

Δf is the frequency shift

If each of the two slopes are constant over the frequency shift, then this is a good approximation; if not, then the hearing loss is calculated at each frequency as the difference in the two BM velocities.

Around 1000 Hz, the implantation loss diminishes to zero, because the stiffened round window and the cochlear aqueduct are inertive, and so adding compliance decreases the admittance in the lower chamber. As the bubble is moved away from the RW, the inertance of the fluid between it and the RW will increase, and the effective compliance will decrease. At this frequency, the inertive admittance of the RW is close to the compliant admittance of the bubble, and so moving the bubble away from the RW will add sufficient inertance to cause a parallel resonance, which will increase the hearing loss. The greater the distance of the bubble from the RW, the lower the frequency of this resonance.

At all audio frequencies, a bubble 0 mm from the round window generally compensates for the stiffening. The further the bubble is from the round window, the worse the compensation, to an increasing extent at higher frequencies. This is shown in Figure 6.10, with a bubble in each of four configurations. The bubbles and their positions are the same as those used in the position and frequency snapshot graphs. (Single element point bubbles with compliance equal to that lost by the stiffening of the round window, at 0, 10 and 20 mm from the round window and a long, achievable bubble from 1 to 16 mm from the RW with a compliance calculated from its physical properties.) In all cases, the loss of hearing is considered to be the equivalent of the reduction in BM velocity at the characteristic place. It can be seen that between 100 Hz and 10 kHz, the long, achievable bubble restores hearing so that the loss is no worse than about 5 dB at all audio frequencies. It is recognized that it is not possible to create a bubble with the compliance of the round window within a single element of the implant.

A realistic bubble would not have the compliance to compensate for the expected increase in stiffness of the round window, because a diaphragm of such a small area would be too stiff, as would the enclosed gas volume. Equally, a bubble that would precisely compensate for the expected RW stiffness would be too large to fit into an implant. A reasonable compromise can be achieved by creating a bubble with the same width as the basilar membrane and a length of about half that of the cochlea, or about two thirds the length of an implant.

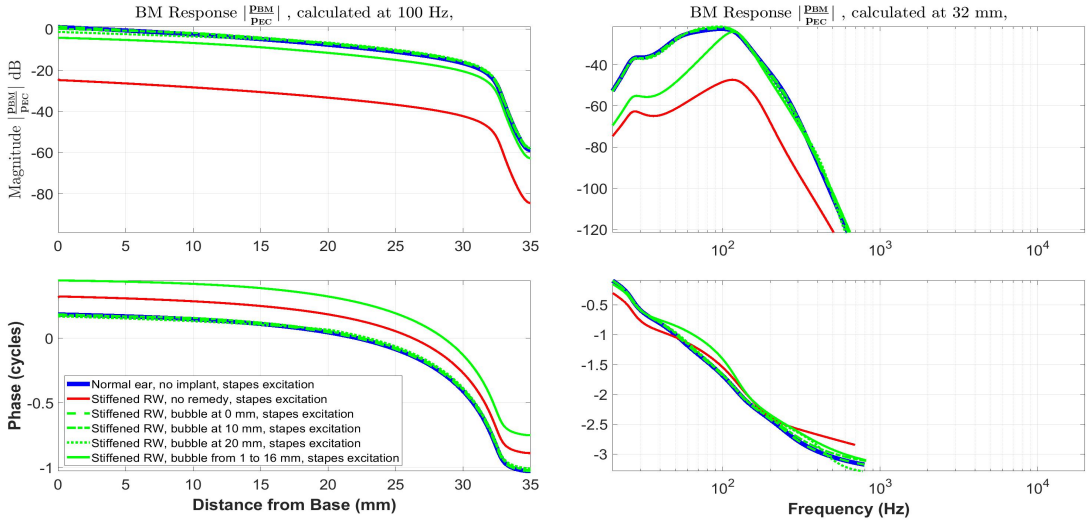

FIGURE 6.4: Normalized Pressure semi-difference across the BM for a normal RW (blue line), a stiffened round window (red line) and a stiffened RW with four bubble configurations (green lines) in the spatial domain at 100 Hz and the frequency domain at 32 mm.

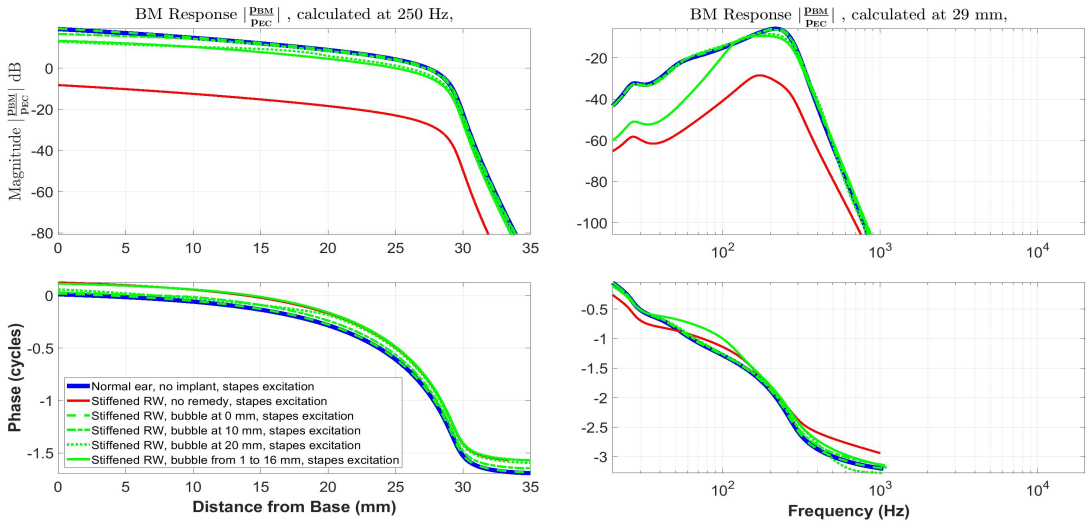

FIGURE 6.5: Normalized Pressure semi-difference across the BM for a normal RW (blue line), a stiffened round window (red line) and a stiffened RW with four bubble configurations (green lines) in the spatial domain at 250 Hz and the frequency domain at 29 mm.

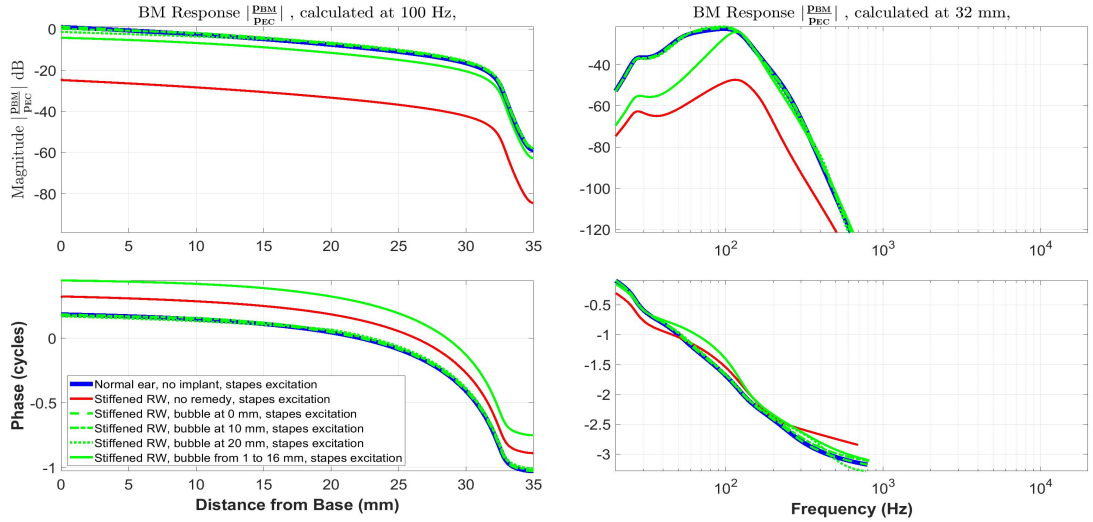

FIGURE 6.6: Normalized Pressure semi-difference across the BM for a normal RW (blue line), a stiffened round window (red line) and a stiffened RW with four bubble configurations (green lines) in the spatial domain at 1000 Hz and the frequency domain at 21 mm.

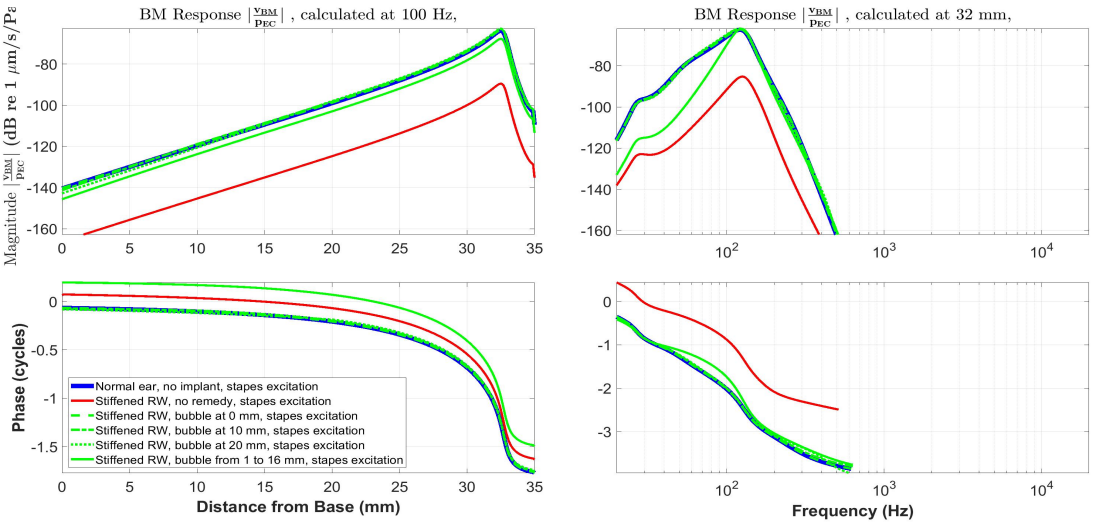

FIGURE 6.7: Normalized BM linear velocity for a normal RW (blue line), a stiffened round window (red line) and a stiffened RW with four bubble configurations (green lines) in the spatial domain at 100 Hz and the frequency domain at 32 mm.

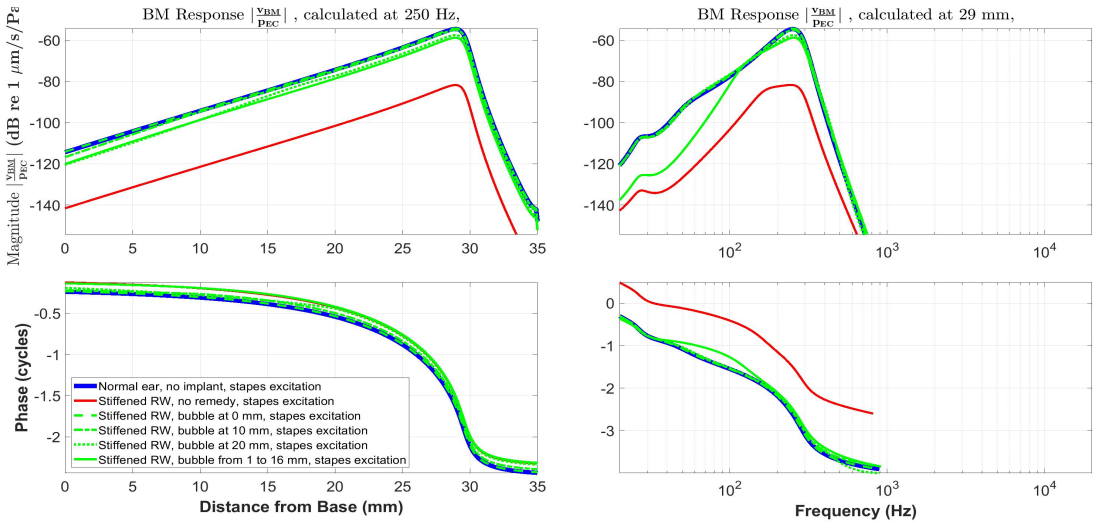

FIGURE 6.8: Normalized BM linear velocity for a normal RW (blue line), a stiffened round window (red line) and a stiffened RW with four bubble configurations (green lines) in the spatial domain at 250 Hz and the frequency domain at 29 mm.

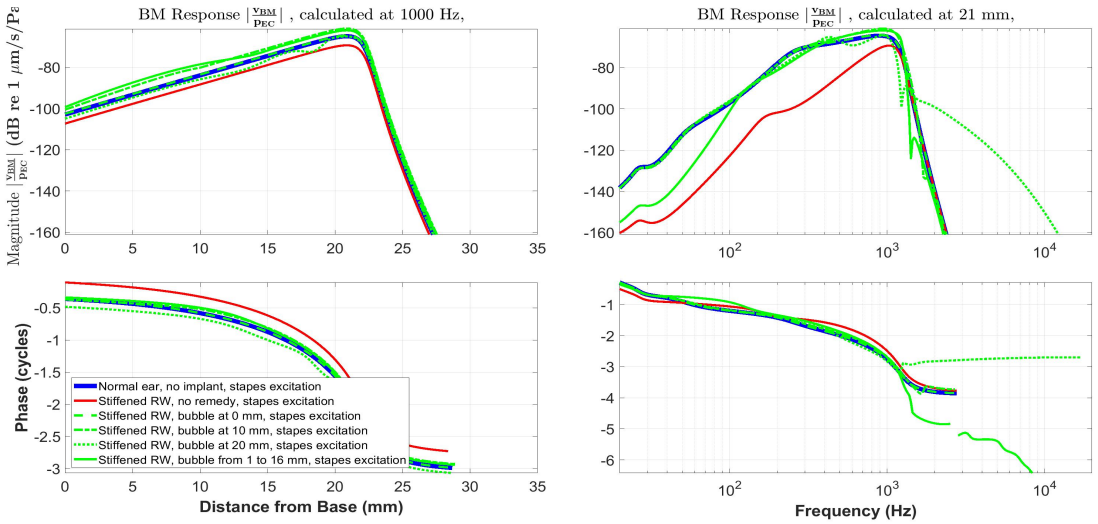

FIGURE 6.9: Normalized BM linear velocity for a normal RW (blue line), a stiffened round window (red line) and a stiffened RW with four bubble configurations (green lines) in the spatial domain at 1000 Hz and the frequency domain at 21 mm.

6.1.2 Hearing Loss

The spatial and frequency domain graphs show clearly the sensitivity at different positions along the cochlea to a particular frequency and to different frequencies at a particular position. They can do this for a cochlea with a normal RW and one with a stiffened RW, with or without a bubble. In this way, each graph can show the loss of sensitivity at one frequency or at one position. To visualize the full extent of hearing loss, it is necessary to show the decrease of sensitivity at the best place for all the audio frequencies. This is achieved in Figure 6.10 below.

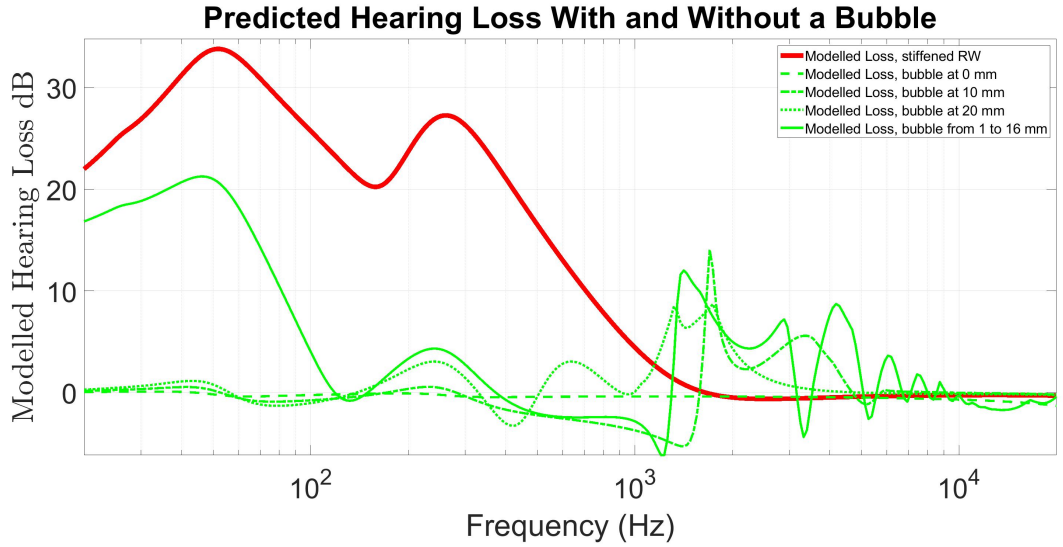

FIGURE 6.10: Hearing loss due to a stiffened RW, with no bubble (red line) and with four different bubble configurations (green lines).

This graph also shows that an ideal point bubble 0 mm from the round window almost exactly compensates for the stiffening of the round window, returning the hearing loss at all frequencies to 0 dB. The model can be used to model a practicable bubble, whose length spans many elements. To replace exactly the normal pressure release function of the round window, the bubble needs to be positioned as close as possible to the round window. Practically, there needs to be some separation, so that the bubble is certain to be within the cochlea, considering the uncertainties of surgical precision and the growth of a callous around the implant. It is considered practicable to avoid any covering of the bubble by the round window itself or a callous, by positioning the bubble in the cochlea so that it is no nearer than ≈ 1 mm to the round window, which is illustrated for the three position/frequency pairs of snapshots in Figures 6.4 to 6.9. The corresponding graph of post implantation hearing loss, with achievable bubble is shown as the solid green line in Figure 6.10. Figures 6.4 to 6.10 show that a practicably achievable bubble will restore hearing loss to better than 4.6 dB across the frequency range of interest.

6.2 Varying the Volume of a Bubble near the Round Window

In this section the two chamber finite element model has been used to compute the normalised pressure difference and BM velocity distributions under the following conditions:

Case	Name
1	Normal RW, bubble volume 0 mm^3
2	Stiff RW, bubble volume 0 mm^3
3	Stiff RW, bubble at 0 mm from RW, and volume 0.5 mm^3
4	Stiff RW, bubble at 0 mm from RW, and volume 1 mm^3
5	Stiff RW, bubble at 0 mm from RW, and volume 1.5 mm^3
6	Stiff RW, bubble at 0 mm from RW, and volume 2 mm^3
7	Stiff RW, bubble at 0 mm from RW, and volume 2.5 mm^3
8	Stiff RW, bubble at 0 mm from RW, and volume 3.3 mm^3
9	Stiff RW, bubble at 0 mm from RW, and volume 4 mm^3
10	Stiff RW, bubble at 0 mm from RW, and volume 5 mm^3
11	Stiff RW, bubble at 0 mm from RW, and volume 7 mm^3
12	Stiff RW, bubble at 0 mm from RW, and volume 15 mm^3
13	Stiff RW, with bubble 1 to 16 mm from RW, and volume 1.5 mm^3

As well as predicting the effects of stiffening the round window, the model has also been used to show that incorporating an achievable bubble in the implant near the round window will restore the acoustic hearing to within a few decibels of its pre-implant level. For four selected bubble volumes, the normalized BM velocity and pressure difference responses, as a function of frequency, are shown in figures 6.11 to 6.16, with bubble size as a parameter, and the corresponding graphs of hearing loss are shown in figure 6.17. Hearing loss is also graphed as a function of bubble volume, with frequency as a parameter in Figure 6.18. These graphs show that a very reasonable recovery of hearing loss to within a few decibels of the pre-implant value can be achieved by including a bubble of only 1.5 mm^3, or one tenth of the ideal volume. In all cases except the last, the calculations are for an ideal point bubble adjacent to the RW. A 15 mm long bubble with a volume of 1.5 mm^3 would fit within an implant.

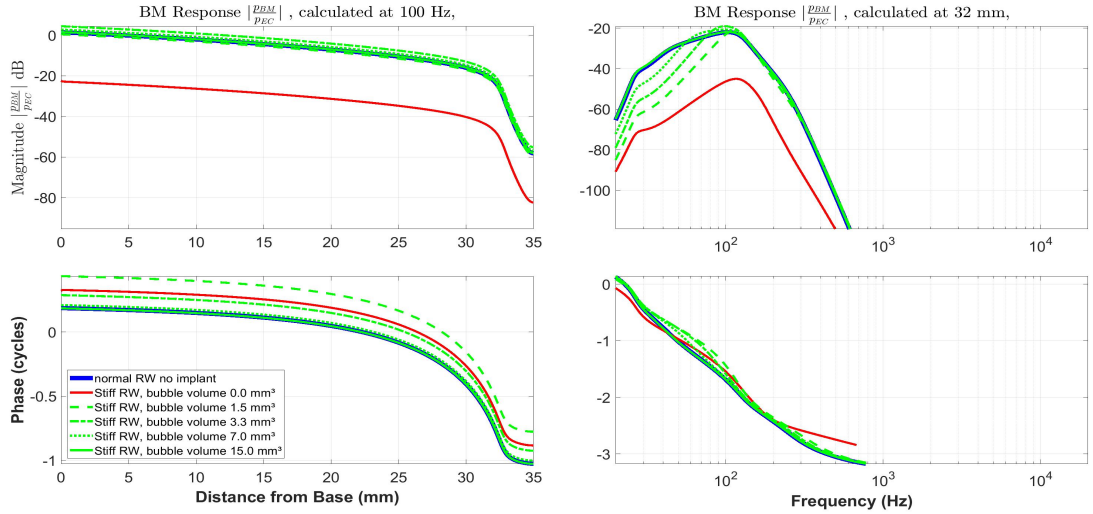

FIGURE 6.11: Pressure semi-difference across the BM for a normal RW (blue line), a stiffened round window (red line) and a stiffened RW with bubbles of four volumes (green lines) in the spatial domain at 100 Hz and the frequency domain at 32 mm.

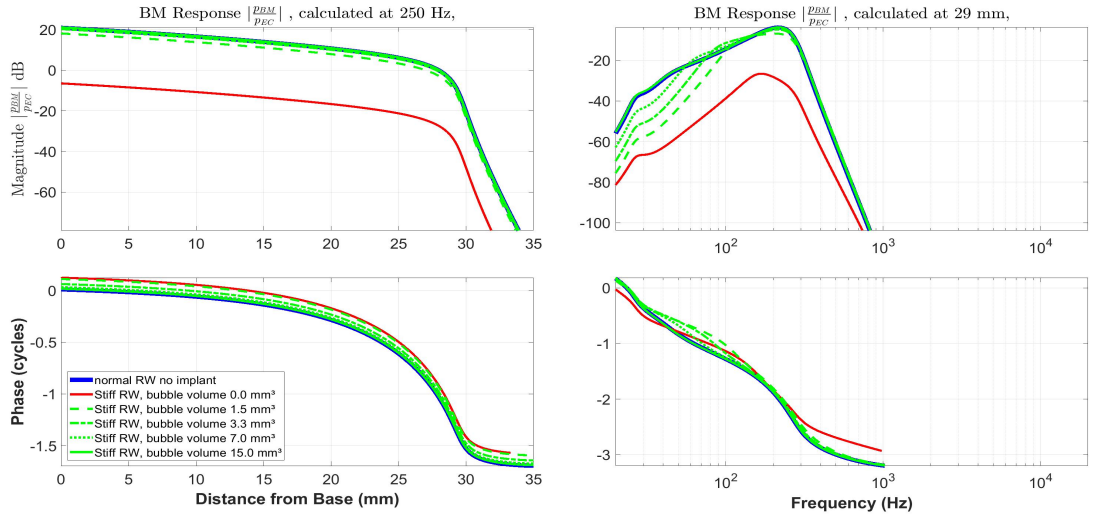

FIGURE 6.12: Pressure semi-difference across the BM for a normal RW (blue line), a stiffened round window (red line) and a stiffened RW with bubbles of four volumes (green lines) in the spatial domain at 250 Hz and the frequency domain at 29 mm.

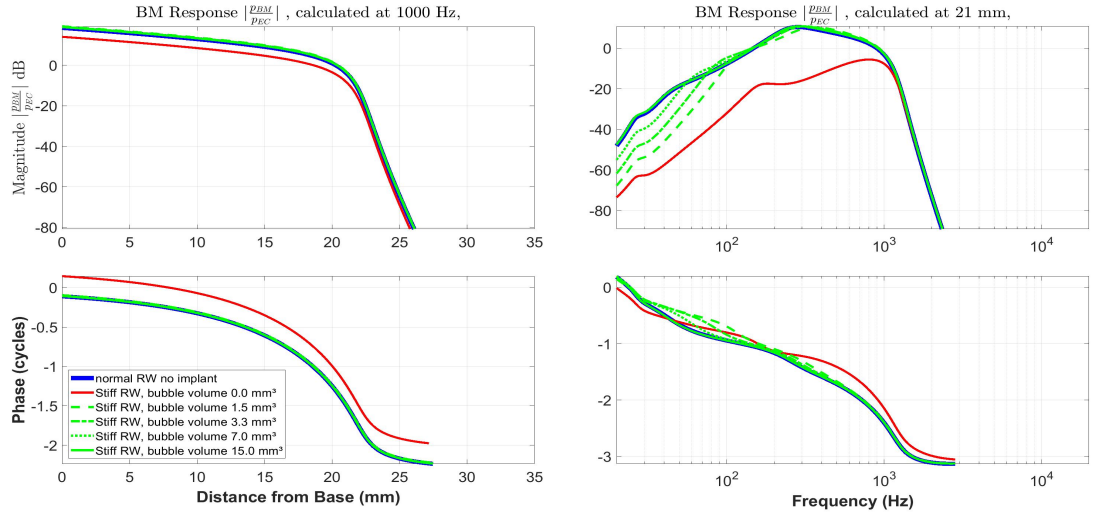

FIGURE 6.13: Pressure semi-difference across the BM for a normal RW (blue line), a stiffened round window (red line) and a stiffened RW with bubbles of four volumes (green lines) in the spatial domain at 1000 Hz and the frequency domain at 21 mm.

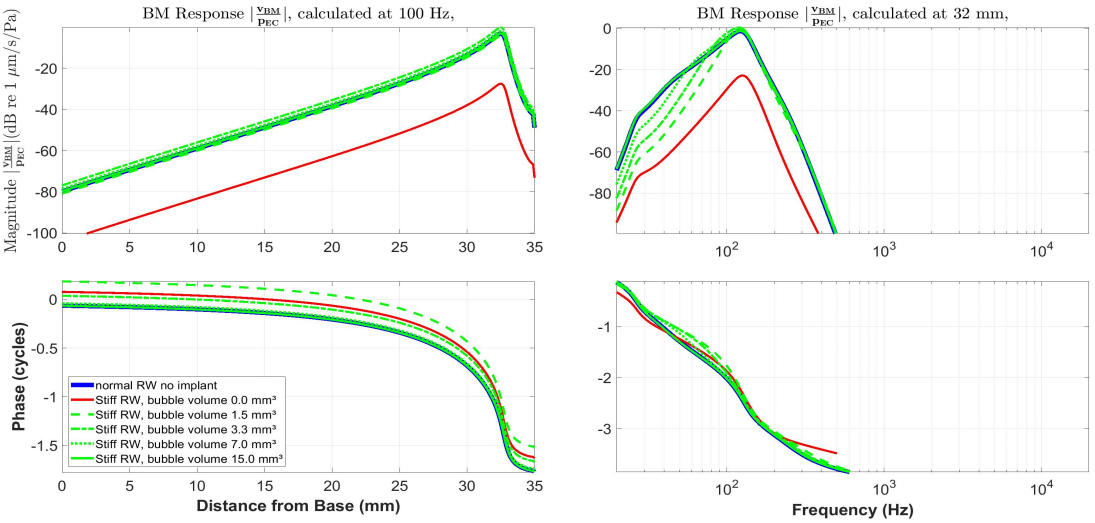

FIGURE 6.14: BM velocity for a normal RW (blue line), a stiffened round window (red line) and a stiffened RW with bubbles of four volumes (green lines) in the spatial domain at 100 Hz and the frequency domain at 32 mm.

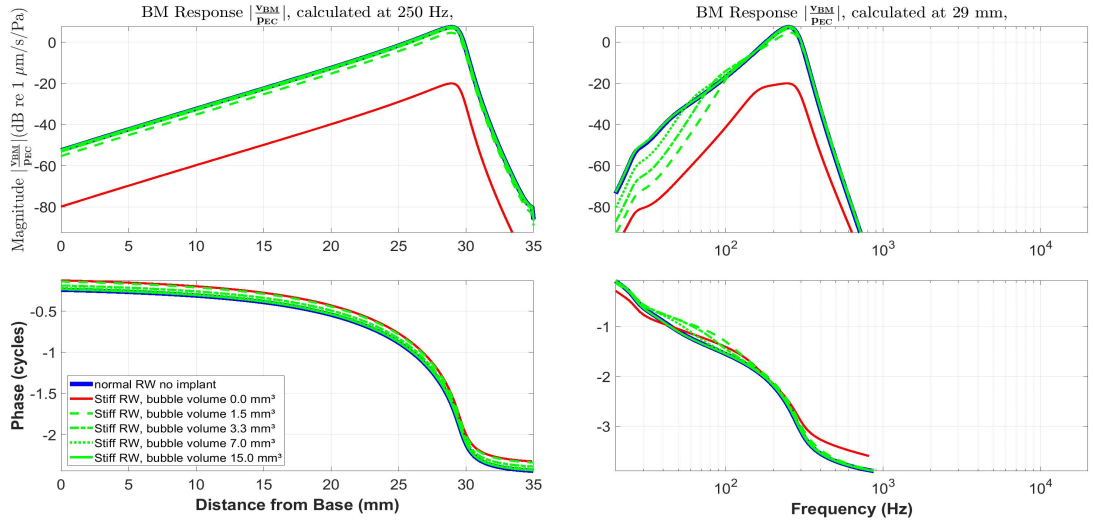

FIGURE 6.15: BM velocity for a normal RW (blue line), a stiffened round window (red line) and a stiffened RW with bubbles of four volumes (green lines) in the spatial domain at 250 Hz and the frequency domain at 29 mm.

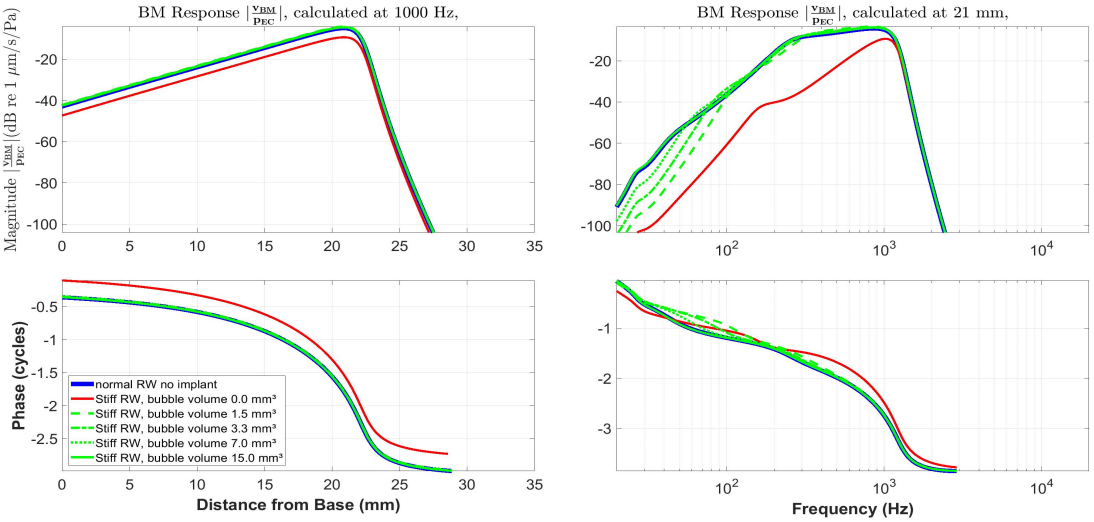

FIGURE 6.16: BM velocity for a normal RW (blue line), a stiffened round window (red line) and a stiffened RW with bubbles of four volumes (green lines) in the spatial domain at 1000 Hz and the frequency domain at 21 mm.

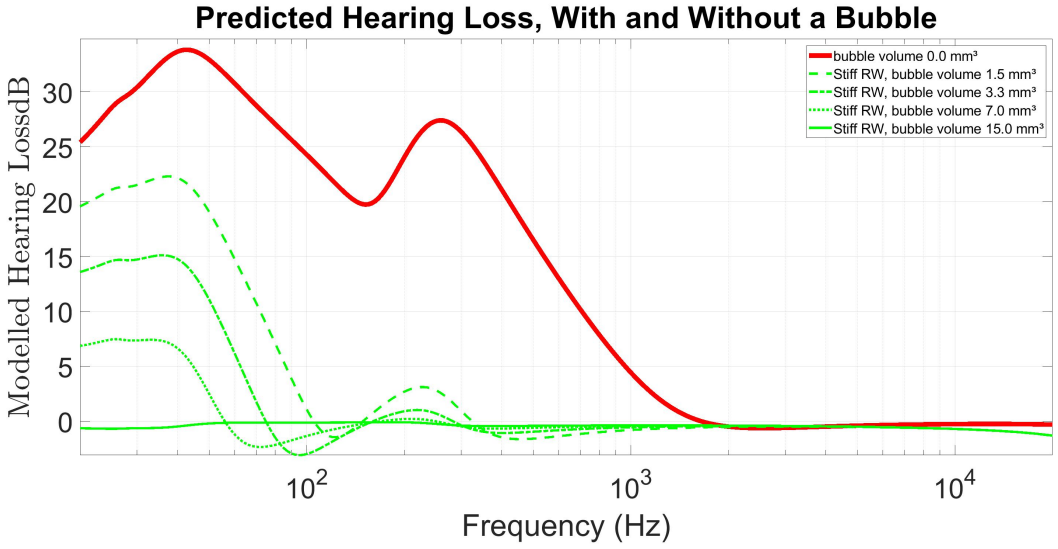

FIGURE 6.17: Hearing loss as a function of frequency for different sized point bubbles located at the RW, with bubble volume as a parameter.

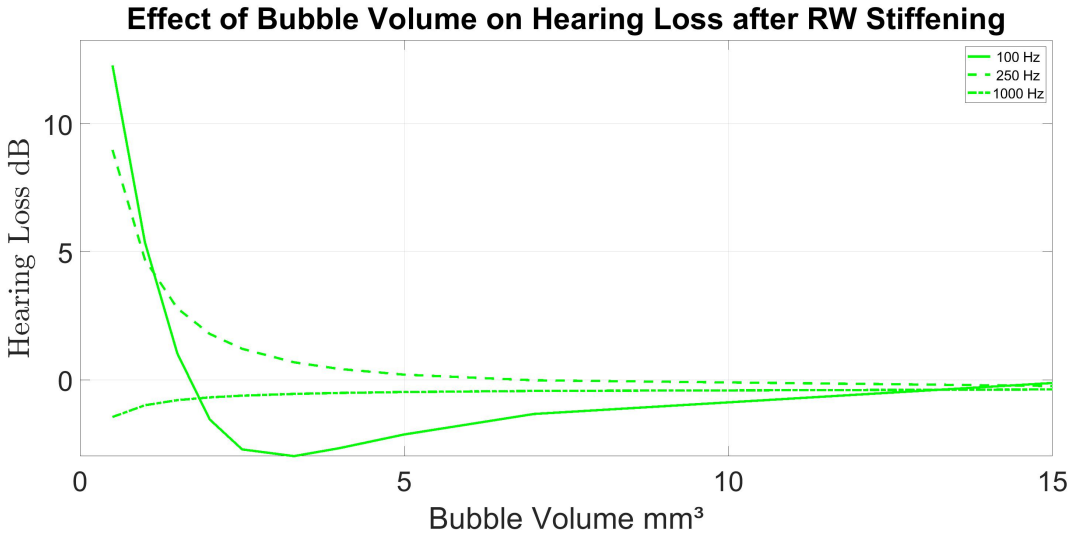

FIGURE 6.18: Hearing loss due to a stiffened RW, as a function of bubble volume, with frequency as a parameter.

6.3 The Configuration of an Achievable Bubble

To make an achievable bubble, it needs to have significant length and a diaphragm to separate the air it contains from the liquid in the chamber. It is estimated that to fit in a cochlear implant, the maximum dimensions that a bubble can have are 15×0.3×0.3 mm, and so the estimated maximum achievable volume is 1.5 mm^3. Figures 6.4 to 6.18 show the effect of bubbles of different volumes and in different positions. Outside the frequency range of interest the graphs showing the effect of varying the position of the bubble have irregular patterns as a result of the reduced

distance of the bubble from the stapes, which changes the inertance of the cochlear fluid that is moving as a result of the excitation by the stapes. The effect on hearing loss is complex and dependent on how the inertance of the fluid interacts with the other impedances in the cochlea. Because the complex and irregular patterns occur outside the frequency range of interest, this matter has not been investigated further. Within (and below) the frequency domain of interest, reducing the fluid inertance will have the effect of increasing the frequency at which a BM response occurs, or shifting the normal ear response to the right. The frequency shift will be small.

6.4 Modelling an Encapsulated Bubble

In order to incorporate a bubble of gas into a cochlear implant, it must be encapsulated within the implant and separated from the cochlear fluid by a light, thin and flexible diaphragm. The two chamber model simulates this diaphragm as a series of independent flexible pistons that are clamped along their lateral extremes, and that slide freely past their longitudinal neighbours. That is to say that they have no longitudinal mechanical coupling, and so they would behave similarly to the basilar membrane. This is shown diagrammatically in Figures 3.2 and 3.3 in Chapter 3. In practice, there would be some longitudinal mechanical coupling in a real diaphragm. Although no encapsulation has been assumed for point bubbles, the distributed bubble has been modelled with a thin silicone rubber diaphragm. The calculations of the combined stiffness of the gas volume of the bubble and the diaphragm are given in Appendix D.

Chapter 7

Acoustic Excitation Within the Cochlea

7.1 Introduction and Motivation

The motivation for the investigation in this chapter is the possibility of including an acoustic actuator within the cochlear implant, and so developing a single device that can provide simultaneously both high frequency electric stimulation and low frequency acoustic stimulation, without the need for an external high power hearing aid.

Electric stimulation from cochlear implants works well for frequencies above 1 kHz, which are required for recognizing the verbal content of speech. Lower frequency hearing is required to recognize the non-verbal content of speech, to appreciate music and to hear some traffic noise (McDermott and Looi (2004)). Furthermore, pitch discrimination is better when sound is transmitted through the normal hearing mechanism, rather than electrically via a cochlear implant, because it is difficult for an implant to select the nerve cells stimulated as finely as a healthy cochlea. The advantages of combined electrical and acoustic stimulation for speech perception have already been discussed in Section 2.5, and the results from Imsiecke et al. (2020) are shown in Figure 2.7. Therefore, low frequency residual acoustic hearing should not only be maintained, but ideally it should be enhanced to normal hearing levels.

A further advantage of EAS is that it provides an opportunity to implant a shorter electrode array, because electrical hearing can be cut off at higher frequencies. A shorter array means easier insertion, less trauma and less risk of tissue damage. Detailed examination of this matter is included in this thesis.

For many cochlear implant patients, implantation stiffens the round window, causing loss of usable acoustic hearing in addition to any pre-existing loss. Inclusion of a bubble within an implant would help to restore low frequency hearing to

pre-implantation levels, as detailed in Chapter 6, but powerful conventional hearing aids are sometimes still required to provide the amplification needed to compensate for any pre-existing low frequency deafness that often accompanies the higher frequency deafness that has justified implantation. This low-frequency hearing loss impairs speech recognition and the enjoyment of music. Conventional ear-canal hearing aids often have insufficient amplification to provide adequate acoustic levels of sensation to overcome this low-frequency loss. For example, the hearing aid and cochlear implant manufacturer, Medel, recommend an EAS system for patients with a hearing loss up to 65 dB for frequencies up to 500 Hz. Their system offers a gain up to 48 dB see https://blog.medel.pro/eas-implant-system (viewed on 15/6/22) and a power output SPL up to 118 dB. However, as the amplification of a conventional hearing aid becomes greater, there is a greater likelihood of oscillation due to feedback from the 'receiver' to the microphone, as measured by Kuk (1994). The measurements in this paper indicate that the hearing aids tested are limited to a maximum achievable gain of 30 dB in ideal circumstances at a few hundred Hertz, and the maximum SPL available was 140 dB. An excitation source within the cochlea could provide the amplification necessary to achieve normal hearing for a patient with 97 dB hearing loss over the full frequency range of interest (100 - 1000 Hz), producing a power output of 141.5 dB (SPL), as shown in this Chapter and in Chapter 8.

This chapter assesses the engineering requirements for an intracochlear actuator, and the feasibility of designing and manufacturing such a device is discussed in Chapter 8.

7.2 Assessing the Requirements of an Intracochlear Actuator

The mechanics of stimulation from an acoustic source within the lower chamber of the cochlea are investigated using both the two chamber model developed in Chapter 3 and the published work of others. An eight stage approach is adopted to enable the subjective requirements of a typical implant user to be converted to the objective requirements of an intracochlear actuator:

1. Determine the frequency range over which the actuator needs to be effective.
2. Determine the maximum hearing sensation level required.
3. Convert the sensation level to the hearing level (in dB above normal threshold) needed to compensate for the pre-implantation hearing loss.
4. Convert the required hearing level to the equivalent sound pressure level for air-conduction at the entrance to the ear canal.
5. Determine the stapes velocity produced by this SPL.

6. Use the two chamber model of the cochlea to convert this stapes velocity to a basilar membrane velocity with normal RW stiffness.

7. Use the two chamber model again to find the intracochlear actuator velocity that would produce the same basilar membrane velocity with a stiffened RW.

8. Finally, use the two chamber model a third time to determine the acoustic impedance seen by the actuator to compute the acoustic pressure required of the actuator to generate the same sensation as 115 dB above normal hearing threshold would generate in a healthy ear.

The optimum changeover frequency from acoustic to electric stimulation will be determined by various hard to predict and subjective factors, such as frequency selectivity and degree of recruitment, both of which vary with hearing loss, see Imsiecke et al. (2020) and Gifford et al. (2017). Fortunately, virtually all of the requirements of an intracochlear actuator are most challenging at the lower end of its required frequency range, and it has to be accepted that it will not be possible to design an actuator that can be configured to give optimum compensation for extreme cases of hearing loss.

7.3 Determination of the Required Frequency Range

In order to replace fully an external acoustic hearing aid, the intracochlear actuator would need to be able to generate, without undue distortion, sufficient acoustic pressure and velocity to produce the same sensation as in a "normal" ear for the entire range of sounds required to be heard acoustically. For this exercise, the range is considered to be expressed in terms of frequency and amplitude. Above a frequency of 500 Hz, a cochlear implant provides acceptable sensation of hearing level by electric stimulation, and so, to allow reasonable overlap for electro-acoustic stimulation, the upper bound of the required frequency range for acoustic stimulation is taken to be 1 kHz.

No research on the contribution to speech recognition of frequencies below 125 Hz has been found, and so it is assumed that the information value of sounds for speech recognition diminishes at frequencies below 100 Hz. From personal subjective experience, it is very rare for speech to contain frequencies below that frequency.

Regarding traffic noise, Bąkowski et al. (2019) state, "The calculations of the equivalent sound level generated by all vehicles, depending on the frequency, showed that the noise with the highest values occurs in the octave band with the center frequency f0= 1000 Hz. The minimum values are in the octave band f0= 125 Hz." The decline from the 1 kHz band to the 125 Hz band is progressive, and the measured values at 125 Hz

are 20 dB less than those at 1 kHz. It is therefore assumed that traffic noise below the 125 Hz band is insignificant.

Very few musical notes have a fundamental frequency below 100 Hz, and those that do are very often rich in harmonics, enabling the ear to "imagine" the fundamental.

Because of all of these factors, 100 Hz is considered to be the lower bound of the required frequency range. The frequency band from 100 Hz to 1 kHz is thus considered to be the range of interest for determining the requirements of an actuator.

7.4 Determination of the Required Amplitude Range

Assuming that the intracochlear actuator is linear, only the upper bound of this amplitude range needs to be considered when determining the duty of the actuator. Clearly, the electronic driver of the actuator will need to apply amplification to match the relationship between sound pressure levels and sensation to that of a "normal" ear. It is unlikely to be possible for an actuator to compensate for the acoustic pre-op deafness in the ears of all patients, because some implant patients are so profoundly deaf that they have virtually no residual acoustic hearing, even at low frequencies. The studies by Verschuur et al. (2016) and Causon et al. (2015) give mean and standard deviation figures for measured pre-op hearing loss at a frequencies between 125 Hz and 1 kHz for a total of over 280 patients. These statistics are used here to determine the maximum pre-op hearing loss below 1 kHz, affecting more than 80% of the patients in the studies. At every measured frequency of 750 Hz or less, 80% of the patients had a pre-op loss of less than 97 dB. At 1 kHz, 63% of the patients had a hearing loss of less than 97 dB. This means that an acoustic actuator could be used in conjunction with an implanted electrode array to compensate for loss of speech perception in 80% of cochlear implant patients, if it could compensate for a 97 dB hearing loss over the frequency range of interest. As a result, it is assumed that an acoustic actuator would be satisfactory, if it could compensate for a 97 dB loss of hearing level over the frequency range 100 Hz to 1 kHz.

7.4.1 Subjective Performance Requirement

Normal conversation is in the range 60 - 70 dB HL. The term ’dB HL’ means the number of decibels above the reference threshold of hearing, which is defined in BS EN ISO 389-7:2019 as:

3.3 reference threshold of hearing at a specified frequency, sound pressure level of a pure tone or a one-third-octave band of noise corresponding to the median value of the binaural thresholds of hearing of otologically normal persons (3.2.) within the age limits from 18 years to 25 years inclusive

The same document defines an otologically normal person as:

3.2 otologically normal person person in a normal state of health who is free from all signs or symptoms of ear disease and from obstructing wax in the ear canals, and who has no history of undue exposure to noise, exposure to potentially ototoxic substances, or familial bearing loss

To allow a reasonable margin for louder sounds without need for user adjustment, an actuator would need to reproduce, without excessive distortion, the equivalent SPL of up to 80 dB HL in a typical implanted ear.

7.4.2 Objective Performance Requirement

Sensation level is reflected in the compound action potential (CAP) of the auditory nerve. It is assumed that sounds that generate equal CAPs will generate equal sensations. Eggermont (1977) have published a graph of CAP measurements plotted against hearing levels for the median of 20 "normal" ears and those of five individuals with sensorineural hearing loss (SNHL) and loudness recruitment, which Eggermont shows is normally associated with severe SNHL. This graph is shown in figure 7.1, and it is used here to convert from subjective to objective requirements for an intracochlear actuator. The graph for the patient with 75 dB hearing loss has been copied and displaced to show the likely result for a patient with 97 dB hearing loss, as a green line. A red vertical line has then been added from the 80 dB point on the horizontal axis to touch the curve for normal ears, to find the sensation level that would be experienced by an otologically normal person when hearing sound 80 dB above normal hearing threshold. At this CAP sensation level, a red horizontal line has been added from the 80 dB point on the normal ear curve, to intersect the graph for a patient with 97 dB hearing loss. From that intersection point, a red vertical line has been added down to the horizontal axis, to find the hearing level that would produce the same sensation in the 97 dB hearing loss implant patient as 80 dB hearing level would produce in a normal ear. So the graph shows that a level of 115 dB above the normal hearing threshold would be required.

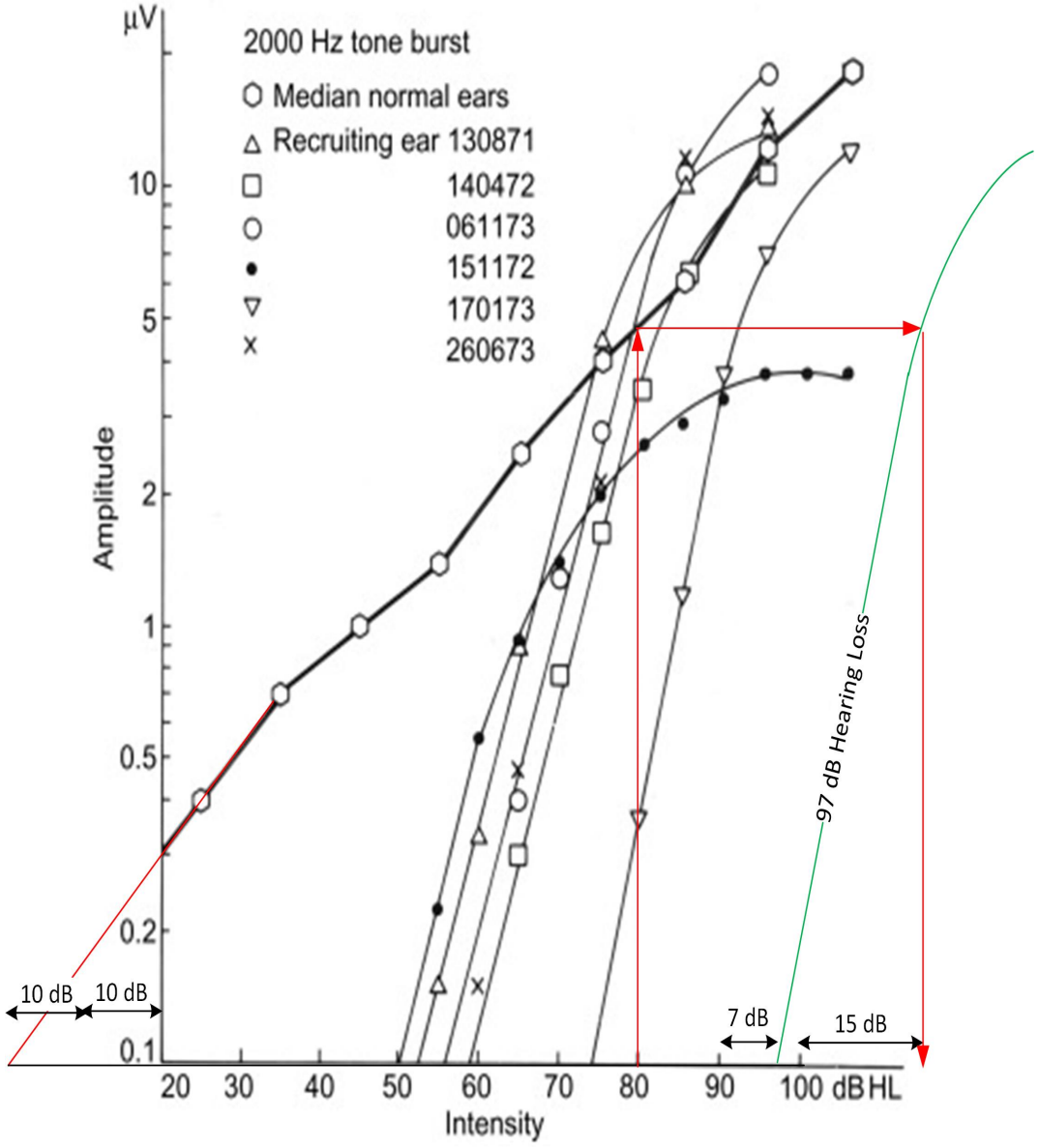

FIGURE 7.1: Compound Action Potential for Ears with Different Hearing Losses. The vertical axis is the amplitude of the compound action potential (CAP), measured using a trans-tympanic technique and expressed in μV. (Taken from Eggermont (1977) fig. 2, with coloured lines and some annotation added.) This graph is captioned by Eggermont as "Equivalent Loudness Levels", and so the compound action potentials plotted here are taken as a proxy for equivalent loudness levels. This figure is published by Sage, who permit re-use of up to three figures from one of their journal articles into a thesis or a dissertation without seeking a license or permission. See `https://us.sagepub.com/en-us/nam/pre-approved-permission-requests-journals`

Once the hearing level requirement is determined, it is a simple matter to convert this to an SPL at the entrance to the ear canal, using the conversion number from BS EN ISO 389-7:2019 for the frequencies concerned, to give the air-conduction sound pressure level needed to achieve the required sensation level. At 100 Hz, in free field conditions, the threshold of normal hearing is 26.5 dB above 0 dB SPL, or 20 μPa (BS EN ISO 389-7:2019). So, an actuator would need to reproduce the same sensation as

would 141.5 dB SPL (or 238 Pa) at 100 Hz and 117.4 dB, (or 15 Pa) at 1000 Hz, free-field in a normal ear[1].

The relationship between SPL and hearing level given in BS EN ISO 389-7:2019 approximates very closely to the equation:

$$T = 25.201(\log f)^2 - 152.32 \log f + 231.34 \tag{7.1}$$

Where T is the difference in dB to be added to the hearing level to give the corresponding SPL, and log means common logarithm (base 10). The conversion number given in the standard for each frequency is plotted in figure 7.3, together with the approximate values calculated using equation 7.1. For simplicity, the present model uses the approximation equation 7.1. The expressions for SPL and pressure in the ear canal at all frequencies <2 kHz are:

$$\begin{aligned}
\mathrm{SPL_{EC}} &= \mathrm{HL} + 25.201(\log f)^2 - 152.32 \log f + 231.34 \text{ dB, or} && (7.2)\\
p_{\mathrm{EC}} &= 20 \times 10^{-6} \times 10^{(\mathrm{HL}+231.34+25.201(\log f)^2 - 152.32 \log f)/20} \text{ Pa.} && (7.3)\\
p_{\mathrm{EC}} &= 10^{(\mathrm{HL}+137.36+25.201(\log f)^2 - 152.32 \log f)/20} \text{ Pa.} && (7.4)\\
p_{\mathrm{EC}} &= 10^{(\mathrm{HL}/20)} \times 10^{(5.567+1.26(\log f)^2 - 7.616 \log f)} \text{ Pa.} && (7.5)\\
p_{\mathrm{EC}} &= 10^{\mathrm{HL}/20} \times 3.69 \times 10^5 \times f^{1.26 \log f - 7.616} \text{ Pa.} && (7.6)
\end{aligned}$$

For a hearing level of 115 dB,

$$\begin{aligned}
\mathrm{SPL_{EC}} &= 115 + 25.201(\log f)^2 - 152.32 \log f + 231.34 \text{ dB, or} && (7.7)\\
\mathrm{SPL_{EC}} &= 25.201(\log f)^2 - 152.32 \log f + 346.34 \text{ dB, and} && (7.8)\\
p_{\mathrm{EC}} &= 20 \times 10^{-6} \times 10^{346.34/20} \times f^{(1.26 \log f)} / f^{7.616} \text{ Pa} && (7.9)\\
p_{\mathrm{EC}} &= 20 \times 10^{-6} \times 10^{(1.3-6+17.317)} \times f^{(1.26 \log f)} / f^{7.616} \text{ Pa} && (7.10)\\
p_{\mathrm{EC}} &= 10^{12.617} \times f^{(1.26 \log f - 7.616)} \text{ Pa.} && (7.11)\\
\text{So: } p_{\mathrm{EC}} &= 266 \text{ Pa at 100 Hz.} && (7.12)\\
&= 13 \text{ Pa at 1 kHz.} && (7.13)
\end{aligned}$$

The corresponding numbers from BS EN ISO 389-7:2019 quoted above for 100 Hz and 1 kHz are 238 Pa and 15 Pa, respectively. This confirms that the regression approximation is within 1.25 dB of the 100 Hz and 1 kHz spot data points in BS EN

[1]Please note that the definition (3.4) of free sound field in BS EN ISO 389-7:2019 is "sound field where the boundaries of the room exert a negligible effect on the sound waves." This may be different from definitions of free-field used elsewhere. Because the specification is derived as a best fit to measured data, rather than theoretical calculation, it is assumed for the present purposes that the measurements were made and the specification intended for air conduction from a separate source with a listener present. The relevant column in Table I of the BS EN ISO 389-7:2019 is headed "free-field listening (frontal incidence)", which further implies the presence of a listener.

ISO 389-7:2019, and the left hand graph [a] in figure 7.3 shows that the approximation remains within that limit between those frequencies.

7.4.3 Stapes Velocity Resulting from the Required Maximum SPL

Xue et al. (2020) have published a graph of the results of their model (validated by another model and two independent sets of measured results) that shows the normalized velocity response from the ear canal to the stapes, V_{FS}/p_{EC}, as a function of frequency. Xue et al. define p_{EC} as the ear canal input pressure. Their model includes the tympanic membrane and the ear canal as separate entities, and so it is assumed that the ear canal pressure is taken as that at the outer end of the ear canal.

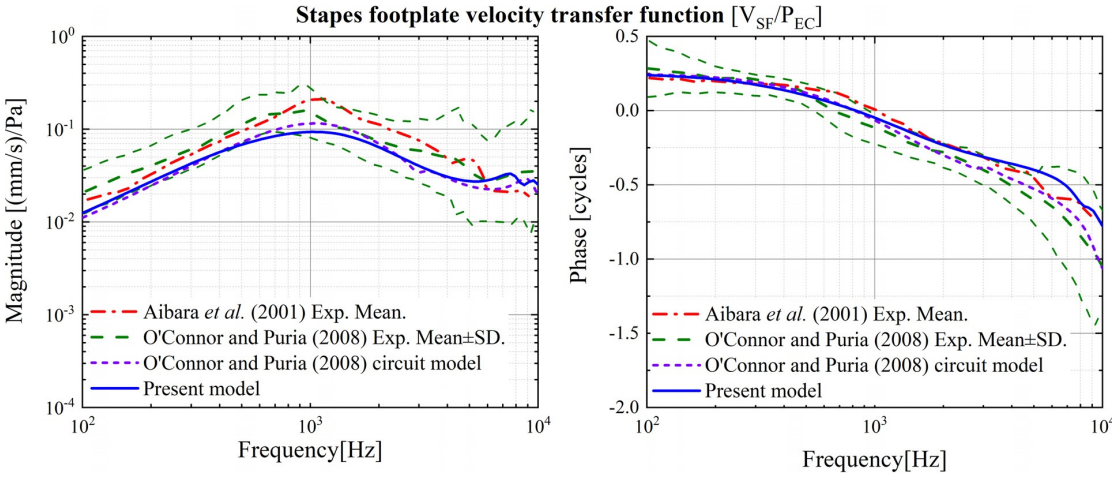

FIGURE 7.2: Stapes footplate velocity normalized to ear canal pressure (v_{ST}/p_{EC}). Reprinted with permission from Xue et al. (2020) (FIG. 6). Copyright 2020, Acoustic Society of America..

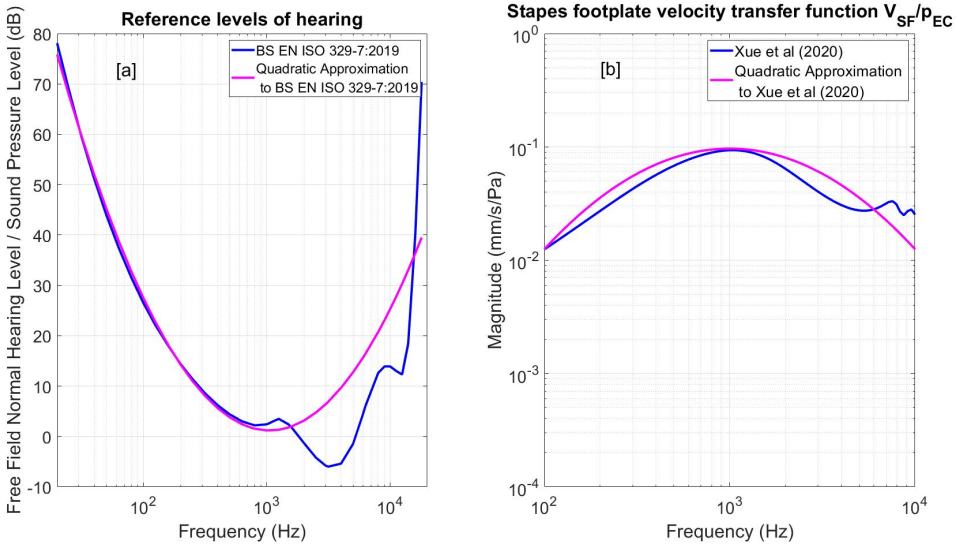

FIGURE 7.3: [a] Plots of data points given in BS EN ISO 389-7:2019 for converting free field SPL to hearing level, together with a plot of equation 7.1 and [b] normalized BM velocity response Xue et al. (2020) extracted from figure 7.2, together with a plot of equation 7.23.

This graph enables the SPL at the outer ear to be converted to a linear stapes velocity. Over the frequency range up to 2 kHz, the graph from the Xue et al model shown in the right hand graph [b] of figure 7.2 approximates closely to a quadratic equation of the form:

$$\log|V_{\mathrm{FS}}/p_{\mathrm{EC}}| = a(\log(f))^2 + b\log(f) + c \tag{7.14}$$

Noting from the graph and the associated text that the maximum of 9.65×10^{-2} occurs at 1 kHz and that the value at 100 Hz is 1.25×10^{-2}, the equation becomes:

$$\begin{aligned} \log|V_{\mathrm{FS}}/p_{\mathrm{EC}}| &= -\log(9.65/1.25)(\log f)^2 + 6\log(9.65/1.25)\log(f) \\ &+ \log(1.25\times10^{-2}) - 8\log(9.65/1.25) \end{aligned} \tag{7.15}$$

This can be re-written as:

$$|V_{\mathrm{FS}}/p_{\mathrm{EC}}| = 10^{-0.888\log f^2 + 6\times0.888\log f - 8\times0.888 + \log(1.25\times10^{-2})} \tag{7.16}$$

$$= f^{0.888\times(6-\log f)} \times 10^{-8\times0.888} \times 1.25\times10^{-2} \tag{7.17}$$

$$\text{At 100 Hz,} \quad = 1.25\times10^{-2} \times 10^{0.888\times(12-8-2\times\log f)} \tag{7.18}$$

$$= 0.0125 \text{ mm/s/Pa} \tag{7.19}$$

$$\text{At 1 kHz,} \quad = 1.25\times10^{-2} \times 10^{0.888\times(18-8-3\times\log f)} \tag{7.20}$$

$$= 0.0965 \text{ mm/s/Pa} \tag{7.21}$$

(The values produced by equations 7.19 and 7.21 are given with the same precision as that used by Xue et al. (2020) in their text, to show that the approximation is precise at these two frequencies. In the context of this thesis, such precision is otherwise not needed.)

Equation 7.17 can then be used with equation 7.6 to compute the stapes velocity required to create the required hearing level.

$$V_{FS} = 10^{HL/20} \times 10^{6.868} \times f^{1.26 \log f - 7.616} \times f^{0.888 \times (6 - \log f)} \times 10^{-9.007} \quad (7.22)$$

$$V_{FS} = 10^{HL/20} \times f^{0.372 \log f - 2.288} \times 10^{-2.139} \quad (7.23)$$

For 115 dB Hearing Level at the ear canal, the linear stapes velocity must thus be:

$$V_{FS} = 4083 \times f^{0.372 \log f - 2.288} \quad (7.24)$$

$$\text{At 100 Hz,} = 4083 \times 100^{0.372 \log 100 - 2.288} \quad (7.25)$$

$$= 3.33 \text{ mm/s,} \quad (7.26)$$

$$\text{if stapes area = 3.2 mm}^2 \text{ Békésy and Wever (1960)} \quad (7.27)$$

$$\text{Volume velocity, } V_S = 11 \times 10^{-9} \text{ m}^3/\text{s} \quad (7.28)$$

$$\text{At 1 kHz, } V_{FS} = 4083 \times 1000^{0.372 \log 1000 - 2.288} \quad (7.29)$$

$$= 1.24 \text{ mm/s} \quad (7.30)$$

$$\text{Volume velocity, } V_S = 4 \times 10^{-9} \text{ m}^3/\text{s} \quad (7.31)$$

Equation 7.23 can be used now with the new model to calculate the basilar membrane velocity required to generate the required hearing level, for all frequencies <= 2 kHz.

The left hand graph in figure 7.3 shows the stapes normalized velocity response from the ear canal derived by Xue et al. (2020), together with the corresponding quadratic approximation of equation 7.23 that is used with the present model to compute the required actuator velocity.

7.4.4 Computation of the Required Basilar Membrane Velocity

The new model computes the normalized velocity response from the stapes to the basilar membrane; this is used in combination with equation 7.23 and the required hearing level to compute the linear BM velocity that occurs when a free field sound wave at 115 dB above normal hearing level is presented to the ear canal. This BM velocity is calculated as a function of frequency. From the work of Eggermont (1977), it is concluded that this is the BM velocity required to produce in the ear of an implant patient the same compound action potential and hence the same sensation in an implanted ear as would 80 dB above normal hearing level produce in a normal ear (with no sensorineural hearing loss and no implant), which is measured by Eggermont et al as 5 μV.

7.4.5 Computation of the Required Actuator Velocity

The cochlear model can be used to calculate the normalized velocity response from the actuator to the BM. This is used to compute the actuator diaphragm velocity needed to produce the same BM velocity as described in subsection 7.4.4. This actuator velocity will produce the same sensation in a typical implanted ear as that produced by the required SPL in the pre-implanted ear of a typical CI candidate. The magnitude of this velocity is shown for all audio frequencies in figure 7.10, and it is tabulated at the end of this Chapter for particular frequencies within the range of interest in Table 7.2.

7.4.6 Computation of the Pressure Required from the Actuator

The cochlear model can also be used to calculate the acoustic impedance that the cochlear presents to the actuator, which is shown in Figure 7.11. This is multiplied by the velocity requirement to give the pressure requirement. The resultant pressure is shown for all audio frequencies in figure 7.12, and it is shown for particular frequencies in the range of interest in Table 7.2. For a magnetic actuator, such as the balanced armature type, the coil current required will be proportional to the diaphragm pressure.

7.4.7 Summary of Requirements

A step-wise approach has been used to determine the velocities and pressures that an intracochlear actuator needs to generate, in order to restore to normal the hearing in an implanted ear over the range of frequencies where electric stimulation does not restore hearing sensation to that of a "normal" ear. The contributions of the new model are in comparing the normalized velocity responses from the stapes and the actuator to the basilar membrane, together with computing the cochlear impedance at the actuator. Discussion of these calculations follows in the next Section. The following Chapter uses these results to determine the feasibility of designing and constructing a suitable actuator, using a variety of different technologies.

7.5 The Cochlear Response due to an Implanted Actuator

When the excitation is from the stapes at low frequencies, all of the flow beyond the vestibular aqueduct is along the upper chamber of the cochlea towards the apex, with negligible flow passing through the BM, until the characteristic place for the frequency is approached, where the flow passes through the BM to the lower chamber, and returns towards the base, where it passes through the cochlear aqueduct and the

round window. An explanation of the modelled behaviour of the cochlear when excited from the stapes is provided in Chapter 5, above.

When the excitation is from an actuator in the lower chamber, the flow divides; some remains within the lower chamber and flows out through the cochlear aqueduct and the round window, and some flows through the BM into the upper chamber, and flows out through the vestibular aqueduct and the stapes to the middle ear. With an unstiffened round window, the former path would be the lower impedance, taking virtually all of the flow, because the round window has an impedance less than that of the middle ear, typically by a factor of ten at low frequencies. When the round window is stiffened by a factor of 170 or so, the situation is reversed at frequencies below a few kHz, and the path through the BM and the upper chamber generally has the lower impedance, and so it takes most of the flow, and the normalized response is more or less the same as that of a normal ear. However, above the 289 Hz frequency at which the middle ear impedance resonates with the cochlear input impedance, that increased impedance remains much greater than that of the combined cochlear aqueduct and the round window, and so the normalized response from an actuator is greater than that for stapes excitation.

Figures 5.6 to 5.8 from Chapter 5 have been augmented to add the normalized responses for four different actuator configurations. These configurations are single element point actuators at 0, 10 and 20 mm from the round window, and an achievable actuator with a diaphragm from 1 to 16 mm from the round window. These normalized responses are shown as magenta lines in Figures 7.4 to 7.6. Because the actuator would be incorporated in a cochlear implant, the round window is considered to be stiffened in each case. The actuator in each case is a hypothetical device whose length occupies just one finite element, to show the effects of locating the actuator in different positions. For comparison, the blue and red lines show the normalized response from the stapes, with a normal and a stiffened round window, respectively.

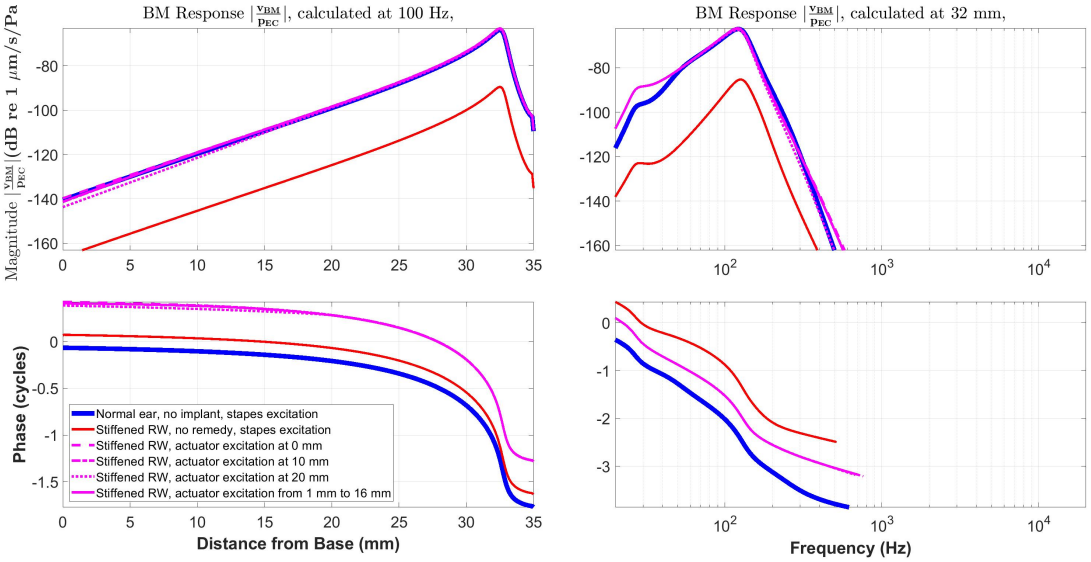

FIGURE 7.4: Normalized Basilar membrane linear velocity response predicted at 100 Hz in the spatial domain and at 32 mm in the frequency domain for a point actuator just one finite element long at each of three positions and for a 15 mm long actuator. For comparison, graphs are also plotted for a normal ear and for an implanted ear, each with excitation from the stapes. The Norton equivalent excitation volume velocity from the actuator is the same as that from the stapes (when the ear canal sound pressure is 115 dB above normal hearing level).

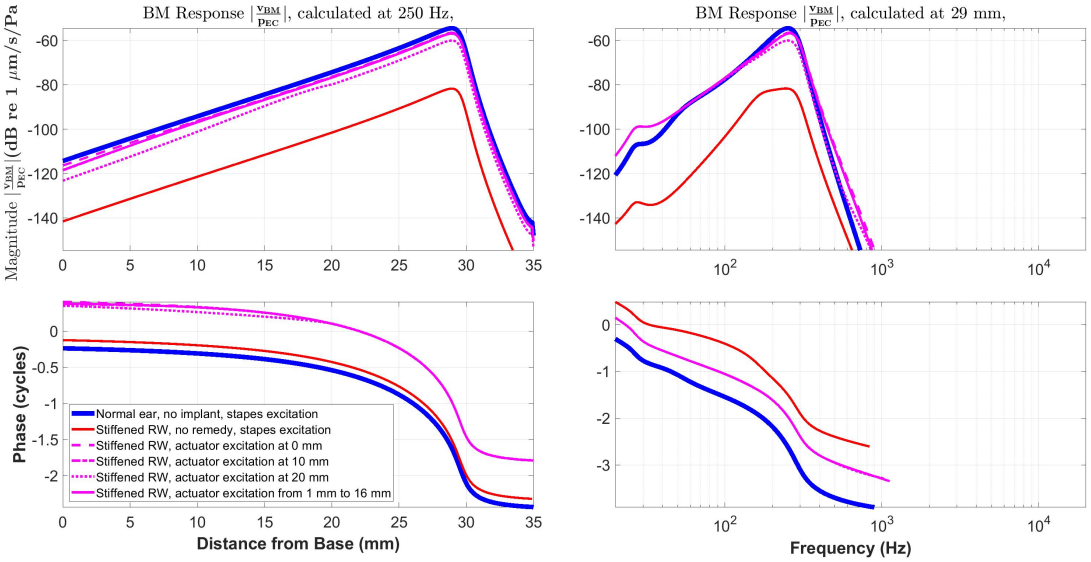

FIGURE 7.5: Normalized Basilar membrane linear velocity response predicted at 250 Hz in the spatial domain and at 29 mm in the frequency domain for a point actuator just one finite element long at each of three positions and for a 15 mm long actuator. For comparison, graphs are also plotted for a normal ear and for an implanted ear, each with excitation from the stapes. The Norton equivalent excitation volume velocity from the actuator is the same as that from the stapes when the ear canal sound pressure is 115 dB above Normal Hearing level. (v_{Exc} is the pressure at the excitation source: the stapes or the actuator as indicated in the legend.)

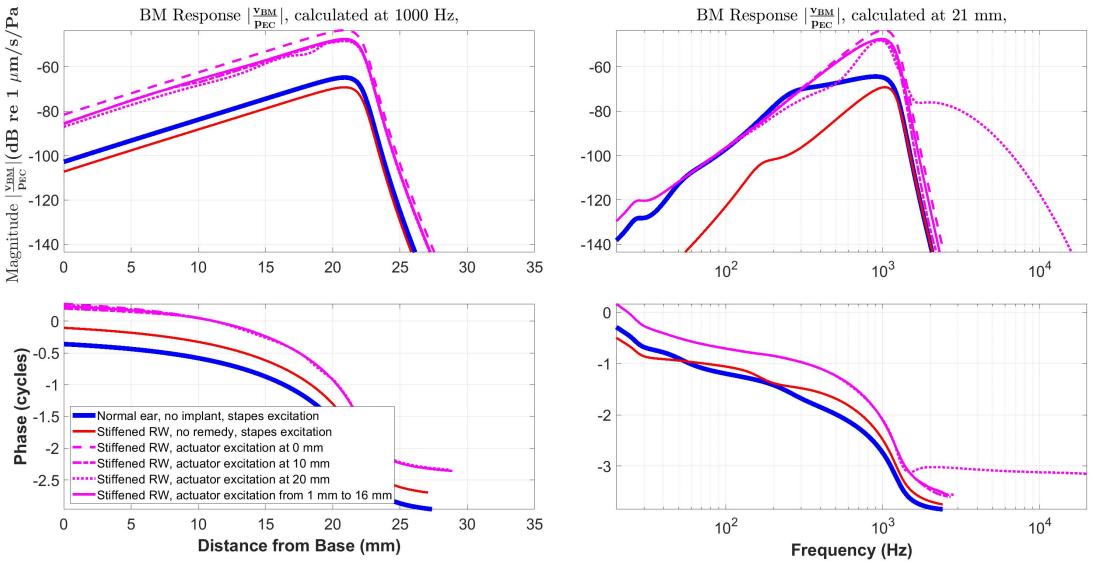

FIGURE 7.6: Normalized Basilar membrane linear velocity response predicted at 1 kHz in the spatial domain and at 21 mm in the frequency domain for a point actuator just one finite element long at each of three positions and for a 15 mm long actuator. For comparison, graphs are also plotted for a normal ear and for an implanted ear, each with excitation from the stapes. The Norton equivalent excitation volume velocity from the actuator is the same as that from the stapes when the ear canal sound pressure is 115 dB above Normal Hearing level.

The graphs show that the location of the actuator makes only a small difference when the actuator is basal to the best place. As shown by Figure 7.6, when the actuator is apical to the normal best place, a peak in the BM response will occur at the actuator location, with a BM velocity magnitude comparable with that at the best place. To avoid multiple 'best places' at high frequencies, the actuator should be located as close as possible to the round window. In the frequency range of interest for low frequency hearing (100 - 1000 Hz), there are only a few decibels difference between the results of locating the bubble at 0, 10 or 20 mm from the round window or extending an actuator from 1 to 16 mm.

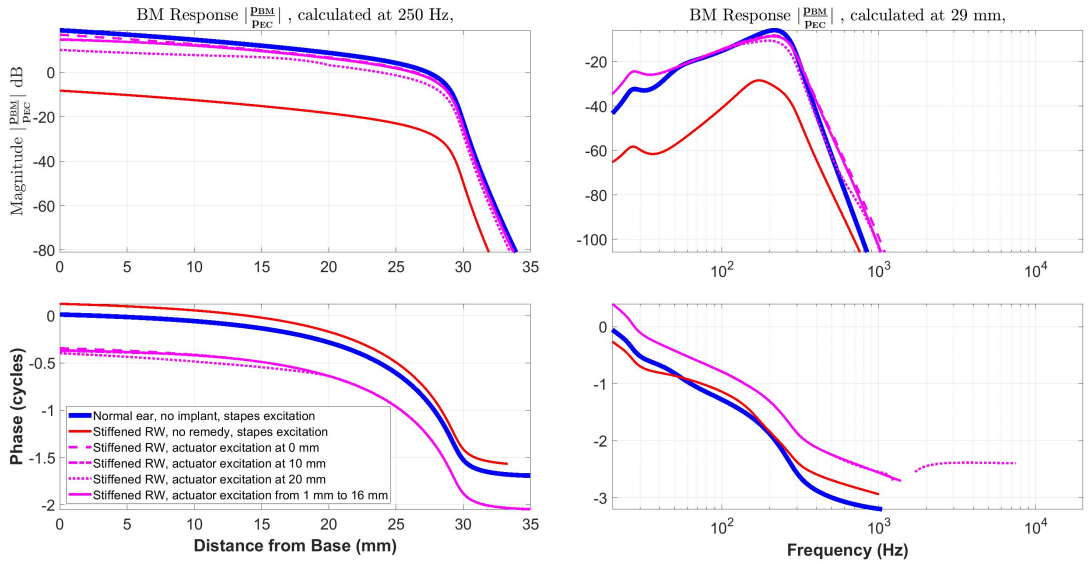

FIGURE 7.7: Basilar membrane pressure difference response predicted at 250 Hz in the spatial domain and at 29 mm in the frequency domain for a point actuator just one finite element long at each of three positions and for a 15 mm long actuator. For comparison, graphs are also plotted for a normal ear and for an implanted ear, each with excitation from the stapes. The Norton equivalent excitation volume velocity from the actuator is the same as that from the stapes when the ear canal sound pressure is 115 dB above Normal Hearing level. (p_{EC} is the pressure in the ear canal.)

Provided that the actuator is basal to the best place, the velocity and pressure responses with excitation from an actuator are very similar to those of a normal ear with stapes excitation. This will be the case for the frequency range of interest when the actuator is no more than 20 mm from the RW.

7.5.1 Comparison with a Lumped Component Model

To verify the modelled relationship between actuator velocity and BM velocity, the volume velocity normalized response has been calculated by both the present model and the lumped component models developed byElliott et al. (2016) and Xue et al. (2020), modified to include a point intracochlear actuator at the RW, as shown in Figure 7.8. The input parameters of the two lumped element models are given in Table 7.1, and the results are plotted as a function of frequency on the same graph in figure 7.9. The normalized responses are similar. The minima occur at the resonant frequency of the stiffened RW in parallel with the cochlear aqueduct. The trough is narrower for the two lumped models than the present model, because the viscous resistance of the cochlear aqueduct is less, and the frequency of the resonance is higher for the Xue et al. model, because it models a less compliant, greater inertance RW.

TABLE 7.1: Table of values of parameters input to two lumped element models.

Input parameters					
	Xue symbol	SI units	Xue	ENV	ENV symbol
Wave inertance	MCH	kg.m-4	6.46E+07	7.00E+07	LFL
Wave resistance	RCH	kg.s-1.m-4	3.04E+10	2.00E+10	RWA
RW inertance	MRW	kg.m-4	7.30E+05	1.00E+06	LRW
RW stiffness	KRW	kg.s-2.m-4	2.79E+13	1.00E+13	$1/C_0$
RW resistance	RRW	kg.s-1.m-4	5.00E+07	2.50E+09	RRW
VA inertance	MVA	kg.m-4	5.00E+06	5.10E+07	LVA
VA resistance	RVA	kg.s-1.m-4	9.80E+10	1.10E+10	RVA
CA inertance	MCA	kg.m-4	7.10E+08	5.60E+08	LCA
CA resistance	RCA	kg.s-1.m-4	2.50E+11	3.50E+11	RCA
ME stiffness	KME	kg.s-2.m-4	1.38E+14	8.33E+13	1/CME
ME resistance	RME	kg.s-1.m-4	1.80E+10	1.00E+10	RME
ME inertance	MME	kg.m-4	5.70E+05	4.40E+05	LME
Source	Xue (2020) table I and fig 8a			ENV (2016) table 1	
	Xue = Xue et al.			ENV = Elliott et al..	

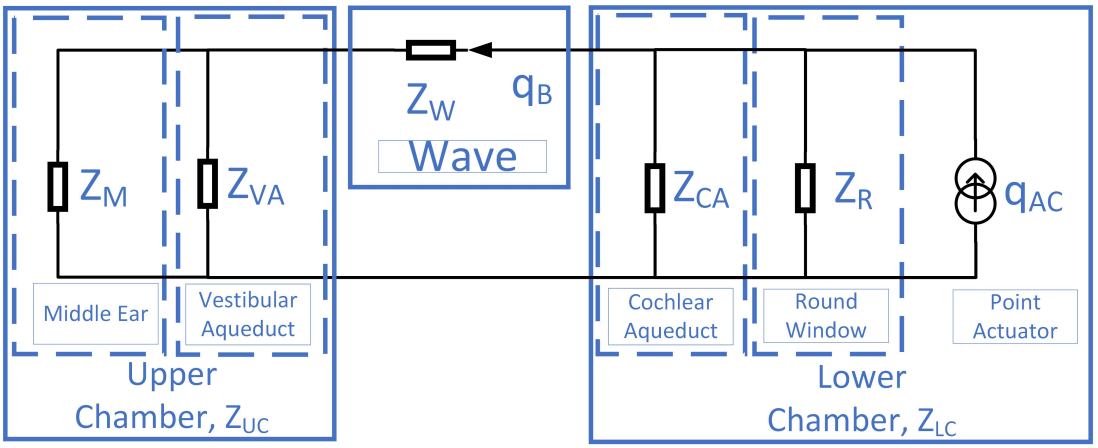

FIGURE 7.8: Circuit diagram of the cochlear structures lumped element models, including a point intracochlear actuator at the RW to the BM

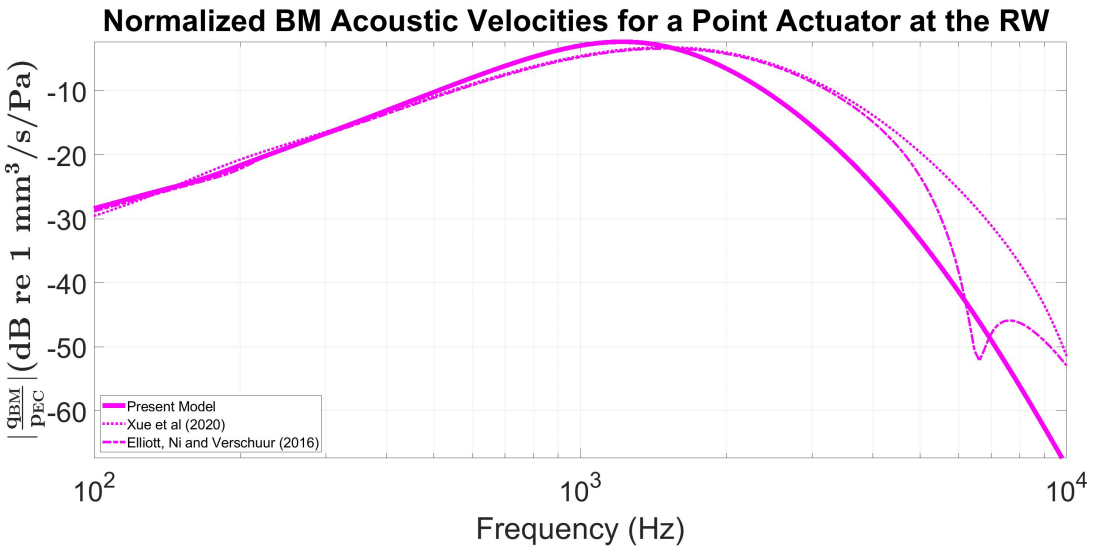

FIGURE 7.9: Normalized BM Responses to a Point Actuator at the RW. The minimum at 13 kHz is attributed to a resonance in the lower chamber, ie of the RW in parallel with the cochlear aqueduct.

7.6 Actuator Diaphragm Velocity Needed to Emulate 115 dB HL at the Ear Canal

The velocity normalized responses from the ear canal has been divided by that from a 15 mm long actuator to calculate the actuator diaphragm velocity needed to produce the same BM velocity and hence the same sensation. The results are shown in figure 7.10, below. It can be seen from the graph that the greatest velocity required is 2.42 mm/s. This figure is included in Table 7.2, and it used in the following chapter to determine the capability of various transducer technologies to generate sufficient velocity when the actuator is small enough to fit within an implant.

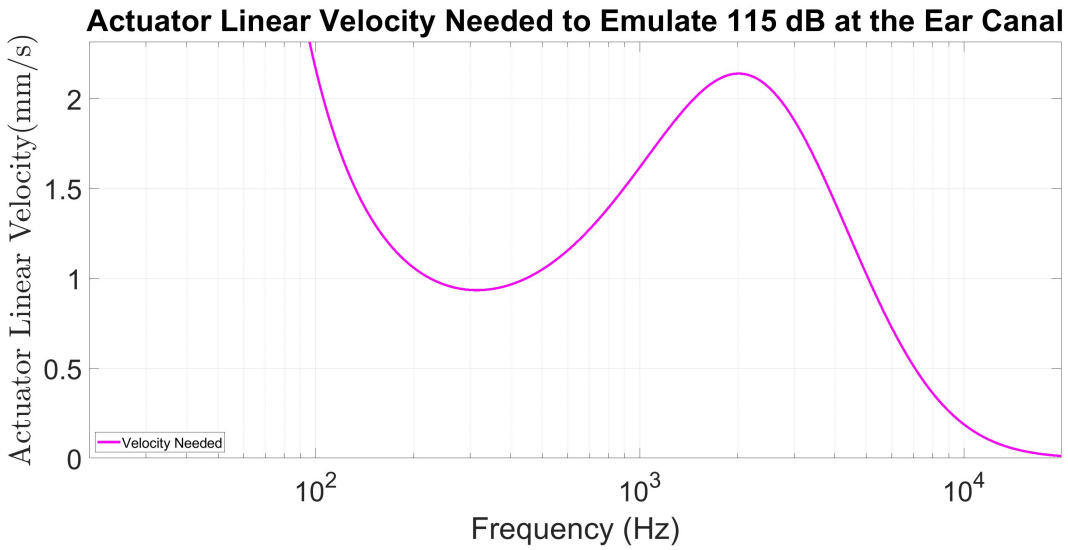

FIGURE 7.10: Actuator Diaphragm Linear Velocity Needed to Emulate 115 dB at the Ear Canal for a diaphragm area of 4.8 mm²

7.7 Actuator Diaphragm Pressure when Emulating 115 dB at the Ear Canal

The actuator diaphragm pressure has been calculated by multiplying the actuator linear velocity calculated in section 7.6 by the diaphragm area and the impedance of the lower chamber at the actuator, as calculated by the new model and shown in figure 7.11.

The modelled magnitude of the impedance presented to the actuator by the cochlear fluid rises to a peak at about 157 Hz, as the parallel resonant frequency of the middle ear and the vestibular aqueduct is approached. As the series resonance of the middle ear and the wave impedance is approached at about 318 Hz, the impedance falls to a minimum. There is then a slow and small increase to about 833 Hz, where the wave impedance itself rises to a gentle peak. At about 2.3 kHz, the middle ear resonates as a series circuit producing a relatively sharp minimum in the impedance presented to the actuator. The pressure developed in the lower chamber when excited by an intracochlear actuator is computed by multiplying the actuator diaphragm velocity by the cochlear input impedance presented to the diaphragm. The result of the multiplication is shown in figure 7.12, below. It can be seen from the graph that the greatest pressure required is 910 Pa. This figure is used in the following chapter to determine the capability of various transducer technologies to generate sufficient velocity and pressure when the actuator is small enough to fit within an implant. The present model gives a falsely high value of cochlear input impedance at the stapes, because the taper of the real cochlear is not modelled. As explained in Chapter 5, the lack of taper causes the wave impedance to be too high. The wave impedance is

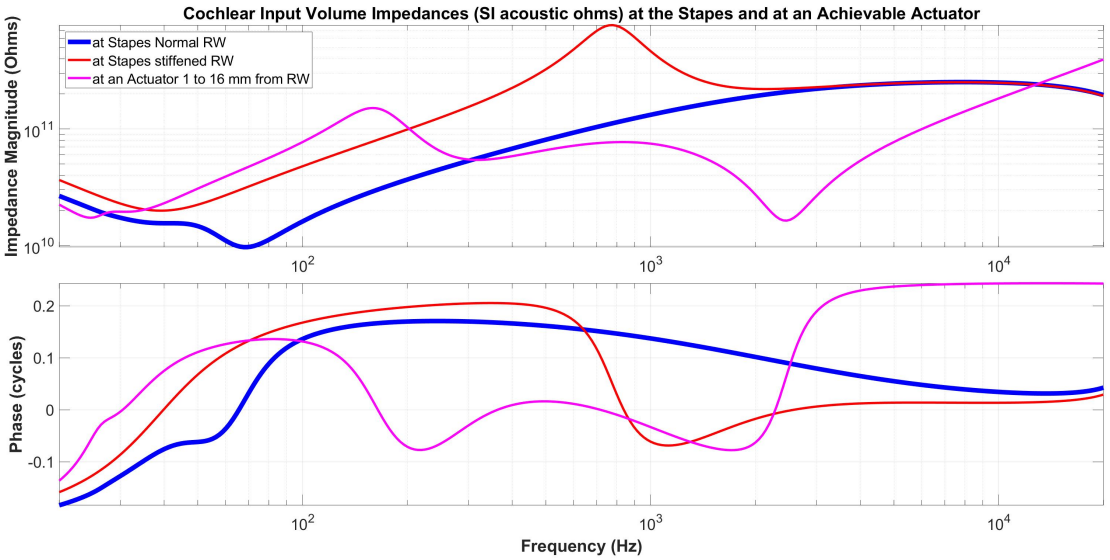

FIGURE 7.11: Graph of Cochlear Input Impedance Presented to an Actuator in the Lower Chamber, Extending from 1 to 16 mm from the stiffened Round Window, together with the impedances Presented to the Stapes with a Normal and Stiffened RW.

broadly unaffected by the location of excitation, and so it is reasonable to assume that the modelled cochlear input impedance at an actuator would also be falsely high. In that case, the pressure requirement of the actuator would be exaggerated by the present model, and the calculated value would be pessimistic.

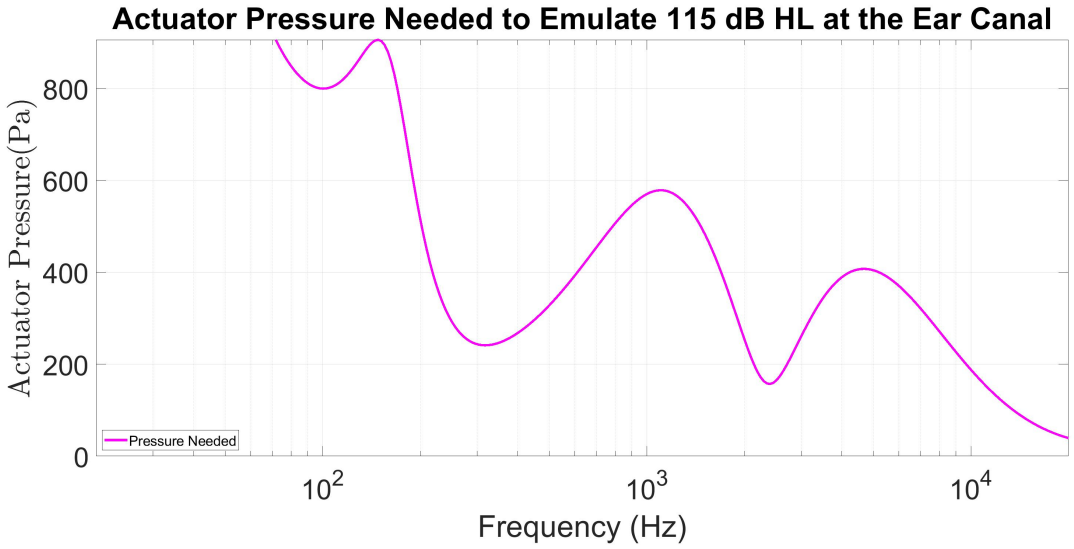

FIGURE 7.12: Actuator Diaphragm Pressure when Emulating 115 dB at the Ear Canal

7.8 Other Requirements

Clearly, an intracochlear acoustic actuator would need to have a diaphragm that could be embedded in the electrode array of a cochlear implant. The feasibility of designing such an actuator is examined in Chapter 8. No evidence has been found of the

f	**Linear velocity**	**Volume velocity**	**Linear Displacement**	**Required pressure**	**Pressure$*\omega$**	**Cochlear Impedance**
Hz	mm/s	mm^3/s	μm	kPa	MPa/s	GΩ
100	2.2	10	3.4	0.8	0.5	77.5
148	1.3	6.4	1.4	0.91	0.84	146
159	1.3	6.1	1.3	0.88	0.88	151
980	1.6	7.7	0.26	0.57	3.5	75.1

TABLE 7.2: **Velocity, displacement, pressure and pressure$*\omega$ requirements of an intracochlear actuator, together with the cochlear impedance at the actuator, for the frequencies at which each Variable is a maximum are shown in red.** The conversion from linear (mechanical) to volume (acoustic) velocity uses a diaphragm area of 15×0.32=4.8 mm^2. (The value of pressure$*\omega$ is useful for calculating the maximum and minimum reactive parts of actuator impedances.)

existence of any commercially available actuators sufficiently small to meet this requirement. The actuator modelled is a hypothetical one measuring 15 mm long by 0.3 mm wide by 0.3 mm deep, located from 1 to 16 mm from the round window.

The requirements of the electronic driver circuitry are similar to those of the drivers for conventional ear canal hearing aids as are used presently for conventional electro-acoustic stimulation, and the requirements of the driver are not considered to be challenging, and so this matter is not examined any further in this thesis.

7.9 Summary of Actuator Requirements

To summarise the results from this study, it has been shown that in order to generate a BM velocity that corresponds to 80 dB above normal Hearing Level in a normal ear over the frequency range from 100 Hz to 1 kHz, assuming a sensorineural hearing loss of 97 dB, would require an intracochlear actuator capable of generating a volume velocity of 10 mm^3/s, when driving into an acoustic impedance of 90 GΩ at 100 Hz. A maximum of 910 Pa of pressure would be required within the frequency range of interest at 148 Hz, as shown in Table 7.2. It is assumed that an implant's electrode array would provide satisfactory hearing at frequencies greater than the range of interest by electric stimulation of the auditory nerve. Clearly, an implantable actuator has to fit within an implant. The values in Table 7.2 are used in the following chapter to test by calculation the feasibility of a number of actuator technologies. The calculations show that more than one technology is feasible.

Chapter 8

Intracochlear Acoustic Stimulation Feasibility

8.1 Motivation

Traditionally, combined electro- and acoustic- stimulation (EAS) has been achieved by using a cochlear implant to stimulate the auditory nerve electrically and an external, conventional hearing-aid to deliver amplified sound to the outer ear for transmission to the hair cells in the organ of Corti and thence to the auditory nerve, in the normal way. For the severely deaf patients that qualify for a cochlear implant, this technique has the disadvantage that a large amount of amplification is required to achieve adequate levels of acoustic stimulation. Achieving so much amplification is difficult, partly because the hearing aid becomes prone to acoustic feedback, when the loop gain exceeds unity around the acoustic circuit including the microphone and the acoustic actuator.

Additionally, part of the power requirement of the hearing aid is approximately proportional to the power output and hence to the amplification, which is, in turn, governed by the hearing loss. Typically, a patient that qualifies for a conventional hearing aid, but not an implant, and having a hearing loss of, say, 50 dB, would need to change the battery in the appliance about once per week. A patient with a hearing loss of 80 dB (the minimum loss to qualify for an implant) may thus require a change of battery daily or after only hours use.

If the acoustic stimulation is achieved by an actuator coupled directly to the cochlear fluid, both the feedback and the power problems would be greatly mitigated. This is because the acoustic coupling between the actuator output and the external microphone would be greatly diminished, and it is also anticipated that the power requirement would generally be greatly reduced.

Although it is beyond the scope of this project to undertake the detailed design of an intracochlear actuator, it is pertinent and possible to examine the feasibility of doing so, by performing calculations using the laws of physics and the properties of available materials.

After reviewing the requirements for such an actuator in the previous Chapter, the feasibility of creating one using a number of different technologies is discussed in this Chapter.

8.2 Actuator Diaphragm Velocity and Pressure Requirements

The approach adopted to determine sound pressure and velocity requirements is set out in section 7.2 of the preceding chapter, and the results are summarized in Table 7.2. It is shown that an actuator with a diaphragm 15 mm long and 0.32 mm wide, with a volume of 1.5 mm^3, will produce sufficient basilar membrane velocity to create the same sensation as 115 dB above normal hearing level in the ear canal, if it is capable of generating a diaphragm linear velocity of 2.2 mm/s, a volume velocity of 10×10^{-9} m^3/s, a linear displacement of 3.4 $\mu m/s$ without undue distortion and a pressure of 910 Pa, across the frequency range 100 - 1000 Hz. Even with shorter electrode arrays, cochlear implants work very well at frequencies down to 500 Hz, and so the advantages of EAS are not as great as at lower frequencies. This overlap of frequency range capability will ensure that satisfactory restoration of hearing can be achieved for severely deaf patients over the audio frequency range above 100 Hz, by the combination of electric and acoustic stimulation.

8.3 Achievability of the Required Cochlear Fluid Pressure and Flow

The achievability of the cochlear fluid pressure and velocity requirements can be determined in two ways. One is scaling, using the relationship between size and sound output level determined for a range of existing commercial actuators, and that relationship can be extrapolated to the size of an actuator that would fit into an implant, as in Section 8.4. Additionally, the sound pressure and velocity capability can be calculated from first principles for an actuator of the size required. The results of the two sets of calculations can then be compared. The calculations from first principles are set down in Section 8.5 for a balanced armature actuator, which is how the most commonly used actuator in hearing aids is described.

In Subsections 8.7.1 to 8.7.7, below, the calculations are repeated for a number of other actuator technologies, to test the feasibility of each technology.

8.4 Scaling of Commercially Available Actuators

The scaling of physical parameters with size can provide useful insight into the performance of different transducers, particularly as they are miniaturized Madou (2018). By plotting the non-dimensional coupling factors of a wide variety of moving coil electromagnetic actuators against their masses, Elliott and Zilletti (2014), for example, showed that this coupling factor scaled with the cube root of the actuator mass. This study shows the value of scaling by using dimensionless parameters, which is a technique used in this chapter. However, the choice of scaling factor needs to match the characteristics of the transducer and its environment.

In Chapter 7, it is assumed that the transducer is a constant pressure (Thevenin) source. This is because the acoustic velocity is almost entirely determined by the current in the coil and independent of the back-emf generated by the velocity of the diaphragm, which is negligible when compared with the input voltage of the transducer. Detailed calculations of the back-emf are in Appendix B. Because the relationship between the electrical impedance of the transducer and that of the load is different from the corresponding relationship in Elliott and Zilletti (2014) a different scaling factor of output is used here, and it is SPL/volume. The graphs by Sonion (https://www.sonion.com/wp-content/uploads/What-is-Balanced-Armature-Receiver-Technology_rev002.pdf) and that derived from Knowles data (https://www.knowles.com/subdepartment/dpt-ba-receivers/subdpt-hearing-instruments-receivers) show that that scaling factor for balanced armature transducers is independent of the size of the actuator and hence dimensionless, when the SPL is measured at a constant level of distortion.

To estimate whether commercially available actuators would produce sufficient acoustic pressure and diaphragm velocity when small enough to fit within the cochlea, the maximum SPLs (into an air-filled, 2 cc cavity) of a range of Knowles balanced armature actuators was taken from their technical specifications (as shown in Table 8.1) and plotted in Figure 8.1 against their volumes, and a regression line was computed, which gives a correlation co-efficient (R^2) of 0.94. Assuming that an actuator can be scaled down to this size, an actuator with a volume of 1.5 mm^3 would produce an SPL of 98 dB or a pressure, p of 1.6 Pa in the standard 2 ml test cavity, which has an acoustic impedance of $-1.07i \times 10^8$ acoustic ohms at 100 Hz. The impedance of such a cavity, $Z = \frac{1}{i\omega C}$, where the compliance of the cavity, $C = \frac{V}{\rho c^2}$, V=cavity volume, ρ =density of the fluid (air) in the cavity and c = the velocity of sound in the cavity fluid, and where Z is the ratio of pressure to volume velocity. This pressure would thus generate a volume velocity, q of $15 \times 10^{-9} m^3/s$ in the air-filled standard test cavity. The required maximum volume velocity for an intracochlear actuator is $10 \times 10^{-9} m^3/s$, and so it is predicted that a volume velocity could be produced that is just sufficient to meet the requirement.

Series	Length (mm)	Width (mm)	Height (mm)	Volume (mm^3)	SPL (dB)	SPL (Pa)	Res Freq (kHz)
FK	5.00	2.73	1.93	26	123	28.3	2.7
FH/FFH	5.09	2.80	2.59	37	124	31.7	2.2
DFK	5.00	2.73	3.86	53	130	63.2	2.6
FC/FFC	5.17	3.55	3.00	55	127	44.8	2.5
EH/FEH	5.19	3.55	3.00	55	128	50.2	2.5
FJ	5.08	2.79	5.18	73	129	56.4	2.2
ED/FED	6.32	4.31	2.97	81	129	56.4	2.0
EJ	6.33	4.32	5.97	163	135	112.5	1.8
EF/FEF	7.87	5.59	4.01	176	139	178.3	1.0
CI	9.47	7.18	4.10	279	143	282.5	0.9

TABLE 8.1: Details of Knowles "balanced" armature actuators, including their volume, the maximum SPL that they can produce and their approximate lowest resonant frequency. Retyped by the author using data from (https://www.knowles.com/subdepartment/dpt-ba-receivers/subdpt-hearing-instruments-receivers)

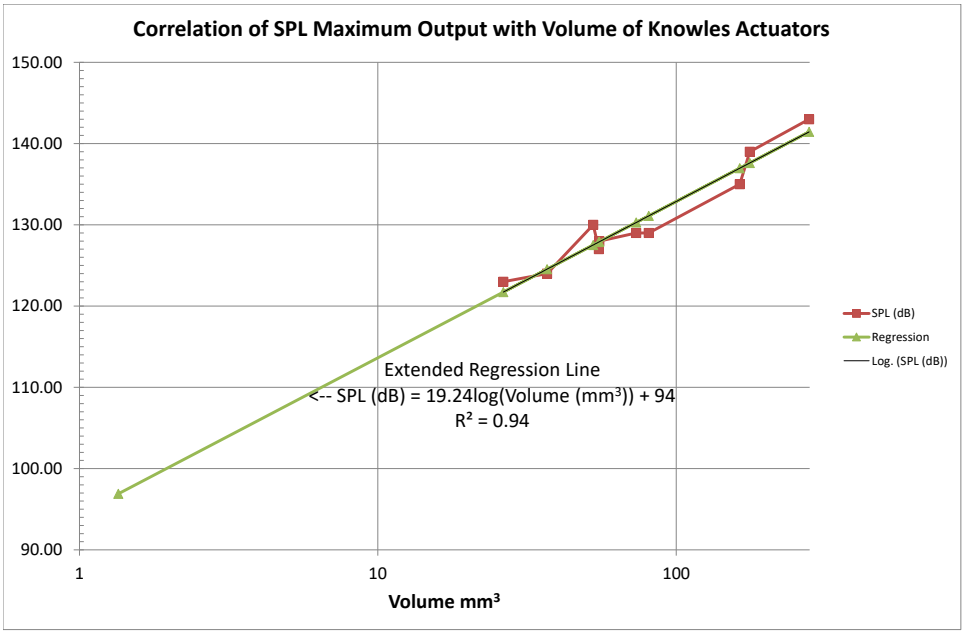

FIGURE 8.1: Correlation and relationship between maximum output and volume (mm^3), on a log scale, for Knowles actuators. Plotted by the author using data from https://www.knowles.com/subdepartment/dpt-ba-receivers/subdpt-hearing-instruments-receivers

Another manufacturer, Sonion, has produced a similar graph for their transducers, which is shown as figure 8.2. Extrapolation of their graph to the volume of an implantable actuator gives a slightly smaller SPL than the corresponding value from

the graph of Knowles actuators, but the quoted values apply to slightly different distortion limits, frequencies and loadings. Sonion produce an actuator with a volume of 13.2 mm^3, which they claim to be the world's smallest, and it is less than an order of magnitude greater than the volume of the proposed implantable actuator.

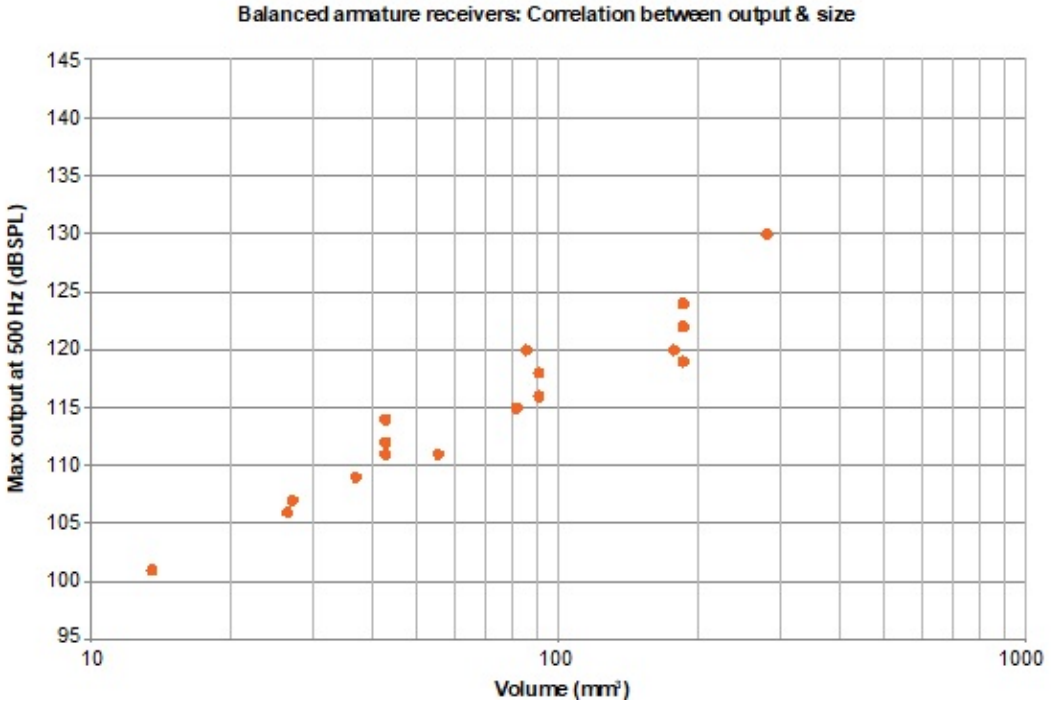

FIGURE 8.2: Sonion Graph of SPL output at 500 Hz and 5% THD against volume (mm^3) for their actuators, measured when coupled to a 2 cc cavity. https://www.sonion.com/wp-content/uploads/What-is-Balanced-Armature-Receiver-Technology_rev002.pdf Copyright permission requested through Sonion web-site in October 2021, but no response received.

A reasonable fit for the data plotted in both of figures 8.1 and 8.2 is a linear relationship between SPL and Volume, with a slope of 20 dB/decade, so that the volume velocity is directly proportional to the square root of actuator volume. This indicates that maximum pressure in the cavity and hence the volume velocity capability of the actuator is directly proportional to its volume, for both Knowles and Sonion balanced armature actuators. The overall level of the Sonion actuators is about 9 dB lower than the Knowles devices of a similar volume; this comparison is influenced by the output levels being quoted at different distortion limits and different frequencies. However, these differences do not affect the slopes of the regression lines, which are comparable and close.

8.5 Calculation of a Balanced Armature Capability from First Principles

Balanced armature actuators using permanent magnets are the most established technology, but they require the use of relatively long ferromagnetic or ferrimagnetic components that are not flexible. The lack of flexibility increases the risk of damage to the cochlea on insertion. The static field from the permanent magnet poses no significant health or safety hazard, and the balanced armature concept avoids significant interference from external vibration. [1] The requirements for sound pressure and velocity in an intracochlear transducer are translated into current, voltage and power requirements of a theoretical balanced armature actuator that is small enough to fit inside an implant, as discussed in section 8.4.

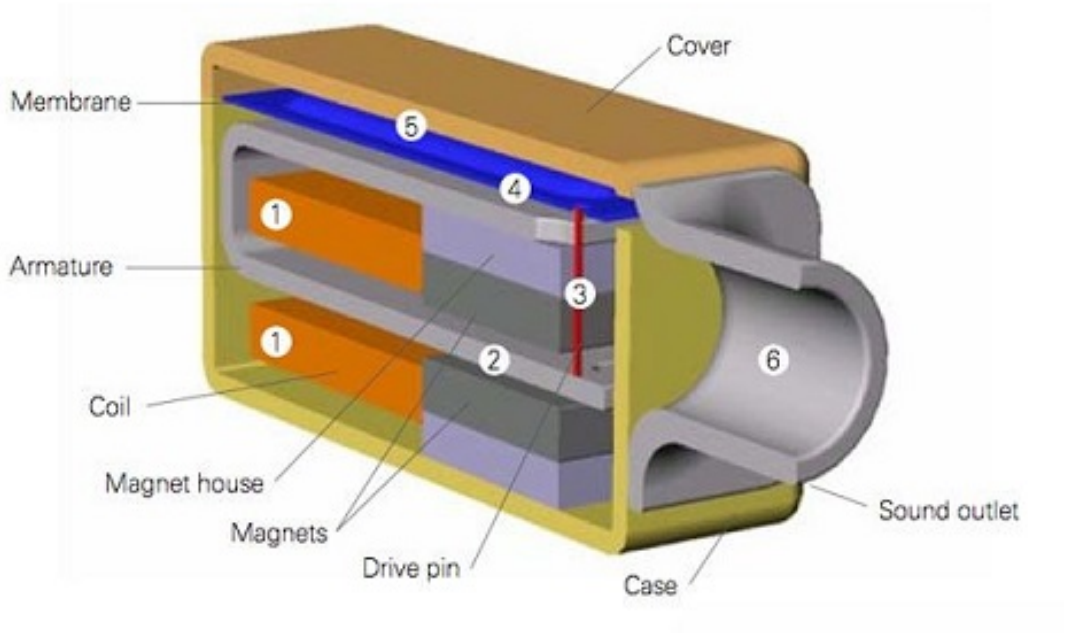

FIGURE 8.3: Cross-section of a Balanced Armature Actuator. url: http://www.aes.org/images/blog_img/25/ID/1570.jpg. Permission to copy requested from the Audio Engineering Society in the USA on 22/5/22, but no response received. NB. In this type of actuator, the magnetic forces are balance by the stiffness of the armature, which is not itself balanced on a pivot as it is in the alternative design shown in figure 8.4; see footnote 2 in the text.

This is done for the actuator shown in figure 8.4 that has four air-gaps, each measuring 0.1 mm tall by 1 mm along the cochlea by 0.3 mm across the cochlea, driving a rigid diaphragm 15 mm by 0.32 mm, as shown in Figure 8.4. The dimensions of the

[1] Commercially available actuators are strictly attracted armature, rather than balanced armature transducers, and they are susceptible to interference from external vibration. This susceptibility is overcome by using a dual design, which uses two armatures and two diaphragms which move in opposite directions, arranged so that the pressure produced by one adds to the pressure from the other. Dual designs require more volume than single designs for the same SPL output.

diaphragm are those used by the model, and they are set by the text file used by the model that also sets the physiology of the ear; the other dimensions stated here are chosen to fit within a 1 mm diameter electrode array.

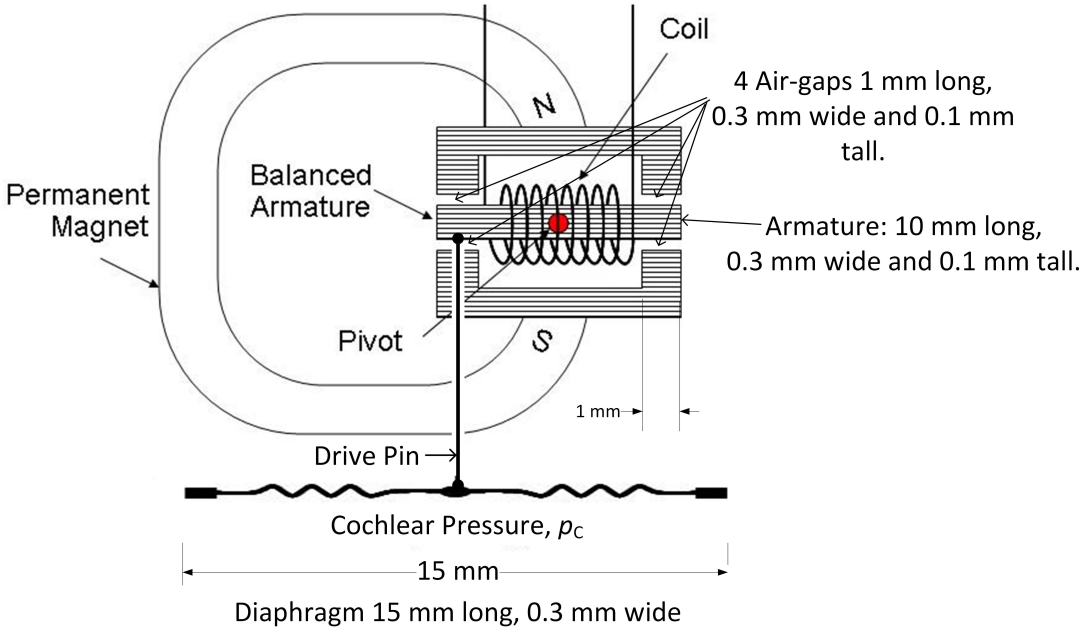

FIGURE 8.4: Diagram of a Balanced Armature Actuator, with the assumed dimensions used in the calculation of its sensitivity. The diagram without dimensions is reproduced with permission from the copyright holder, JH Audio Inc. (see https://images.app.goo.gl/a2WVtx1HoX1rCf447)

$$\text{Airgap pressure, } p_g = \frac{1}{2}B_g^2/\mu_0 \text{ Pa, in each of four gaps;} \tag{8.1}$$

Each air-gap is 0.1 mm long $\times$ 1 mm $\times$ 0.3 mm

$$= \frac{1}{2}\left(B_p \pm \mu_0 NI/l_g\right)^2/\mu_0 \tag{8.2}$$

$$= \frac{1}{2}B_p^2/\mu_0 \pm B_p NI/l_g + \frac{1}{2}\mu_0\left(NI/l_g\right)^2 \tag{8.3}$$

Where B_p = Flux density in the air-gaps due to the permanent magnets.

B_g = Total air-gap flux density due to the permanent magnets and coils.

N = number of turns in the coil,

μ_0 = magnetic permeability of free space, $= 4\pi \times 10^{-7}$.

l_g = air-gap length, armature to magnet pole (= 0.1 mm)

In equation 8.3, the $\pm$ sign is replaced with a + sign when the flux from the coil adds to the permanent flux, and - sign, when it subtracts. The air-gap pressure difference is calculated by subtracting equation 8.3 with a + sign from itself with a - sign, and so the first and last terms cancel while the middle term doubles to form the right hand side

of in equation 8.4.

$$\begin{aligned}
\text{Air-gap pressure difference , } p_\mathrm{d} &= 2p_\mathrm{g} = 2B_\mathrm{p}NI/4l_\mathrm{g} = B_\mathrm{p}NI/2l_\mathrm{g} && (8.4)\\
&\quad \text{each end of armature.} \\
&= && (8.5)\\
\text{Magnetic force on armature} &= 2p_\mathrm{d} \times A_g && (8.6)\\
&= 2A_\mathrm{g}B_\mathrm{p}NI/l_\mathrm{g} && (8.7)\\
\text{Cochlear Pressure, } p_\mathrm{c} &= \text{Force/diaphragm area} = 2\frac{A_\mathrm{g}B_\mathrm{p}NI}{A_\mathrm{d}l_\mathrm{g}} && (8.8)\\
\text{Where } A_\mathrm{d} &= \text{the diaphragm area.} \\
\text{The maximum required pressure, } p_\mathrm{c} &= 0.9 \text{ kPa}, && (8.9)
\end{aligned}$$

$$\begin{aligned}
p_\mathrm{c} &= \frac{2A_\mathrm{g}B_\mathrm{p}NI}{A_\mathrm{d}l_\mathrm{g}}\text{. Assume permanent magnet field strength,} && (8.10)\\
B_\mathrm{p} &= 1 \text{ Tesla, and so} \\
NI &= \frac{p_\mathrm{c}A_\mathrm{d}l_\mathrm{g}}{2A_\mathrm{g}B_\mathrm{p}} = \frac{0.9 \text{ kPa} \times 15 \text{ mm} \times 0.32 \text{ mm} \times 0.1 \text{ mm}}{1 \text{ mm} \times 0.32 \text{ mm} \times 1 \text{ T}} = 1.3 \text{ AT} && (8.11)
\end{aligned}$$

This is the "locked armature" current required to generate the pressure required, because it assumes that the air-gap lengths do not alter when the current is applied.

For the purposes of this feasibility study, the current density rating of enamelled copper wire is assumed to be 1.6 A/mm^2, see footnote [2], below.

$$\begin{aligned}
\text{Cross-sectional area of coil, } A_\mathrm{c} &= 1.3/1.6 = 0.8 \text{ mm}^2, && (8.12)\\
\text{for current density} &= 1.6 \text{ A/mm}^2. && (8.13)
\end{aligned}$$

This should be multiplied by 1.1 $(2\sqrt{3}/\pi)$ to allow for the packing factor of a coil neatly wound with enamelled wire and by 1.3 to allow for the maximum diameter over the insulation (BS EN 60317-0-1:2014+A1:2019) to give 1.2 mm². Assuming a coil length along the armature of 8 mm, the thickness of the coil would be 0.15 mm. Referring to Figure 8.4, the length, l_ci of one inner turn of the coil would be $2 \times 0.1 \text{ mm} + 2 \times 0.32 \text{ mm} = 0.84$ mm, and that of an outer turn, l_co would be $0.84 + 4 \times 0.15 + 2\pi \times 0.25 = 3$ mm. The rms length, l_c is 3.2 mm, and so the total length, L_c would be $3.2 \times N$ mm. The cross-sectional area, a_c of each turn would be

[2]Before metrication was prevalent in the UK, the current rating of enamelled copper wire for coil-winding was traditionally considered to be 1000 A/in^2, evidence for which was scarce, but it was a convenient round number. Suppliers of enamelled copper wire, such as Farnell, publish current ratings, which equate to 1.55 A/mm^2, which is the same current density as 1000 A/in^2, and evidence to support this figure remains as hard to acquire as it was before metrication. This figure appears conservative, because PVC insulated 1mm^2 copper wiring in buildings is rated at 10 A (BS 7671), with the current density rating increasing as cross-sectional area of the conductor decreases, but a considerable reduction would be necessitated for a group of 1000 wires. A search of British, European and international standards has revealed no standards giving current ratings or current density limits for enamelled copper wire, and so reliance has to be placed on suppliers' claims and established practice.

A_c/N mm^2, and so the resistance, R of the coil would be proportional to N^2, when l_c and A_c are fixed by the geometry of the actuator.

$$
\begin{aligned}
R &= \frac{\rho L_c}{a_c} = \frac{\rho N l_c}{A_c/N} && (8.14)\\
&= \frac{\rho N^2 l_c}{A_c}, \text{where } \rho \text{ is the resistivity of the wire.} && (8.15)\\
\text{The required emf, } E &= IR = \frac{(NI)}{N}\frac{\rho N^2 l_c}{A_c} && (8.16)\\
&= \frac{\rho N (NI) l_c}{A_c} \text{ (proportional to } N \text{ and } NI), && (8.17)\\
&\text{(Ohm's law)} && (8.18)\\
\text{If } \rho &= 1.8\times10^{-8}\Omega\text{m (copper at 37°C)} && (8.19)\\
E &= \frac{1.8\times10^{-8}\Omega\text{m}\times N\times 2.2\text{AT}\times 3.5\times10^{-3}\text{m}}{1.4\times10^{-6}\text{m}^2} && (8.20)\\
&\simeq 100N\mu\text{V} && (8.21)\\
I &= \frac{NI}{N} = \frac{2.2}{N}\text{A} && (8.22)\\
\text{Assuming that } N &= 1000, (N = \text{ the number of turns}), && (8.23)\\
\text{Then, } E &\simeq 100 \text{ mV, } I \simeq 2.2 \text{ mA and } R \simeq 45\ \Omega. && (8.24)\\
\text{Wire diameter, } d_c &= \sqrt{\frac{4a_c}{\pi}} = \sqrt{\frac{4\times1.4\times10^{-6}}{N\pi}} && (8.25)\\
&= 133\ \mu\text{m} && (8.26)
\end{aligned}
$$

The wire diameter is about that of a human hair. The breaking force of such a thin copper wire is about 6 N, and it would normally be wound with a tension of 0.5 N to give a 'springback' of less than 80° (BS EN 60317-0-1:2014+A1:2019).

The values calculated in 8.24 and 8.26 are acceptable values for a practicable design.

$$
\begin{aligned}
\text{The required power, } W &= I^2R = \frac{(NI)^2}{N^2}\frac{\rho N^2 l_c}{A_c} = \frac{\rho (NI)^2 l_c}{A_c}, && (8.27)\\
&\text{which is independent of } N. && (8.28)\\
&= \frac{1.8\times10^{-8}\times2.2\times2.2\times3.5\times10^{-3}}{1.4\times10^{-6}} \simeq 217\mu\text{W}. && (8.29)
\end{aligned}
$$

To put the power requirement in perspective, the energy available from a 1.45 V size 13 hearing aid battery is about 400 mWh (https://www.ncbi.nlm.nih.gov/pmc/articles/PMC4423287/), and it lasts typically for one week in a conventional hearing aid that is worn for about 100 hours per week. This means that the typical power consumption of a hearing aid is about 4 mW, and the 200 µW consumption of an intracochlear actuator would amount to only a very small increase. Assuming a reasonable overall efficiency of the system in converting battery power input to electrical power in the actuator, the battery life would be adequate. The system design would need, of course, to consider the transfer of the driving voltage and current from the battery and processor unit, through the magnetic

coupler at the scalp, along the electrode array to the actuator, but there appears to be no problem of principle in doing so.

By using approximate estimates of sizes and other physical properties of the components, it has been shown by two different methods that it should be feasible to construct a permanent magnet balanced armature actuator that is capable of producing the required pressure and velocity requirements, whilst being small enough to fit inside a cochlear implant. Voltage, current and power requirements, together with the tensile strength and heating of the wire needed for a magnetizing coil, have been considered in reaching this conclusion. When the diaphragm and the armature move, the changing magnetic field will induce an emf in the coil. Even though the relatively high input impedance of the cochlea, compared with that of the actuator, will limit the movement to a small fraction of that in air for the same diaphragm pressure, it is shown in Appendix B that the linear velocity requirement of 2.2×10^{-3} m/s would not cause an excessive emf to be induced in the coil. It is also shown there that the inductive voltage-drop caused by the coil will be small in comparison with the resistive volt-drop in the coil.

8.6 General Requirements

For intracochlear acoustic stimulation to be fully feasible, it is necessary to show that there is at least one actuator technology that is suitable for incorporation into a cochlear implant so that the implant can be inserted without undue difficulty and without damage to the cochlea. An important factor in such considerations is the need for sufficient flexibility for the implant to follow the curve of the cochlea for about two complete turns, while remaining rigid enough to avoid kinking or doubling back on itself. Fortunately, the best place acoustically for an actuator is as close as possible to the round window, as shown in previous chapters, and so the actuator would be outside the cochlea for most of the insertion process. Furthermore, the curvature of the cochlea is much less near the base than it is nearer the apex.

The two preceding Sections have shown, each independently of the other, that if a suitably designed balanced armature actuator could be made small enough to fit in an implant, it should produce sufficient acoustic pressure, velocity and displacement over the required frequency range to meet the requirements. However, the overall feasibility is dependent on techniques both to fabricate such a small device and to insert an electrode array containing such a long, rigid device without causing damage to the cochlea. Although it is reasonable to be optimistic that both techniques will become available, it is prudent to explore alternative technologies that are not so dependent on the availability of both of these techniques.

In the following section, the feasibility of using other technologies is explored.

8.7 Other Potential Intracochlear Actuator Technologies

8.7.1 Ceramic and polymeric piezoelectric actuators

Using the material properties in Table 8.2, the feasibility of a piezoelectric transducer is investigated in this subsection.

TABLE 8.2: Properties of piezoelectric materials. PZT is lead zirconate titanate, and its properties are from Preument (2018), who has also provided those for polyvinylidene flouride (PVDF). The terpolymer is poly(vinylidene fluoride-trifluoroethylene-chlorotrifluoroethylene) 65/35/10% (PVDF-TrFE-CTFE); its properties are from Xu et al. (2001) and from the PolyK manufacturuer's web-site, whose URL is given in the text

Material properties	**Unit**	**PZT**	**PVDF**	Terpolymer
Piezoelectric constants				
d33	pC/N=pm/V	300	-25	-200
d31	pC/N=pm/V	-150		
uniaxial: d31			15	
uniaxial: d32			3	
bi-axial: d31 = d32			3	
d15	pC/N=pm/V	500	0	
e31 = d31/sE	C/m^2	-7.5	0.025	
Electromechanical coupling factors				
k33		0.7		
k31		0.3	0.1	
k15		0.7		
Dielectric constant ϵ_T/ϵ_0		1800	10	60
Max. Electric field	MV/m	2	500	400
Max. operating (Curie) Temp	°C	80-150	90	92
Density	kg/m^3	7600	1800	
Young's modulus 1/sE	GPa	50	2.5	0.4
Maximum stress Traction	MPa	80	200	
Maximum stress Compression	MPa	600	200	
Maximum strain Brittle		50%		

Assume 15 mm$\times$0.32 mm$\times$0.3 mm PZT or P(VDF–TrFE–CTFE) actuator, only moving in the thickness direction.

$$
\begin{aligned}
\text{The mechanical stiffness of such a device, } K &= \frac{E}{L} = \frac{F}{A\Delta L} \\
\text{Where } E &= \text{Young's Modulus, and} \\
F &= \text{force exerted} \\
\text{So that the acoustic impedance, } Z_{\text{acoustic}} &= \frac{p}{q} = \frac{F}{j\omega A^2 \Delta L} = \frac{K}{j\omega A^2} \\
&= \frac{EA}{j\omega A^2 L} = \frac{E}{j\omega A L} \\
\text{Assuming, } A &= 15 \times 10^{-3} \times 0.32 \times 10^{-3} \\
&= 4.8 \times 10^{-6}\ \text{mm}^2 \\
L &= 0.3 \times 10^{-3}\ \text{m} \\
Z_{\text{acoustic}} &= \frac{E}{j\omega \times 4.8 \times 10^{-6} \times 0.3 \times 10^{-3}} \\
&= \frac{E}{j\omega \times 1.44}\ \text{G}\Omega \\
\Delta L &= d_{33} V, \text{ where} \\
V &= \text{the applied voltage, and} \\
d_{33} &= \frac{\text{strain resulting}}{V},
\end{aligned}
$$

both measured in the material's poling direction.

$$
\text{The voltage requirement is thus } V = \frac{\Delta L}{d_{33}}
$$

So the linear actuator velocity, v_{AC} depends on only d_{33} and the maximum voltage that can be applied to the piezoelectric element. This maximum voltage is determined by the lesser of the maximum that can be accommodated within the implant and the breakdown electric field strength of the material multiplied by the length of the piezoelectric element, L. The acoustic impedance is dependent on only the Young's Modulus of the piezoelectric material and the dimensions of the piezoelectric element.

8.7.1.1 For PZT

(See Table 8.2, above, or table 4.1 in Preument (2018) for PZT properties),

$$
\begin{aligned}
\text{Assume density = 1,780 kg/m}^3\text{, mass} &= 1.78 \times 10^3 \times 10^{-6}\ \text{kg} \\
&= 1.78\ \text{g} \\
E &= 50\ \text{GPa.} \\
\text{Internal } Z_{\text{acoustic}} &= \frac{E}{j\omega \times 1.44} \\
&= 17 \times 10^{15}\Omega \text{ or Pas/m at 159 Hz,}
\end{aligned}
$$

151 Hz is the frequency at which the cochlear impedance is a maximum, see Table 7.2. At this frequency, the cochlear impedance at the actuator, $Z_C = 158 \times 10^9 \Omega$, and so the actuator's internal $Z_{\text{acoustic}} >> Z_C$. The actuator is therefore of much higher impedance than the acoustic input impedance of the cochlea at the actuator, and so it can be considered to be a constant velocity source.

From table 7.2, the maximum displacement, ΔL occurs at 100 Hz, with the value, 3.4 μm.

$$\begin{aligned} d_{33} &= 3 \times 10^{-10}\ \text{m/V} \\ V &= \frac{\Delta L}{d_{33}} = \frac{3.4 \times 10^{-6}}{3 \times 10^{-10}} \\ &= 12,800\ \text{V} \\ \text{Electric field} &= \frac{V}{0.3\ \text{mm}} = 43\ \text{MV/m} \\ \text{Dielectric breakdown strength of PZT} &= 6.7\ \text{MV/m} \end{aligned}$$

Because the required electric field exceeds the material's breakdown strength, a simple PZT transducer is inherently not feasible.

8.7.1.2 For P(VDF-TrFE-CTFE)

$$\begin{aligned} \text{From Table 8.2, above or Xu et al. (2001), } E &= 0.4\ \text{GPa} \\ \text{Internal } Z_{\text{acoustic}} &= -\frac{E}{j\omega \times 1.44} \\ &= \frac{4 \times 10^8}{2\pi f \times 1.44 \times 10^{-9}} \\ &= 1.34 \times 10^{13}\Omega \text{ at 159 Hz.} \end{aligned}$$

Again, 159 Hz is the frequency at which the cochlear impedance is a maximum, see Table 7.2. At this frequency, the cochlear impedance at the actuator, $Z_C = 151 \times 10^9 \Omega$, and so the actuator's internal $Z_{\text{acoustic}} >> Z_C$. The actuator is therefore of much higher impedance than the acoustic input impedance of the cochlea at the actuator, and so it can be considered to be a constant velocity source.

From table 7.2, the maximum displacement, ΔL occurs at 100 Hz, with the value, 3.4 µm.

$$
\begin{aligned}
d_{33} &= 2 \times 10^{-10} \text{ m/V, at 20°C, graph slope Fig 2(b) Xu et al (2001)} \\
V &= \frac{\Delta L}{d_{33}} \\
&= \frac{3.4 \times 10^{-6}}{2 \times 10^{-10}} \\
&= 19 \text{ kV at 100 Hz} \\
\text{Electric field} &= \frac{V}{0.3 \text{ mm}} = 64 \text{ MV/m} \\
\text{Breakdown strength} &= 400 \text{ MV/m (PolyK)} \\
&\quad \text{http://www.polyk-lab.com/PVDF-TRFE-CFE-CTFE}
\end{aligned}
$$

For P(VDF-TrFE-CTFE), the driving voltage required would be excessive for both the dielectric breakdown strength of the material and a reasonable voltage to be accommodated within an implant. For P(VDF-TrFE-CTFE), the required electric field would be less than the breakdown strength by a factor of five, but the driving voltage would be excessive. However, the driving voltage, but not the electric field, could be reduced by deploying a "sandwich" structure with alternate layers of piezoelectric material poled in opposite directions, as in Figure 8.5, below.

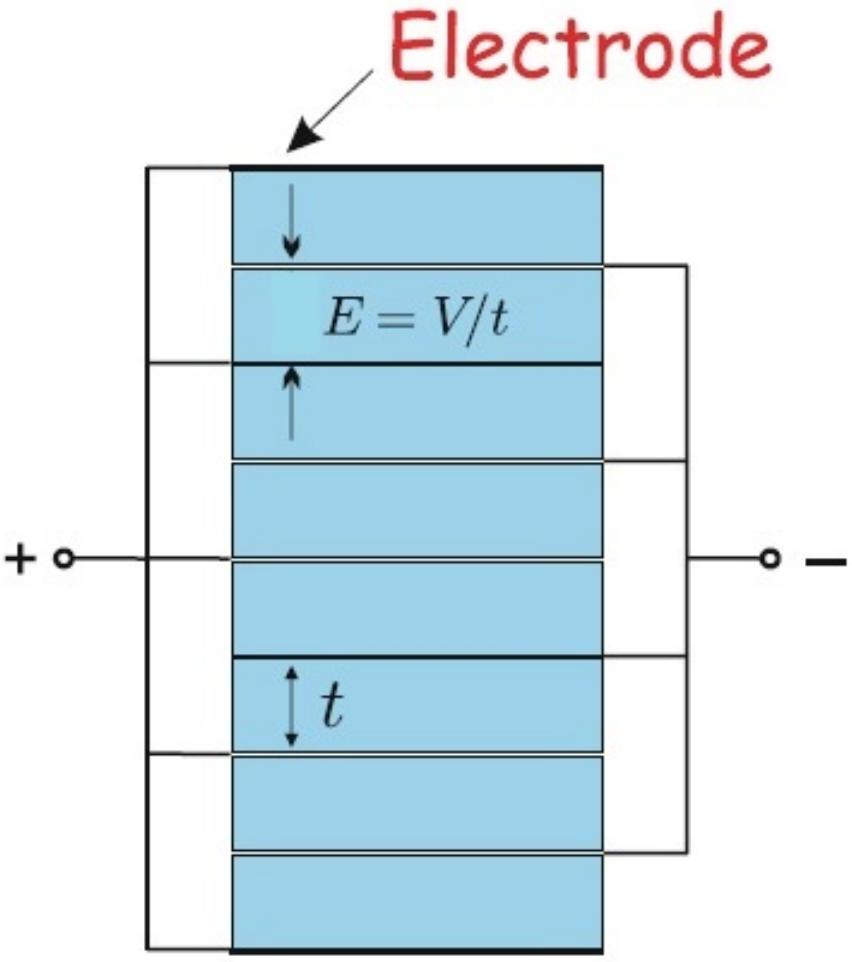

FIGURE 8.5: Diagram of "sandwich" transducer, with n piezoelectric layers of thickness t, showing that for the same the electric field, E, the required overall extension of length, ΔL, can be achieved with an applied voltage of V/n between each of the n layers, where V is the voltage required for a single layer actuator of the same height. Reprinted/adapted by permission from Springer Nature Customer Service Centre GmbH: Springer Nature, Vibration Control of Active Structures - An Introduction, by André Preumont © (2018)

Piezoelectric materials contract with one polarity of electric field and expand for the opposite polarity, according to which way they are poled. This allows the possibility of the inversion of layers so that alternate layers are poled upwards and downwards, and adjacent electrodes are of the same polarity, requiring no insulation between electrodes. This allows nearly twice as many layers in the same height, and so nearly halve the required driving voltage, because it is necessary to include only one metal electrode between layers to make a connection to the power source.

Polymeric piezoelectric film is available commercially with thicknesses down to 3μm , and an electrode thickness of less than 1 μm is readily achievable. Such a film would permit 75 layers in 300 μm, and hence a maximum driving voltage of about 250 V, which is a great improvement over 19 kV, but still unacceptable for implantation.

Unfortunately, although this "Sandwich" technique reduces the driving voltage required, it does not overcome the problem of excessive electric field, because the reduced driving voltage is applied to an equally reduced thickness of material. As a result, this technology is not feasible to provide an implantable ceramic actuator that meets the requirements determined in Chapter 7.2.

8.7.2 Axially constrained piezo membrane

As shown in Table 8.2, polymeric piezoelectric transducers are very much more flexible than ceramics, but their relationships between displacement and driving voltage (d_{33}) are similar. Because they are flexible, it is easier to form them into sinusoidal domes, so that elongation by the application of a longitudinal electric field produces amplified transverse movement when the ends of the dome are constrained. This opens the possibility of an actuator with a domed membrane that generates enough transverse acoustic velocity to meet the requirements in Table 7.2. This has been investigated, and the mathematics are set out in Appendix E.

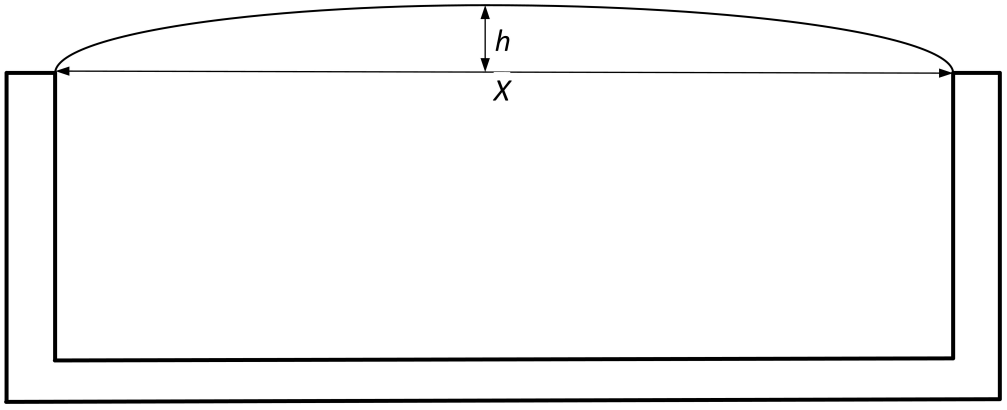

FIGURE 8.6: Axially Constrained Polymer Piezoelectric Membrane Actuator

The conclusion is that such an arrangement would produce a transverse displacement 780 times greater than the longitudinal elongation of the membrane, without excessive non-linear distortion. A transformation factor, $\frac{\Delta h}{\Delta L}$, of 780 should be achievable for this type of construction. This would reduce the driving voltage required from 19 kV to c. 25 V and the electric field from 64 MV/m to 82 kV/m. 25 V is acceptable within an implant, if rather higher than desirable. However, a voltage gradient of 82 kV/m will need to be contained within the implant and not allowed to enter the cochlear fluid. This should be possible by applying a thin insulating layer of bio-compatible material over the piezo membrane. The transformation factor of 780 is sufficient for an actuator of this configuration to meet the requirements of Table 7.2 when small enough to fit within an electrode array. This technology is feasible if an actuator of this type can be made sufficiently small and it can be inserted without damage to the cochlea or itself.

8.7.3 MEMS Xylophone (Cantilever) Technology

Zhao (2018) has successfully produced an implantable electro-acoustic transducer sufficiently small to be incorporated into a cochlear implant. The device is designed as a microphone, and so it is intended for lower power levels than would be needed for an actuator. The technique uses bimorphs consisting of two 400 µm by 200 µm, 1.5 μm thick layers of aluminium nitride semiconductor piezoelectric material with opposite poling to form a cantilever, in which one wafer expands longitudinally and the other contracts when a transverse electric field is applied, as does a bimetallic strip when it is heated. As well as successfully testing the overall performance as a hydrophone in the cochlea of a live guinea pig, Zhao had tested his completed device as an actuator in water, and the sensitivity is $2 - 3 \times 10^{-8}$ m/V, measured at the tip of each cantilever; the mean displacement would be about half of this. To achieve the required mean linear displacement of 3.8 μm, this would require around 250 - 400 V, which is excessive to be contained within an electrode array, and the electric field within the aluminium nitride would exceed its electric breakdown strength. The corresponding electric field would be about 200 MV/m; the dielectric strength of aluminium nitride has been measured by Ruemenapp and Peier (1999) to be a little over 20 MV/m for AC fields and around 75 MV/m for DC in laboratory conditions.

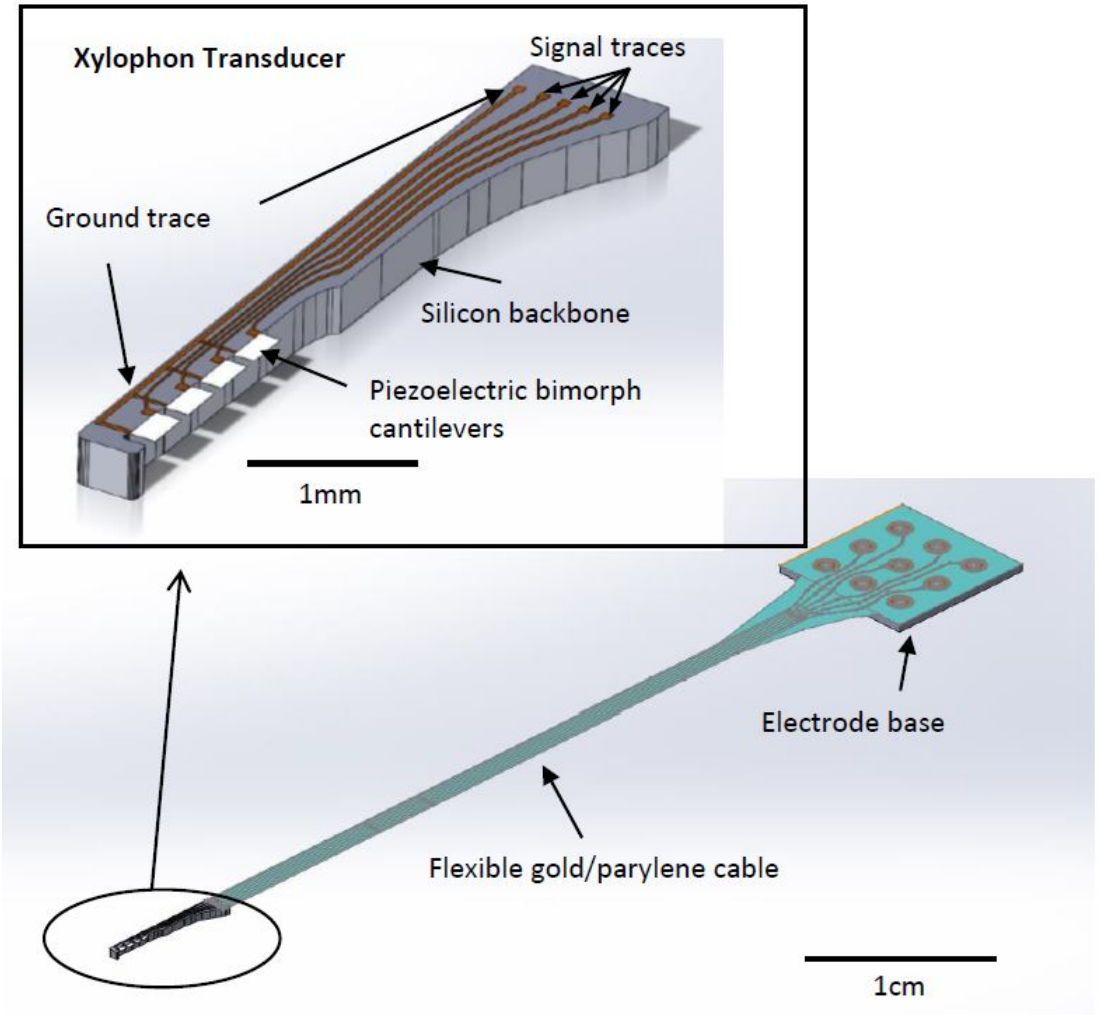

FIGURE 8.7: Photographs of the ultraminature MEMS xylophone transducer, showing the four piezoelectric bimorph cantilevers. (From Zhao (2018), reproduced with permission of the author.)

As it stands, this is not a feasible technology for the proposed purpose. However, the constrained piezoelectric dome technology described in Subsection 8.6 would benefit from the fabrication techniques described by Zhao, by exploiting the transformation factor of the dome, instead of the cantilever and the much greater dielectric strength and flexibility of polymers, while utilizing the fabrication technique and benefits of d_{31} coupling with transverse excitation used in the MEMS cantilever.

Regarding scale, it is interesting to note that Tu et al. (2018) publish details of larger, but otherwise similar cantilever transducers, 17.5 mm by 5 mm, 8 µm thick that "yield useful mechanical output at low driving voltages below 100 V." The output displacement is not specified in the text, but the graphs show it to be a few µm at 90 V input, above the resonant frequency (c. 13 Hz).

8.7.4 Attracted armature actuators without permanent magnets

It is possible to make an attracted armature actuator, similar to a Knowles or Sonion actuator, but with no permanent magnet. The magnetic field generated by the current in the coil around the armature causing the air gap to shorten and compression of the spring of the armature. This arrangement has the advantage over balanced or attracted armature actuators that it is less prone to the latch-up that can occur with permanent magnet versions if there is enough force due to shock to cause the armature to touch the poles of the magnet. This latch-up can be avoided or mitigated by fitting non-magnetic caps over the poles of the permanent magnets, known as shock-protectors, and so this advantage is considered to be minimal.

$$\text{As before, } p_c = 910 \text{ Pa at 148 Hz, where it is greatest.} \tag{8.30}$$

$$\text{Air-gap pressure} = p_g = p_c \frac{A_{\text{diaphragm}}}{A_{\text{gap}}} \tag{8.31}$$

$$p_{\text{gap}} = \frac{1}{2}\mu_0 H^2 \text{ Pa} \tag{8.32}$$

$$= \frac{1}{2}\mu_0 \frac{N^2 I^2}{l_g^2} \text{ Pa} \tag{8.33}$$

$$NI = l_g \sqrt{\left(\frac{2 p_c A_{\text{diaphragm}}}{\mu_0 A_{\text{gap}}}\right)} \tag{8.34}$$

$$\text{Assume air-gap is } 0.1 \text{ mm tall} \times 1 \text{ mm long} \times 0.32 \text{ mm wide.} \tag{8.35}$$

$$NI = 0.1 \times 10^{-3} \sqrt{\left(\frac{2 \times 910 \times 15 \times 10^{-3} \times 0.32 \times 10^{-3}}{4\pi \times 10^{-7} \times 1 \times 10^{-3} \times 0.32 \times 10^{-3}}\right)} \tag{8.36}$$

$$= 0.1 \times 10^{-3} \sqrt{\left(\frac{2 \times 910 \times 15}{4\pi \times 10^{-7}}\right)} = 18\text{AT} \tag{8.37}$$

$$\text{Area of coil} = > 12\text{mm}^2 \text{ of coil cross section for } 1.5 \text{ A/mm}^2 \tag{8.38}$$

A coil with such a large cross-section would not fit inside a cochlear implant, and so this technology is not feasible. Attracted armature actuators without permanent magnets have few advantages over actuators that have permanent magnets, and they require more current and power to achieve the required acoustic pressure level.

8.7.5 Moving coil actuators

Moving coil (dynamic) actuators use components similar to those in balanced armature devices, but the smallest available designs generally occupy volumes very much larger than balanced armature devices with similar outputs, because they are mainly used in over-ear headphones, rather than in-ear earphones. They may have some sound quality advantages when coupled to cochlear perilymph liquid, where the acoustic load impedance is greater, and so the diaphragm velocity and displacement is much less than for air-loading.

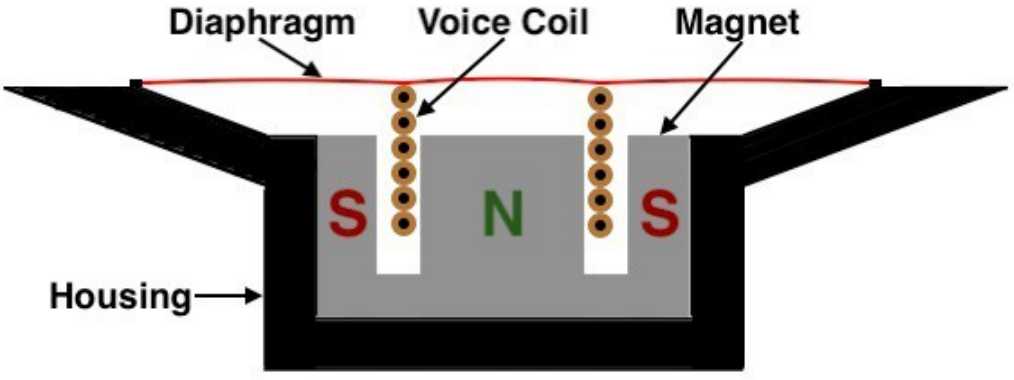

FIGURE 8.8: Diagram of a Moving Coil Actuator reproduced with permission of the copyright holder My New Microphone: https://mynewmicrophone.com/how-do-headphones-work-illustrated-guide-for-all-hp-types/

$$
\begin{aligned}
\text{Assume diaphragm area, } A_\text{d} &= 15 \times 0.3 \text{ mm} = 4.5 \text{ mm}^2 \\
\text{Force on coil} &= BlI \\
\text{where: } B &= \text{Flux density in air gap 1 T assumed} \\
l &= \text{length of wire in the coil} \\
&\simeq 2 \times (15 + 0.3) \times N \text{ turns} \simeq 30N \text{ mm.} \\
\text{Pressure, } p_\text{c} &= \text{Force / diaphragm area} \\
&= \frac{BlI}{A_\text{d}} \\
&= \frac{1 \times I \times 30N \times 10^{-3}}{15 \times 0.32 \times 10^{-6}} \simeq 670NI\text{Pa.} \\
\text{Required Pressure} &= 0.91 \text{ kPa} \\
\text{NI} &= 1.4 \text{ AT} \\
\text{Assume } 1.5\text{A/mm}^2\text{, Area of winding} &= 0.9 \text{ mm}^2 \text{ of coil cross section}
\end{aligned}
$$

This cross-section is too large be fitted into the magnetic air-gap of such a device, and the precision required for the positioning of the coil within the air-gap would be an extreme challenge. The air-gap needs to be narrow, around 0.1 mm, to avoid the flux spreading and B reducing, and the length of the coil is ultimately limited by the diameter of the implant, which is around 1 mm; this limits the coil cross section area to much less than 0.1 mm². This technology is not feasible, unless more optimistic assumptions can be justified. Future work may provide such justification, and so make this technology usable.

8.7.6 Magnetostriction calculations

Terfenol-d appears to have the best magnetostrictive properties; it has a d_{33} of 6-10 nm/AT and a relative permeability, μ_r of 2-10. The properties of Terfenol-d have been published by one of its manufacturers, TdVib LLC on their web-page: http://tdvib.com/terfenol-d/. The actuator is assumed a cuboid piece of Terfenol $15 \times 1 \times 0.32$ mm, this gives an actuator "diaphragm" area, A_{d}, of 4.8 mm^2 and an actuator length, l_{actuator} of 1 mm. The effective length of the magnetic air-path, $l_{air-path}$, is assumed to be three times the 1 mm dimension of the actuator, $l_{actuator}$. The number of ampere-turns can be calculated from the maximum displacement given in Table 7.2.

$$
\begin{aligned}
\text{Required displacement, } \Delta l &= d_{33} \times H_{Terfenol} \times l_{Terfenol} \text{ m} \\
\text{Magnetic field strength required, } H_{Terfenol} &= \frac{\Delta l}{d_{33} \times l_{Terfenol}} \text{ AT/m} \\
&= H_{air-path} \times \mu_r \\
\text{Required ampere-turns} &= H_{air-path} \times l_{air-path} \\
\text{Assume } l_{air-path} &= 3 \times l_{Terfenol} \\
\text{AT} &= 3H_{Terfenol} \times \mu_r \times l_{Terfenol} \\
&= 3\frac{\Delta l \times \mu_r \times l_{Terfenol}}{d_{33} \times l_{Terfenol}} \\
&= 3\frac{3.4 \times 10^{-6} \times 2}{10 \times 10^{-9}} = 2000 \text{ AT} \\
\text{Assume 1.5 A/mm}^2\text{, Area of winding} &= 1500 \text{ mm}^2 \text{ of coil cross section.}
\end{aligned}
$$

Such a large coil could not be fitted in a cochlear implant, and so this technology is not feasible, even assuming the most optimistic case of the smallest μ_r and the greatest d_{33}. The size of the coil could be reduced by an order of magnitude by placing a negligibly magnetostrictive ferromagnetic bar parallel to the Terfenol to reduce the length of the air-path. However, reducing the coil size by an order of magnitude would not make this technology feasible.

8.7.7 Externally excited permanent magnet attracted armature calculations

The final technology considered is one in which the cochlear implant contains a simple permanent magnet, which is made to vibrate by the magnetic field from a current-carrying coil on the scalp or in the outer ear. (The axes of symmetry of the magnet and the coil are to be approximately collinear.) This concept was suggested by an ex-colleague and friend of the author, Dr B G Gaydon, whose contact details are available from the author. This technology will cause significant electromagnetic fields to be imposed on the scalp, skull and brain, as well as the inner ear and the auditory nerve. However, the calculations in Appendix C show that such electromagnetic fields are within the Exposure Limit Values stipulated in the European Council Directive

2013/35/EU. An advantage of this concept to the design and development engineer is that the necessary change to the implant is minimal and simple, and the external coil can be readily changed if necessary for any reason (eg redesign or failure).

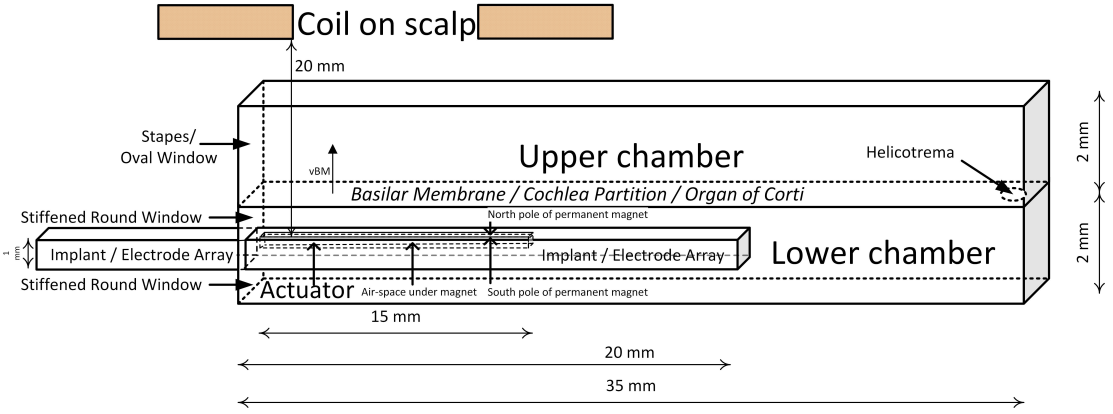

FIGURE 8.9: Diagram of the modelled cochlea with an implant containing an externally excited permanent magnet. This diagram is not to scale. The north pole of the permanent magnet forms the top surface of the implant. the south pole is on the underside of the magnet, and there is an air-space, or bubble below it so that the magnet can move independently of the implant. The Actuator is composed of the magnet and the bubble.

Assume a small permanent bar magnet fixed to an implant. Assume that it is 20 mm from the scalp, where there is a 10 mm radius circular coil of wire. As shown in figure 8.9, the magnet would have pole faces 15 mm by 0.32 mm, and it would be 0.1 mm "long" in the z direction. The axis of the implanted permanent magnet is assumed to be collinear with the axis of the coil, and hence perpendicular to its diameter.

Calculations of the power demand and coil size of this type of actuator are set down in Appendix F. The coil size that would be required is about 40 mm outside diameter and 12.5 mm thick. The power requirement would be about 200 mW. Both of these are technically achievable, but too great to be acceptable.

This power requirement would require a change of a size 13 battery too frequently, but a larger battery pack within a pocket and connected by a thin cable would make this feasible. Such a battery pack could be rechargeable overnight. Rechargeable AA cells are available with a 2.85 Ah capacity; a battery of four of these would have a capacity of 13 Wh, and would need charging after about 60 hours' use. [It is, perhaps, worth noting in this context that the first personal electronic hearing aid, made for Irene Ewing by Thomas Littler in the 1930s weighed 28 pounds or 12.7 kg. Dawes (2014)]

Appendix C considers the potential health effects of the generated magnetic field on the human body, using the EU Directive 2013/35/EU. The Appendix shows that the arrangement described in this section would comply with the requirements of that directive.

Despite the heavy battery drain, this technology may be worth investigating further, because of its simplicity, and since everything except the permanent magnet is accessible without surgery, to enable design-change and repair. Furthermore, manufacture would be possible without the need for the development of techniques for fabrication of highly miniaturized components.

This technology is feasible with a suitably located battery pack, but improvements in both size of external coil and power consumption are necessary to make it acceptable for widespread use. Such improvements could include reducing the current required to generate the required pressure by fitting a suitably sized and clad ferromagnetic core to the coil, and inserting the core into the ear canal to reduce the length of the air gap from the assumed 20 mm to about 10 mm. This would reduce the cross sectional area of the coil and the power requirement by a factor of up to 4, or the power requirement alone by a factor of up to 16. Its success would be dependent on the geometry of the individual ear, particularly on there being an approximate right angle between the ear canal and the basal turn of the cochlea.

8.8 Summary

A number of actuator technologies have been considered for use as intracochlear transducers. Their feasibility has been assessed using both the requirements for such an actuator derived in the previous chapter and theoretical estimates of their capabilities. In addition a scaling study has been conducted for commercial hearing aid "receivers", which supports the theoretical estimates. It is shown that although some technologies do not appear feasible in this application, several are feasible if their construction could be miniaturized, perhaps using MEMS technology. Feasible technologies include the balanced armature, two piezoelectric geometries and an externally excited intracochlear permanent magnet. Although feasibility could only be definitively established by demonstrating a prototype, which is beyond the scope of this thesis, the ability of several technologies to meet the requirements of an intracochlear actuator, in principle, is encouraging.

The following actuator technologies have been considered, together with a note about conclusions drawn regarding the feasibility of their producing the required acoustic pressure and velocity:

TABLE 8.3: Summary of the technologies considered and their feasibilities.

Actuator Technology	Feasible	Section	Note
Balanced armature with permanent magnets	Yes	8.5	1
Ceramic and polymeric piezoelectric	No	8.7.1	2
Polymeric piezoelectric constrained dome	Yes	8.7.2	3
MEMS xylophone (cantilever)	No, but	8.7.3	4
Attracted armature without permanent magnets	No	8.7.5	5
Moving coil	No	8.7.6	6
Magnetostrictive	No	8.7.7	7
Externally excited permanent magnet	Yes, but	8.7.8	8
For an explanation of 'No, but' and 'Yes, but', see Note.			

Notes on Table 8.3

1. Balanced armature actuators are established technology, which would be feasible, provided both that they can be fabricated at the required scale and that an electrode array can be satisfactorily inserted, when it contains a rigid device between 1 and 16 mm from the round window.

2. Linear piezoelectric actuators are not feasible, because the electric field required exceeds the electric breakdown strength of suitable piezoelectric material.

3. Piezoelectric actuators appear to be feasible if a thin film of the material can be formed into a longitudinally constrained dome, whose longitudinal elongation is limited so that a longitudinal electric field causes amplified transverse movement. This technology is feasible provided both that the dome can be adequately constrained, and that the electrode array can be inserted without causing damage to either the cochlea or the dome.

4. MEMS cantilever actuators designed as microphones are probably not feasible as actuators, because of the rather excessive voltage requirements (c. 300 V). However, the proven fabrication technique of this type of microphone could be beneficially investigated for use in combination with the constrained piezoelectric dome technology.

5. Balanced armature actuators without permanent magnets are not feasible for this purpose, because of the excessive current requirement that results in a coil that would not fit into an electrode array.

6. Moving coil actuators are not feasible, because the axial length of the coil would need to be too large to fit transversely into an electrode array.

7. Magnetostrictive actuators are not feasible, because they require excessive currents.

8. An actuator composed of a permanent magnet within an electrode array excited by a coil attached to the scalp would be feasible, provided that an electrode array containing a rigid magnet from 1 to 16 mm could be inserted without causing damage to the cochlea. However, larger batteries in a separate battery pack would be required, and there may be complications if an MRI scan is required for any purpose after implantation.

Chapter 9

Conclusions and Further Work

Post implantation loss of residual acoustic hearing can occur because stiffening of the round window results from the presence of the implant that is inserted through it. A new two-chamber finite element model has been developed from first principles that quantifies the hearing loss resulting from this cause. This model has then been used to calculate the optimum size and position of a compliant element, such as a bubble, that would need to be incorporated into the cochlear implant to overcome the effect of round window stiffening. The model has been used further to calculate the requirements of an intracochlear actuator that could restore low frequency hearing to that of a normal ear. Several different actuator technologies have been examined to see whether a theoretically scaled actuator that would fit in an implant would be capable of meeting the requirements.

9.1 Development of a Model

A model has been developed that can be used to compare the sensitivity of cochleas with different mechanical properties. The characteristics of the upper and lower chambers can be set independently. The relevant physiology of the ear is defined by values entered into two text files that are read by the Matlab model as its input variables. The same text files have been copied into the Latex code that has produced this thesis, to ensure that the model and the thesis relate to the same cochlea. The model takes into account middle ear, round window and aqueduct impedances, together with cochlear fluid compressibility and the dimensions of the cochlea. The model generates graphs of basilar membrane velocity and pressure difference in both the spatial and frequency domains. The model can be readily scaled to facilitate the simulation of prototype implants on non-human mammals.

The model includes a simplified method of calculating the round window impedance and, for the aqueducts, a formulation based on the Hagen-Poiseuille formula that

applies at all frequencies and avoids the need to decide whether the aqueducts are tubes of "very small radius" or "intermediate radius". This avoids a factor of three discrepancy in the resistance of the cochlear aqueduct at 100 Hz using the "intermediate" formula, or a factor of 2.5 error for the vestibular aqueduct at 100 Hz and a factor of four error at 1 kHz using the "very small" formula.

The model has been verified by comparison with previous single chamber models and validated by comparison with the available measurements on humans and other mammals.

9.2 Modelling an Implanted Cochlea

There is discrepancy between results predicted by the model and the measurements of cochlear input impedance, which is explained by the lack of taper in the model. There is also a slight underestimate of the hearing loss due to round window stiffening, which is explained by modelling only the loss due to stiffening the RW, whereas the measurements average the losses from all causes, including tissue damage. The model can be used to simulate the mechanical effect of an implanted cochlea and to calculate, as a function of frequency, the extent of residual acoustic hearing loss caused by stiffening of the round window. The stiffening factor can be set by altering a number in one of the input text files. Again, BM velocity and pressure can be calculated in the spatial and frequency domains in a way that facilitates comparison with a normal ear. The hearing loss caused by the stiffening of the round window is shown as a function of frequency and compared with measured results.

9.3 Modelling a Cochlea Implanted with an Electrode Array containing a Bubble

The model can be used to simulate the effects of introducing to the lower chamber an implant containing a compressible element such as a bubble to test proposed remedies for post-implantation loss of residual acoustic hearing. Graphs are produced in the normal way to show the effects of different bubble positions and sizes on BM velocity and pressure difference in the spatial and frequency domains; the graphs facilitate comparison between a normal ear and one with a stiffened round window. Graphs are also produced to show the effect of different bubble sizes on predicted hearing loss as a function of frequency. This facilitates balancing the completeness of restoration of residual hearing against the size of the bubble, and it is found that a bubble size of about 1 mm^3 reduces the loss of residual hearing from about 20 dB to about 5 dB, over the frequency range of interest, and a bubble size of 5 mm^3 reduces the loss to less

than 1 dB 9as shown in Figure 6.18. Bubble parameters are set by entering the relevant dimensions into a third text file that is read by the model.

9.4 Modelling Intracochlear Excitation

The model can be used to simulate the effects of acoustic excitation sources at various axial positions within the implant. BM velocity and pressure difference are simulated by the model in the spatial and frequency domains for actuators at different positions and of different sizes, from which hearing loss is calculated as a function of frequency. Graphs of these quantities are also produced to facilitate comparison of the predicted effects of different actuator positions and sizes with those for a stiffened RW with no actuator or bubble. The results are used to determine the pressure, velocity and displacement requirements for an intracochlear actuator.

9.5 Determining the Requirements of an Actuator

A method has been developed to relate ear canal acoustic pressure in a deaf ear to that in a normal ear, so that the same hearing sensation occurs in each case. This ear canal pressure has been translated into an unloaded (Norton equivalent) middle ear volume velocity using an existing lumped element model, and the present model has converted that middle ear Norton velocity into a BM velocity at the characteristic place. The model then calculates the velocity and pressure requirements of an implanted actuator if it is to produce the same sensation in an implanted ear as would a particular sound pressure level in the ear canal of a normal ear. The model produces a table of requirements for the volume velocity of the actuator and the pressure that it needs to generate.

These requirements have then been used to test the feasibility of using various types of actuator as sources of intracochlear excitation. Eight potential technologies have been considered, of which four appear to be feasible, subject to the development of suitable designs and the acceptability of certain limitations.

9.6 Further Work

In order to achieve completion of the model in a reasonable time, it has been necessary to make certain limiting assumptions before knowing what impact these assumptions would have on the accuracy of the model.

The results of using the model have also revealed some areas of interest for further investigation and ideas for improvement that there has not been time to pursue.

All of these concepts are discussed briefly in the following Subsections.

9.6.1 Taper

The decision not to model the taper of the real cochlea has probably had more impact on the model than any other of the assumptions made. Fortunately, the effect of making this assumption has been limited, and it appears that the effect has been to make the model pessimistic in its predictions of performance. The impact of not including tapering has been to increase the impedance of the wave propagating from the stapes to the characteristic place and returning to the round window. This, in turn, has affected the cochlear input impedance and the normalized response of the unloaded stapes velocity to BM velocity. The impact on the normalized response from a velocity source actuator to the BM is less in the frequency range of interest, because the distance that the wave has to travel is less. Including taper in the present model would also improve its comparison with the Peterson and Bogert (1950) model, which does include tapering.

9.6.2 Three Dimensional Modelling

The present model is a one dimensional model of a three dimensional cochlea. This necessitates assumptions to be made and correction factors to be applied, without accurate knowledge of the extent of the errors that these introduce. It also limits the ability of the model to predict the effects of the position of the implant in the lower chamber, which it is difficult to control during the surgical insertion process. Extending the present model to three dimensions would enable assessment of the importance of controlling implant position within the cross section of the lower chamber for acoustic hearing purposes.

9.6.3 Chamber, Helicotrema and Implant Viscosities

Although including further viscosity calculations alone in the present model is unlikely to have much impact on its results, it is possible that chamber and helicotrema viscosity calculations would make more difference to results when the model is enhanced to include taper.

It has been assumed that the presence of the implant in the lower chamber would have little impact beyond that of causing stiffening of the round window. This is because the speed of sound and the density of the silicone rubber of the implant are both virtually the same as those of the perilymph. However, when taper is modelled and chamber viscosity included, a more detailed examination may be merited of the acoustic properties of implants, particularly the mechanical loss angle.

9.6.4 Design and Manufacture

Clearly, the model will be of use to the world only if it leads to the design, manufacture, fitting and user acceptance of improved implants. The next stage of this is to obtain the interest of those with the necessary skills to begin the designing process and progressing it to the point of testing prototype enhanced implants, containing a bubble or an actuator, initially on an inanimate physical model of the cochlea. The author is aware that the Target Fabrication Department of the Atomic Weapons Establishment (at Aldermarston, Berkshire, UK) has a manufacturing facility capable of making very small intricate objects, such as a 2 mm bicycle. This facility is available to other organizations for research purposes. They have confirmed that they could investigate this in principle, but, understandably, they could not make any commitment until a more specific design is presented for manufacture. Their ability to manufacture would depend very much on the detail of the design and the requirements of the product. They do not provide design consultancy, and so the design department of a manufacturer would need to be involved. Similar facilities may be available at other establishments, such as the Catholic University of Leuven. Because this thesis is concerned only with theoretical feasibility, this facility has not been investigated further.

9.6.5 Modelling Excitation from the Round Window with an Actuator in the Middle Ear

The model is capable of simulating a cochlea stimulated by vibrating the round window, for example by attaching a middle ear implant to a cochlear implant. This has not been pursued in this thesis, but it has the advantage of using two established technologies that would need no more than the design of the interface where the two devices are coupled, although such excitation would be complicated after implantation by progressive stiffening of the round window. Investigation of this matter could reasonably be undertaken in parallel with enhancing the model as suggested in the two preceding subsections.

9.6.6 Masking

The frequency domain graphs output by the model show that at certain positions along the cochlea the frequency that causes the maximum BM velocity is less than the characteristic frequency for that place. This phenomenon is reflected in published measurements of BM velocity or displacement in small mammals. It is possible that this could contribute to the explanation of the masking by low frequency sounds of those of higher frequency.

9.6.7 Investigation of Techniques for Improving the Magnetic Coupling between an Implanted Permanent Magnet and an External Coil

At a late stage in the project, it was suggested that an actuator could be constructed by embedding just a permanent magnet in a cochlear implant and using a coil on the scalp to vibrate it. This has been explored in this thesis and found to be feasible, subject to its having a larger than usual battery. The need for such a large (pocket size) battery arises from the huge air-gap between the permanent magnet and the coil. At a later stage, it was suggested that improvements to the power consumption could be made by decreasing the effective size of the air-gap and/or shaping the magnetic field generated by the coil. These are outlined in Section 8.7. Unfortunately the suggestions were made too late in the project to pursue them within the time-frame available, but they could be the subject of further work.

9.6.8 Determination of Characteristic Place as a Function of Frequency in Live Humans

As detailed below, there is a clear discrepancy between the frequency range of the human ear calculated from measured values of BM elasticity, the best frequency localization measured directly and the accepted KRM BM structure / travelling wave theory. For many decades, there were few measurements in live humans of the relationship between the characteristic place on the basilar membrane and the audio frequency of excitation. Probably the most notable measurements were those of von Békésy in 1942. Von Békésy also measured BM elasticity, and he reported his results in Békésy (1941). The elasticity measurements were made over the range 3 - 30 mm of a 35 mm cochlea, and the range of measured elasticities over that range was close to two orders of magnitude. The BM is traditionally considered to be a KRM (stiffness, resistance, mass) structure with constant mass and damping along the length of the cochlea, as modelled, for example, by Elliott and Ni (2018). In such a structure, the resonant frequency at a particular place, and hence the best frequency, will be proportional to the square root of the elasticity. For a uniform BM width, this means that the best frequency range for the region 3 to 33 mm will be close to just one order of magnitude. This will be increased by a factor of 3.3 for a typically tapered cochlea (Wever (1949), to a factor of 33. The measured best frequency range for locations from 3 to 33 mm of a 35 mm human cochlea is reported by Greenwood (1990), with a little extrapolation, as 12,500 to 50 Hz, which is a factor of 250. Resolving this disparity would facilitate improvements both to the present model and to other finite element models of the cochlea.

As described in Békésy (1952), reliable measurements of the elasticity of the BM are possible, because the tissue does not change its mechanical properties post mortem, if it is kept under water. However, his direct observation of BM vibration patterns were

accomplished by drilling a hole in the bony wall of the cochlea. Békésy refers to the difficulty of making such measurements. There would be benefit in having available an easier, reliable technique for measuring best frequency localization.

Recently, much work has been done to develop tomographic methods that have the spatial resolution and the speed to make accurate and reliable measurements, but these methods require the use of costly equipment. Another possibility is to use the tonotopic technique developed by Stevens et al. (1937) to determine the relationship between frequency and characteristic place by measuring audiometrically the frequency limen in live humans. Their work assumed a uniform distribution of hair-cells along the organ of Corti, which subsequent published work, such as Wright et al. (1987), has shown not to be the case, even in young adults. There is now an opportunity to re-visit this work, with a view to developing an inexpensive and ethical approach to measurements that would improve the understanding of cochlear mechanics and be quicker and more economical than tomographic techniques. Tomographic methods could be used to validate the results of measurements of the frequency limen and its integration along the cochlea. The use of Greenwood's equation in the present model certainly gives a closer correspondence of modelled characteristic place to measured results than an exponential taper, but it still leaves plenty of room for improvement in relating cochlear action to the mechanical properties of the basilar membrane, particularly elasticity. Now that a two chamber distributed model has been developed, a more precise relationship between characteristic frequency and cochlear location may be useful to designers of implants and to the surgeons that control the depth of insertion into the cochlea.

Such further work would enable a revised version of the present model to use an elasticity taper based on measured values of BM elasticity as an input. The present model would then enable alternative theories of sensing and discrimination to be tested for the audio frequency ranges where they may be more applicable, to see how well each theory correlated with data from measurements of both best frequency localization and BM elasticity.

Appendix A

Deviations from Previous Models

This Appendix discusses various differences between the model developed in this thesis and previously published models. Most of the differences clarify typographical errors in previous reports, but slightly modified models for the round window and the aqueduct impedances have been developed from first principles.

A.1 Calculation of Required Bubble Size

Initially, the unencapsulated bubble size of 0.15 mm^3 recommended in Elliott et al (2016) was loaded into the model, but the predicted reduction in hearing loss was not as expected. On further investigation, it was discovered that the 0.15 mm^3 figure in the 2016 paper was too small by a factor of 100. The authors of the paper kindly accepted that this was the case, and so larger, more compliant bubbles were modelled from then onwards.

A.2 Differences found between input variable values and a formula in Elliott and Ni (2018) and the associated Matlab code

The minor difference found in a formula is that there is a minus sign after the equals sign in equation 20 of the published paper, whereas the corresponding equation in the code has no minus sign. The formula in the paper is considered to be correct, and so a minus sign has been added to line 143 in the Matlab code for the purpose of making a comparison.

In the paper, the BM width at the apex is 0.15 mm, whereas the Matlab script uses a value of 0.2 mm. The final value used for the present model is 0.2 mm. The value in

the paper of the average scala area is 0.8 mm, whereas the value used in the Matlab script is 0.822 mm. The value used by the script is now used in the present model for the comparison.

These differences are trivial for most purposes, but they are noticeable when making a comparison of the results of two models.

A.3 Interpretation of the Law of Conservation of Momentum

Equation (12) in Elliott and Ni (2018) is written:

$$\left|\frac{\partial p(x)}{\partial x}\right|_{x=0} = i\omega\rho v_1 \tag{A.1}$$

This is difficult to understand without further explanation, because $\left|\frac{\partial p(x)}{\partial x}\right|_{x=0}$ is the x direction component of the pressure gradient, which is a vector whose direction is along the x axis. In contrast, v_1 (the BM velocity) is a vector in the z direction. A strict interpretation of the Law of Conservation of Momentum means that the horizontal velocity of the fluid, u_1, rather than the vertical velocity of the BM, v_1, is related to the pressure gradient by the equation

$$\left|\frac{\partial p(x)}{\partial x}\right|_{x=0} = i\omega\rho \left|u_1\right|_{x=0} \tag{A.2}$$

However, if $|u_0|_{x=0} = 0$ when the stapes/oval window is locked, the Law of Conservation of Mass (and hence Volume for an incompressible fluid) provides a relationship between v_1 and u_1:

$$\begin{aligned} v_1 B\Delta &= A_{CH} u_1 && \text{(A.3)} \\ \text{Where } B &= \text{Effective chamber height} \\ \Delta &= \text{BM element length} \\ A_{CH} &= \text{Chamber area} = Bh \\ \text{and so: } u_1 &= \frac{\Delta v_1}{h} \\ \left|\frac{\partial p(x)}{\partial x}\right|_{x=0} &= \frac{\Delta}{h} i\omega\rho v_1 && \text{(A.4)} \end{aligned}$$

Strictly this is correct only when $\frac{dv}{dz}$ is constant, but this will be a very close approximation when the wavelength is $>> h$, which will be so for all frequencies within the audio range. Equation (A.4) appears to be more in accordance with the Law of Conservation of Momentum than equation (12) in Elliott and Ni (2018).

A.4 Modelling the Impedance of the Round Window

Nakajima et al. (2009) found that, as frequency was increased above 500 Hz, the rate of increase of round window impedance became asymptotic to 3 dB per octave, and the phase of the impedance became asymptotic to 45 degrees. They concluded that the acoustic resistance of the round window is proportional to the square root of frequency and the inertance or inductance is inversely proportional to the square root of frequency. They went on to model this as a network of 6 parallel branches, each containing a resistance and inertance in series, with values determined by a Foster or Cauer network iterative process. Frear et al. (2018) have adopted the same approach. Elliott et al (2016) use a single resistance value that is independent of frequency. The present model differs by modelling the resistance and inertance as being proportional and inversely proportional to the square root of frequency, respectively. This approach is simpler than the iterative technique (for both understanding and modelling), and it produces results that are slightly closer to the mean of the measured values reported in Nakajima et al. (2009). In Nakajima et al.'s paper, Figure 13 shows that the measured results are generally less than those modelled in the frequency range of interest; the present model produces results less than their model in this range, and so closer Nakajima et al.'s measured results.

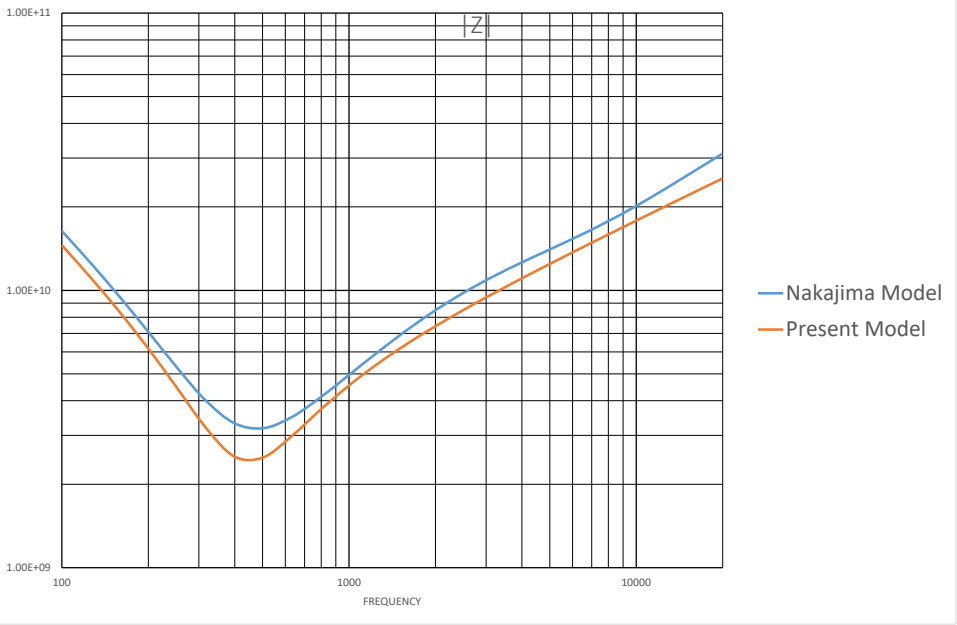

FIGURE A.1: Comparison of Round Window Impedance Calculations using Foster or Cauer Networks used by Nakajima et al. (2009) and Simpler $\sqrt{f}$ Method used in the Present Model.

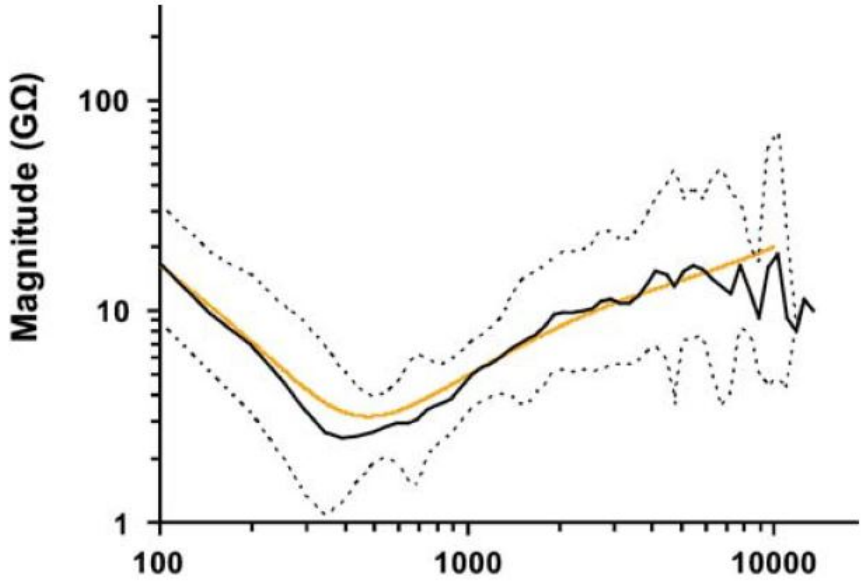

FIGURE A.2: Round window impedance, |ZRW|=|PST/UStap| is plotted with a black line for the mean and dotted lines for the standard deviation. Below 300 Hz, ZRW behaves as a compliance. Above 300 Hz, ZRW becomes dominated by inertia and resistance. This behavior is consistent with distributed loss and inertia, wherein impedance increases as approximately the square root of frequency much as in a system with "skin effect." Behavior of a lumped parameter model for this system is plotted with a gold-colored line. The graph shows that the mean of the measured data is smaller than the modelled values over the frequency range 100 - 1000 Hz. Reprinted by permission from Springer Nature, JARO - Journal of the Association for Research in Otolaryngology, from Differential intracochlear sound pressure measurements in normal human temporal bones,Nakajima et al., © 2009

Xue et al. (2020) derive the round window impedance values for their model from Frear et al. (2018), but neither paper specifies the values that they have used for the resistances or inertances in each of the six network branches. The present model uses the model of the ear in Xue et al. (2020) to calculate only the relationship between ear canal pressure and unloaded stapes velocity.

A.5 Calculation of the Impedances of the Aqueducts

The cochlea has two aqueducts: the cochlear aqueduct and the vestibular aqueduct. The former equalizes perilymphatic pressure between the cranial cavity and the scala tympani and hence the scala vestibuli, via the helicotrema. The latter equalizes endolymphatic pressure between the scala media and the endolymphatic sac. The cochlear and vestibular aqueducts have the effect of adding lumped inertance and damping to the cochlea near the round and oval windows, respectively.

All but one of the previous cochlear models studied calculate the impedances of the aqueducts using the formula for tubes of very small radius given in Beranek (1954).

Beranek's criterion for a tube being of very small radius depends on the frequency, f, and it is that the radius, $a < 0.002/\sqrt{f}$. It is clear from Beranek's text that this criterion is for air at 100 kPa and 20 °C. This criterion is derived from the boundary layer thickness, given by $\delta = \sqrt{\frac{\mu}{\omega\rho}}$, where μ is the co-efficient of viscosity, which will be different for different fluids, and it is assumed to be that of water for cochlear fluids. The ratio of boundary layer thickness in water at 37 °C to that in air at 20 °C is 0.21. This means that the corresponding criterion for cochlear fluids (whose viscous properties closely resemble those of water) is $a < 0.00042/\sqrt{f}$. It is assumed that Beranek was using the metre as the unit of length and the Hz as the unit of frequency. If the frequency range of interest is 100 Hz to 1 kHz, then the criterion becomes $a < 0.042$ mm to $a < 0.0133$ mm. As observed by Elliott et al. (2016), neither aqueduct meets this criterion in the frequency range of interest, because the smallest aqueduct radius used in the models studied is 0.075 mm. All of the models, including that developed in this thesis, refer to Stenfelt (2015) for vestibular aqueduct dimensions and to Gopen et al. (1997) for those of the cochlear aqueduct.

As stated in Chapter 5, the dimensions used for the aqueducts are:

	Radius	**length**	**Units**
Cochlear Aqueduct	0.075	10	mm
Vestibular Aqueduct inner	0.15	1.5	mm
Vestibular Aqueduct outer	0.3	8.5	mm

The calculations of aqueduct impedances in Appendix B of Elliott et al. (2016) are based on the formula given by Beranek (1954) for tubes that meet his criterion for intermediate sized tubes, which is $a > 0.01/\sqrt{f}$ for air, which becomes $a > 0.0021/\sqrt{f}$ for the water-like cochlear fluids. For the frequency range of interest, this amounts to a radius of 2.1 mm at 100 Hz and 0.66 mm at 1 kHz. However, the largest radius used in both this and the other models is 0.3 mm, and so this criterion is also not met. (NB. The 1954 edition of Beranek's book and the 1987 reprint both misprint this criterion as $a < 0.01\sqrt{f}$, whereas the 2012 edition, Beranek and Mellow (2012), written jointly with Mellow has corrected this to $a < 0.01/\sqrt{f}$.) This means that the aqueducts have diameters that lie between those suitable for calculating their impedances using Beranek's formulae for very small and intermediate sized tubes. The significance of using either formula where the relevant criterion is not met depends on both the frequency range of interest and the purpose of the modelling. It is clear that the two aqueducts qualify under Beranek's criteria for small tubes at only the lowest audio frequencies, and it is also clear that they qualify as intermediate diameter tubes in only the upper frequencies of the audio range. At frequencies at which residual acoustic hearing is impaired by implantation, the aqueducts have radii between those that meet Beranek's criteria for very small and intermediate tubes. Beranek states that interpolation is necessary in such circumstances to determine the aqueduct acoustic resistances, but he offers no formulation for doing so. To address

this and to avoid any significant inaccuracy in the present model from applying the wrong formula, the Hagen-Poiseuille formula has been used. This can be applied to a tube of any radius less than, say, 0.1λ where λ is the wavelength. Ostadfar (2016) has applied this formula to an oscillating flow in a circular tube, to give the volume velocity,$Q_\varphi(t)$ in terms of the driving pressure, $P_0(t)$ as:

$$Q_\varphi(t) = \int_{r=0}^{a} 2\pi r U_\varphi(r,t)\,\mathrm{d}r = \frac{i\pi P_0 a^2}{\rho\omega l}\left(1 - \frac{2\mathrm{J}_1\left(\sqrt{i\frac{\rho\omega}{\mu}}a\right)}{\sqrt{i\frac{\rho\omega}{\mu}}a\mathrm{J}_0\left(\sqrt{i\frac{\rho\omega}{\mu}}a\right)}\right)e^{i\omega t} \tag{A.5}$$

Where:

Q_φ =volume velocity of oscillatory flow
$U_\varphi(r,t)$ = linear velocity of oscillatory flow
P_0 = peak acoustic pressure
l = tube length
a = tube radius
ρ = density
ω = angular frequency
μ = dynamic viscosity

J_1 is a Bessel function of the first order
J_0 is a Bessel function of zero order.

If $\sqrt{\frac{i\rho\omega}{\mu}}$ is written as k_v, then equation A.5 can be written:

$$Q_\varphi(t) = Q_0 e^{i\omega t} = \frac{-i\pi P_0 a^2}{\rho\omega l}\left(1 - \frac{2\mathrm{J}_1(k_\mathrm{v}a)}{k_\mathrm{v}a\mathrm{J}_0(k_\mathrm{v}a)}\right)e^{i\omega t} \tag{A.6}$$

(k_v is equal to $\frac{\sqrt{i}}{\delta}$, where δ is the viscous boundary layer thickness.)

From this equation, the acoustic impedance of an aqueduct due to viscous dissipation, Z_v can be calculated as:

$$Z_\mathrm{v} = \frac{P_0}{Q_0} = \frac{\rho\omega l}{i\pi a^2}\left(\frac{k_\mathrm{v}a\mathrm{J}_0(k_\mathrm{v}a)}{k_\mathrm{v}a\mathrm{J}_0(k_\mathrm{v}a) - 2\mathrm{J}_1(k_\mathrm{v}a)}\right) \tag{A.7}$$

The analysis by Beranek and Mellow is similar to Ostadfar's, but it is more comprehensive (and harder to follow), because it also considers molecular slip, which is not significant for liquids. Some details in the derivation in Ostadfar (2016) are unclear. On further examination, two typographic errors have been found in equation

1.67 of Ostadfar (2016)[1] To address this, Matlab has been used to calculate the aqueduct resistances for the present model, according to the corrected Ostadfar's formula for viscous losses, and then enhanced to account for thermal losses, as described below.

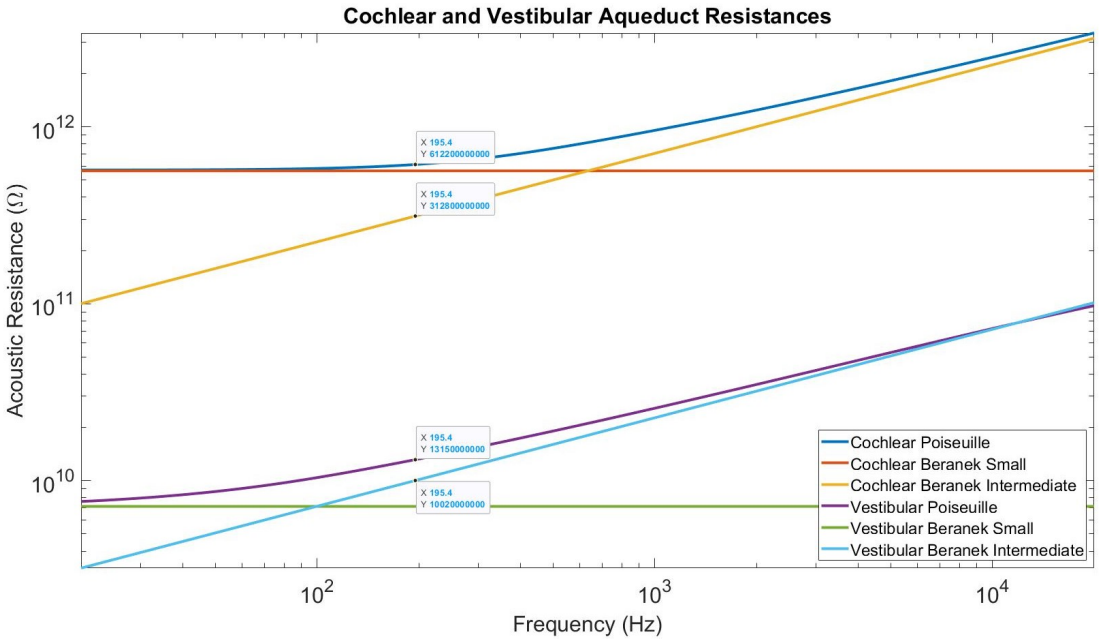

FIGURE A.3: Cochlear and Vestibular Duct Resistances. Whereas the approximations for small or intermediate sized tubes have been used in previous models, the more accurate Poiseuille formula has been used in the present model.

Beranek and Mellow's formulae for the resistances of very small tubes (R constant with frequency) and intermediate tubes ($R\alpha 1/f$) are comparable with Ostadfar's formula, for the two aqueducts, when they have sizes corresponding to the means of the measurements by Gopen et al. (1997) and by Clemis and Valvassori (1968).

The mathematics in Beranek and Mellow (2012) is the same as the Poiseuille formula for tubes of radius in the range covering the aqueducts, but Elliott et al. (2016) state that Beranek has assumed a factor of two increase in the boundary layer thickness, because of thermal losses in air that do not occur in water. Beranek and Mellow (2012) compute the acoustic resistance due to viscosity alone in their equation 4.23 as

$$R_A = \frac{l}{a}\frac{\sqrt{2\omega\rho_0\mu}}{\pi a^2}\ \mathrm{Nsm}^{-5} \tag{A.8}$$

[1] 1. For pulsatile flow the velocity, Q_φ , must be a function of the pulsatile pressure, P_φ, and not the static pressure, P_s. 2. The total volume velocity into the tube cannot be a function of the radius at which it is measured, and so the argument of the first order Bessel function should be Λ, rather than ζ. After correcting these two errors, this equation becomes consistent with equations 4.197 and 4.198 in Beranek and Mellow (2012), and it gives results identical with those obtained using an alternative formulation for oscillatory flow determined by the Hagen-Poisseuille equation in Wikipaedia.

This is the acoustic resistance for an intermediate-sized tube. This is equivalent to the real part of the specific impedance, Z_V, given in their equation 4.251

$$R_V = \frac{1}{a}\sqrt{2\omega\rho_0\mu}\ \mathrm{Nsm}^{-3} \tag{A.9}$$

R_V is defined in their equation 4.248 as being the real part of Z_V, and immediately following their equation 4.241, they state that the first [real] term is the resistance due to viscous flow. It is therefore concluded that their equation 4.23 and Beranek (1954)'s equation 5.54 make no allowance for thermal losses, and so it is not necessary to double the resistance as Elliott et al. suggest.

To be more precise, the Prandtl number needs to be used to calculate the thermal losses or diffusivity and to increase the aqueduct resistance accordingly. The Prandtl number is defined as the ratio of dissipation by momentum to dissipation by thermal conductivity. Baumgart (2011) gives the same formula for calculating the Prandtl number as Beranek and Mellow (2012), which is:

$$Pr = C_\mathrm{p}\mu/k_\mathrm{th} \tag{A.10}$$

In this equation C_p is the specific heat at constant pressure, k_{th} is the thermal conductivity, and μ is the dynamic viscosity (NB η is used elsewhere). Baumgart (2011) gives the Prandtl number for water as ≈ 10, at 20°C. When this is calculated for a temperature of 37°C using his formula, then $Pr = 4.71$. The total dissipation and hence the total acoustic duct resistance is assumed to be related to the resistance due to viscosity alone by the equation:

$$R_\mathrm{total} = R_\mathrm{viscous}\left(1 + \frac{1}{Pr}\right) \tag{A.11}$$

This is an approximation, because the thermal losses may modify the flow profile across the tube, and hence change the viscous losses. However, if the thermal losses are only about 20% of the total, the resultant error is unlikely to have much overall significance in the modelling of a minor component of the inner ear. Using this relationship, and the value of P_r calculated for 37°C,

$$R_\mathrm{total} = R_\mathrm{viscous}\left(1 + \frac{1}{4.71}\right) = 1.21 \tag{A.12}$$

This value is used in the present model. The resultant aqueduct impedances have been calculated as functions of frequency by adding the inertance of the fluid and the stiffness of the cranial cavity that terminates each aqueduct; the impedances are shown graphically in Figure A.4.

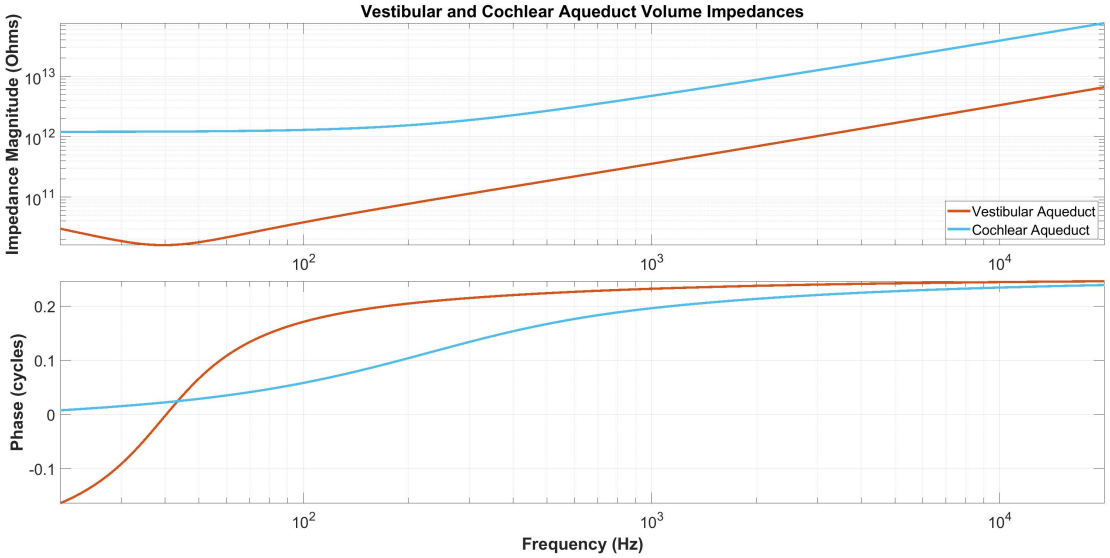

FIGURE A.4: Cochlear and Vestibular Duct Impedances Calculated by the Present Model.

Appendix B

Transducer Characteristics of Miniaturized Balanced Armature Actuators

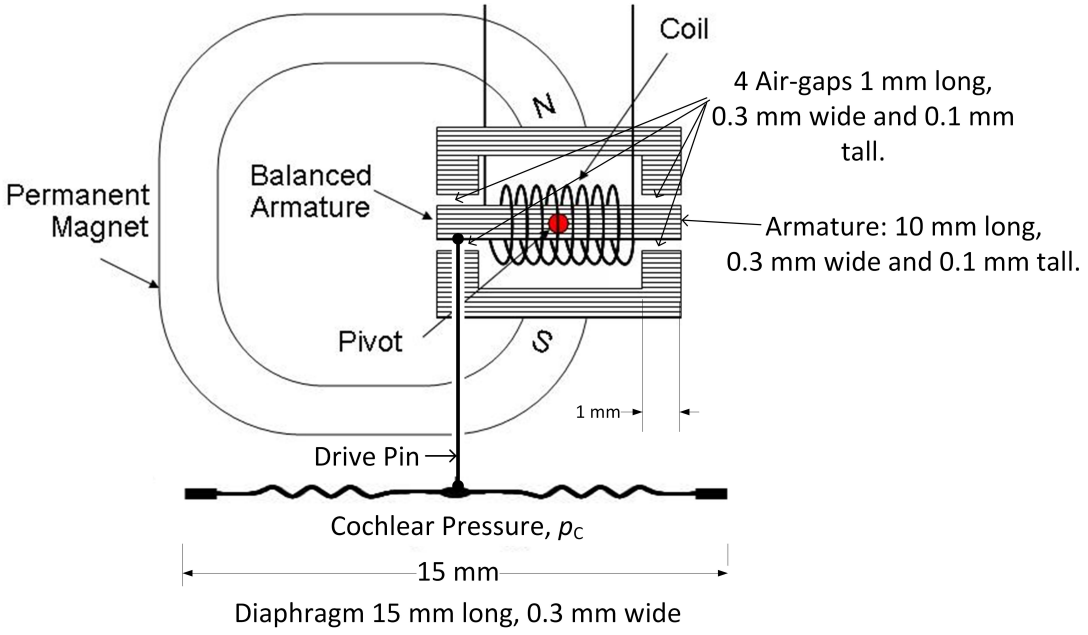

FIGURE B.1: Diagram of a Balanced Armature Actuator, with the assumed dimensions used in the calculation of its sensitivity.

B.1 Calculation of the Electrical to Acoustic Transduction Coefficient, $T2$

From equation 8.8:

$$\begin{aligned}
\text{Cochlear Pressure, } p_c &= \text{Force/diaphragm area} = \frac{2A_g B_p N I}{A_d l_g} && \text{(B.1)}\\
&= T_2 I && \text{(B.2)}\\
\text{Where } A_d &= \text{the diaphragm area.}\\
I &= \text{Actuator current.}\\
T_2 &= \frac{2A_g B_p N}{A_d l_g} = \frac{2 \times 0.3\text{e}-6 \times 1 \times 1000}{3.2\text{e}-6 \times 0.1\text{e}-3} = 1.875\text{e}6 && \text{(B.3)}
\end{aligned}$$

Where T_2 is the cochlear pressure, p_c, when unit current is injected into the electrical input, and the acoustic output is blocked, so that the diaphragm does not move.

B.2 Calculation of the Electrical Impedance

The resistive part of the electrical impedance is calculated in Section 8.5. The inductive part of the electrical impedance is that caused by the magnetization of the magnetic circuit, which becomes the locked 'rotor' impedance, when the resistive voltage drop of the coil is added to it. If the mmf of the ferro-magnetic components is neglected, the inductive, or magnetizing impedance will be controlled by the number of turns and the geometry of the air-gaps.

$$\begin{aligned}
E &\simeq N\frac{d\Phi_a}{dt} = N\omega B A_g \text{ for each air-gap, and also overall,} && \text{(B.4)}\\
&\quad \text{there are two series pairs of air-gaps, in parallel with each other.}\\
&\simeq i\omega\mu_0 N^2 \frac{A_g}{l_g} I && \text{(B.5)}\\
Z_{\text{inductive}} &= \frac{E}{I} \simeq i\omega\mu_0 N^2 \frac{A_g}{l_g}\\
\text{Numerically, } A_g &= 1\text{ mm} \times 0.3\text{ mm} = 0.3 \times 10^{-6}\text{ m}^2\\
B_p &= 1\text{ T}\\
N &= 1000\\
A_d &= 15\text{ mm} \times 320\text{ µm} = 4.8 \times 10^{-6}\text{ m}^2\\
l_g &= 0.1\text{ mm} = 0.1 \times 10^{-3}\text{ m}\\
Z_{\text{resistive}} &= 45\ \Omega\text{, from Equation 8.24} && \text{(B.6)}\\
Z_{\text{electrical}} &= Z_{\text{resistive}} + Z_{\text{inductive}} = 45 + 1.38 \times 10^{-3} i\omega\ \Omega && \text{(B.7)}
\end{aligned}$$

It can be seen from this that the imaginary part, $Z_{\text{inductive}}$, very much the minor term within the frequency range of interest ($\omega = 628$ to 6283 rad/s. (For simplicity in Section 8.3, $Z_{\text{electrical}}$ is considered to be only its resistive part. Its inductive part is less than 20% of its resistive part within the frequency range of interest, and so the maximum error arising from this is 2%. This is considered adequate accuracy for considerations of feasibility, but for completeness, the reactive term is taken into account in calculating the overall actuator impedance.)

B.3 Calculation of the Acoustic to Electrical Transduction Coefficient *T*1

When the diaphragm and the armature move, the changing magnetic field will induce an emf in the coil. Even though the high impedance of the cochlear fluid will limit the movement to a small fraction of that in air for the same diaphragm pressure, it is advisable to check that the linear velocity requirement of 2.2×10^{-3}m/s would not cause an excessive emf to be induced in the coil. The emf will be:

$$\begin{aligned} E &= N\frac{\mathrm{d}\Phi_{\mathrm{a}}}{\mathrm{d}t} = N\frac{\mathrm{d}B_{\mathrm{a}}}{\mathrm{d}t}A_{\mathrm{a}}, \\ \text{Where } \Phi_{\mathrm{a}} &= \text{flux,} \\ B_{\mathrm{a}} &= \text{flux density and} \\ A_{\mathrm{a}} &= \text{area of the armature.} \end{aligned}$$

The flux in parallel paths of a magnetic circuit divides in inverse proportion to the reluctance of each path, when there is no difference in the currents surrounding the parallel paths. Assuming that the reluctances of all parts of the magnetic circuits except the air gaps are negligible, this means that the flux in the armature will be related to the lengths of the air-gaps. If the air-gaps are all of length l_{g} when the armature is held centrally between the poles of the magnets, and they change to two gaps of length $l + \delta l$ and two of $l - \delta l$ when the armature and the diaphragm move, then the flux in the armature and the emf that it induces in the coil will be given in

terms of the flux from the permanent magnet, Φ_p by the equations:

$$\begin{aligned}
\Phi_a &= \Phi_p \left(\frac{2l_g}{2\left(l_g - \delta l_g\right)} - \frac{2l_g}{2\left(l_g + \delta l_g\right)} \right) = \Phi_p l_g \left(\frac{l_g}{\left(l_g - \delta l_g\right)} - \frac{l_g}{\left(l_g + \delta l_g\right)} \right) \\
&= 2\Phi_p l_g \left(\frac{\delta l_g}{l_g^2 - \left(\delta l_g\right)^2} \right) \simeq \frac{2\Phi_p \delta l_g}{l_g}, \text{ assuming that } \left|\delta l_g\right| \ll l_g, \\
\text{Where } \Phi_p &= \text{total flux from the permanent magnet.} \\
\Phi_p &= B_p A_g \\
\Phi_a &\simeq \frac{2\Phi_p \delta l_g}{l_g} \simeq \frac{2B_p A_g \delta l_g}{l_g} \\
E &= N\frac{d\Phi_a}{dt} \\
E &\simeq 2NB_p A_g \frac{d\left(\delta l_g\right)}{dt}, \text{ assuming that } B_p \text{ remains constant with } \delta l_g, \\
&\quad \text{and hence with time.}
\end{aligned}$$

$\frac{d(\delta l_g)}{dt}$ will be equal to the linear velocity of the diaphragm. The induced emf is given in terms of the linear velocity by the following equation:

$$E \simeq \frac{2NB_p A_g}{l_g} v_d, \tag{B.8}$$

$$\simeq \frac{2NB_p A_g}{l_g A_d} q_d, \tag{B.9}$$

$$\text{Where } v_d = \text{diaphragm linear velocity} = 2.2 \times 10^{-3} \text{ m/s}. \tag{B.10}$$

$$\text{Where } q_d = \text{diaphragm volume velocity} = 10 \times 10^{-9} \text{ m/s}. \tag{B.11}$$

$$\text{Using the same values as used above :} \tag{B.12}$$

$$E \simeq 14 \times 10^{-3} \text{ m}^2 \text{ T/s} \simeq 16 \text{ mV}. \tag{B.13}$$

This emf is less than the 100 mV emf required to drive the required current through the resistance of the coil, and so it can be neglected in calculations of the voltage and power requirements.

Adopting the convention that v_d is positive when a positive current is driving the flow **into the cochlea**, then the back EMF is given by Equation B.8:

$$\text{Back EMF, } E \simeq \frac{2NB_p A_g}{l_g} v_d \simeq \frac{2NB_p A_g}{A_d l_g} q_d, \tag{B.14}$$

$$\text{Where } v_d = \text{diaphragm linear velocity}$$

$$q_d = \text{diaphragm volume velocity, and so} \tag{B.15}$$

$$T_1 = -\frac{2A_g B_p N}{A_d l_g} = -\frac{2 \times 0.3\text{e}-6 \times 1 \times 1000}{3.2\text{e}-6 \times 0.1\text{e}-3} = -1.875\text{e}6 \tag{B.16}$$

Where T_1 is the open circuit voltage at the electrical terminals when unit volume velocity is injected **into the actuator** from the cochlea.

B.4 Calculation of the Acoustic Impedance

Sun and Hu (2016) have published a lumped element model of a balanced armature receiver, which calculates a resonant frequency of 2958 Hz for the first mode. They do not specify the overall volume of the receiver, but it appears to be reasonably similar in size to a Knowles FK series, which has a volume of 26 mm^3. Knowles actuators show a reasonable correlation (R^2=0.66) between resonant frequency and the reciprocal of the fifth root of volume. By scaling in this way, a resonant frequency of about 5 kHz is obtained for a 1.5 mm^3 actuator.

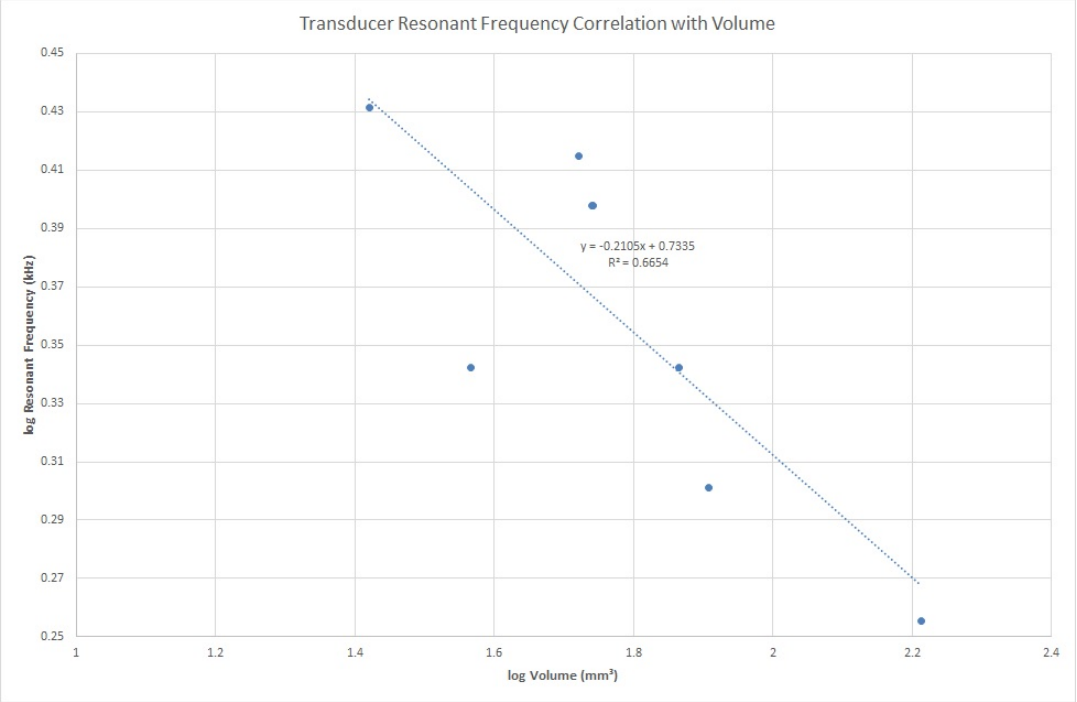

FIGURE B.2: Loglog Graph of Transducer Resonant Frequency as a Function of Volume, showing Regression Line and Equation

The mechanical stiffness of their model is 727 N/m and the mass is 2.11 mg. The stiffness will be inversely proportional to the volume, because the rear volume of the actuator is the principle contributor to the stiffness, and so the mechanical stiffness of a 1.5 mm^3 actuator is 12.6 kN/m; the corresponding acoustic stiffness is 547 TPa/mm^3 for a 4.8 mm^2 diaphragm. However, the mass of the armature and diaphragm will not scale according to the volume, because their thicknesses cannot be scaled. It is difficult to scale the magnetic circuit and to ensure sufficient magnetic flux can be transferred from the permanent magnet(s) to the air-gap(s) without saturation. The thickness of the diaphragm will need to be sufficient to keep it rigid, so that the force applied at a point will result in widespread deflection. It is therefore assumed that the moving mass will be inversely proportional to the volume raised to the power of about 0.6 for a Knowles or Sonion type actuator, so that the resonant frequency scales as shown in Figure B.2. Using this scaling for the 2.11 mg mass calculated by Sun and Hu matches

reasonably closely the mass calculated from the size of the actuator and diaphragm in Figure 8.4. The value assumed for the mechanical mass is 2.4 mg, which is an acoustic inertance of 104 kPa/m³ for a diaphragm area of 4.8 mm².

$$\begin{aligned}
\text{Stiffness, } k &= m\omega_{\text{res}}^2 = 2.4 \times 10^{-6} \times (2 \times \pi \times 5 \times 10^3)^2 = 12.6 \text{ kN/m} && \text{(B.17)}\\
&= \frac{12.6 \times 10^3}{(4.8 \times 10^{-6})^2} = 547 \text{ TPa/m}^3 \text{ for a } 4.8 \text{ mm}^2 \text{ diaphragm.} && \text{(B.18)}\\
Z_{\text{acoustic}} &= 104 \times 10^3 i\omega - 547 \times 10^{12} i/\omega \ \Omega && \text{(B.19)}\\
&= 0.1i - 569i \simeq -548i \text{ G}\Omega \text{ at 159 Hz} && \text{(B.20)}
\end{aligned}$$

B.5 Calculation of the Internal Impedance of the Actuator

$$\begin{aligned}
Z_{\text{internal}} &= Z_{\text{acoustic}} - \frac{T_1 T_2}{Z_{\text{electrical}}} && \text{(B.21)}\\
T_2 = -T_1 &= 1.875\text{e}6 && \text{(B.22)}\\
Z_{\text{internal}} &= Z_{\text{acoustic}} - \frac{T_1 T_2}{Z_{\text{electrical}}} && \text{(B.23)}\\
Z_{electrical} &= 45 + 1.38 \times 10^{-3} i\omega \ \Omega, \text{ from Equation B.7}\\
Z_{\text{internal}} &= 104 \times 10^3 i\omega - 547 \times 10^{12} i/\omega + \frac{(1.875\text{e}6)^2}{45 + 1.38 \times 10^{-3} i\omega} \text{ G}\Omega && \text{(B.24)}\\
&= 78 - 550i \text{ G}\Omega \text{ at 159 Hz, and} && \text{(B.25)}\\
&= 75 - 563i \text{ G}\Omega \text{ at 980 Hz.} && \text{(B.26)}
\end{aligned}$$

The maximum cochlear input impedance magnitude at the actuator calculated by the present distributed model is 151 G acoustic ohms at 159 Hz.

Appendix C

The Health Effects of a Magnetic Field from a Scalp-Mounted Coil

Table A1 of Directive 2013/35/EU of the European Parliament and of the Council of 26 June 2013 requires that static magnetic fields (from 0 to 1 Hz) are limited to 2 T, to avoid sensory effects. (There is a greater limit of 8 T to avoid health effects that applies in controlled conditions.) The Action Levels in Table B2 for alternating magnetic fields are frequency dependent, but the lowest limit within the audio frequency range is 100μ T. The assumed field from the permanent magnet is 1 T, which is within the limit for a static magnetic field. With 307 AT in the coil, the magnetic flux density at the centre of the coil $(z = 0)$, where it is greatest would be:

$$B_{\text{coil}} = \mu_0 H = \frac{\mu_0 N I a^2}{2(z^2 a^2)^{\frac{3}{2}}} = \frac{4\pi \times 10^{-7} \times 307 \times a^2}{2(0 + a^2)^{\frac{3}{2}}} = \frac{4\pi \times 10^{-7} \times 307}{2a} \quad \text{(C.1)}$$

$$= \frac{4\pi \times 10^{-7} \times 307}{2 \times 10 \times 10^{-3}} \simeq 19 \text{ mT} \quad \text{(C.2)}$$

This greatly exceeds the Action Levels of 100 - 1000 μT for the audio frequency range. However, these Action levels apply to whole body exposure, and they are intended as a simplified way of specifying large scale magnetic fields, such as that from an electric generator. For small scale fields the Directive requires more precise calculations or measurements of the electric field induced by the magnetic field, to ensure that the Exposure Limit Values specified in Tables A2 and A3 of the Directive are not exceeded.

The Exposure Limit Value to avoid sensory effects for electric fields in Table A3 of the Directive is $2 \times 10^{-3} f$ Vm^{-1} between 25 Hz and 400 Hz. Above that frequency, the ELV to avoid health effects is stricter, and it is $0.27 \times 10^{-3} f$ Vm^{-1} from 1.64 kHz to 10 MHz. Between 400 Hz and 1.64 kHz, the ***E / f*** limit tapers. In all cases, the maximum electric field calculated here is less than the Exposure Limit Value stipulated in the

Directive. The Exposure Limit Values for electric fields in the Directive are specified as peak values, whereas those used in this document are RMS values throughout; in transcribing the values from the Directive, they have been adjusted to RMS values for sinusoidal waveforms.

The electric field, **E** is related to the magnetic vector potential, **A** by the equation:

$$\begin{aligned} \mathbf{E} &= -\frac{\mathrm{d}\mathbf{A}}{\mathrm{dt}} - \mathbf{grad}V \text{ (BandB eqn 6.6)} \\ &\text{In the absence of significant electrostatic charges,} \\ \mathbf{grad}V &= 0, \text{and so} \\ \mathbf{E} &= -\frac{\mathrm{d}\mathbf{A}}{\mathrm{dt}} \end{aligned}$$

Assuming a coil with a single turn, **A** is a function of the current in the coil, given by the equation:

$$\begin{aligned} \mathbf{A} &= \frac{\mu I}{4\pi}\int\frac{\mathbf{ds}}{r} \text{(Bleaney and Bleaney (1965) eqn 5.49), where} \\ \mu &= \text{magnetic permeability at the point of measurement} = \mu_r\mu_0 \\ I &= \text{current in the coil} \\ \mathbf{ds} &= \text{a vector element of the coil carrying current} \\ r &= \text{distance between the current carrying element and the measurement point.} \end{aligned}$$

By symmetry, **A** will be independent of the angle, Φ subtended at the centre of the coil, between the point of measurement and the x axis. For simplicity, the point of measurement is chosen to be vertically above the x axis, so that its y co-ordinate is zero.

Calculation of **A** on the surface of the coil is difficult, because the current density distribution within the wire then needs to be considered, rather than considering the current to be concentrated in a filament of negligible radius. To keep the calcuation as simple as possible, a point of measurement is chosen to be a distance of 1 mm above the coil, which is one tenth of the radius of the coil, and which is assumed to be much greater than the diameter of the wire. 1 mm is a reasonable estimate of the thickness of the encapsulation that would separate the coil from human tissue. The x, y and z co-ordinates of the point of measurement are a, 0 and $0.1a$, respectively, where a is the radius of the coil.

Because the current lies only in the plane where $z = 0, \mathbf{ds}_z = 0,$ and$A_z = 0.A_x$ is given by the equation from Bleaney and Bleaney:

$$\begin{aligned} A_x &= \frac{\mu I}{4\pi}\int_0^{2\pi}\frac{-a\sin\phi\mathbf{d}\varphi}{r(\varphi)} \\ &= \frac{\mu I}{4\pi}\left[\int_0^{\pi}\frac{-a\sin\varphi\mathbf{d}\varphi}{r(\varphi)}+\int_0^{\pi}\frac{-a\sin(-\varphi)\mathbf{d}\varphi}{r(-\varphi)}\right] \\ \text{By inspection, } r(-\varphi) &= r(\varphi), \text{and} \\ \sin(-\varphi) &= -\sin(\varphi), \text{andso} \\ A_x &= 0 \end{aligned}$$

The equation for A_y given by Bleaney and Bleaney (1965) is:

$$\begin{aligned} A_y &= \frac{\mu I}{4\pi}\int_0^{2\pi}\frac{a\cos\varphi\mathbf{d}\varphi}{r(\varphi)} \\ r(\varphi) &= \sqrt{a^2+z^2-2az\cos\varphi}, \text{ if } z = 0.1a, \\ \text{then } r(\varphi) &= \sqrt{1.01a^2-0.2a^2\cos\varphi} \\ &= a\sqrt{1.01}\sqrt{1-0.2\cos\varphi/1.01} \\ &\simeq 1.005a\sqrt{1-0.198\cos\varphi} \\ A_y &\simeq \frac{\mu I}{4.02\pi}\int_0^{2\pi}\frac{\cos\varphi\mathbf{d}\varphi}{\sqrt{1-0.198\cos\varphi}} \\ (1+x)^n &= \sum_{k=0}^{\infty}\binom{n}{k}x^k \\ &= \sum_{k=0}^{\infty}\left(\frac{n!}{k!(n-k)!}\right)x^k = \sum_{k=0}^{\infty}\left(\frac{n^n\left(\frac{1}{n}n\right)!}{n^{(n-k)}\left(\frac{1}{n}n-\frac{1}{n}k\right)!}\right)\frac{x^k}{k!} \\ &= \sum_{k=0}^{\infty}\left(\frac{\left(\frac{-1}{n}k-1\right)!(-1)^k}{\left(\frac{-1}{n}\right)^{(2k-1)}(k-1)!}\right)\frac{x^k}{k!} \\ \text{If } n &= -\frac{1}{2}; \frac{-1}{n} = 2 \\ (1+x)^{-\frac{1}{2}} &= 1+\sum_{k=1}^{\infty}\frac{(2k-1)!(-1)^k x^k}{2^{(2k-1)}(k-1)!k!} \quad = 1-\frac{x}{2}+\frac{3x^2}{8}-\frac{5x^3}{16}+\frac{35x^4}{128}-\cdots \\ (1-x)^{-\frac{1}{2}} &= 1+\sum_{k=1}^{\infty}\frac{(2k-1)!x^k}{2^{(2k-1)}(k-1)!k!} \quad = 1+\frac{x}{2}+\frac{3x^2}{8}+\frac{5x^3}{16}+\frac{35x^4}{128}+\cdots \\ \text{If } x &= 0.198\cos\varphi \\ A_y &\simeq \frac{\mu I}{4.02\pi}\int_0^{2\pi}\left(1+\sum_{k=1}^{\infty}\frac{(2k-1)!(0.198\cos\varphi)^k}{2^{(2k-1)}(k-1)!k!}\right)\cos\varphi\mathbf{d}\varphi \\ &\simeq \frac{\mu I}{4.02\pi}\int_0^{2\pi}\cos\varphi\mathbf{d}\varphi+\frac{\mu I}{4.02\pi}\int_0^{2\pi}\sum_{k=1}^{\infty}\frac{(2k-1)!(0.198\cos\varphi)^k}{2^{(2k-1)}(k-1)!k!}\cos\varphi\mathbf{d}\varphi \end{aligned}$$

$$\frac{\mu I}{4.02\pi}\int_0^{2\pi}\cos\varphi\mathbf{d}\varphi = [\sin\varphi]_0^{2\pi} = 0$$

$$A_y \simeq \frac{\mu I}{4.02\pi}\int_0^{2\pi}\sum_{k=1}^{\infty}\frac{(2k-1)!(0.198\cos\varphi)^{k+1}}{2^{(2k-1)}(k-1)!k!}\mathbf{d}\varphi$$

$$A_y \simeq \frac{\mu I}{4.02\pi}\int_0^{2\pi}\sum_{k=1}^{\infty}\frac{(2k-1)!0.198^{k+1}\cos^{k+1}\varphi}{2^{(2k-1)}(k-1)!k!}\mathbf{d}\varphi$$

$$= \frac{\mu I}{4.02\pi}\sum_{k=1}^{\infty}\frac{(2k-1)!0.198^{k+1}}{2^{(2k-1)}(k-1)!k!}\int_0^{2\pi}\cos^{k+1}\varphi\mathbf{d}\varphi$$

$$\int_0^{2\pi}\cos^{k+1}\varphi\mathbf{d}\varphi = \left[\frac{1}{k+1}\cos^k\varphi\sin\varphi\right]_0^{2\pi} + \frac{k}{k+1}\int_0^{2\pi}\cos^{k-1}\varphi\mathbf{d}\varphi$$

$$\left[\frac{1}{k+1}\cos^k\varphi\sin\varphi\right]_0^{2\pi} = 0$$

$$\int_0^{2\pi}\cos^{k+1}\varphi\mathbf{d}\varphi = \frac{k}{k+1}\int_0^{2\pi}\cos^{k-1}\varphi\mathbf{d}\varphi;$$

When $k+1$ is even:

$$\int_0^{2\pi}\cos^{2k}\varphi\mathbf{d}\varphi = \eta(k)\int_0^{2\pi}\mathbf{d}\varphi = 2\pi\eta(k),$$

where $\eta(k)$ is a function of only k.

When $k+1$is odd :

$$\int_0^{2\pi}\cos^{2k+1}\varphi\mathbf{d}\varphi = \eta(k)\int_0^{2\pi}\cos\varphi\mathbf{d}\varphi$$

$$= [\eta(k)\sin\varphi]_0^{2\pi} = 0;$$

and so all odd powers of $\cos\varphi$ integrate to zero over the interval 0 to 2π.

$$\sum_{k=1}^{\infty}\int_0^{2\pi}\cos^{k+1}\varphi\mathbf{d}\varphi = \sum_{k=1}^{\infty}\int_0^{2\pi}\cos^{2k}\varphi\mathbf{d}\varphi + \sum_{k=1}^{\infty}\int_0^{2\pi}\cos^{2k+1}\varphi\mathbf{d}\varphi$$

$$\int_0^{2\pi}\cos^{2k+1}\varphi\mathbf{d}\varphi = 0$$

$$\sum_{k=1}^{\infty}\int_0^{2\pi}\cos^{k+1}\varphi\mathbf{d}\varphi = \sum_{k=1}^{\infty}\int_0^{2\pi}\cos^{2k}\varphi\mathbf{d}\varphi$$

$$\int_0^{2\pi}\cos^{2k}\varphi\mathbf{d}\varphi = \left[\frac{(2k)!\varphi}{2^{2k}(k!)^2}\right]_0^{2\pi} = \frac{2\pi(2k)!}{2^{2k}(k!)^2}$$

$$\sum_{k=1}^{\infty}\int_0^{2\pi}\cos^{k+1}\varphi\mathbf{d}\varphi = \sum_{k=1}^{\infty}\frac{2\pi(2k)!}{2^{2k}(k!)^2}$$

$$A_y = \frac{\mu I}{4.02\pi}\sum_{k=1}^{\infty}\frac{2\pi(2k-1)!0.198^{k+1}}{2^{(2k-1)}(k-1)!k!}\frac{(2k)!}{2^{2k}(k!)^2}$$

$$= \frac{2\pi\mu I}{2.01}\sum_{k=1}^{\infty}\frac{(2k)!(2k-1)!0.198^{k+1}}{2^{(4k-1)}(k!)^3(k-1)!}$$

$$= \frac{2\pi\mu I}{2.01}\sum_{k=1}^{\infty}\frac{((2k)!)^20.198^{k+1}}{2^{4k}(k!)^4}$$

$$
\begin{aligned}
\mathbf{E}_y = -\frac{\mathrm{d}\mathbf{A}}{\mathrm{dt}} &= -\omega A_y \text{for a sinusoidal wave-form, where} \\
\omega &= \text{the angular frequency in rad/s.} \\
&= -\frac{2\pi\omega\mu I}{2.01}\sum_{k=1}^{\infty}\frac{((2k)!)^2 0.198^{k+1}}{2^{4k}(k!)^4} \\
&= -\frac{2\pi\omega\mu I}{2.01}(0.0495 + 0.005513 + 0.000758 + 0.000115 + \ldots) \\
&\simeq -\frac{2\pi\omega\mu I}{2.01} \times 0.05598, \\
&\simeq -\pi\omega\mu N I 2.01 \times 0.05598, \text{ for a multi-turn coil.} \\
\text{where } N &= \text{the number of turns.} \\
NI &\simeq 307 \text{ AT} \\
&\simeq -2\pi f \times 4 \times 10^{-6} \times 307 \times 0.056, \text{assuming that } \mu = 4\pi \times 10^{-7} \text{ then} \\
\mathbf{E} &\simeq 123 f\mu \text{ V/m, where f is the frequency in Hz.}
\end{aligned}
$$

The lowest Exposure Limit Value in the European Parliament Directive 2013/35/EU is $2800f$ μV/m for sensory effects, and $380f$ μV/m for health effects, at frequencies within the audio range. When the current in the coil is at its maximum, the greatest electric field induced in the tissues of the head will be less than the Exposure Limit Values.

Appendix D

Calculation of Encapsulated Bubble Impedance

It is assumed that the diaphragm is composed of a number of adjacent strips, or beams, of silicone rubber arranged with their length across the cochlea, each with a width, Δ, of one element, and of the same length as the width of the BM, B. The thickness of the beam, t is that of the diaphragm. Each beam is assumed to act independently of its neighbours; that is, there is no longitudinal mechanical coupling between the elements of the diaphragm, and so the assembly of beams behaves similarly to the basilar membrane, which has little mechanical coupling along the length of the cochlea.

For a uniformly loaded, uniform beam of length, B, width, Δ, second moment of area, I and Young's Modulus, E, the deflection, y, at position z is related to the force per unit length, q, by the following equation:

$$y = \frac{qz^2(B-z)^2}{24EI} \tag{D.1}$$

$$y_{Average} = \frac{q}{24EIB}\int_0^B z^2(B-z)^2 \mathrm{d}z \tag{D.2}$$

$$= \frac{q}{24EIB}\int_0^B (z^2B^2 - 2z^3B + z^4)\mathrm{d}z \tag{D.3}$$

$$= \frac{q}{24EIB}(\frac{B^5}{3} - \frac{B^5}{2} + \frac{B^5}{5}) \tag{D.4}$$

$$= \frac{q}{720EI}B^4 \tag{D.5}$$

The pressure, p, acting on the beam will be related to the force per unit length and hence to the average deflection by the following formulae:

$$p = \frac{q}{\Delta} \tag{D.6}$$

$$y_{Average} = \frac{pB^4\Delta}{720EI} \tag{D.7}$$

The average stiffness, s_{beam} of the beam is a component of the impedance of an equivalent piston, and it is calculated by using the following formulae:

$$s_{beam} = \frac{p}{y_{Average}} \tag{D.8}$$

$$= \frac{720EI}{B^4\Delta} \tag{D.9}$$

The second moment of area of the beam, I, about its neutral axis is given in terms of its thickness,t and its length, B by:

$$I = \frac{t^3\Delta}{12} \tag{D.10}$$

$$s_b = \frac{720Et^3\Delta}{12B^4\Delta} = \frac{60Et^3}{B^4} \tag{D.11}$$

The gas within the bubble will contribute additional stiffness by increasing pressure on the opposite side of the beam as the deflection increases. The bubble is modelled as a series of similar, independent, cuboid elemental volumes, V, of depth, d, parallel with the deflection, width along the cochlea, Δ, and length across the cochlea, B, with each beam acting as a rigid sliding piston, with no mechanical coupling to its neighbours. The total stiffness, s, the additional stiffness due to the gas, s_g, gas pressure, p_g, average deflection and acoustic impedance $\rho_0 c_0$ are related by the following equations:

$$s_g = \frac{-\mathrm{d}p_g}{\mathrm{d}y_{Average}} \tag{D.12}$$

$$= -B\Delta\frac{\mathrm{d}p_g}{\mathrm{d}V} = -B\Delta\frac{\mathrm{d}p_g}{\mathrm{d}\rho_g}\frac{\mathrm{d}\rho_g}{\mathrm{d}V} \tag{D.13}$$

$$\frac{dp_g}{d\rho_g} = {c_0}^2\,(\text{gas}) \tag{D.14}$$

$$s_g = -B\Delta{c_0}^2\,(\text{gas})\frac{\mathrm{d}}{\mathrm{d}V}\left(\frac{m}{V}\right) \tag{D.15}$$

$$= B\Delta{c_0}^2\,(\text{gas})\frac{m}{V^2} = \frac{\rho_g{c_0}^2\,(\text{gas})}{d} \tag{D.16}$$

$$\text{Bubble stiffness, } s_b = s_{beam} + s_g = \frac{60Et^3}{B^4} + \frac{\rho_g{c_0}^2\,(\text{gas})}{d} \tag{D.17}$$

The mass of the beam, M_{beam} can be calculated from its thickness, t, and its density, ρ_{beam}:

$$m_{beam} = \rho_{beam} t B \Delta \tag{D.18}$$

$$\text{Mass per unit area, } m_{beam} = \frac{M_{beam}}{B\Delta} \tag{D.19}$$

$$= \rho_{beam} t \tag{D.20}$$

The damping term of the impedance, r, can be determined from the value of mechanical $\tan\delta$ given in the published data-sheet for the silicone rubber, via the resonance quality factor, Q.

$$r_{beam} = \frac{1}{Q}\sqrt{s_{beam} m_{beam}} \tag{D.21}$$

$$= \tan\delta \sqrt{s_{beam} m_{beam}} \tag{D.22}$$

$$= \tan\delta \sqrt{\frac{720EI}{B^4\Delta}\rho_{beam} t} \tag{D.23}$$

$$= \tan\delta \sqrt{\frac{60Et^4}{B^4}\rho_{beam}} \tag{D.24}$$

$$= \tan\delta \frac{t^2}{B^2}\sqrt{60E\rho_{beam}} \tag{D.25}$$

Assuming that the acoustic compression of the gas in the bubble is adiabatic, there will be no damping from it. As long as the damping is the minor term of the impedance of the bubble, it will not be important to match its damping to that of the round window. Similarly, the mass of both the bubble and the round window can be neglected for frequencies below the resonances of both. The significant challenge is to match, as nearly as necessary, the combined stiffness of the bubble and the silicone rubber membrane that separates it from the cochlear fluid to that of the round window.

The constants of the silicone rubber that composes each 'beam' and hence the diaphragm have been obtained from "Materials and Coatings for Medical Devices: Cardiovascular" published by ASM international (2009), and they are general for a number of different types of Silicone Rubber, including Silastic MDX-4-4210, which is commonly used in the manufacture of cochlear implants. They are as shown in D.1.

The stiffness, resistance and inertance values calculated above are linear values that relate linear displacement, velocity and acceleration to pressure. They are converted to the corresponding volume values by dividing by the area of the bubble's diaphragm, $B \times L_b$, where L_b is the total length of the bubble. The formulae for these volume

values are:

$$K_b = \frac{60Et^3}{L_b B^5} + \frac{\rho_g {c_0}^2 \text{ (gas)}}{B \times L_b \times d} \tag{D.26}$$

$$R_b = \tan\delta \frac{t^2}{L_b B^3} \sqrt{60E\rho_{beam}} \tag{D.27}$$

$$M_b = \frac{\rho_{beam} t}{L_b B} \tag{D.28}$$

TABLE D.1: Table of properties of bubble materials (Silastic MDX-4-4210 and air)

Property	**Symbol**	**Value Range**	**Value Assumed**	**Unit**
Tensile strength		6.03-10		MPa
Bulk modulus		1.5-2		GPa
Young's modulus	E	0.003-0.03	0.01	GPa
Shear modulus		0.0003-0.02		GPa
Flexural strength (modulus of rupture)		3.73-3.9	3.73	MPa
Elongation		388-961		%
Mechanical loss coefficient	$\tan\delta$	0.517-1.22	0.868	
Poisson's ratio		0.47-0.49	0.48	
Yield strength (elastic limit)		3.73-3.9	3.73	MPa
Fatigue strength at 10^7 cycles		3.55-3.71		MPa
Fracture toughness		0.157-0.277		MPa/m$^{0.5}$
Flexural modulus		0.003-0.03		GPa
Velocity of sound in air	c_0		353	m/s

To complete the calculations of the acoustic properties to give numeric values, it is necessary to assume values for the geometric dimensions of the bubble. The thickness, t of the beam needs to be as thin as possible, while being strong enough to resist without permanent deformation from the rigours of insertion of the implant. The value assumed is 8μm. The assumed maximum achievable length, L_b, width, B and depth t are 15, 0.32 and 0.32 mm, respectively, and so the stiffness, resistance and inertance of the bubble, K_b, R_b and M_b respectively, are calculated as follows, using the

relevant values from the table above:

$$K_b = \frac{60 \times 0.01 \times 10^9 \times (8 \times 10^{-6})^3}{15 \times 10^{-3}(0.32 \times 10^{-3})^5} + \frac{1.2 \times 353^2}{15 \times 0.32 \times 0.32 \times 10^{-9}}$$
$$= 1.03 \times 10^{14} \text{ Pa/m}^3 \quad \text{(D.29)}$$
$$R_b = 0.8685 \frac{(8 \times 10^{-6})^2}{15 \times 10^{-3} \times (0.32 \times 10^{-3})^3} \sqrt{0.6 \times 10^9 \times 1110}$$
$$= 9.23 \times 10^7 \text{ Pa.s/m}^3 \quad \text{(D.30)}$$
$$M_b = \frac{1110 \times 8 \times 10^{-6}}{15 \times 10^{-3} \times 0.32 \times 10^{-3}} = 1.85 \times 10^3 \text{ kg/m}^4 \quad \text{(D.31)}$$

These values are entered into Table 5.1 and the Impedances.txt file, which is read by the model's Matlab script and used as input variables.

Appendix E

Calculations for a Longitudinally Constrained Dome Actuator

This Appendix contains the mathematical calculations of the transformation factor (transverse displacement / longitudinal elongation) that can be achieved without excessive distortion, by using a longitudinally constrained dome.

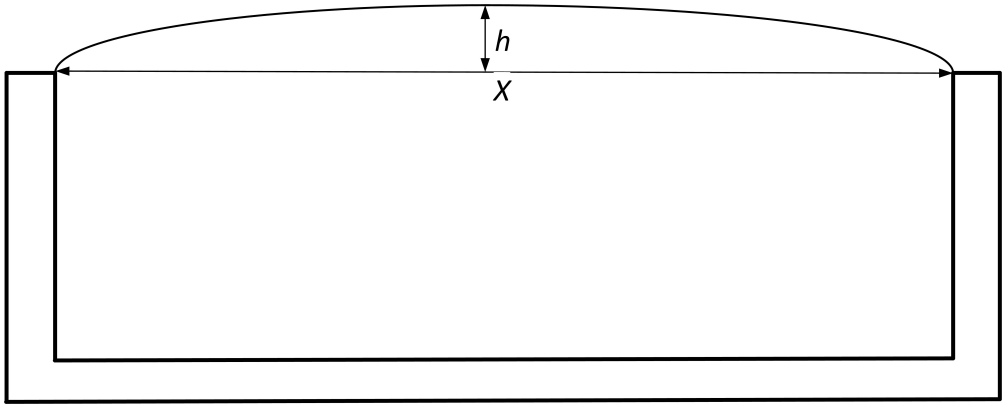

FIGURE E.1: Axially Constrained Polymer Piezoelectric Membrane Actuator

$$
\begin{aligned}
\text{Bending Moment, BM} &= -2Fy = EIk, \text{where :} \\
F &= \text{horizontal force applied along the beam} \\
E &= \text{Youngs Modulus} \\
I &= \text{Second Moment of Area} \\
k &= \text{Curvature} = (\text{radius of curvature})^{-1} \\
k &= \frac{y''}{(1+y'^2)^{\frac{3}{2}}} \\
\text{If } y' \ll 1, \text{ then } k &\simeq y'' \\
-2Fy &\simeq EIy'' \\
y'' &\simeq \frac{-2F}{EI}y \\
y &= a\sin cx + b\cos cx \\
y' &= ac\cos cx - bc\sin cx \\
y'' &= -ac^2\sin cx - bc^2\cos cx
\end{aligned}
$$

$$
\begin{aligned}
\text{Boundary conditions: } y &= 0, \text{ when} \\
x &= 0 \text{ and} \\
x &= X, \text{ axial distance between constraints} \\
cX &= \pi \\
b &= 0 \\
\frac{y''}{y} &= -c^2 = \frac{-2F}{EI} \\
c &= \sqrt{\frac{2F}{EI}} = \frac{\pi}{X} \\
\frac{2F}{EI} &= \frac{\pi^2}{X^2} \\
y &= h, \text{ when } x = X/2 \text{ and} cx = \pi/2, \text{ where :} \\
h &= \text{greatest height of membrane.} \\
h &= a\sin\frac{\pi}{2} \\
a &= h \\
y &= h\sin\left(\frac{\pi x}{X}\right) \\
y' &\simeq \frac{h\pi}{X}\cos\left(\frac{\pi x}{X}\right) \\
y'' &\simeq -\frac{h\pi^2}{X^2}\sin\left(\frac{\pi x}{X}\right) \\
\text{Membrane length, } L &= \int_0^X \sqrt{1+y'^2}dx \\
&= \int_0^X \sqrt{1+\frac{h^2\pi^2}{X^2}\cos^2\left(\frac{\pi x}{X}\right)}dx.
\end{aligned}
$$

Expanding with the binomial series:

$$\begin{aligned}
\sqrt{1+z^2} &= 1+\frac{1}{2}z-\frac{1}{8}z^2+\frac{1}{16}z^3-\frac{5}{128}z^4\dots \\
\sqrt{1+\frac{h^2\pi^2}{X^2}\cos^2\left(\frac{\pi x}{X}\right)} &= 1+\frac{h^2\pi^2}{2X^2}\cos^2\left(\frac{\pi x}{X}\right)-\frac{h^4\pi^4}{8X^4}\cos^4\left(\frac{\pi x}{X}\right) \\
&+ \frac{h^6\pi^6}{16X^6}\cos^6\left(\frac{\pi x}{X}\right)\dots \\
&= \sum_{m=0}^{\infty}\frac{(2m)!}{(-4)^m(m!)^2(1-2m)}\frac{h^{2m}\pi^{2m}}{X^{2m}}\cos^{2m}\left(\frac{\pi x}{X}\right) \\
L &= \int_0^X\left(\sum_{m=0}^{\infty}\frac{(2m)!}{(-4)^m(m!)^2(1-2m)}\frac{h^{2m}\pi^{2m}}{X^{2m}}\cos^{2m}\left(\frac{\pi x}{X}\right)\right)dx \\
L &= \sum_{m=0}^{\infty}\left(\frac{(2m)!}{(-4)^m(m!)^2(1-2m)}\frac{h^{2m}\pi^{2m}}{X^{2m}}\int_0^X\cos^{2m}\left(\frac{\pi x}{X}\right)dx\right) \\
\int\cos^{2m}\left(\frac{\pi x}{X}\right)dx &= \frac{X}{\pi}\sin\left(\frac{\pi x}{X}\right)\sum_{r=0}^{m-1}\frac{(2m)!(r!)^2}{2^{2m-2r}(2r+1)!(m!)^2}\cos^{2r+1}\left(\frac{\pi x}{X}\right) \\
&+ \frac{(2m)!}{2^{2m}(m!)^2}x \\
\int_0^X\cos^{2m}\left(\frac{\pi x}{X}\right)dx &= \frac{X}{\pi}\sin\pi\sum_{r=0}^{m-1}\frac{(2m)!(r!)^2}{2^{2m-2r}(2r+1)!(m!)^2}\cos^{2r+1}\pi \\
&+ \frac{(2m)!}{2^{2m}(m!)^2}X \\
&- \frac{X}{\pi}\sin 0\sum_{r=0}^{m-1}\frac{(2m)!(r!)^2}{2^{2m-2r}(2r+1)!(m!)^2}\cos^{2r+1}0+\frac{(2m)!}{2^{2m}(m!)^2}0 \\
&= \frac{X}{\pi}0\sum_{r=0}^{m-1}\frac{(2m)!(r!)^2}{2^{2m-2r}(2r+1)!(m!)^2}\cos^{2r+1}\pi+\frac{(2m)!}{2^{2m}(m!)^2}X \\
&= \frac{(2m)!}{2^{2m}(m!)^2}X
\end{aligned}$$

$$
\begin{aligned}
L &= \sum_{m=0}^{\infty}\left(\frac{(2m)!}{(-4)^m(m!)^2(1-2m)}\frac{h^{2m}\pi^{2m}}{X^{2m}}\frac{(2m)!}{2^{2m}(m!)^2}X\right)\\
L &= X\sum_{m=0}^{\infty}\left(\frac{(-1)^m}{(1-2m)}\left(\frac{h^m\pi^m}{X^m}\frac{(2m)!}{4^m(m!)^2}\right)^2\right)\\
&= X\left(1+\frac{1}{2}\frac{\pi^2h^2}{X^2}-\frac{1}{8}\frac{\pi^4h^4}{X^4}+\frac{1}{16}\frac{\pi^6h^6}{X^6}\ldots\right)\\
L+\Delta L &= X\sum_{m=0}^{\infty}\left(\frac{(-1)^m}{(1-2m)}\left(\frac{(h+\Delta h)^m\pi^m}{X^m}\frac{(2m)!}{4^m(m!)^2}\right)^2\right)\\
&= X\left(1+\frac{\pi^2(h+\Delta h)^2}{2X^2}-\frac{\pi^4(h+\Delta h)^4}{8X^4}+\frac{\pi^6(h+\Delta h)^6}{16X^6}\right.\\
&\quad\left.\ldots\right)\\
\text{If } \Delta h &<< h,\\
\Delta L &\simeq X\left(1+\frac{1}{2}\frac{\pi^2(h^2+2h\Delta h+(\Delta h)^2)}{X^2}-1-\frac{1}{2}\frac{\pi^2h^2}{X^2}\right)\\
\Delta L &\simeq \left(\frac{1}{2}\frac{\pi^2(2h\Delta h+(\Delta h)^2)}{X}\right)\\
\frac{\Delta h}{\Delta L} &\simeq \frac{2X}{\pi^2(2h+\Delta h)}\simeq\frac{2X(2h-\Delta h)}{\pi^2(2h)^2}\text{. For <10\% non-linearity,}\\
\Delta h &< 0.2h\\
\text{For } X &= 15\text{ mm and } \Delta h = 3.8\ \mu\text{m, as in Table 7.2:}\\
h &> \frac{3.8\times10^{-6}}{0.2}=19\times10^{-6}\text{ m, and so}\\
\frac{\Delta h}{\Delta L} &\simeq \frac{X}{h\pi^2}\simeq\frac{15\times10^{-3}\text{m}}{19\times10^{-6}\text{m}}\simeq 780
\end{aligned}
$$

A transformation factor, $\frac{\Delta h}{\Delta L}$, of 780 should be achievable for this type of construction, without undue distortion of the sound. This would reduce the driving voltage required from 19,220 V to c. 25 V and the electric field from 64 MV/m to 82 kV/m. 25 V is acceptable within an implant, if rather higher than desirable. However, a voltage gradient of 82 kV/m will need to be contained within the implant and not allowed to enter the cochlear fluid. This should be possible by applying a thin insulating layer of, say, silicone rubber over the piezo membrane. This technology thus appears to be feasible.

Appendix F

Externally Excited Intracochlear Permanent Magnet Actuator

The magnetic air-gap pressure is the same as the energy per unit volume of the air-gap, which is:

$$
\begin{aligned}
p_{\mathrm{g}} &= \frac{1}{2}BH && \text{(F.1)}\\
\text{where} B &= \text{air-gap flux density (T).} \\
&= B_r + \mu_0\mu_r H, && \text{(F.2)}\\
\text{where} B_r &\text{ is the remanence of the permanent magnet, and} && \text{(F.3)}\\
H &\text{ is the magnetic field strength from the coil.} \\
p_{\mathrm{g}} &= \frac{1}{2}(B_r + \mu_0\mu_r H)H && \text{(F.4)}\\
&= \frac{1}{2}(B_r H + \mu_0\mu_r H^2) \\
&= \frac{H}{2}(B_r + \mu_0\mu_r H) \text{ but } B_r \gg \mu_0\mu_r H, \text{and so} \\
p_{\mathrm{g}} &\simeq \frac{1}{2}B_r H && \text{(F.5)}\\
& && \text{(F.6)}
\end{aligned}
$$

$$
\begin{aligned}
H &= \text{air-gap magnetic field (A/m) from the coil} \\
&= \frac{NIa^2}{2(z^2+a^2)^{\frac{3}{2}}}, \text{Bleaney and Bleaney's equation (5.54).} \\
\text{Where } a &= \text{the coil radius,} \\
z &= \text{the distance from the coil along the axis of symmetry, and} \qquad \text{(F.7)} \\
NI &= \text{the number of ampere turns in the coil} \qquad \text{(F.8)} \\
p_{\mathrm{g}} &\simeq \frac{B_r NIa^2}{4(z^2+a^2)^{\frac{3}{2}}} \qquad \text{(F.9)} \\
NI &\simeq -\frac{4p_{\mathrm{g}}(z^2+a^2)^{\frac{3}{2}}}{B_r a^2} \qquad \text{(F.10)}
\end{aligned}
$$

The magnetic force on the magnet will be the sum of the air-gap pressures at each end of the magnet $\simeq 2p_{\mathrm{g}}$, multiplied by its cross-sectional area. Assuming that the magnet lies between a low acoustic impedance cavity and the cochlea fluid, the pressure in the cochlear fluid would be the force on the magnet divided by its cross-sectional area ie $\simeq 2p_{\mathrm{g}}$. This means that the required air gap pressure would need to be half the required 0.8 kPa pressure in the cochlear fluid.

Substituting numbers from the second paragraph of Subsection 8.7.7 into equation (F.10):

$$
\begin{aligned}
NI &\simeq \frac{2 \times 0.91 \text{ kPa} \times \left(20^2 \times 10^{-6} \text{ m}^2 + 10^2 \times 10^{-6} \text{ m}^2\right)^{\frac{3}{2}}}{1\text{T}\,(10^2 \times 10^{-6} \text{ m}^2)} = \\
&\simeq \frac{1820 \times (500 \times 10^{-6})^{\frac{3}{2}} \text{Pa m}^3}{1 \times 10^{-4} \text{ T m}^2} = \frac{1820 \times 500^{1.5} \times 10^{-9} \text{ Pa m}^3}{1 \times 10^{-4} \text{T m}^2} = \frac{18.2 \times 5^{1.5} \text{Pa m}}{1\text{T}} \\
&\simeq 200 \text{ AT}
\end{aligned}
$$

Although this number of ampere turns is much greater than that required by intracochlear moving coil and balanced armature devices, the room available outside the skull to accommodate a coil is much greater. The coil cross section at 1.5 A/mm² would give $A_c = 133\text{mm}^2$, which becomes 177 mm², or 13 × 13 mm, to allow for a 75% packing factor. This is large enough to merit investigating reduction, but within an order of magnitude of what may be considered to be reasonable. The effective length of a turn is $l_c = 24\pi \times 10^{-3} = 0.076$ m. For a coil of N turns:

$$
\begin{aligned}
R &= \frac{\rho N^2 l_c}{A_c} = 6.78 N^2 \mu\Omega, \text{ where } \rho \text{ is the resistivity of the wire.} \\
\text{The required emf, } E &= IR = \frac{(NI)}{N}\frac{\rho N^2 l_c}{A_c} = \frac{\rho N (NI) l_c}{A_c} \\
&= \frac{1.8 \times 10^{-8}\ \Omega\ \text{m} \times N \times 200\ \text{AT} \times 0.076\text{m}}{200 \times 10^{-6}\ \text{m}^2} \\
&= 1.2N\ \text{mV, or 12 V for 10,000 turns, which is reasonable.} \\
\text{The required power, } W &= \frac{\rho (NI)^2 l_c}{A_c}, \text{which is independent of } N. \\
&= \frac{1.8 \times 10^{-8}\ \Omega\ \text{m} \times 200\ \text{AT} \times 200\text{AT} \times 0.076\ \text{m}}{200 \times 10^{-6}\ \text{mm}^2} \\
&\simeq 200\ \text{mW.}
\end{aligned}
$$

References

Ryuichi Aibara, Joseph T Welsh, Sunil Puria, and Richard L Goode. Human middle-ear sound transfer function and cochlear input impedance. *Hearing research*, 152(1-2):100–109, 2001.

JB Allen. Two-dimensional cochlear fluid model: New results. *The Journal of the Acoustical Society of America*, 61(1):110–119, 1977.

Barry J Anson. The endolymphatic and perilymphatic aqueducts of the human ear: Developmental and adult anatomy of their parietes and contents in relation to otological surgery. *Acta Oto-Laryngologica*, 59(2-6):140–153, 1965.

Andrzej Bąkowski, Leszek Radziszewski, Vladimir Dekỳš, and Paweł Świetlik. Frequency analysis of urban traffic noise. In *2019 20th International Carpathian Control Conference (ICCC)*, pages 1–6. IEEE, 2019.

Johannes Baumgart. The hair bundle: Fluid-structure interaction in the inner ear. *PhD Thesis, der Technischen Universitat Dresden*, 2011.

Georg von Békésy. Contribution to theory of hearing. mode of vibration of the basilar membrane. *Phys. Zeits*, 29:793, 1928.

Georg von Békésy. On the measurement of the amplitude of vibration of the ossicles with a capacitive probe. *Akustishe Zeitschrift*, 6(1):16, 1941.

Georg von Békésy. Über die schwingungen der schneckentrennwand beim präparat und ohrenmodell. *Akust. Z.*, 7:173–186, 1942.

Georg von Békésy. The variation of phase along the basilar membrane with sinusoidal vibrations. *The Journal of the Acoustical Society of America*, 19(3):452–460, 1947.

Georg von Békésy. On the elasticity of the cochlear partition. *The Journal of the Acoustical Society of America*, 20(3):227–241, 1948.

Georg von Békésy. The vibration of the cochlear partition in anatomical preparations and in models of the inner ear. *The Journal of the Acoustical Society of America*, 21(3): 233–245, 1949.

Georg von Békésy. Direct observation of the vibrations of the cochlear partition under a microscope. *Acta oto-laryngologica*, 42(3):197–201, 1952.

Georg von Békésy and Ernest Glen Wever. *Experiments in hearing*. McGraw-Hill New York, 1960.

Leo Leroy Beranek. Acoustics. *American Institute of Physics for Acoustical Society of America: New York, NY*, 1987:285–324, 1954.

Leo Leroy Beranek and Tim Mellow. *Acoustics: sound fields and transducers*. Academic Press, 2012.

Betty Isabelle Bleaney and Brebis Bleaney. Electricity and magnetism, 1965.

Engbert de Boer. Auditory physics. physical principles in hearing theory. ii. *Physics Reports*, 105(3):141–226, 1984.

Engbert de Boer. Auditory physics. physical principles in hearing theory. iii. *Physics Reports*, 203(3):125–231, 1991.

Bruce P Bogert. Determination of the effects of dissipation in the cochlear partition by means of a network representing the basilar membrane. *The Journal of the Acoustical Society of America*, 23(2):151–154, 1951.

Andrew Causon, Carl Verschuur, and Tracey A Newman. Trends in cochlear implant complications: implications for improving long-term outcomes. *Otology & Neurotology*, 34(2):259–265, 2013.

Andrew Causon, Carl Verschuur, and Tracey A Newman. A retrospective analysis of the contribution of reported factors in cochlear implantation on hearing preservation outcomes. *Otology & Neurotology*, 36(7):1137–1145, 2015.

Jack D Clemis and Galdino E Valvassori. Recent radiographic and clinical observations on the vestibular aqueduct:(a preliminary report). *Otolaryngologic Clinics of North America*, 1(2):339–352, 1968.

Nigel P Cooper, Anna Vavakou, and Marcel van der Heijden. Vibration hotspots reveal longitudinal funneling of sound-evoked motion in the mammalian cochlea. *Nature communications*, 9(1):1–12, 2018.

Laura Dawes. 100 years of deaf education and audiology at the university of manchester, 2014.

Engbert de Boer. Auditory physics. physical principles in hearing theory. i. *Physics reports*, 62(2):87–174, 1980.

Anandhan Dhanasingh and Claude Jolly. An overview of cochlear implant electrode array designs. *Hearing research*, 356:93–103, 2017.

Wei Dong and Nigel P Cooper. An experimental study into the acousto-mechanical effects of invading the cochlea. *Journal of The Royal Society Interface*, 3(9):561–571, 2006.

Robert J Dooling and Stewart H Hulse. *The comparative psychology of audition: Perceiving complex sounds*. Psychology Press, 2014.

Jos Eggermont. Electrocochleography and recruitment. *Annals of Otology, Rhinology & Laryngology*, 86(2):138–149, 1977.

Stephen J Elliott and Guangjian Ni. An elemental approach to modelling the mechanics of the cochlea. *Hearing research*, 360:14–24, 2018.

Stephen J Elliott and Michele Zilletti. Scaling of electromagnetic transducers for shunt damping and energy harvesting. *Journal of sound and vibration*, 333(8):2185–2195, 2014.

Stephen J Elliott, Ben Lineton, and Guangjian Ni. Fluid coupling in a discrete model of cochlear mechanics. *The Journal of the Acoustical Society of America*, 130(3):1441–1451, 2011.

Stephen J Elliott, Guangjian Ni, and Carl A Verschuur. Modelling the effect of round window stiffness on residual hearing after cochlear implantation. *Hearing Research*, 341:155–167, 2016.

Julius Richard Ewald. *Eine neue Hörtheorie*. E. Strauss, 1899.

Megan J Foggia, Rene Vielman Quevedo, and Marlan R Hansen. Intracochlear fibrosis and the foreign body response to cochlear implant biomaterials. *Laryngoscope investigative otolaryngology*, 4(6):678–683, 2019.

Darcy L Frear, Xiying Guan, Christof Stieger, John J Rosowski, and Hideko Heidi Nakajima. Impedances of the inner and middle ear estimated from intracochlear sound pressures in normal human temporal bones. *Hearing research*, 367:17–31, 2018.

C Daniel Geisler and Allyn E Hubbard. New boundary conditions and results for the peterson-bogert model of the cochlea. *The Journal of the Acoustical Society of America*, 52(6B):1629–1634, 1972.

René H Gifford, Timothy J Davis, Linsey W Sunderhaus, Christine Menapace, Barbara Buck, Jillian Crosson, Lori O'Neill, Anne Beiter, and Phil Segel. Combined electric and acoustic stimulation (eas) with hearing preservation: effect of cochlear implant low-frequency cutoff on speech understanding and perceived listening difficulty. *Ear and hearing*, 38(5):539, 2017.

Quinton Gopen, John J Rosowski, and Saumil N Merchant. Anatomy of the normal human cochlear aqueduct with functional implications. *Hearing research*, 107(1-2): 9–22, 1997.

Donald D Greenwood. Critical bandwidth and the frequency coordinates of the basilar membrane. *The Journal of the Acoustical Society of America*, 33(10):1344–1356, 1961.

Donald D Greenwood. A cochlear frequency-position function for several species—29 years later. *The Journal of the Acoustical Society of America*, 87(6):2592–2605, 1990.

Wolfgang K Gstoettner, Paul Van de Heyning, Alec Fitzgerald O'Connor, Constantino Morera, Manuel Sainz, Katrien Vermeire, Sonelle McDonald, Laura Cavalle, Silke Helbig, Juan Garcia Valdecasas, et al. Electric acoustic stimulation of the auditory system: results of a multi-centre investigation. *Acta oto-laryngologica*, 128(9):968–975, 2008.

Hermann von Helmholtz. *On the Sensations of Tone as a Physiological Basis for the Theory of Music*. Longmans, Green, 1885.

Hermann von Helmholtz and Hermann Ludwig Ferdinand von Helmholtz. *Die Lehre von den Tonempfindungen als physiologische Grundlage für die Theorie der Musik*. Vieweg, 1877.

Allyn E Hubbard and C Daniel Geisler. A hybrid-computer model of the cochlear partition. *The Journal of the Acoustical Society of America*, 51(6B):1895–1903, 1972.

Allyn E Hubbard and David C Mountain. Analysis and synthesis of cochlear mechanical function using models. In *Auditory Computation*, pages 62–120. Springer, 1996.

Marina Imsiecke, Benjamin Krüger, Andreas Büchner, Thomas Lenarz, and Waldo Nogueira. Interaction between electric and acoustic stimulation influences speech perception in ipsilateral eas users. *Ear and hearing*, 41(4):868, 2020.

Jan Kiefer, Marcel Pok, Oliver Adunka, Ekkehard Stürzebecher, Wolfgang Baumgartner, Marcus Schmidt, Jochen Tillein, Qing Ye, and Wolfgang Gstoettner. Combined electric and acoustic stimulation of the auditory system: results of a clinical study. *Audiology and Neurotology*, 10(3):134–144, 2005.

Lawrence E Kinsler, Austin R Frey, Alan B Coppens, and James V Sanders. *Fundamentals of acoustics*. John wiley & sons, 2000.

Jonathan C Kopelovich, Lina AJ Reiss, Christine P Etler, Linjing Xu, J Tyler Bertroche, Bruce J Gantz, and Marlan R Hansen. Hearing loss after activation of hearing preservation cochlear implants might be related to afferent cochlear innervation injury. *Otology & neurotology: official publication of the American Otological Society, American Neurotology Society [and] European Academy of Otology and Neurotology*, 36 (6):1035, 2015.

Magne Kringlebotn, T Gundersen, A Krokstad, and Ø Skarstein. Noise-induced hearing losses: can they be explained by basilar membrane movement? *Acta Oto-Laryngologica*, 86(sup360):98–101, 1978.

Emile ter Kuile. Die richtige bewegungsform der membrana basilaris. *Archiv für die gesamte Physiologie des Menschen und der Tiere*, 79(9):484–509, 1900. URL https://doi.org/10.1007/BF01795325.

Francis K Kuk. Maximum usable real-ear insertion gain with ten earmold designs. *Journal of the American Academy of Audiology*, 5(1):44–51, 1994.

Yizeng Li and Karl Grosh. Direction of wave propagation in the cochlea for internally excited basilar membrane. *The Journal of the Acoustical Society of America*, 131(6): 4710–4721, 2012.

Zhe-Xi Luo, Irina Ruf, Julia A Schultz, and Thomas Martin. Fossil evidence on evolution of inner ear cochlea in jurassic mammals. *Proceedings of the Royal Society B: Biological Sciences*, 278(1702):28–34, 2011.

Marc J Madou. *Fundamentals of microfabrication: the science of miniaturization*. CRC press, 2018.

Torsten Marquardt and Johannes Hensel. A simple electrical lumped-element model simulates intra-cochlear sound pressures and cochlear impedance below 2 khz. *The Journal of the Acoustical Society of America*, 134(5):3730–3738, 2013.

Hugh J McDermott and Valerie Looi. Perception of complex signals, including musical sounds, with cochlear implants. In *International congress series*, volume 1273, pages 201–204. Elsevier, 2004.

Julien Meaud and Karl Grosh. The effect of tectorial membrane and basilar membrane longitudinal coupling in cochlear mechanics. *The Journal of the Acoustical Society of America*, 127(3):1411–1421, 2010.

Albert Mudry and Mara Mills. The early history of the cochlear implant: a retrospective. *JAMA Otolaryngology–Head & Neck Surgery*, 139(5):446–453, 2013.

Hideko Heidi Nakajima, Wei Dong, Elizabeth S Olson, Saumil N Merchant, Michael E Ravicz, and John J Rosowski. Differential intracochlear sound pressure measurements in normal human temporal bones. *Journal of the Association for Research in Otolaryngology*, 10(1):23, 2009.

Stephen T Neely and DO Kim. A model for active elements in cochlear biomechanics. *The journal of the acoustical society of America*, 79(5):1472–1480, 1986.

Renato Nobili, Fabio Mammano, and Jonathan Ashmore. How well do we understand the cochlea? *Trends in neurosciences*, 21(4):159–167, 1998.

Elizabeth S Olson. Intracochlear pressure measurements related to cochlear tuning. *The Journal of the Acoustical Society of America*, 110(1):349–367, 2001.

Ali Ostadfar. *Biofluid mechanics: Principles and applications*. Academic Press, 2016.

LC Peterson and Bruce P Bogert. A dynamical theory of the cochlea. *The Journal of the Acoustical Society of America*, 22(3):369–381, 1950.

James O Pickles. An introduction to the physiology of hearing. 4th. *UK: Emerald Group Publishing Limited*, 2012.

Marcus Pietsch, L Aguirre Dávila, P Erfurt, E Avci, T Lenarz, and A Kral. Spiral form of the human cochlea results from spatial constraints. *Scientific reports*, 7(1):1–11, 2017.

André Preument. *Vibration Control of Active Structures An Introduction*. Springer International Publishing, 2018.

Sunil Puria. Measurements of human middle ear forward and reverse acoustics: implications for otoacoustic emissions. *The Journal of the Acoustical Society of America*, 113(5):2773–2789, 2003.

Alicia M Quesnel, Hideko Heidi Nakajima, John J Rosowski, Marlan R Hansen, Bruce J Gantz, and Joseph B Nadol Jr. Delayed loss of hearing after hearing preservation cochlear implantation: Human temporal bone pathology and implications for etiology. *Hearing research*, 333:225–234, 2016.

Tianying Ren and Alfred L Nuttall. Basilar membrane vibration in the basal turn of the sensitive gerbil cochlea. *Hearing research*, 151(1-2):48–60, 2001.

Tianying Ren, Wenxuan He, and David Kemp. Reticular lamina and basilar membrane vibrations in living mouse cochleae. *Proceedings of the National Academy of Sciences*, 113(35):9910–9915, 2016.

William S Rhode and NIGEL P Cooper. Nonlinear mechanics in the apical turn of the chinchilla cochlea in vivo. *Aud. Neurosci*, 3(101):U121, 1996.

J Thomas Roland Jr, Bruce J Gantz, Susan B Waltzman, and Aaron J Parkinson. Long-term outcomes of cochlear implantation in patients with high-frequency hearing loss. *The Laryngoscope*, 128(8):1939–1945, 2018.

George R.T. Ross. *Aristotle De Sensu and De Memoria. Text and Translation, with Introduction and Commentary, by G.R.T. Ross ...* The University Press, 1906. URL https://books.google.co.uk/books?id=g4dCygAACAAJ.

Till Ruemenapp and Dirk Peier. Dielectric breakdown in aluminium nitride. In *1999 Eleventh International Symposium on High Voltage Engineering*, volume 4, pages 373–376. IET, 1999.

Christopher Shera. Symmetries and asymmetries in cochlear mechanics. *Workshop on the Mathematics of Hearing*, 2017.

Christopher A Shera and George Zweig. A symmetry suppresses the cochlear catastrophe. *The Journal of the Acoustical Society of America*, 89(3):1276–1289, 1991.

EG Shower and Rulon Biddulph. Differential pitch sensitivity of the ear. *The Journal of the Acoustical Society of America*, 3(2A):275–287, 1931.

Charles R. Steele and Larry A. Taber. Comparison of wkb and finite difference calculations for a two-dimensional cochlear model. *The Journal of the Acoustical Society of America*, 65(4):1001–1006, 1979a. . URL https://doi.org/10.1121/1.382569.

Charles R. Steele and Larry A. Taber. Comparison of wkb calculations and experimental results for three-dimensional cochlear models. *The Journal of the Acoustical Society of America*, 65(4):1007–1018, 1979b. . URL https://doi.org/10.1121/1.382570.

Charles R. Steele and J Zais. Basilar membrane properties and cochlear response. In *Mechanics of Hearing*, pages 29–36. Springer, 1983.

Stefan Stenfelt. Inner ear contribution to bone conduction hearing in the human. *Hearing research*, 329:41–51, 2015.

Stanley Smith Stevens and Hallowell Davis. *Hearing: its psychology and physiology.* Wiley, 1938.

Stanley Smith Stevens, Hallowell Davis, and MH Lurie. The localization of pitch perception on the basilar membrane. *The Journal of General Psychology*, 13(2):297–315, 1935.

Stanley Smith Stevens, John Volkmann, and Edwin Broomell Newman. A scale for the measurement of the psychological magnitude pitch. *The journal of the acoustical society of america*, 8(3):185–190, 1937.

Wei Sun and Wenxiang Hu. Lumped element multimode modeling of balanced-armature receiver using modal analysis. *Journal of Vibration and Acoustics*, 138(6), 2016.

Mario Svirsky. Cochlear implants and electronic hearing. *Physics Today*, 70(8):52–58, 2017. . URL https://doi.org/10.1063/PT.3.3661.

Nguyen Dien Kha Tu, Myoung-Sub Noh, Youngpyo Ko, Jong-Ho Kim, Chong Yun Kang, and Heesuk Kim. Enhanced electromechanical performance of p (vdf-trfe-ctfe) thin films hybridized with highly dispersed carbon blacks. *Composites Part B: Engineering*, 152:133–138, 2018.

Thomas R van de Water. Historical aspects of inner ear anatomy and biology that underlie the design of hearing and balance prosthetic devices. *The Anatomical*

Record: Advances in Integrative Anatomy and Evolutionary Biology, 295(11):1741–1759, 2012.

Carl Verschuur, William Hellier, and Chermaine Teo. An evaluation of hearing preservation outcomes in routine cochlear implant care: Implications for candidacy. *Cochlear implants international*, 17(sup1):62–65, 2016.

Max A Viergever and JJ Kalker. On the adequacy of the peterson-bogert model and on the effects of viscosity in cochlear dynamics. *Journal of Engineering Mathematics*, 8(2): 149–156, 1974.

Max A Viergever and JJ Kalker. A two-dimensional model for the cochlea. *Journal of Engineering Mathematics*, 9(4):353–365, 1975.

G von Bekesy. Zur theorle des horens 1 uber die bestimmung des elnem relnen tonempflnden entsprechenden erregungsge-bletes der basllarmembran vermlttelst ermudungsersohelnungen. *Physllallsche Zeltschrlft*, 30:115–125, 1929.

Ernest Glen Wever. *Theory of hearing*. Wiley, 1949.

Tony Wright, A Davis, G Bredberg, L Ülehlová, and H Spencer. Hair cell distributions in the normal human cochlea: a report of a european working group. *Acta Oto-Laryngologica*, 104(sup436):15–24, 1987.

Haisheng Xu, Z-Y Cheng, Dana Olson, T Mai, QM Zhang, and G Kavarnos. Ferroelectric and electromechanical properties of poly (vinylidene-fluoride–trifluoroethylene–chlorotrifluoroethylene) terpolymer. *Applied Physics Letters*, 78(16):2360–2362, 2001.

Lin Xue, Houguang Liu, Wenbo Wang, Jianhua Yang, Yu Zhao, and Xinsheng Huang. The role of third windows on human sound transmission of forward and reverse stimulations: A lumped-parameter approach. *The Journal of the Acoustical Society of America*, 147(3):1478–1490, 2020.

Yong-Jin Yoon, Sunil Puria, and Charles R Steele. Intracochlear pressure and derived quantities from a three-dimensional model. *The Journal of the Acoustical Society of America*, 122(2):952–966, 2007.

Chuming Zhao. *Ultraminiature Piezoelectric Implantable Acoustic Transducers for Biomedical Applications*. PhD thesis, Mechanical Engineering, The University of Michigan, 2018.

George Zweig, R Lipes, and JR Pierce. The cochlear compromise. *The Journal of the Acoustical Society of America*, 59(4):975–982, 1976.

Józef Zwislocki. Theory of the acoustical action of the cochlea. *The Journal of the Acoustical Society of America*, 22(6):778–784, 1950.

Józef Zwislocki-Mościcki. *Theorie der Schneckenmechanik: qualitative und quantitative analyse*. PhD thesis, ETH Zurich, 1948.